DEVELOPMENT OF TOOLS TO ESTIMATE ACTUAL CORROSION GROWTH RATES OF GAS PIPELINES

Final Report
SwRI® Project 20.14082
Contract Number: DTPH 56-08-T-000003

Prepared for

U.S. Department of Transportation
Pipeline Hazardous Materials Safety Administration
400 Seventh Street, SW, Room 2103
Washington, DC 20590

Prepared by

Frank Song
Southwest Research Institute®
6220 Culebra Road
San Antonio, TX 78238

October 2011

SOUTHWEST RESEARCH INSTITUTE®
SAN ANTONIO HOUSTON WASHINGTON, DC

DEVELOPMENT OF TOOLS TO ESTIMATE ACTUAL CORROSION GROWTH RATES OF GAS PIPELINES

Final Report
SwRI® Project 20.14082
Contract Number: DTPH 56-08-T-000003

Prepared for

U.S. Department of Transportation
Pipeline Hazardous Materials Safety Administration
400 Seventh Street, SW, Room 2103
Washington, DC 20590

Prepared by

Frank Song
Southwest Research Institute®
6220 Culebra Road
San Antonio, TX 78238

October 2011

Gary R. Walter for D. Ferrill

David Ferrill, Director
Department of Earth, Material, and Planetary Sciences
Southwest Research Institute

EXECUTIVE SUMMARY

Both external and internal corrosion of gas pipelines can pose threats to pipeline safety by thinning the pipe wall, leading to leaks or ruptures. To ensure the pipeline safety, it is important to know both pipeline internal and external corrosion rates. The corrosion rates can be used to determine inspection intervals for inline inspection and pressure tests or the reassessment interval for direct assessments. For external corrosion, the corrosion rate under a coating disbonded from a pipe surface is of most concern because it cannot be measured in the field. The default corrosion rate (0.4 mm/y in the NACE Standard SP 0502-2008) is generally too large for most conditions. It has been argued that a cathodic protection (CP) permeable coating may significantly mitigate pipeline external corrosion even when the coating disbonds. However, it is also argued that under a so-called CP-impermeable (or shielding) coating, such as high density polyethylene coating or a three-layer coating, CP may still provide protection because its current penetrates the coating-disbonded region through the holiday (when present). It is unclear how effective these coatings are in protecting the pipeline external surface when disbonded. For internal corrosion, the chemistry and condition at the pipe surface control the corrosion rate, although they cannot be directly measured or known. The amount of liquid water inherently different in the dry and wet gas pipelines can significantly affect the corrosion rate, while the same models have so far been used for predicting the different corrosion rates.

In an earlier Pipeline and Hazardous Materials Safety Administration (PHMSA)-funded project (DTRS56-04-T-0002 completed in 2006), models were developed to predict pipeline external and internal corrosion rates for natural gas pipelines. However, the external model did not consider the effect of coating permeability and the effect of the geometry of the coating disbondment. The internal corrosion model was unable to distinguish the different corroding conditions for wet and dry gas pipelines.

The objective of this work is to expand the earlier modeling work and develop guidelines for pipeline operators to predict corrosion growth rates through

- Improving the existing external corrosion rate model of Southwest Research Institute® (SwRI®) to include the effect of coating permeability including carbon dioxide (CO_2) and the geometry of the coating disbondment, and validating the model with laboratory and field data,
- Developing a thin-film internal corrosion model to predict the pipe corrosion rates in dry gas pipelines due to gas quality upsets, and validating the model using laboratory and field corrosion growth rate data, and
- Improving the current SwRI internal corrosion rate model for wet gas pipelines by including the effects of carbon dioxide (CO_2) hydrogen sulfide (H_2S), and oxygen (O_2), and validating the model using laboratory and field corrosion rate data.

For both internal and external corrosion, comprehensive mechanistic models were developed in this work. These mechanistic models form the foundation of this modeling work and were validated with laboratory data and field data or field observations. Methods were then developed to simplify the models, and the simplified models were verified. Finally, practical guidelines were developed that may be used to guide field corrosion rate predictions.

For external corrosion, the models enable predicting the chemistry and corrosion rate in a coating-disbonded region when the disbondment gap varies with location, for different CP levels at the holiday, and when the coating is and is not permeable to CP current and oxygen or carbon dioxide. The model-predicted results are qualitatively consistent with laboratory test results in terms of pH, chloride concentration, and potentials measured in simulated coating-disbonded regions. A few key model results are summarized.

Unlike conventional crevice corrosion often associated with a large cathode-to-anode area ratio, the area ratio for the pipeline corrosion under a disbonded coating is rather small. Irrespective of CP levels, the pH in the disbonded region falls in the neutral or alkaline range as long as the soil is not acidic. Predicted corrosion rate is, in this case, not significant. Pitting, microbiologically induced corrosion, and corrosion due to alternative current or direct current interferences are not part of this study.

When the pipe surface at a holiday is maintained with CP (e.g., -850 mV or -900 mV vs. copper/copper sulfate (CSE)), irrespective of coating permeability to CP, the pH in the coating-disbonded region increases over time and the corrosion rate decreases. With time, the pH in the disbonded region may exceed that near the holiday. In the absence of CP and in aerated soil, the overall pH in the disbonded region decreases over time and can fall below that near the holiday.

CP shielding is perhaps partially true for coatings with a holiday. In the presence of CP, the increase of pH over time in coating-disbonded regions and the shift of potential in a more negative direction reduces the local corrosion rate over time. Corrosion may happen when the soil is aerated and wet and the CP is either lacking or inadequate.

The variation of gap with location in a coating-disbonded region (narrow-gapped region is ¼ of the gap elsewhere) appears to have an insignificant effect on the solution chemistry and corrosion rate (relative to a disbondment of uniform gap). The gap effect on the solution chemistry, such as sodium ion (Na^+) concentration if present, may be summarized as follows. With CP, as the gap narrows (in the direction away from the holiday) Na^+ tends to accumulate and its concentration increases. Conversely, as the gap expands, the Na^+ diffusion flux decreases and it tends to dissipate out, leading to a reduced concentration.

A permeable coating behaves like a membrane, which, under cathodic polarization at the holiday, tends to raise the cation (e.g., Na^+) concentration and pH more rapidly (relative to an impermeable coating). The Na^+ concentration and the pH may exceed those at the holiday, and subsequently, the mass transport across the coating starts to reverse to the opposite direction. At a holiday potential of -900 mV_{CSE}, the cathodic current appears to be able to sufficiently suppress the corrosion caused by either O_2 or CO_2 (combination not studied) if it penetrates into the disbonded region both from the holiday and across the coating. The practical implication is that in the presence of sufficient CP, a permeable coating, when disbonded, can still be capable of protecting the substrate steel from corrosion attack.

The model can be scaled with respect to time and geometry of the coating-disbonded region (gap and length). For a disbonded region of uniform gap, such scaling has been verified

by model simulations and is useful for reducing model computations and scaling experiments when needed. The geometry scaling factor is found to be L^2/δ_0 (or $L/\sqrt{\delta_0}$), and the time-scaling factor is t/δ_0, where L is the disbondment length, δ_0 is gap, and t is time.

For pipeline internal corrosion, a comprehensive CO_2 corrosion model was developed and validated with laboratory and field data for a wide range of conditions. This model considers both diffusion and migration of ionic species in solution. The general fundamentals of the model are the same for both wet and dry natural gas pipelines. Nevertheless, the corroding conditions of these two systems are different, and thus the predicted corrosion rates are different.

In dry gas pipelines, ferrous ions as a corrosion product cannot escape the solution boundary layer at the pipe wall, and thus precipitation of $FeCO_3$, for example, will occur. The precipitate reduces mass transport and the exposed pipe surface area available for corrosion, and leads to an overall reduced corrosion rate compared to a wet gas system. For wet gas systems where precipitates can dissolve and travel out of the boundary layer into the bulk solution, precipitation may or may not occur at the steel surface depending on the balance between the formation rate and the dissolution rate of a precipitate. This model result suggests that when an internal corrosion rate in a dry gas system is predicted, the fact that the rate in this dry gas system is smaller than in a wet gas system should be considered.

The model can be simplified by neglecting ionic migration across the solution boundary layer to yield the same results. This simplification can greatly reduce the challenges in numerical solution of the differential equations, from nonlinear to linear equations.

Predicting the effect of H_2S on CO_2 corrosion rate is still a challenge. In this work, charts are provided to show conditions where $FeCO_3$ is dominant over FeS (and vice versa) and the CO_2 corrosion model is applicable. O_2 in a CO_2 corrosion system can increase the corrosion rate by diffusion. In the meantime, the generated hydroxyls from O_2 reduction reduce the corrosion rate. This interactive effect of O_2 on CO_2 corrosion rate leads to a situation that oxygen diffusion is not entirely the controlling step in contributing to CO_2 corrosion. In practical prediction of pipeline internal corrosion, it should be considered that the additive total of CO_2 corrosion rate without O_2 and O_2 corrosion rate (controlled by its diffusion) overestimates the actual corrosion rate.

It is recommended that an industrial survey and field data analysis (a correlation of soil condition, CP level, sample results of chemistry and corrosion in coating-disbonded regions) be performed to understand the conditions where CP both works and fails for a shielding coating. This helps the root causes of pipeline external corrosion.

The effect of solid precipitation on pipeline external corrosion in a coating-disbonded region needs to be studied. It is possible that calcareous deposits formed at the holiday block the pathway of CP penetration into the disbonded region.

The effects of H_2S and O_2 on CO_2 corrosion need to be further explained experimentally before a reliable mechanistic model can be developed for field use.

ACKNOWLEDGMENTS

This project was performed under the DOT Contract DTPH56-08-T-000003. James Merritt (PHMSA/DOT) provided management oversight. The author wishes to thank the Department of Transportation (DOT), Pipeline Research Council International (PRCI), and CenterPoint Energy for their support. During this project, PRCI members of the corrosion committee provided project review and comments on the intermediate results. Mark Piazza of PRCI and Rickey Payne of CenterPoint Energy assisted in putting this project together. The earlier contribution to this project by Dr. Fraser King of Integrity Corrosion Consulting Ltd. and the assistance of Dr. Hui Yu of SwRI is greatly appreciated.

TABLE OF CONTENTS

Page

EXECUTIVE SUMMARY i

ACKNOWLEDGMENTS vi

1.0 INTRODUCTION 1-1
- 1.1 Background 1-1
- 1.2 Objectives 1-3
- 1.3 Technical Approach 1-2
- 1.4 Report Outline 1-3
- 1.5 References 1-3

2.0 PIPELINE EXTERNAL CORROSION 2-1
- 2.1 Background and Objective 2-1
- 2.2 Model Geometry 2-1
- 2.3 General Equations for the Model 2-1
  - 2.3.1 General Governing Equations 2-2
  - 2.3.2 Initial and Boundary Conditions 2-4
- 2.4 Selective Model Results and Model Validation 2-5
- 2.5 Key Model Results and Discussion 2-8
  - 2.5.1 Aerated Dilute NaCl Solution Without CO_2 2-8
    - 2.5.1.1 Crevice Gap Varying with Distance 2-8
    - 2.5.1.2 Crevice Corrosion Considering Penetration of Current and O_2 via Coating 2-9
  - 2.5.2 Dilute NaCl Solution Containing CO_2 2-11
  - 2.5.3 Summary of Model Results 2-12
- 2.6 Model Simplification 2-13
  - 2.6.1 Background 2-13
  - 2.6.2 Scaling Theory for Crevice Corrosion 2-13
  - 2.6.3 Key Model Results and Verification of Scaling Theory 2-14
  - 2.6.4 Summary of the Model Scaling Results 2-17
- 2.7 Practical Implications of the Model Results 2-17
  - 2.7.1 Understanding the Term “CP Shielding” and Corrosion Under a “Shielded” Coating 2-17
  - 2.7.2 The Significance of a Permeable Coating 2-17
  - 2.7.3 The Effect of Crevice Geometry Parameters 2-18
- 2.8 References 2-18

3.0 PIPELINE INTERNAL CORROSION 3-1
- 3.1 Background 3-1
- 3.2 Model Description 3-1
  - 3.2.1 Volumetric Reaction Rates 3-2
  - 3.2.2 Electrochemical Reaction Rates at the Metal Surface 3-3
- 3.3 Reaction Rates and Boundary Conditions for the System of Concern 3-5
  - 3.3.1 Volumetric Reaction Rates 3-6
  - 3.3.2 Initial and Boundary Conditions 3-6
  - 3.3.3 Moving Boundary Condition for a Dry Gas System 3-7
- 3.4 Model Validation with Lab and Field Data 3-8

TABLE OF CONTENTS (Continued)

Page

3.5 Results 3-10
3.6 Model Simplification 3-10
3.7 Effect of H_2S and O_2 on CO_2 Corrosion 3-11
3.8 Summary 3-13
3.9 Practical Implications of the Model Results 3-13
3.9.1 Understanding the Differences in Corrosion Rate Between Wet and Dry Gas Systems 3-13
3.9.2 The Effect of H_2S and O_2 on Pipeline Internal Corrosion Rate 3-14
3.10 References 3-14

4.0 CONCLUSIONS AND RECOMMENDATIONS 4-1
4.1 Conclusions 4-1
4.1.1 Pipeline External Corrosion 4-1
4.1.2 Pipeline Internal Corrosion 4-2
4.2 Recommendations 4-3
4.2.1 Pipeline External Corrosion 4-3
4.2.2 Pipeline Internal Corrosion 4-3

APPENDIX A Derivation of Equation (2-1) as a Model Governing Equation A-1

APPENDIX B Reversible and Irreversible Homogeneous and Heterogeneous Reactions, Chemical Equilibrium Formula, and Kinetic Rates in the Crevice Corrosion System Without CO2 ..... B-1

APPENDIX C Crevice Corrosion Considering the Effect of Flow Induced by Gap Varying with Metal Dissolution C-1

APPENDIX D Derivation of Model Governing Equations with CO_2 in Crevice D-1

APPENDIX E Results of Crevice Corrosion Considering Passivity of Steel at pH 10.5 or Greater E-1

MANUSCRIPTS

MS #1 A mathematical model developed to predict the chemistry and corrosion rate in a crevice of variable gap MS-1

MS #2 Predicting the chemistry, corrosion potential, and rate in a crevice formed between substrate steel and a disbonded permeable coating with a mouth MS-28

MS #3 Theoretical investigation into time and dimension scaling for crevice corrosion MS-42

MS #4 A Model Developed to Predict the Internal Corrosion Rates of Wet and Dry Gas Pipelines.... ..... MS-61

LIST OF FIGURES

Figure Page

1-1 A schematic showing the external corrosion rate-controlling condition in a coating disbonded region 1-4
1-2 A schematic showing the condition at the steel surface for pipe internal corrosion..... 1-5
1-3 A schematic showing the technical approach used in this work to model pipeline internal and external corrosion 1-5

2-1 Model crevice geometry showing the coordinators and dimensions of the crevice and transport 2-22
2-2 At a fixed mouth potential of -0.9 V_{CSE}, evolution of concentrations of (a) Na^+ and (b) Cl^- over time and distance into the disbanded region from the holiday 2-22
2-3 Variation of [Cl^-] with time at various distances from opening 2-23
2-4 Similar to Figure 2-3, but here the mouth potential is fixed at -0.9V_{CSE} 2-23
2-5 pH changes along static simulated cracks, for various potentials applied at the crack mouth, for HY80 steel in seawater 2-24
2-6 Variation of [Cl^-] with time at various distances from opening 2-24
2-7 pH profiles within the crevice after 72 h of test 2-25
2-8 Similar to Figure 2-2, but here the mouth potential is fixed at -0.9V_{CSE} 2-25
2-9 Potential profiles within the crevice at 0.5 hour and at 72 h of test 2-26
2-10 Potential distribution in a 0.13-mm-thick crevice at various times 2-26
2-11 At a fixed mouth potential of -0.8071 V_{CSE}, a comparison of Na^+ concentrations in two crevices at different times 2-27
2-12 Similar to Figure 2-11, but here for a comparison of crevice pHs: (a) near the mouth and (b) away from the crevice mouth 2-27
2-13 Similar to Figure 2-11, but here for a comparison of crevice potentials (a) near the mouth and (b) away from the crevice mouth 2-28
2-14 Similar to Figure 2-11, but here for comparison of crevice corrosion current densities 2-28
2-15 At a fixed mouth potential of -0.9V_{CSE}, a comparison of the model results for four cases studied at both the initial and steady-state conditions 2-29
2-16 Similar to Figure 2-15, but for crevice chemistry: (a) Na^+ concentration, (b) Cl^- concentration, and (c) pH in the crevice 2-29
2-17 At a potential of -0.88V_{CSE} and a CO_2 partial pressure of 0.05 atm at mouth, a comparison of model results obtained when CO_2 permeation through the coating is and is not considered 2-30
2-18 Similar to Figure 2-17, but for crevice chemistry: (a) Na^+ concentration, (b) Cl^- concentration 2-30
2-19 Similar to Figure 2-17, but for crevice pH 2-30
2-20 Similar to Figure 2-17, but for (a) crevice potential and (b) corrosion current density. 2-31
2-21 At a fixed mouth potential of -0.9V_{CSE}, a scaling plot for a comparison of Na^+ concentrations in the three crevices at different times 2-31
2-22 Similar to Figure 2-21, but here the scaling plot is for a comparison of crevice pH 2-32
2-23 Similar to Figure 2-21, but here the scaling plot is for a comparison of (a) crevice potential and (b) corrosion current density 2-32

LIST OF FIGURES (Continued)

Figure Page

3-1 Schematic diagram showing the chemical, electrochemical, and mineral (precipitation) reactions that may occur in a boundary layer 3-15
3-2 Model-predicted maximum (or initial) and steady-state corrosion rates vs. experimental data 3-15
3-3 Model-predicted time-dependent corrosion rates vs. experimental data measured in a solution 3-15
3-4 Model-predicted time-dependent corrosion rates vs. experimental data measured in a solution 3-16
3-5 Model-predicted maximum (or initial) and at 0.1_{th} hour instant corrosion rates vs. experimental data 3-16
3-6 Model-predicted maximum (or initial) and steady-state corrosion rates vs. experimental data measured in lab 3-17
3-7 Model-predicted maximum (or initial) and steady-state corrosion rates vs. experimental data in lab 3-17
3-8 Model-predicted maximum corrosion rates for both wet and dry gas systems at 25 °C 3-17
3-9 Predicted corrosion rates and porosity for only the dry gas system at the same condition of Figure 3-8 3-18
3-10 Model-predicted corrosion rates for both wet and dry gas systems at 25 °C and P_{CO2}=1atm 3-18
3-11 For the same conditions of Figure 3-10, the porosity variations with time for both wet and dry gas systems 3-19
3-12 Verification of model simplification by comparison of corrosion rates obtained from the model by considering and not considering the voltage drops in the boundary layer 3-19
3-13 Region of a dominant precipitate: Siderite or Mackinawite 3-19
3-14 Siderite-Mackinawite boundary determined based on Equation (3-36) for varying temperatures and the ratio of partial pressure 3-20
3-15 The interactive effect of CO_2 and oxygen on steel corrosion 3-20

LIST OF TABLES

Table Page

2-1 Initial and Boundary Conditions for Systems Without CO_2 2-20
2-2 Initial and Boundary Conditions for Systems with CO_2 2-20
2-3 Scenarios Modeled Without CO_2 and Locations of Results 2-21

1.0 INTRODUCTION

1.1 Background

Both external and internal corrosion of gas pipelines can threaten pipeline safety by thinning the pipe wall, leading to leaks or ruptures. External corrosion results mainly from factors such as corrosive soil environment (gas, salts, or bacteria), coating degradation or damage (holiday generation), inadequate cathodic protection (CP), and alternating current or direct current interferences. Internal corrosion occurs due to the presence of liquid water and corrosive gas species, including carbon dioxide, hydrogen sulfide, oxygen, solids, condensates, and bacteria. There is a significant difference in internal corrosion for wet gas and dry gas pipelines due to the significant differences in the amount of corrosive electrolyte present inside the pipelines.

In the pipeline industry, no single approach provides all the necessary information for a confident estimate of the corrosion rate. For external corrosion, the challenge is to understand the conditions at the pipe surface under a coating-disbonded from the pipe. Such conditions, (e.g., solution chemistry) cannot be known or measured directly in the field, although they can control the corrosion process. These conditions under the disbonded coating are, however, linked to the known conditions in the soil, as schematically shown by Figure 1-1(a). This link is governed by the fundamental principles of mass conservation, charge conservation, and chemical reactions in the solution and electrochemical reactions at the metal surface (Figure 1-1(b)). These fundamental principles are the basis of the external corrosion model to be developed.

For internal corrosion, the conditions including corrosion kinetics at the pipe surface are unknown, but these conditions are related to the electrolyte chemistry at the pipe surface, which is further related to the main gas composition (see Figure 1-2). The relationship between the conditions at the pipe surface and those of the liquid electrolyte and the main gas composition is governed by the fundamental principles of mass conservation, charge conservation, and chemical reactions in the electrolyte.

The overall fundamental mechanisms for modeling pipeline corrosion, both internal and external, are the same, although the process and the steps needed for the modeling are different. The author and coworkers have performed significant research to model the processes of pipeline external corrosion and internal corrosion. A work recently completed for PHMSA (DOT contract DTRS56-04-T-0002) involved the development of models for predicting external and internal corrosion rates for natural gas pipelines.[1]

1.2 Objectives

The goal of this work is to expand the earlier modeling work and develop guidelines for pipeline operators to predict field corrosion growth rates through

- Improving the existing external corrosion rate model of SwRI[1] to include the effect of CO_2 permeation from soil into a coating-disbonded region, and validate the model with laboratory and field data,

- Developing a thin-film internal corrosion model to predict corrosion rates in dry gas pipelines due to gas quality upsets (e.g. water condensation), and validating the model using laboratory and field corrosion rate data, and
- Improving the current existing internal corrosion rate model of SwRI[1] for wet gas pipelines by including the effects of CO_2, H_2S, and O_2, and validating the model using laboratory and field corrosion rate data.

1.3 Technical Approach

Mathematical models developed to simulate corrosion processes may be categorized as mechanistic, empirical, or semi-empirical models. Mechanistic models are in general complex and not easy to implement in field applications. By contrast, empirical models are easy to use but not suited for application in conditions beyond the experimental data range used to develop the models. A simplified mechanistic model, on the other hand, can be potentially useful because it allows for data extrapolation and is also easy for field implementation. An overall four-step modeling approach was proposed to develop a mechanistic model and then, use it in the field. This approach is schematically shown in Figure 1-3 and explained next.

The first step, labeled "1" on the left side of the triangle chart, forms the foundation of the modeling approach. In this step, a comprehensive fundamental model is to be developed. Such a model may consist of complex differential equations, such as the Laplace's equation and/or the Nernst-Plank equation. [1-6] The fundamental nature of this model allows the model to be used in broad ranges of conditions.

The second step is validation or calibration of the fundamental model with field or/and laboratory data. Once validated, the model can be used to predict the conditions where either experimental data are lacking or the development of such data can be expensive or impossible. For instance, it would be extremely challenging, even if possible, to directly measure the field corrosion rates in a coating-disbonded region on buried pipelines.

The third step is simplification of the fundamental model into simpler models through mathematical manipulations and sensitivity analyses. During this process, the rate-controlling variables or groups of variables may be identified and only these variables or variable groups need to be used in the simpler models. These simpler models still retain the nature of the fundamental models while requiring only the values of the known controlling variables to evaluate the overall system performance. When necessary, verification and/or further validation of these simpler models may be needed.

The end goal of the overall modeling approach is Step 4, development of guidelines to guide field applications of the model(s). These guidelines can be developed more readily from the simpler relations and from the analysis of the comprehensive model results. When possible, these guidelines could be integrated into industrial standards, regulatory documents, or industrial operating manuals. The success of this step requires a collaborative effort of the research institutions that develop the procedures, the pipeline operators who implement them in field operations, and the regulators who ensure their proper use.

1.4 Report Outline

A significant portion of this report has already been presented in manuscripts for publications in journals or conference proceedings. These manuscripts are appended at the end of this report, and our aim is not to repeat it in the main text. When needed, it will be instead cited or briefly described.

This report will mainly consist of four chapters. Chapter 2 will describe the external corrosion model, Chapter 3 will describe the internal corrosion model, and Chapter 4 will summarize the findings and recommendations for future work.

1.5 References

1. F.M. Song, N. Sridhar, "An Approach to Determining Reassessment Intervals through Corrosion," DOT Contract No. DTRS56-04-T-0002, Final Report submitted in October 2006.
2. F.M. Song, D.W. Kirk, J.W. Graydon, D.E. Cormack, Corrosion 58, 12 (2002): 1015-1024.
3. F.M. Song, D.A. Jones, D.W. Kirk, Corrosion 60, 2 (2005): 145-154.
4. F.M. Song, N. Sridhar, Corrosion 62, 8 (2006): 676-686.
5. F.M. Song, N. Sridhar, Corros. Sci. 50, 1 (2008): 70-83.
6. F.M. Song, Electrochimica Acta 56 (2011): 6789-6803.

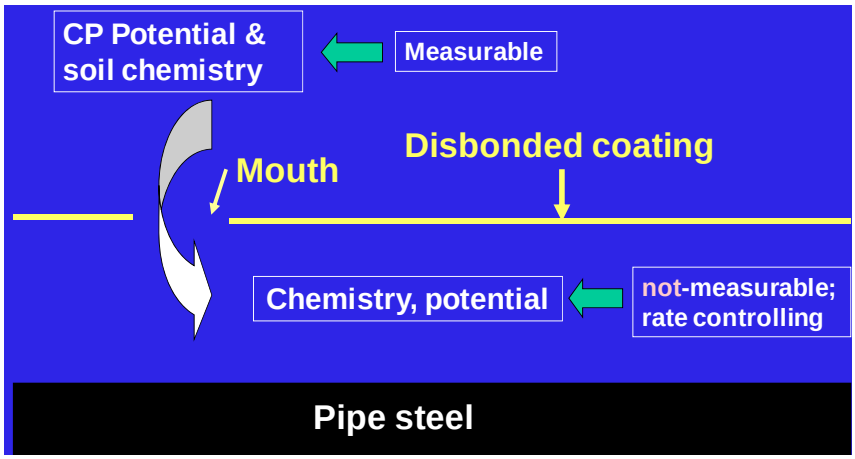

(a)

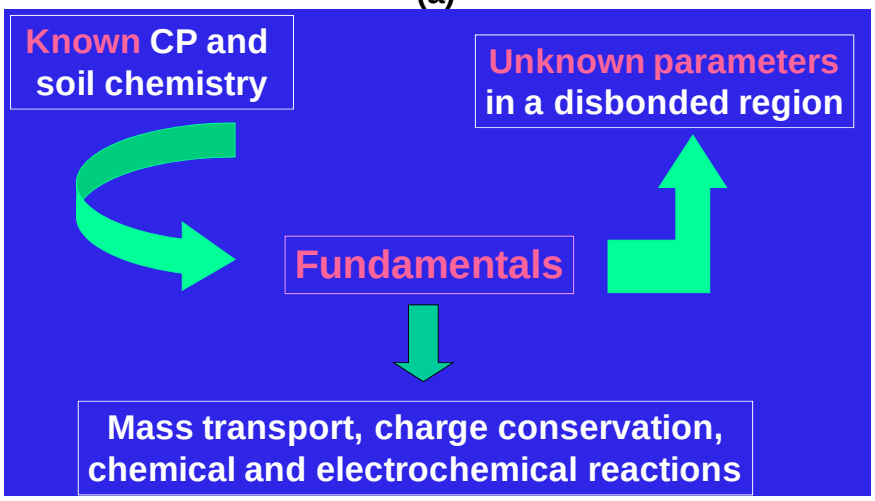

(b)

Figure 1-1. (a) A schematic showing that the external corrosion rate-controlling condition in a coating-disbonded region, which cannot be directly measured, is linked to the measurable conditions in soil. (b) The basis of the modeling that bridges the conditions inside and outside the coating-disbonded region comprises fundamental principles consisting of mass transport, charge conservation, and chemical and electrochemical reactions. These fundamental principles are the basis of the model to be developed.

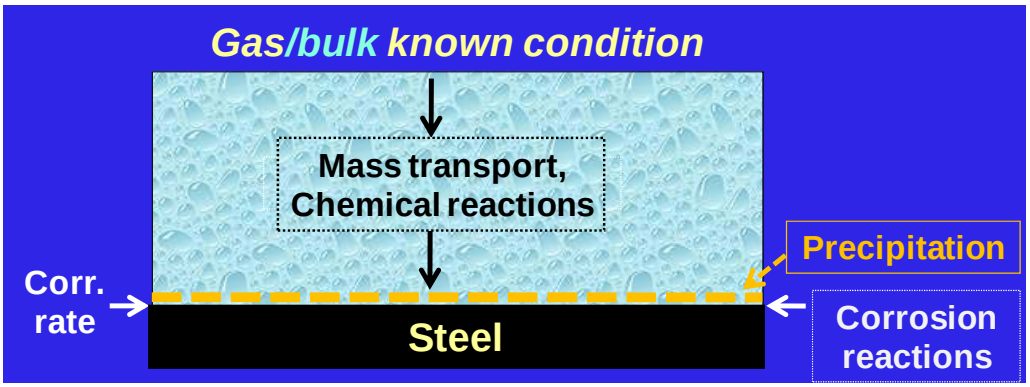

Figure 1-2. A schematic showing that for pipe internal corrosion, the condition at the steel surface, which cannot be directly measured, is linked to the known or measured bulk conditions following fundamental principles and is the basis of the model to be developed. The fundamental principles here consist of mass transport, charge conservation, and chemical reactions.

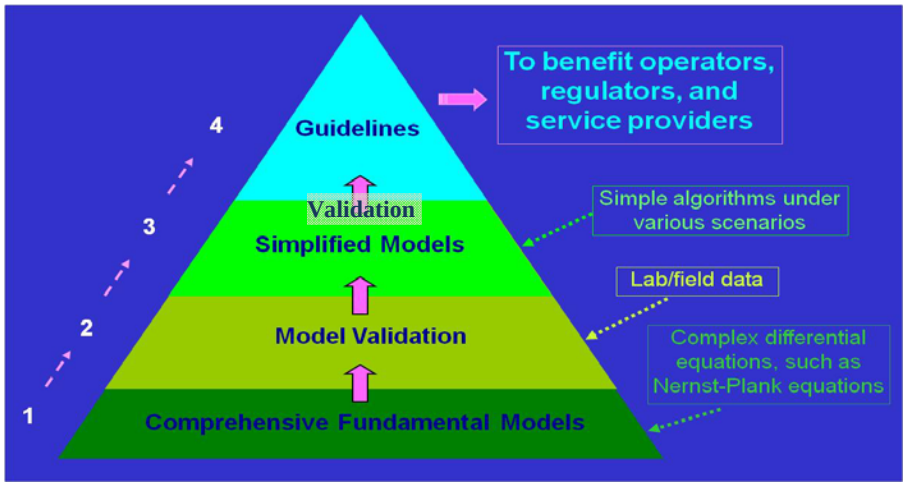

Figure 1-3. A schematic showing the technical approach used in this work to model pipeline internal and external corrosion.

2.0 PIPELINE EXTERNAL CORROSION

2.1 Background and Objective

Significant research has been performed to understand the mechanisms of external corrosion of a steel pipe surface with its coating-disbonded with or without a holiday.[1-25] In laboratory tests[4,17-24] or in mathematical modeling,[5-13] the disbonded region is simulated by a crevice that is generally assumed to have a uniform gap. In reality, this gap rarely is uniform. Even if the gap is initially uniform, it can become nonuniform as the metal dissolves and/or deposits such as precipitates form at different rates along the coating disbondment. In addition, the effect of ionic current or oxygen or carbon dioxide diffusion through a permeable disbonded coating on the pipe corrosion has not been studied in experimental tests, although models were reported that consider the effect of current or oxygen permeation through the coating.[7,13,26,27] A goal of this work is to understand from a fundamental perspective, by mathematical modeling, the effect of variable gap (with location) and the permeability of a coating (to CP and/or oxygen or carbon dioxide) on the pipe corrosion rate. The model results will be used as a guide for simplifying the model and provide guidelines for field use.

2.2 Model Geometry

The crevice geometries to be used in this modeling work, formed when a coating on the steel pipe surface disbonds from the holiday, are shown at the left edge of Figure 2-1. For the crevice geometry shown in Figure 2-1a, the temporal and spatial variation of the crevice chemistry and corrosion potential and rate were modeled extensively in an earlier work.[13] Corrosion in a crevice with its gap varying with distance from the holiday, as shown in Figure 2-1b, has not been studied.

Figure 2-1b represents an extreme case where the gap sharply changes between its size at the holiday and a quarter of the gap at $\frac{x}{\delta_{s0}} = 5$, 6, 15, and 100, where x is distance from the holiday and δ_{s0} is the gap size at the holiday edge. It is expected that such a sharp variation of gap would yield the most significant impact on the crevice corrosion, relative to a gap that varies gradually or is uniform, as shown in Figure 2-1a.

The gap is designed to have abrupt variations at x/δ_{s0}= 5 and 6 because past studies[5-13] showed that the change of variables would occur most strongly within the first 10 gaps from the mouth. Abrupt changes of the gap are designed to also occur in intermediate (x/δ_{s0}= 15) and longer (x/δ_{s0}=100) distances to understand how the gap changes at these locations would have an effect on the corrosion process.

2.3 General Equations for the Model

Equations necessary for predicting the evolution, over time and distance, of the solution chemistry, corrosion potential, and rate in a coating-disbonded region are given in MS #1 attached at the end of this report. This section provides more general fundamental equations for the model.

2.3.1 General Governing Equations

For a dilute solution containing multiple species in a one-dimensional crevice, mass conservation for an arbitrary species numbered by i may be written as

$$\delta_s \frac{\partial c_i}{\partial t} + \overline{v}_x \delta_s \frac{\partial c_i}{\partial x} + \frac{\partial}{\partial x}(\delta_s N_{ix}) + N_{iyc} = \delta_s R_i + R_{si} \tag{2-1}$$

The derivation of Equation (2-1) is shown in Appendix A. In Equation (2-1), c_i is concentration of the ith species in the solution; R_i is the total net volumetric production rate (after consumption deducted) of the ith species; R_{si} is the total surface reaction rate of the ith species including corrosion reactions; subscripts x and y refer to x and y coordinators (e.g., see Figure 1a); and δ_s is gap at distance x and varies with x and time t. Other terms in Equation (2-1) are defined in the following discussion. The variation of δ_s with t can be the result of depletion of the metal by corrosion as follows:

$$\frac{\partial \delta_s}{\partial t} = \beta r_{Fe} \tag{2-2}$$

With Equation (2-2), the average flow velocity across the gap, $\overline{v}_x$, which results from the variation of δ_s with t, can be determined by

$$\overline{v}_x = \beta \delta_s^{-1} \int_x^L r_{Fe} dx \tag{2-3}$$

where r_{Fe} is the corrosion rate, L is the total length of the disbondment, and β is a unit conversion factor from steel corrosion rate r_{Fe} in mol/m^2/s to m/s, or

$$\beta = \frac{10^{-3} M_M}{\rho_M} \tag{2-4}$$

where M_M and ρ_M are molar weight and density of the metal (steel), respectively, in standard units.

In Equation (2-1), N_i is flux of the ith species in the solution and can be expressed by

$$N_i = -D_i(\nabla \cdot c_i - \frac{z_i F}{RT} c_i \nabla \phi) \tag{2-5}$$

where D_i and z_i are diffusion coefficient and charge of the ith species; F, R, respectively and T are Faraday's constant, universal gas constant, and temperature, respectively and ϕ is electrostatic potential of the solution.

When the velocity in Equation (2-1) can be neglected due to negligible variation of the gap with time, Equation (2-1) becomes

$$\delta_s \frac{\partial c_i}{\partial t} + \frac{\partial}{\partial x}(\delta_s N_{ix}) + N_{iyc} = \delta_s R_i + R_{si} \tag{2-6}$$

In Equation (2-1) or (2-6), the total net production rate of the ith species, R_i, can result from homogenous reactions in solution, such as CO_2 hydration if present, and mineral (precipitation) reactions, while it is only the former reactions that are of concern in this modeling work for external corrosion.

For a homogeneous reaction involving the ith species, for such a reaction numbered by h, in the form of

$$\sum_i \nu_{i_r,h} A_{i_r} \leftrightarrow \sum_i \nu_{i_p,h} A_{i_p} \tag{2-7}$$

where the subscripts r and p represent reactant and product, respectively, the volumetric reaction rate may be written as[28]

$$r_h = k_{h_f} \prod_i c_i^{\nu_{i_r,h}} - k_{h_b} \prod_i c_i^{\nu_{i_p,h}} \tag{2-8}$$

where k_{h_f} and k_{h_b} are the forward and backward reaction rate constants, respectively. The total net volumetric production rate of the ith species for all such reactions is

$$R_i = \sum_h \nu_{i,h} r_h \tag{2-9}$$

At the steel surface, only the electrochemical reactions are of concern; the total rate for the ith species yields R_{si}. For such a reaction numbered by e, in the form of

$$\sum_i \nu_{i_r,e} M_{i_r}^{z_{i,r}} \leftrightarrow \sum_i \nu_{i_p,e} M_{i_p}^{z_{i,p}} + n_e e^- \tag{2-10}$$

where z_i represents charge carried by the species M_i, the following charge balance must be met

$$\sum_e \nu_{i,e} z_i - n_e = 0 \tag{2-11}$$

where $\nu_{i,e}$ and n_e are, respectively, the stoichiometric coefficient of the ith species and the number of electrons transferred during the eth electrochemical half-cell reaction.

The total net production rate of all the electrochemical reactions involving the ith species is

$$R_{si,e} = \sum_e \nu_{i,e} r_{i,e} = \sum_e \frac{\nu_{i,e} i_{i,e}}{n_e F} \tag{2-12}$$

where $i_{i,e}$ is anodic or cathodic current density involving the ith species.

The current density of the eth electrochemical reaction (Equation (2-10)) may be generally written by the Butler-Volmer equation as[29]

$$i_e = i^0_{e_ref}\left(\prod_i \left(\frac{c_i}{c_{i_ref}}\right)^{\nu_{i_r,e}} \exp\left(\frac{\alpha_{a_e}F}{RT}\eta_e\right) - \prod_i \left(\frac{c_i}{c_{i_ref}}\right)^{\nu_{i_p,j}} \exp\left(-\frac{\alpha_{c_e}F}{RT}\eta_e\right)\right) \quad (2\text{-}13)$$

or by the Tafel equations when either the anodic or the cathodic portion of the electrochemical reaction is rate controlling. $i^0_{e_ref}$ is exchange current density of Equation (2-10) at a reference condition corresponding to the concentration of the ith species c_{i_ref}; α_{a_e} and α_{c_e} are transfer coefficients of the anodic and cathodic half-cell reactions, respectively; and η_e is overpotential or the electrode potential relative to that at the reference condition.

For corrosion of pipe steel in a coating-disbonded region, the anodic reaction is iron oxidation

$$Fe \rightarrow Fe^{2+} + 2e^- \quad (2\text{-}14)$$

The cathodic reactions are

$$H^+ + e^- \rightarrow 0.5H_2 \quad (2\text{-}15)$$

$$H_2O + e^- \rightarrow 0.5H_2 + OH^- \quad (2\text{-}16)$$

$$4H^+ + O_2 + 4e^- \rightarrow 2H_2O \quad (2\text{-}17)$$

and, in the presence of CO_2,

$$H_2CO_3 + e^- \rightarrow H_2CO_3^- + 0.5H_2 \quad (2\text{-}18)$$

The total net surface reaction rate of the ith species in Equation (2-1) or (2-6) is

$$R_{si} = \sum_e R_{si,e} \quad (2\text{-}19)$$

2.3.2 Initial and Boundary Conditions

The initial and boundary conditions for solving the model-governing equations in this work are given for two scenarios: (1) no CO_2 in the corrosion system (Table 2-1) and (2) CO_2 present in the corrosion system (Table 2-2). Table 2-1 also shows the initial and boundary conditions in a model presented in an earlier work[13] where the initial and mouth conditions are the same. For either scenario, only concentrations of the primary species are provided with the realization that the concentrations of the secondary species are dependent on and can be determined from the concentrations of the primary species through the equilibrium relations

between the primary and the secondary species. The equilibrium relations involved for both scenarios of pipeline external corrosion are provided in Appendix B.

For Scenario (1) without CO_2, the crevice solution used in the modeling of this work is an aerated dilute sodium chloride solution simulating soil water absent of CO_2. Shown in Table 2-1, the bulk chemistry is different from that initially present in the disbonded region with the latter more dilute, and both solutions are assumed to be saturated by ferrous hydroxide, which is only sparsely soluble in water. Neglecting the effect of homogeneous ferrous ion oxidation on the crevice corrosion rate due to justifications given elsewhere,[27,30] the following species in the solution are of concern: (1) $\underline{Na^+}$, (2) $\underline{Cl^-}$, (3) Fe^{2+}, (4) $\underline{H^+}$, (5) OH^-, (6) $Fe(OH)^+$, (7) $\underline{O_2}$, (8) $\underline{H_2(aq)}$, (9) $\underline{Fe(OH)_2}$, and (10) $\underline{H_2O}$, where the underlined species are defined as the primary species. Some of their concentrations can be known, such as species (8)-(10), and the concentrations of the remaining primary species are given in Table 2-1 together with the potential at the holiday. The concentrations of the secondary species, or species (3), (5), and (6), can be computed from the concentrations of the primary species based on the equilibrium equations given in Appendix A.

For Scenario (2) with CO_2, the solution species are (1) $\underline{Na^+}$, (2) $\underline{Cl^-}$, (3) Fe^{2+}, (4) $\underline{H^+}$, (5) OH^-, (6) $Fe(OH)^+$, (7) $\underline{CO_2}$, (8) H_2CO_3, (9) HCO_3^-, (10) $\underline{CO_3^{2-}}$, (11) $\underline{H_2(aq)}$, (12) $\underline{FeCO_3}$, and (13) $\underline{H_2O}$. The concentrations of the primary species underlined are either given in Table 2-2 or known such as species (11)-(13). The solution is assumed to be saturated by ferrous carbonate with a very low solubility. The concentrations of the secondary species can be determined from the concentrations of the primary species. As shown in Table 2-2, the bulk chemistry is different from that initially present in the disbonded region with the latter more dilute.

The boundary condition at the mouth for both scenarios is a constant concentration and a fixed potential (see Tables 2-1 and 2-2). The boundary condition at the crevice tip is zero flux for each species and zero current. The coating at the crevice tip is considered to be impermeable to ionic and molecular species.

2.4 Selected Model Results and Model Validation

Model results obtained from using the crevice geometry of Figure 2-1(a) with a uniform gap are used to qualitatively compare with laboratory data. Only model results obtained from chemistry absent of CO_2 for a mouth potential of -0.900 V vs. saturated $Cu/CuSO_4$ electrode (CSE) are used for this comparison. In this section, the model results are also discussed where needed. Such a model validation will also be made briefly in Section 2.5.2 when the model results for a solution containing CO_2 are discussed.

Figure 2-2 shows the Na^+ and Cl^- concentrations obtained in this work and those obtained in an earlier work.[13] Shown in Table 2-1, the initial and mouth concentrations are the same for earlier work and they are different for this work. For both works, the mouth potential was -0.9 V_{CSE}, representing significant CP.

Figure 2-2(a) shows that Na^+ concentration increases over time for both works. This increase in Na^+ concentration results from the synergistic action of Na^+ diffusion and migration

into the crevice. The diffusion results from a higher concentration of Na^+ at the mouth, and the migration results from a more negative steel potential at the mouth imposed by CP (relative to the potential inside the crevice) and the positive charge carried by Na^+. The potential that is more negative at the mouth than inside the crevice creates an electrochemical driving force that pumps Na^+ into the crevice. The Na^+ concentration obtained in this work is overall smaller than that in the previous work because a smaller initial concentration was given with this work. However, the difference in Na^+ concentration between these two works decreases over time and disappears at 10^7 s, when steady state is reached. Over time, the Na^+ concentration in the crevice becomes greater than that at the mouth and leads to the Na^+ diffusion reversed in direction. With a greater concentration inside the crevice, Na^+ now tends to diffuse from inside the crevice toward the mouth and counters the driving force of migration, which, driven by CP, still pumps Na^+ into the crevice from the mouth. When the diffusion and migration rates in opposite directions balance each other, steady state is reached.

Figure 2-2(b) shows the evolution of Cl^- concentration in the crevice. For both works, the initial Cl^- concentration is uniform in the crevice, although the magnitude is different. Carrying a negative charge, Cl^- is pumped out from the crevice by CP. For the previous work, with the same concentration at the mouth and initially in the crevice, the Cl^- concentration decreases over time until steady state is reached at 10^7 s. This result is generally consistent with the experimental results shown in Figure 2-3.[31] where under cathodic polarization with the mouth potential of -1.00 V_{SCE}, the Cl^- concentration measured at the three locations: (4, 15,and 18 cm inside the crevice from the mouth) decreases over time, although within the time of the test and with the mouth Cl^- concentration not maintained, the Cl^- concentration near the mouth instead drops quickly and becomes smaller than inside the crevice.

For the present modeling work, the Cl^- concentration at the mouth is set to be greater than initially in the crevice, and thus, Cl^- tends to diffuse into the crevice, opposite to the direction of Cl^- migration driven by CP. The countering balance between Cl^- migration and diffusion in opposite directions is the net flux of Cl^-. In Figure 2-2(b), the sharp increase of Cl^- concentration near the mouth suggests that near the mouth, Cl^- diffusion is dominant over migration. With time, as the Cl^- concentration in the crevice increases and the Cl^- concentration gradient decreases near the mouth, this diffusion dominance decreases. When the diffusion flux balances the migration flux, steady state is established and the Cl^- concentration merges to the curve at 10^7 s, the same curve of the earlier work.[13] In both this work and the earlier work, because CP tends to draw out Cl^- from inside the crevice, the Cl^- concentration in the crevice cannot surpass its concentration at the mouth..

Figure 2-4 shows a comparison of crevice pHs obtained in this work and the earlier work. The pHs in both works increase over time (reasons were detailed elsewhere[13]). The Na^+ concentration in the crevice becomes progressively greater than Cl^-, and their net positive charge is mainly balanced by OH^- formed from cathodic reactions (e.g., water reduction) which accumulates inside the crevice. In essence, the original NaCl solution is partially substituted by NaOH solution. With in-crevice Na^+ and Cl^- concentrations initially smaller in this work than in the earlier work, the pH of this work is smaller than that of the earlier work and their largest difference is shown at intermediate times, such as 10^4 s. At steady state or 10^7 s, the two curves merged into one. The model-predicted variation, in time and location, of the crevice pH under

CP is in qualitative agreement with experimental data reported in earlier papers [19-22,25,32] and with field observations where calcareous deposits and alkaline pH were found under a disbonded high density polyethylene (HDPE)-coating, suggesting ingression of CP through the holiday and alkalinity of the solution inside the disbondment.

Landles et al.[32] conducted experimental tests at room temperature to simulate a crack by using a crevice (0.25 mm in thickness and 7 cm in length) assembled between an HY80 steel plate (bottom) and an acrylic plate (top). All the crevice edges except the mouth were sealed with a gasket. The mouth directly connected to the bulk solution with the same chemistry as at the mouth (1N CO_3^{2-} and 1N HCO_3^- solution) and was maintained constant over time. Reference electrodes and pH electrodes were placed through holes in the acrylic plate with the tip facing downward into the crevice solution. The holes were equally spaced along the crevice longitudinal direction from the mouth and epoxy sealed. These electrodes were used to measure the local steel potentials and pHs in the crevice.

Figure 2-5 shows the pH variation vs. distance along the crevice for different potentials applied at the crevice mouth. In general, the crevice pH shifts toward the acidic direction when the mouth potentials are more positive than the open circuit potential (OCP) slightly more negative than -0.7 V_{SCE}. Conversely, the pH shifts toward the alkaline direction when the potentials were more negative than the OCP, relevant to the model results in Figure 2-4. The qualitative agreement between the model and experimental results is good.

When the mouth is cathodically polarized and the pH at the mouth is not controlled, unlike in Figure 2-5 other studies [20,31,33] show that the pH at the mouth increases more rapidly than inside the crevice. Within the time of test, Figure 2-6 shows that except at the two locations (8 and 12 cm from the mouth), the farther into the crevice the lower the pH.[31] Under all conditions, the pH in the entire crevice has a significant shift toward the alkaline direction. At 18 cm from the mouth or at the farthest end of the crevice, the pH increased from 6.5 to above 8.5.[31] This general trend with the crevice pH shifting toward the alkaline direction is consistent with the results predicted from this model. Corresponding to the change of pH, the same study showed the corresponding change of Cl^- concentration over time as shown in Figure 2-3. Figure 2-3 shows that a higher pH corresponds to a lower Cl^- concentration, because CP draws Cl^- out from inside the crevice. This experimental result is in general agreement with the results of this model. The model shows that CP tends to pump Na^+ in and draw Cl^- out of the crevice, and OH^- balances the difference in charge between Na^+ and Cl^- and the solution pH increases. From a different study,[33] Figure 2-7 shows that with CP, the pH in the entire crevice is elevated, and for two potentials applied at the mouth (-1.00 V_{SCE} and -1.20 V_{SCE}), the pH in the crevice is higher than at the mouth.

Figure 2-8 shows a comparison of the crevice potential and current density at different times obtained in this work and in the earlier work.[13] A significant difference is seen at time zero, and the potential or the corrosion current density has a sharp change at the mouth. At 10^7 s, the two curves are merged into one irrespective of the different initial conditions. For both works, the potential in the entire crevice shifts in the more negative direction except at the mouth where the potential is maintained unchanged. Farther into the crevice from the mouth, the

potential shift (relative to open circuit potential) is less significant. This shift in potential agrees qualitatively with many experimental results.

Figure 2-9 shows crevice steel potential at different times, measured at (1) 0.5 hour and (2) 72 hours from beginning of the test.[33] A comparison of the two figures suggests that the presence of CP shifted the potential in the entire crevice toward the more negative direction, and the closer the location in the crevice to the mouth the more significant the shift in potential. Similar results[33] are also shown in Figure 2-10.

2.5 Key Model Results and Discussion

2.5.1 Aerated Dilute NaCl Solution Without CO_2

Several scenarios were modeled, and the results were prepared as three manuscripts (MS #1, #2, and #3) for publication in journals and conference proceedings. These manuscripts are appended at the end of this report, and only some key results are presented in this section. In addition to the manuscripts, Appendix C reports the results of the effect of convective flow, induced by corrosion itself due to metal depletion (or formation of deposits) on the crevice corrosion. For the two conditions presented in Appendix C (no CP and significant CP), it is found that the flow velocity is extremely small and its effect is insignificant. These results in Appendix C will not be described further in the main content of this report.

Presented here is a key portion of the model results where the effect of convective flow is not a factor.

2.5.1.1 Crevice Gap Varying With Distance

For the crevice geometry shown in Figure 2-1(b) where the gap varies along the crevice longitudinal direction, two conditions have been explored to understand how variation of crevice gap may affect the chemistry and corrosion inside the crevice. The first condition concerns no CP imposed at the crevice mouth. The second condition assumes a fixed potential at the mouth (-0.900 V_{CSE}), a condition of significant CP. For both conditions, the mouth solution is an aerated NaCl solution. The model equations and results are given in MS #1 appended at the end of this report. In this section, only a key portion of the model results for the no CP condition is reported.

At the mouth potential maintained at -0.8071 V_{CSE}, it was found that the CP current passing across the crevice mouth is negligible. With oxygen present at the mouth and depleted inside the crevice by corrosion reactions, a differential oxygen concentration cell is set up and leads to a gradient of potential and variation of crevice solution chemistry. The time-dependent variation of the crevice potential and solution chemistry is discussed next.

Figure 2-11a shows a comparison of Na^+ concentrations near the mouth for the two crevice geometries shown in Figures 1a and 1b. The concentrations in the two crevices are the same until after 10^2 s when the change of gap at $\frac{x}{\delta_{s0}}=5$ is reached. At 10^4 s and 10^7 s, a steeper variation of Na^+ concentration occurs in the crevice of variable gap in the gap-narrowed region

with $\frac{x}{\delta_{s0}}$=5-6. Compared to the crevice of constant gap, the Na^+ concentration in the crevice of variable gap is greater around $\frac{x}{\delta_{s0}}$=5 but is smaller around $\frac{x}{\delta_{s0}}$=6. This effect may be explained by treating Na^+ diffusion in the crevice similar to flow. The total rate of Na^+ diffusion (analogous to flow rate) is approximately the same across an edge of the gap-narrowed region. However, the diffusion flux of Na^+ (analogous to flow velocity) can have a significant variation immediately before and after the edge, because the flux is inversely proportional to the cross-sectional area of the crevice or the gap size. For that reason, the diffusion flux, reflected by the slope on the Na^+ concentration curve, is greater in the gap-narrowed region. Around the left edge ($\frac{x}{\delta_{s0}}$=5), the Na^+ tends to volumetrically squeeze into the gap-narrowed region, while, as the gap suddenly expands at $\frac{x}{\delta_{s0}}$=6, the Na^+ tends to dissipate out and the Na^+ diffusion flux decreases (relative to the crevice of constant gap). At 10^7 s when steady-state corrosion is reached, the net flux, consisting of diffusion and migration, of Na^+ or Cl^- is zero. That is, diffusion and migration fluxes are balanced out.

Similar variation of Na^+ concentration is also shown in Figure 2-11b across the second gap-narrowed region with $\frac{x}{\delta_{s0}}$=15-100. However, the change of Na^+ concentration in the range of $\frac{x}{\delta_{s0}}$=5-6 is greater than in the range of $\frac{x}{\delta_{s0}}$=15-100 because the Na^+ concentration gradient is greater near the mouth and is more greatly affected by the sharp change of gap. Even with a steeper change of Na^+ concentration due to the sharp change of gap (relative to a constant crevice gap), the Na^+ concentration in the two crevices are overall not significantly different.

Figures 2-12a and b show a comparison of the crevice pHs for the two crevices shown in Figures 1a and b. Although the sharp change of the crevice gap has resulted in a different pH relative to the crevice of constant gap, the overall difference in pH between the two crevices is insignificant.

Figure 2-13 shows a comparison of the crevice potentials in the two crevices. The sharp change of gap only has an effect on the crevice potential in the region of the gap changes, and this effect is greater near the mouth (e.g., $\frac{x}{\delta_{s0}}$=5) than deep in the crevice (e.g., $\frac{x}{\delta_{s0}}$=100). The overall effect is not significant. A similar result is shown in Figure 2-14 with corrosion current density, which is also not significantly affected by the gap change.

2.5.1.2 Crevice Corrosion Considering Penetration of Current and O_2 via Coating

Although an intact coating on buried pipes is generally not permeable to ions or CP current, it allows for permeation of gases, such as oxygen and carbon dioxide. Some coatings can become permeable to ions when deteriorated. The effect of coating permeability to CP on the crevice corrosion is not well known (e.g., how the CP penetration through the coating interacts with CP from the mouth and how this interaction may affect the steel corrosion rate in the coating-disbonded region). In the presence of oxygen, it is unclear whether the CP penetration through the coating can sufficiently suppress the corrosion resulting from the oxygen diffusion through the coating.

Several cases were modeled and compared: (1) neither current nor oxygen penetration through the coating, (2) only CP current penetration, (3) only oxygen penetration, and (4) penetration of both oxygen and CP current. All organic coatings used on buried steel pipelines are permeable to O_2, while some become permeable to ions only after deterioration. For that reason, the coating porosity used for ions is assumed to be 0.001, while it is assumed to be 0.11 when used for oxygen. This difference in porosity accounts for the fact that oxygen can permeate the coating matrix. The model equations and results are presented in MS #2 appended at the end of this report. In this section, only Case 4 is reported. The results may have implications for understanding of the performance of existing coatings and the design of new coatings.

Figure 2-15 shows a comparison of (1) steel potential and (2) corrosion current density for the four cases with the penetration of either O_2 or current, neither, or both. At time zero, when no O_2 diffusion through the coating is considered, the initial corrosion potential and current density is only affected by CP penetration through the coating. Thus, the two dark curves without current penetration through the coating overlap, and similarly, the two gray curves with current penetration overlap.

At 10^8 s, the corrosion process reaches steady state. The effect of O_2 diffusion through the coating is clearly demonstrated. With no current penetration through the coating, the steel potential with O_2 diffusion through the coating is more positive and the corrosion current density is greater (dark dashed curve) than if no O_2 diffuses through the coating (dark solid curve). This same effect of O_2 diffusion through the coating also applies when CP current penetrates the coating. From without to with O_2 penetration through the coating, the steel potential shifts in the more positive direction, and the corrosion current density is greater.

By comparing the two conditions, (1) neither current nor O_2 permeation through the coating (dark solid curve) and (2) both current and O_2 permeation through the coating (gray dashed curve)), Figure 2-15 shows that the corrosion current density inside the crevice is smaller for the latter. This result can have significant implications for coating design and for an understanding of the protectiveness of a coating once it disbonds and becomes permeable. Even though a much larger (100 times more) overall porosity of the coating was used for O_2 than for ions, the CP can still adequately suppress the increased corrosion current density by O_2 diffusion through the coating. This suggests that in the field, a permeable coating, when disbonded, can still allow adequate CP current to pass through and protect the steel pipe from corrosion attack, despite O_2 permeation through the coating. The CP penetration through the coating can still be effective, despite a much greater permeability of the coating to O_2 than to ions, because the current penetration can be driven by the potential gradient across the coating, which does not occur with O_2.

Figure 2-16 shows a comparison of the crevice chemistry for all four cases. The initial conditions are the same, and all curves for the four cases overlap at time zero for each figure. At steady state (10^8 s), the effect of O_2 or/and current penetration through the coating is clearly exhibited. Irrespective of current penetration through the coating, O_2 diffusing through the coating is electrochemically reduced at the steel surface. This reduction of O_2 generates hydroxyls, which attract cations such as Na^+ and repel anions such as Cl^-. This effect, superimposed by additional generation of hydroxyls from CP as well as by the potential-driven

ionic migration, leads to an increased Na^+ concentration in the crevice, a decreased Cl^- concentration, and, correspondingly, an increased pH.

Because the mass transport of any ion through the coating is much slower than through the solution, the effect by CP through the coating is less significant than through the mouth. The chemistry change in the crevice is mainly attributed to the ionic transport from the mouth. Although CP tends to pump Na^+ into the crevice across the coating (controlled by migration), with a higher concentration inside the crevice Na^+ tends to diffuse out across the coating, and this diffusion is more dominant than migration. Thus, a CP-permeable coating functions like a membrane. The Na^+ concentration in the crevice is smaller than if the coating is impermeable to CP. Conversely, the Cl^- concentration in the crevice with a CP permeable coating is greater than in the crevice with an impermeable coating to CP. Due to the decrease in Na^+ concentration, the solution pH in the crevice with a CP-permeable coating is smaller.

2.5.2 Dilute NaCl Solution Containing CO_2

The evolution over time of the crevice chemistry, potential, and corrosion rate was modeled when CO_2 diffusion through the holiday and the coating is considered. The transport of ions through the coating is not considered. The model governing equations is given in Appendix D.

The solution species include (1) $\underline{Na^+}$, (2) $\underline{Cl^-}$, (3) Fe^{2+}, (4) $\underline{H^+}$, (5) OH^-, (6) $Fe(OH)^+$, (7) $\underline{CO_2}$, (8) H_2CO_3, (9) HCO_3^-, (10) $\underline{CO_3^{2-}}$, (11) $\underline{H_2(aq)}$, (12) $\underline{FeCO_3}$, and (13) $\underline{H_2O}$, where the underlined species are defined as the primary species. Their concentrations can be either given such as those listed in Table 2-2 for the initial and boundary conditions, or known, such as species (11)-(13). The concentrations of the primary species can be used to determine the concentrations of the secondary species based on the equilibrium relations between the primary and the second species. The CO_2 partial pressure of 0.05 atm at the mouth and the coating permeability coefficient to CO_2 at 100 times that of a new HDPE coating are used for the modeling, which represents a worst-case scenario of the CO_2 effect on pipeline crevice corrosion. The CO_2 permeability coefficient in a new coating is 1.36×10^{-11} mol/m.s.atm. The mouth potential of -0.88 V_{CSE}, a potential more negative than recommended by the international CP standards, is used for the modeling.

To ensure the steel corrosion rate is more realistic at the initial condition with CO_2, values of some model parameters (relative to those used for non-CO_2 conditions) are modified. The exchange current density and Tafel slope of iron are changed from 2×10^{-4} A/m^2 and 0.04 V to 2×10^{-3} A/m^2 and 0.06 V, respectively. The exchange current density of water is changed from 2×10^{-3} A/m^2 to 2×10^{-4} A/m^2. The model results are reported next.

Figure 2-17(a) shows a comparison of the in-crevice CO_2 partial pressures (which can be converted to concentration by Henry's law) with or without CO_2 diffusion through the coating. Clearly, CO_2 diffusion through the coating has led to a slightly greater in-crevice CO_2 partial pressure. At steady state (reached at 10^3 s or greater), the in-crevice CO_2 partial pressure is greater with CO_2 diffusion through the coating than without. CO_2 diffuses into the crevice from the mouth, dissolves in solution, and dissociates into other carbon species. CO_2 partial pressure

decreases from the mouth into the crevice due to the increase of crevice pH. This pH variation will be shown later. In intermediate times such as 10^4 s, a dip of the curve is shown, which corresponds to the greatest pH.

Figure 2-17(b) shows that the carbonate concentration in the crevice is much greater with CO_2 permeation through the coating than without, particularly at longer times such as 10^4 s or greater.

Figure 2-18(a) shows the in-crevice Na^+ concentration. Irrespective of CO_2 diffusion through the coating, the overall variation of Na^+ concentration is similar, suggesting that the overall acidity brought into the crevice by CO_2 transport (through holiday and coating) is unable to balance out the alkalinity-generating power from steel corrosion and cathodic polarization by CP. With CO_2 permeation through the coating, the Na^+ concentration in the crevice is smaller than if the coating is impermeable to CO_2. This result is more clearly shown with 10^4 s or greater. Overall, the Na^+ concentration in the crevice increases over time and eventually exceeds that at the mouth where the Na^+ concentration is set to be constant. The continuous injection of CO_2 into the crevice through the coating reduces the solution alkalinity and the Na^+ concentration.

Contrary to the change of Na^+ concentration, Figure 2-18(b) shows that the Cl^- concentration in the crevice is greater with CO_2 permeation through the coating than without. Irrespective of CO_2 permeation through the coating, the Cl^- concentration in the crevice increases over time, suggesting that diffusion of Cl^- from soil through the holiday and the coating into the crevice is more dominant than the potential-driven migration. The potential-driven migration tends to draw out of Cl^-. These two forces must, however, balance out at steady state. Because the potential-driven migration of Cl^- is opposite in direction to its diffusion, the Cl^- concentration in the crevice cannot exceed its concentration at the mouth.

Figure 2-19 shows the crevice pH, which increases over time. The formation of hydroxyls inside the crevice overpowers the acidity brought in by CO_2 through the holiday and the coating. The shapes of the pH curves are consistent with those of CO_2 partial pressure following the discussion given earlier with Figure 2-17(a); the peak pH corresponds to the dip of CO_2 partial pressure.

Figure 2-20(a) shows the steel potential and corrosion current density in the crevice. The initially sharp gradient of the potential near the mouth becomes increasingly leveled off over time, and overall, the crevice potential shifts in the more negative direction, corresponding with the increase of solution pH. The corrosion current density decreases over time as shown in Figure 2-20(b). Relative to the condition with no CO_2 diffusion through the coating, CO_2 diffusion through the coating tends to slightly increase the corrosion current density (Figure 2-20(b)) and shifts the crevice potential in the more positive direction (Figure 2-20(a)).

2.5.3 Summary of Model Results

Due to the specific crevice geometry (a small area of crevice mouth), the overall temporal and spatial variation of crevice chemistry, potential, and corrosion rate in a crevice of varying gap is not significantly different from the corresponding change in a crevice of uniform gap.

Regardless of the variation of crevice gap, when a holiday is protected with cathodic polarization, the pH in the crevice increases over time and the corrosion rate decreases. Given a sufficient time and with the cathodic polarization continuously maintained at the mouth, this pH increase can go farther into the disbonded region and becomes greater than at the mouth. These model-predicted results are qualitatively consistent with experimental data in the literature.

A permeable coating behaves like a membrane, which, under a cathodic polarization at the crevice mouth, tends to raise the in-crevice sodium ion concentration and pH more rapidly relative to an impermeable coating. Later, as the sodium ion concentration and pH in the crevice become greater than at the mouth, the permeable coating tends to reverse the transport direction for ions. At a mouth potential of -0.900 V vs. saturated $Cu/CuSO_4$, the cathodic current is sufficient to suppress all O_2 penetrating the crevice both from the mouth and through the coating. The practical implication is that in the presence of sufficient cathodic polarization, a permeable coating, when disbonded, can still be capable of protecting the substrate steel from corrosion attack.

Compared to the condition without CO_2 in the system, CO_2 diffusion through the holiday and the coating tends to slightly increase the corrosion current density and shifts the crevice potential in the more positive direction.

2.6 Model Simplification

2.6.1 Background

The crevice chemistry, potential, and corrosion rate can vary with time and with the crevice geometrical parameters, such as crevice gap and length. The effect of the geometrical parameters may be combined with the model independent variables, such as time t and distance x, to reduce the number of model variables and potentially alleviate model computations with respect to the various effects of the crevice geometrical parameters and time. One chart plotted with scaling variables can cover information that otherwise must be obtained by multiple charts due to the variation of the crevice geometrical parameters (e.g., length and gap) and time. For this project, scaling is used as a way to simplify the model.

Previous work for scaling crevice corrosion focused on crevices of uniform gap, and the corrosion is in steady-state condition. Scaling for the unsteady-state condition has not been performed, and the effect of variable crevice gap on the scaling has not been investigated. They are studied in this work.

The scaling model and results are presented as a manuscript MS #3 attached at the end of the report. Only the key components of the model and results are presented in this section.

2.6.2 Scaling Theory for Crevice Corrosion

Equation (2-1) may alternatively be written as

$$\frac{\partial c_i}{\partial(t/\delta_s)} + \delta_s \frac{\partial N_{ix}}{\partial x} = \delta_s R_i + R_{si} - N_{iyc} - N_{ix}\frac{\partial \delta_s}{\partial x} \tag{2-20}$$

where

$$\delta_s \frac{\partial N_{ix}}{\partial x} = [-D_i \frac{\partial^2 c_i}{\partial(x/\sqrt{\delta_{s0}})^2} - \frac{z_i D_i F}{RT}\frac{\partial}{\partial(x/\sqrt{\delta_{s0}})}(c_i \frac{\partial \varphi}{\partial(x/\sqrt{\delta_{s0}})})](\delta_s \delta_{s0}^{-1}) \tag{2-21}$$

For a crevice of uniform gap shown in Figure 2-1a ($d\delta_s/dx=0$ and $\delta_s = \delta_{s0}$), applying Equation (2-20) for Na^+ yields

$$\frac{\partial c_1}{\partial(t/\delta_s)} + \delta_s \frac{\partial N_{1x}}{\partial x} = -N_{1yc} \tag{2-22}$$

where N_{1yc} does not contain δ_s. Following Equations (2-20) and (2-21), both time scaling and dimension scaling ($\frac{t}{\delta_{s0}}$ and $\frac{x}{\sqrt{\delta_{s0}}}$) are applicable to Na^+. Likewise, the scaling applies to Cl^-.

With no gap involved in the equation of electroneutrality ($\sum_{j=1}^{6} z_j c_j = 0$), the scaling also applies to that equation as a governing equation. The scaling also applies to H^+ because all reaction rates are not a direct function of gap and time.

2.6.3 Key Model Results and Verification of Scaling Theory

Three crevices of different gaps are investigated to understand and verify the dimension- and time-scaling method. Two of the crevices have uniform gaps as shown in Figure 2-1(a): one gap is δ_{s0} and the other is $\delta_{s0}/4$. The third crevice has a variable gap as shown in Figure 2-1(b), where the gap $\delta_s=\delta_{s0}$ except at x=5-6 and 15-100, where $\delta_s=\delta_{s0}/4$.

When the pipe steel is exposed in an alkaline solution, it can be passivated, and the effect of this passivity on the model scaling is presented in Appendix E. In this section and in MS #3 attached at the end of this report, the steel is assumed to be active and the Tafel equation for steel dissolution kinetics is used.

In scaling, to maintain the same total scaling length $\frac{L}{\sqrt{\delta_s}}$ for the two crevices of uniform gaps with a gap ratio of four, the total length of the crevice with the larger gap, L_L, is set to be twice the length of the smaller gap, L_S (or $L_L=2L_S$). For the crevice of variable gap, its scaling-equivalent total length is $L_v = \sum_i \Delta L_i \sqrt{\frac{\delta_{s0}}{\delta_{sj}}}$ relative to the crevices of uniform gaps.

When $L_V=200\delta_{s0}$, the equivalent length for the crevice with uniform gap of δ_{s0} is $L_L=243\delta_{s0}$ (or $L_L=1.215L_V$), and the equivalent length for the crevice with uniform gap of $\delta_{s0}/4$ is $L_S=121.5\delta_{s0}$. For the crevice of variable gap, to satisfy its scaling length, its equivalent gap δ_{se} is $\delta_{se}=(\frac{L_V}{L_L})^2\delta_{s0}=0.6774\delta_{s0}$.

Following time-scaling theory, to maintain a constant scaling time t/δ, a smaller crevice gap requires a smaller time to retain the same crevice condition. The time needed for the crevice with the smaller uniform gap should be only one-quarter of the time for the crevice of a larger uniform gap, or $t_S=0.25t_L$. For the variable crevice, the equivalent time is $t_v=\frac{\delta_{se}}{\delta_{s0}}t_L=0.6774t_L$.

These crevice dimensions are used in the scaling model computations. The initial and boundary conditions used for all three crevices are the same as those shown in Table 2-1. For any given crevice, the Na^+ and Cl^- concentrations at the mouth are equal and each is 10 times its value in the initial condition. The pH at the mouth is the same as its initial value. Although the model studied the condition with no CP and the condition with substantial CP, only the results with substantial CP or an at mouth potential of -0.9 V_{CSE} are reported here.

Figure 2-21 is a scaling plot showing Na^+ concentration computed for different times for the three crevices. In this figure, the x coordinate is plotted as scaling distance $\frac{x}{\sqrt{\delta_{se}}}$, where δ_{se} is the equivalent gap applicable to all three crevices. Next to each curve, the scale time $\frac{t}{\delta_{se}}$ is labeled. For the crevice of uniform and larger gap with $\delta_{se}=\delta_{s0}=0.5$ mm, the time scales at 0, 2×10^8, 2×10^9, 2×10^{10}, and 2×10^{11} s/m correspond with actual times of 0, 10^5, 10^6, 10^7, and 10^8 s, respectively. For the crevice with a uniform but smaller gap at 0.5/4 mm, the actual times correspond to a quarter of the actual times described previously. Likewise, for the crevice of variable gap, the same scale time represents 0.6774 multiplied by those actual times.

For the two crevices with uniform gaps, the Na^+ concentrations overlap for each of the same scale times. They are, however, different from the Na^+ concentration in the crevice of variable gap. This difference is greatest at the intermediate times, such as 2×10^{10} s/m. At steady state (e.g., at the scale time of 2×10^{11} s/m), this difference in Na^+ concentration is smaller but still obvious. These model results verify that for the crevices of uniform gaps, both time scaling and dimension scaling are valid, while for the crevice of variable gap, the scaling is not valid.

Figure 2-21 shows that starting from the same initial concentration, prior to or at the scale time of 2×10^8 s/m, the Na^+ concentration in the crevice of variable gap increases faster and is greater than in the crevices of uniform gaps. This result is attributed to the last term on the right side of Equation (2-20), which is analogous to a "reaction" source term. Initially, both the concentration-driven diffusion flux and the voltage-driven migration flux of Na^+ are greater than zero. When the gap decreases at the scale distance ($\frac{x}{\sqrt{\delta_{se}}}$) about 0.4 $m^{0.5}$, the rightmost term of Equation (2-20) is greater than zero, likely producing Na^+ and increasing the local Na^+ concentration. The Na^+ concentration in the gap-narrowed region ($\frac{x}{\sqrt{\delta_{se}}}$=0.4~1.5 $m^{0.5}$) is greater than in the crevices of uniform gaps.

As the Na^+ transport passes the location of the last gap change (gap expansion) at $\frac{x}{\sqrt{\delta_{se}}}$ =1.5 $m^{0.5}$, the gap expansion behaves as consuming Na^+ and the Na^+ concentration becomes smaller than in the crevices of uniform gaps. With increasing time, this effect of gap expansion on Na^+ concentration increases. At the scale time of 2×10^9 s/m, the Na^+ concentration in nearly the entire crevice of variable gap becomes smaller than in the crevices of uniform gaps, and this difference is even greater at 2×10^{10} s/m.

This difference shrinks, however, as steady state is approached, because the value of the "reaction" source term becomes smaller and eventually becomes zero at steady state. At steady state, Equation (2-22) is simplified so the Na^+ net flux is zero, which has the same form as the Na^+ transport equation for crevices of uniform gaps. Thus, close results between crevices of uniform and variable gaps are expected.

At the scale time 2×10^{11} s/m (steady state for Na^+ transport), the Na^+ concentration in the crevice of variable gap is still different from that in the crevices of uniform gaps because, for H^+, its flux at steady state is not zero across the crevice and affects the Na^+ concentration distribution in the crevice. In the gap-narrowed region, the Na^+ concentration gradient is greater than in the regions with a larger gap. An analogy to flow was used to describe this effect [10]. The diffusion rate (analogous to flow rate) is the same across the edges of the gap-narrowed region, but the diffusion flux of Na^+ (analogous to flow velocity) varies significantly, reflected by the slope of the curve in Figure 2-21.

Figure 2-22 shows a comparison of the pHs predicted for the three crevices. The curves for the two crevices of uniform gaps overlap for each scale time, while they are different from the corresponding curves with the crevice of variable gap except at time zero. At time zero, the same initial conditions were given for all three crevices set by the model. The variation of solution pH can be evaluated based on the variation of Na^+ concentration. As detailed elsewhere [9-10], in the presence of CP, a higher Na^+ concentration corresponds to a lower Cl^- concentration; their difference in charge, which is positive, has to be balanced by hydroxyls, and a higher pH results.

Figure 2-23 shows (1) crevice potentials and (2) corrosion current densities predicted for the three crevices. In general, the curves with the two crevices of uniform gap approximately overlap for each scale time except very near the mouth. This discrepancy near the mouth is small and results from the presence of O_2 in the crevice. The O_2 exists only near the mouth, and its mass transport equation cannot be scaled in the same way as other dissolved species. This difference in dimension scaling with respect to O_2 was examined in MS #3 appended at the end of this report. The two curves for the crevices of uniform gaps are clearly different from those in the crevice of variable gap, and this difference increases over time. Again, this discrepancy in results between the crevices of uniform and variable gaps suggests that dimension scaling does not apply to the crevice of variable gap.

2.6.4 Summary of the Model Scaling Results

Modeling was performed for two crevices of uniform gaps and a crevice of variable gap. The model results confirm the validity of time scaling and dimension scaling for crevices of uniform gap. The scaling does not apply to the crevice of variable gap.

Dimension scaling and time scaling of crevice corrosion can be used to scale experiments or reduce model computations when broad ranges of the effects of crevice geometrical parameters and time on crevice corrosion are studied.

2.7 Practical Implications of the Model Results

2.7.1 Understanding the Term "CP Shielding" and Corrosion Under a "Shielded" Coating

It appears that the pipeline industry has an inadequate understanding of how CP may perform in a coating-disbonded region. Despite of decades of laboratory and analytical studies on this subject, researchers do not appear to have communicated adequately the broad laboratory results and field observations to pipeline practitioners. This section summarizes some experimental and modeling results and their implications in field conditions.

CP shielding is only partially true. In the presence of CP, the increase of pH over time in coating-disbonded regions and the shift of potential in a more negative direction reduce the local corrosion rate over time. The worst corrosion may happen when the soil is aerated and wet and the CP is either lacking or inadequate. Even then, the corrosion may not be as bad as often believed unless microbiologically influenced corrosion (MIC) and alternating current (AC) and direct current (DC) interferences and acidic soils are present. Unlike traditional crevice corrosion, which when supported by a large area ratio of cathode to anode can lead to severe corrosion, the corrosion under a disbonded coating is conversely associated with a small cathode (holiday)-to-anode area ratio.

Modeling provides a powerful tool to predict and interpret complex experimental results and complex interplays among multiple parameters in a corrosion process. It also helps to further the understanding of the corrosion process without having to conduct exhaustive experimental tests under numerous conditions.

2.7.2 The Significance of a Permeable Coating

A permeable coating behaves like a membrane. Relative to an impermeable coating, under CP a permeable coating tends to raise the in-crevice Na^+ concentration and pH more rapidly. When the Na^+ concentration in the crevice becomes greater than at the holiday, it tends to diffuse out through the coating and reversely counter its migration, leading to a smaller in-crevice Na^+ concentration over time (relative to an impermeable coating).

When a coating is permeable to both oxygen and CP, even if the coating permeability to oxygen is 20 times that of CP, the CP is found to be effective due to the CP-driven migration of ions.

CO_2 diffusion through the holiday and the coating only slightly increases the crevice corrosion rate and slightly shifts the crevice potential in the more positive direction.

2.7.3 The Effect of Crevice Geometry Parameters

The effect of the geometrical parameters on corrosion of steel pipes of a coating disbondment may be combined with model independent variables, such as time t and distance x, to reduce the number of model variables and potentially alleviate model computations when the various effects of the disbondment geometrical parameters and time are concerned. One chart plotted with scaling variables can cover information that otherwise must be obtained by multiple charts. Geometry scaling can also be used for scaling experiments (crevice length and gap) and overcoming challenges of testing with extremely small or large crevice geometries.

The geometry scaling factor is found to be L^2/δ_0 (or $L/\sqrt{\delta_0}$), and the time-scaling factor t/δ_0, where L is disbondment length, δ_0 is crevice gap, and t is time. These scaling factors were verified by modeling for two crevices of uniform gaps by fixing the value of $L/\sqrt{\delta_0}$. This verification was done with the substrate steel under both active and passive states.

2.8 References

1. H. Leidheiser, W. Wang, L. Igetoft, Progress in Organic Coatings 11 (1983) 19-40.
2. C.G. Munger, Corrosion Prevention by Protective Coatings (NACE, 1984) 47-61.
3. J.M. Leeds, Pipe Line & Gas Industries, March (1995) 21-26.
4. M. Meyer, X. Campaignolle, F. Coeuille, M.E.R. Shanahan, "Impact of Aging Processes on Anticorrosion Properties of Thick Polymer Coatings for Steel Pipelines," in Proceedings of the Corrosion/2004 Research Topical Symposium: Corrosion Modeling for Assessing the Condition of Oil and Gas Pipelines, F. King and J. Beavers (eds.) (NACE, 2004) 93-146.
5. F.M. Song, Corrosion 66(9) (2010) 095004.
6. F.M. Song, D.W. Kirk, D.E. Cormack, D. Wong, Materials Performance 44(4) (2005) 26-29.
7. F.M. Song, D.W. Kirk, D.E. Cormack, D. Wong, Materials Performance 42(9) (2003) 24-26.
8. F.M. Song, D.W. Kirk, J.W. Graydon, D.E. Cormack, Corrosion 58(12) (2002) 1015-1024.
9. F.M. Song, D.W. Kirk, J.W. Graydon, D.E. Cormack, Corrosion 59(1) (2003) 42-49.
10. F.M. Song, D.A. Jones, D.W. Kirk, Corrosion, 60(2) (2005) 145-154.
11. F.M. Song, N. Sridhar, Corrosion 62(8) (2006) 676-686.
12. F.M. Song, N. Sridhar, Corrosion 62(10) (2006) 873-882.
13. F.M. Song, N. Sridhar, Corrosion Science 50(1) (2008) 70-83.
14. N. Sridhar, D.S. Dunn, M. Seth, Corrosion 57 (7) (2001) 598-613.
15. N. Sridhar, "Modeling the Conditions Under Disbonded Coating Crevices—A Review," in Proceedings of the Corrosion/2004 Research Topical Symposium: Corrosion Modeling for Assessing the Condition of Oil and Gas Pipelines, F. King and J. Beavers (eds.) (NACE, 2004) 53-92.

16. M.E. Orazem, D.P. Reimer, C. Qiu, K. Allahar, "Computer Simulations for Cathodic Protection of Pipelines," in Proceedings of the Corrosion/2004 Research Topical Symposium: Corrosion Modeling for Assessing the Condition of Oil and Gas Pipelines, F. King and J. Beavers (eds.) (NACE, 2004) 25-52.
17. R.R. Fessler, A.J. Markworth, R.N. Parkins, Corrosion 39(1) (1983) 20-25.
18. T.R. Jack, G.V. Boven, M. Wilmott, R.L. Sutherby, R.G. Worthingham, Materials Performance (8) (1994) 17-21.
19. A. Turnbull, A.T. May, Materials Performance 22 (1983) 34.
20. J.J. Perdomo, I. Song, Corrosion Science 42 (2000) 1389.
21. M.H. Peterson, T.J. Lennox, Jr., Corrosion 29 (1973) 406.
22. A.C. Toncre, N. Ahmad, Materials Performance 19(6) (1980) 39.
23. M.D. Orton, Materials Performance 24(6) (1985) 17.
24. F. Gan, Z.-W. Sun, G. Sabde, D.-T. Chin, Corrosion 50(10) (1994) 804.
25. R. Brousseau, S. Qian, Corrosion 50(12) (1994) 907-911.
26. F. King, T. Jack, M. Kolar, R. Worthingham, "A Permeable Coating Model for Predicting the Environment at the Pipe Surface under CP-Compatible Coatings," (NACE, 2004) paper no. 04158.
27. F.M. Song, Corrosion Science 50 (2008) 3287-3295.
28. K. Kumaresan, Y. Mikhaylik, R.E. White, J. Electrochem. Soc. 155 (2008) A576-A582.
29. J. Newman, K.E. Thomas-Alyea, Electrochemical Systems, 3rd edition, John Wiley and Sons, Inc. (2004) 209-214.
30. F.M. Song, D.W. Kirk, J.W. Graydon, D.E. Cormack, Corrosion 58(2) (2002) 145-155.
31. M.C. Yan, J.Q. Wang, E.H. Han, W. Ke, Corrosion Engineering Science and Technology 42 (1) (2007) 42-49.
32. K. Landles, J. Congleton, R.N. Parkins, "Potential Measurements Along Actual and Simulated Cracks," in Embrittlement by the Localized Crack Environment, R.P. Gangloff (ed.) (AIME, 1984) 59.
33. X., Chen, X.G., Li, C.W., Du, Y.F., Cheng, Corrosion Science 51 (2009) 2242-2245.

Table 2-1: Initial and Boundary Conditions for Systems Without CO_2

Condition	c_1 *(mol/m³)*	c_2 *(mol/m³)*	c_4 *(mol/m³)*	c_7^0 *(mol/m³)*	ϕ *or* $i_{totx}=\sum_1^6 z_j F N_{jx}$ *(V)* *(A/m²)*
Initial	0.3128	0.3128	6.014×10^{-7}	0*	
Mouth with CP	3.128	3.128	6.014×10^{-7}	0.2601	$\phi=0$
Mouth with no CP	3.128	3.128	6.014×10^{-7}	0.2601	$i_{totx}=0$
Condition	N_{1x} (mol/m²·s)	N_{2x} (mol/m²·s)	$\sum_1^6 z_j N_{jx}$ (mol/m²·s)	N_{7x} (mol/m²·s)	i_{totx} (A/m²)
Crevice tail	0	0	0	0	0
Previous work [13]	c_1 *(mol/m³)*	c_2 *(mol/m³)*	c_4 *(mol/m³)*	c_7^0 *(mol/m³)*	ϕ *(V)*
Initial and mouth	0.3128	0.3128	6.31×10^{-7}	0.2601	0

** This value may also be determined from O_2 diffusion via coating at steady state (prior to holiday formation).*

Table 2-2: Initial and Boundary Conditions for Systems with CO_2

Condition	c_1 *(mol/m³)*	c_2 *(mol/m³)*	c_4 *(mol/m³)*	p_{CO_2} *(atm)*	c_9 *(mol/m³)*	ϕ *or* $i_{totx}=\sum_1^6 z_j F N_{jx}$ *(V)* *(A/m²)*
Initial	2.7×10^{-7}	2.7×10^{-7}	9.32×10^{-4}	0.05	4.1×10^{-5}	
Mouth with CP	100	100	9.32×10^{-4}	0.05	4.1×10^{-5}	$\phi=0$
Condition	N_{1x} (mol/m²·s)	N_{2x} (mol/m²·s)	$\sum_1^6 z_j N_{jx}$ (mol/m²·s)	N_{7x} (mol/m²·s)	N_{9x} (mol/m²·s)	i_{totx} (A/m²)
Crevice tail	0	0	0	0	0	0

Table 2-3: Scenarios Modeled Without CO_2 and Locations of Results

No.	*Condition*	*Location*
i	Constant gap, no current & no O_2 penetration via coating	Appendix MS#1
ii	Variable gap vs. x, no current & no O_2 penetration via coating	Appendix MS#1
iii	Variable gap vs. x, no current but O_2 penetration via coating	Appendix MS#2
iv	Variable gap vs. x, current but no O_2 penetration via coating	Appendix MS#2
v	Variable gap vs. x, current & O_2 penetration via coating	Appendix MS#2
vi	Variable gap vs. t, no current & no O_2 penetration via coating	Appendix C

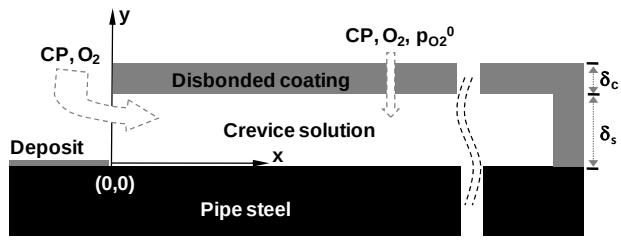

(a)

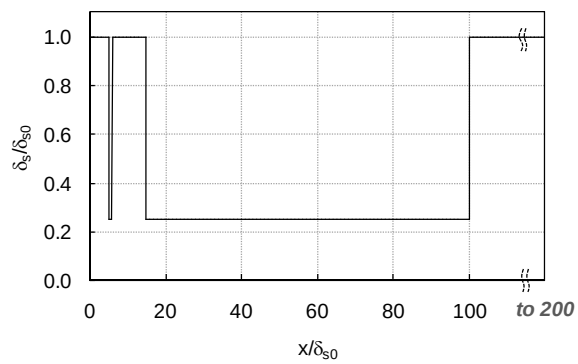

(b)

Figure 2-1. Model crevice geometry showing the coordinators and dimensions of the crevice and transport of CP current and O_2 into the crevice through the disbonded coating: (a) uniform gap and (b) variable gap).

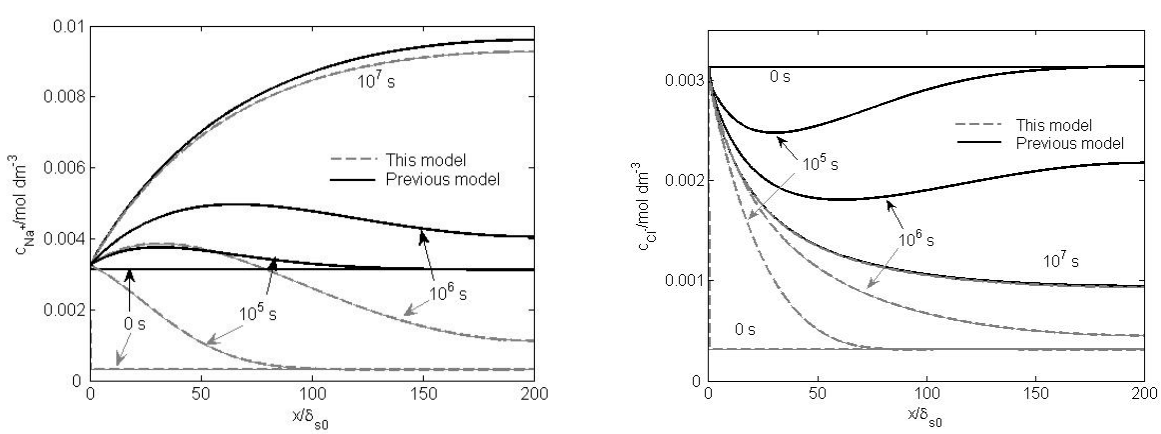

(a) (b)

Figure 2-2. At a fixed mouth potential of -0.9 V_{CSE}, evolution of concentrations of (a) Na^+ and (b) Cl^- over time and distance into the disbonded region from the holiday. The crevice geometry used for simulation is Figure 2-1a. For this work, the concentrations of Cl^- and Na^+ are initially the same in the crevice but they are respectively smaller than at the mouth. The results are compared with those in a previous work where the Cl- and Na+ concentrations are the same at the mouth and initially in the crevice.

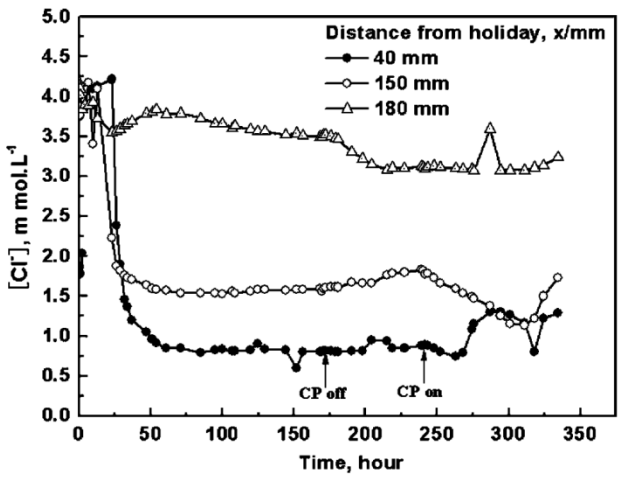

Figure 2-3. Variation of $[Cl^-]$ with time at various distances from opening after potential at opening was controlled at -1.00 V_{SCE} in NS4 bulk solution bubbled with 5% CO_2+95% N_2: crevice thickness 0.5 mm.[31]

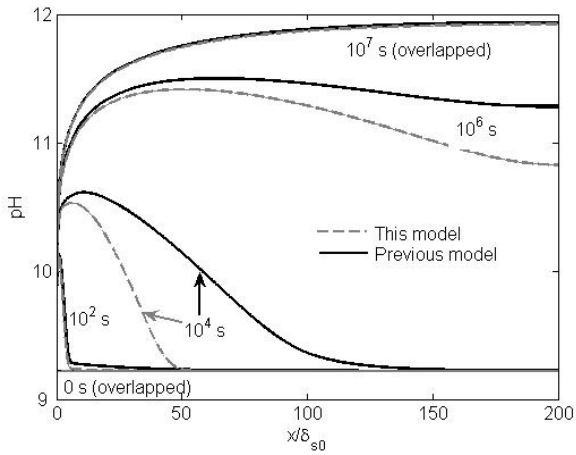

Figure 2-4. Similar to Figure 2-3, but here the mouth potential is fixed at -0.9 V_{CSE}.

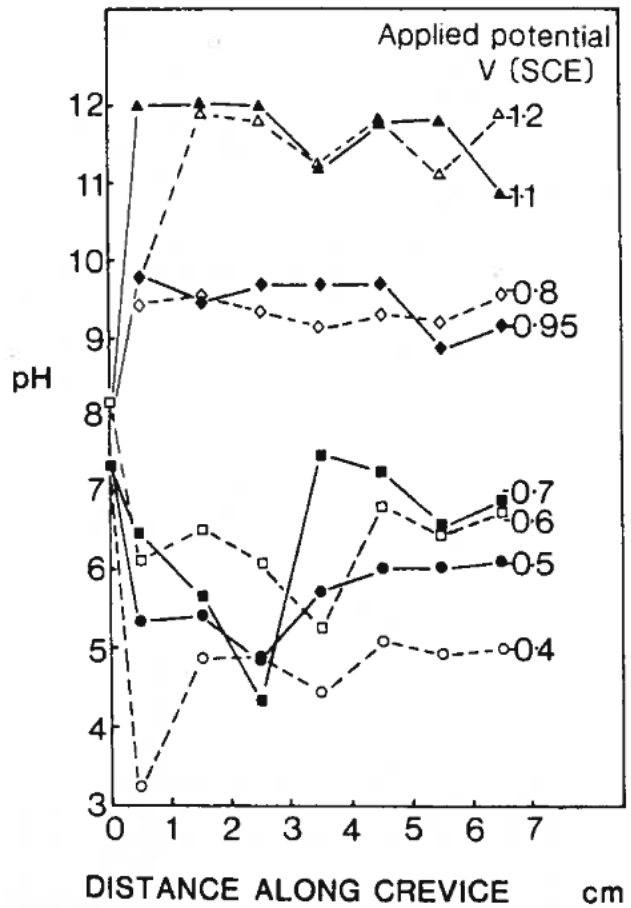

Figure 2-5. pH changes along static simulated cracks, for various potentials applied at the crack mouth, for HY80 steel in seawater.[32]

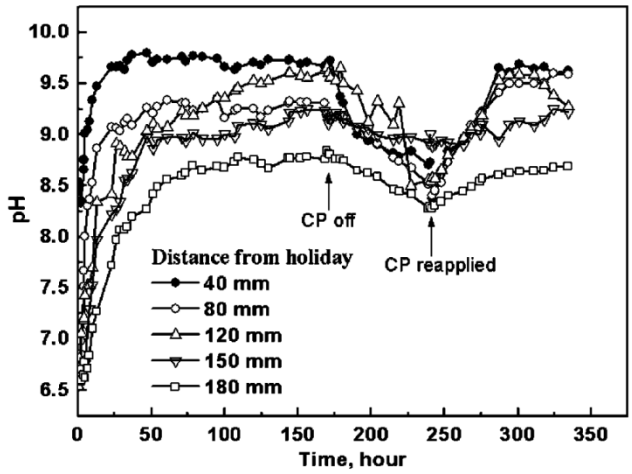

Figure 2-6. Variation of pH with time at various distances from opening after potential at opening was controlled at -1000 mV_{SCE} in NS4 bulk solution bubbled with 5%CO_2+95%N_2: crevice thickness 0.5 mm.[31]

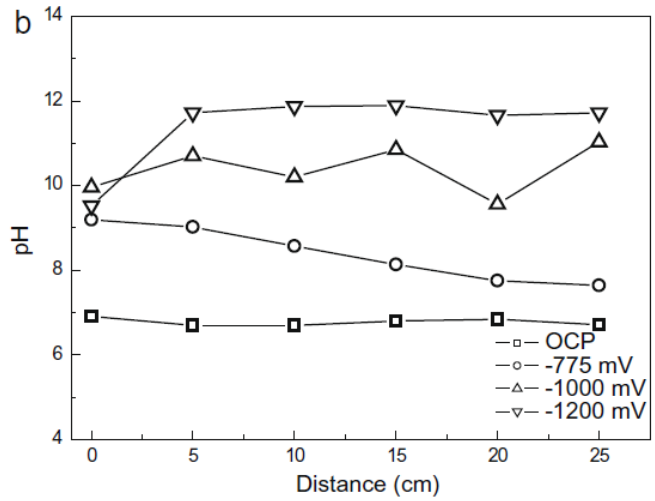

Figure 2-7. pH profiles within the crevice after 72 h of test; potential in unit against SCE.[34]

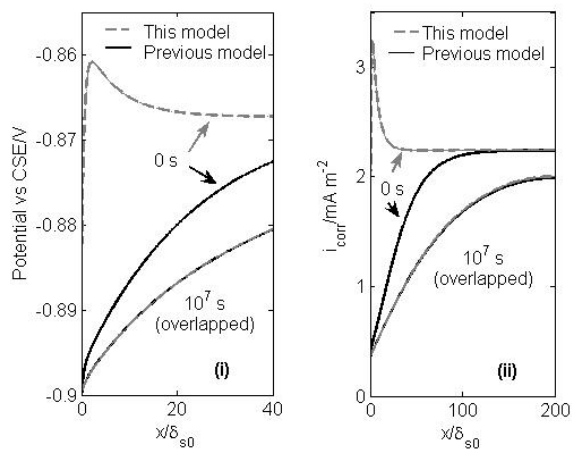

Figure 2-8. Similar to Figure 2-2, but here the mouth potential is fixed at -0.9 V_{CSE}.

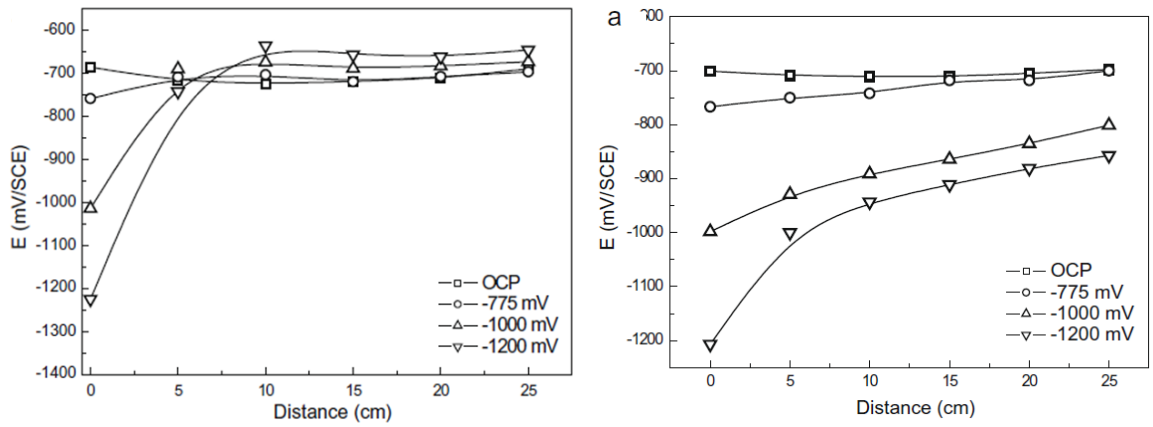

Figure 2-9. Potential profiles within the crevice at 0.5 hour and at 72 h of test.[34]

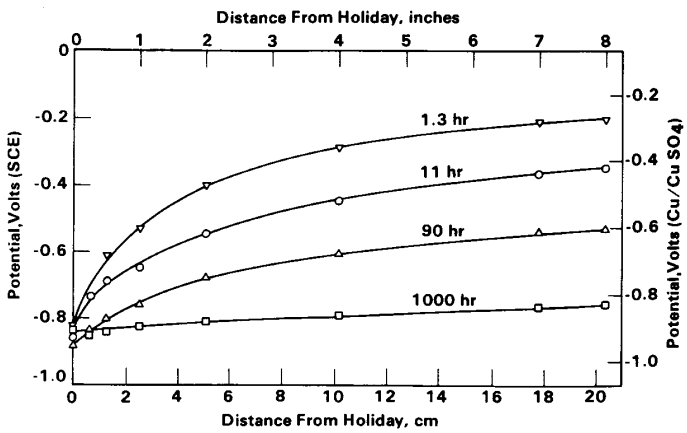

Figure 2-10. Potential distribution in a 0.13-mm-thick crevice at various times after the holiday potential was set at -0.850 V_{SCE} in a solution of 1N-1N carbonate-bicarbonate solution.[17]

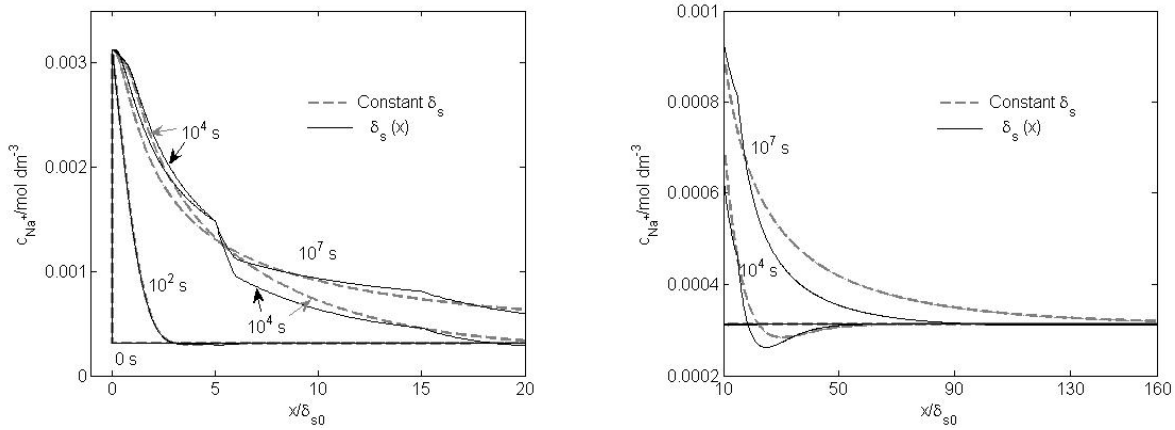

(a) (b)

Figure 2-11. At a fixed mouth potential of -0.8071 V_{CSE}, a comparison of Na^+ concentrations in two crevices at different times between a constant gap shown by Figure 2-1a (gray lines) and variable gap vs. x shown by Figure 2-1b (gray lines): (a) near the mouth and (b) away from the crevice mouth.

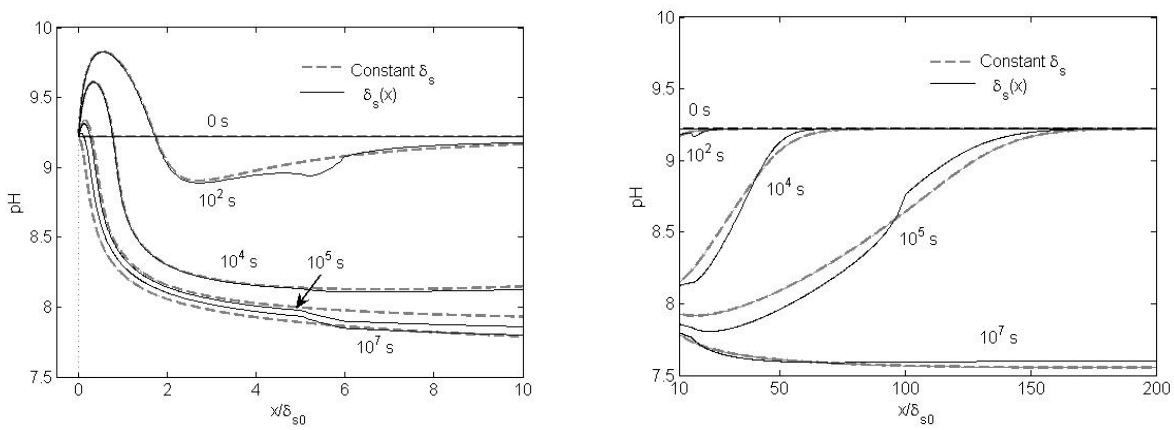

(a) (b)

Figure 2-12. Similar to Figure 2-11, but here for a comparison of crevice pHs: (a) near the mouth and (b) away from the crevice mouth.

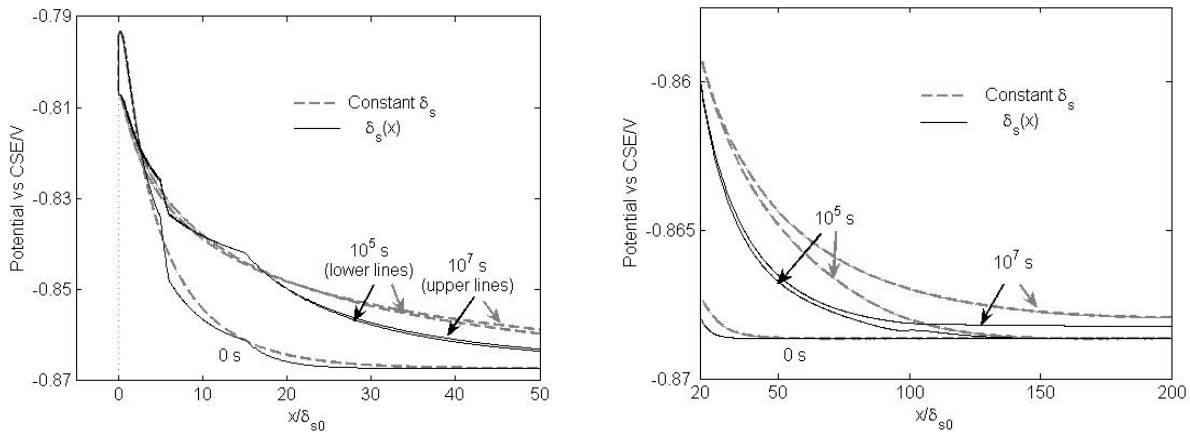

Figure 2-13. Similar to Figure 2-11, but here for a comparison of crevice potentials: (a) near the mouth and (b) away from the crevice mouth [note the reduced scale of potential from (a)].

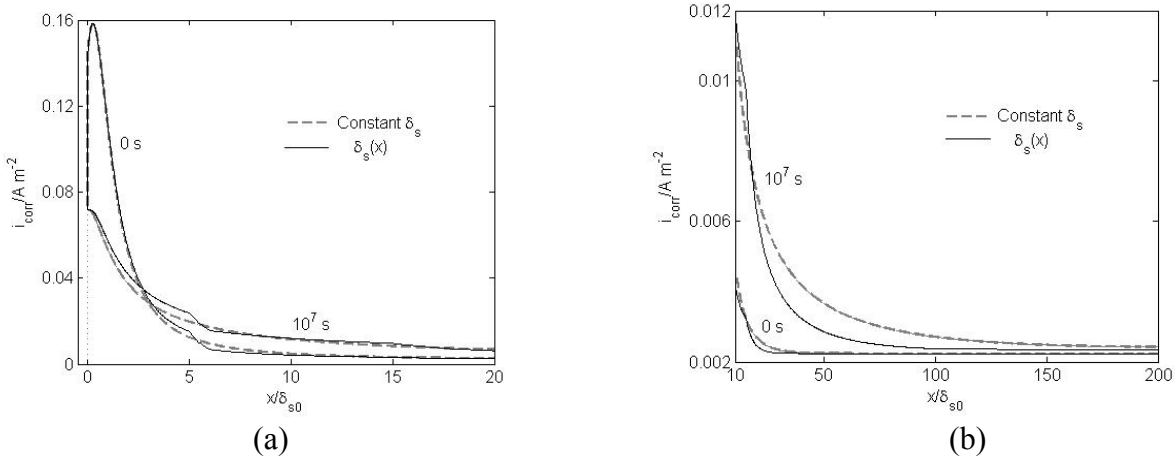

Figure 2-14. Similar to Figure 2-11, but here for a comparison of crevice corrosion current densities: (a) near the mouth and (b) away from the crevice mouth [note the reduced scale of i_{corr} from (a)].

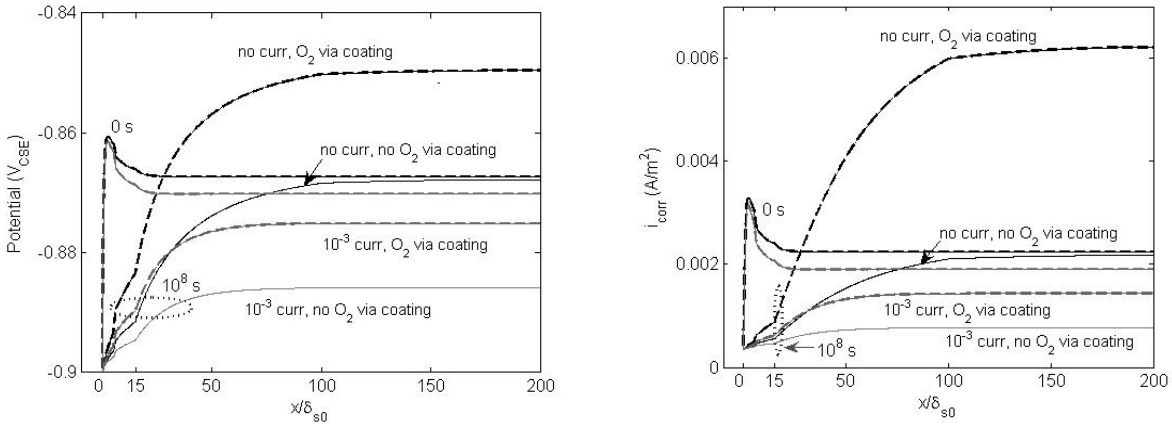

(a) (b)

Figure 2-15. At a fixed mouth potential of -0.9 V_{CSE}, a comparison of the model results for four cases studied at both the initial and steady-state conditions: (a) crevice potential and (b) corrosion current density.

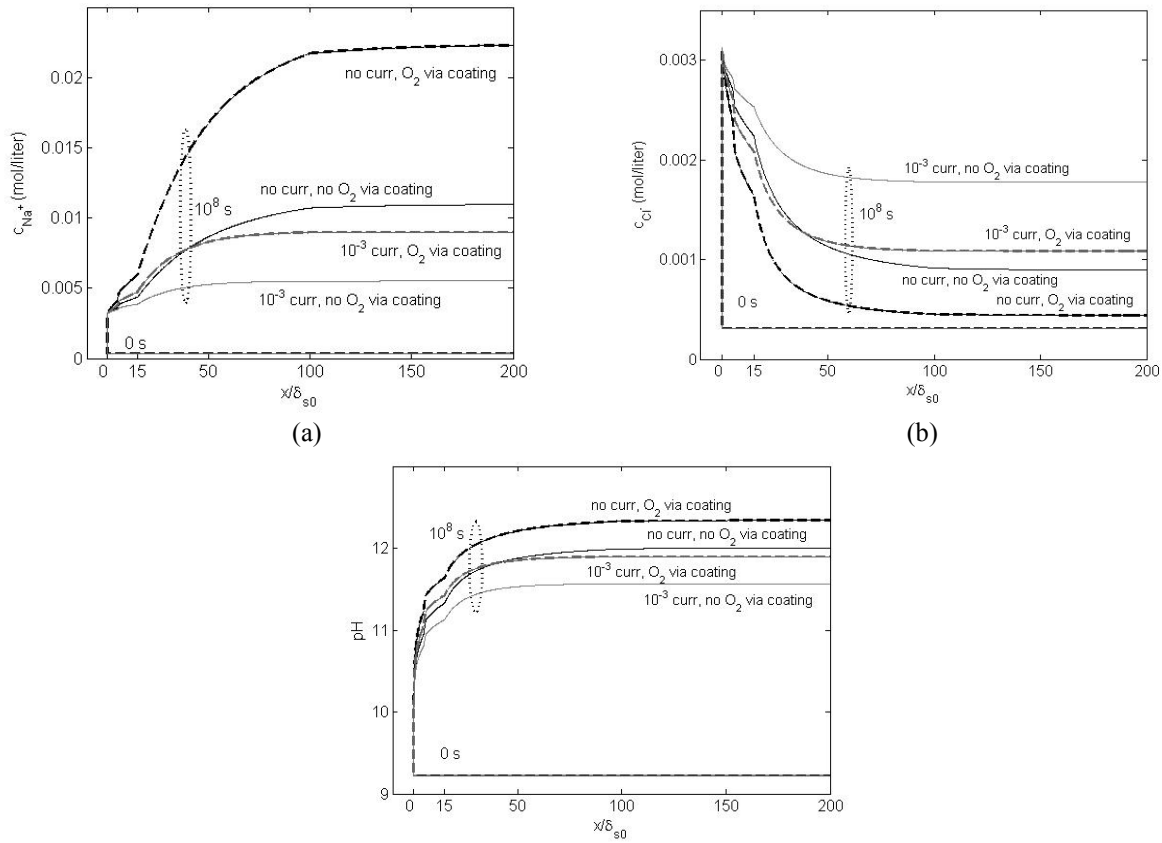

(a) (b)

(c)

Figure 2-16. Similar to Figure 2-15, but for crevice chemistry: (a) Na^+ concentration, (b) Cl^- concentration, and (c) pH in the crevice.

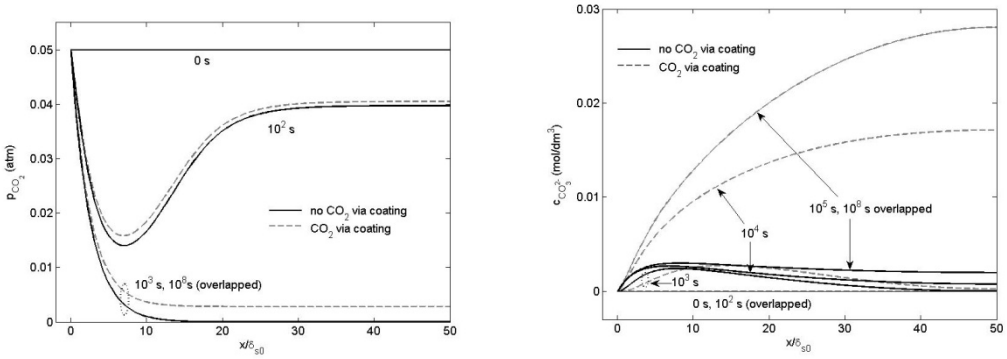

(a) (b)

Figure 2-17. At a potential of -0.88 V_{CSE} and a CO_2 partial pressure of 0.05 atm at mouth, a comparison of model results obtained when CO_2 permeation through the coating is and is not considered: (a) in-crevice CO_2 partial pressure and (b) concentration of carbonate.

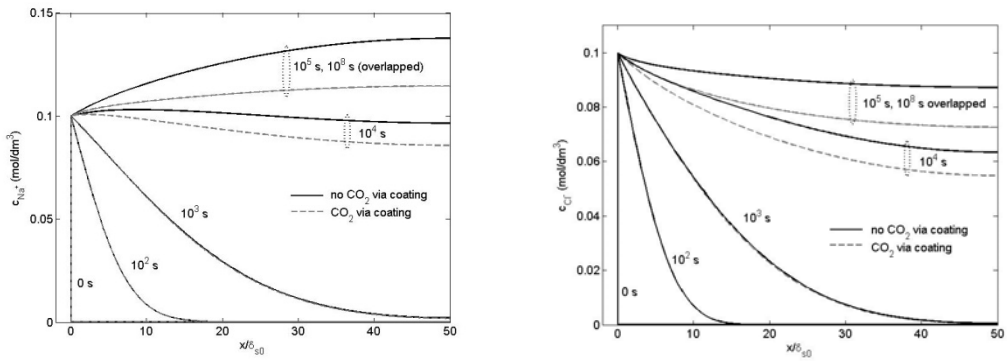

(a) (b)

Figure 2-18. Similar to Figure 2-17, but for crevice chemistry: (a) Na^+ concentration and (b) Cl^- concentration.

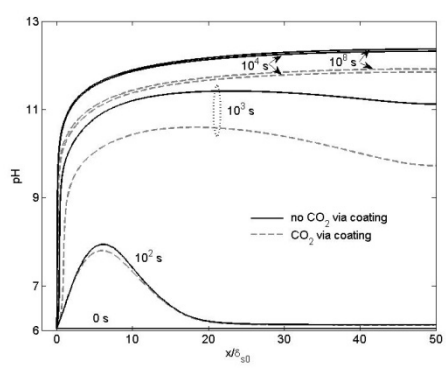

Figure 2-19. Similar to Figure 2-17, but for crevice pH.

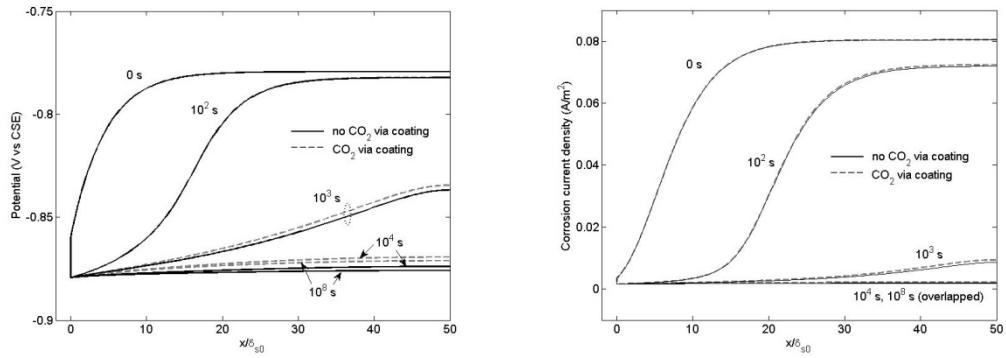

(a) (b)

Figure 2-20. Similar to Figure 2-17, but for (a) crevice potential and (b) corrosion current density.

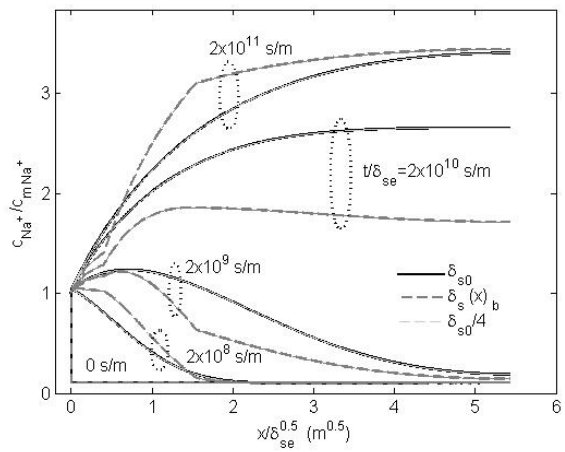

Figure 2-21. At a fixed mouth potential of -0.9 V_{CSE}, a scaling plot for a comparison of Na^+ concentrations in the three crevices at different times: constant gap of δ_{s0} in Figure 2-1a (black solid lines), variable gap vs. x of Figure 2-1b or $\delta_s(x)_b$ (gray solid lines), and constant but reduced to a quarter of the gap or $\delta_{s0}/4$ (gray broken lines).

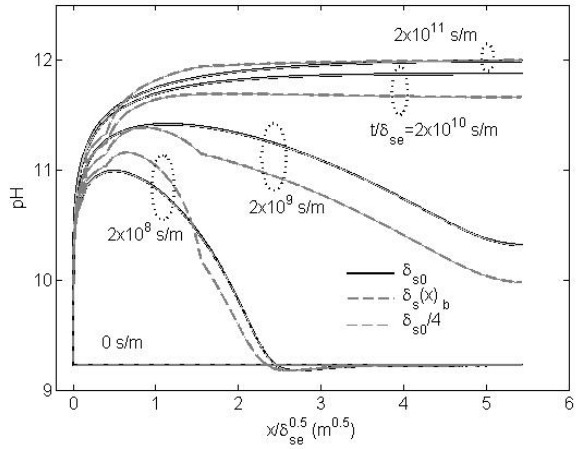

Figure 2-22. Similar to Figure 2-21, but here the scaling plot is for a comparison of crevice pH.

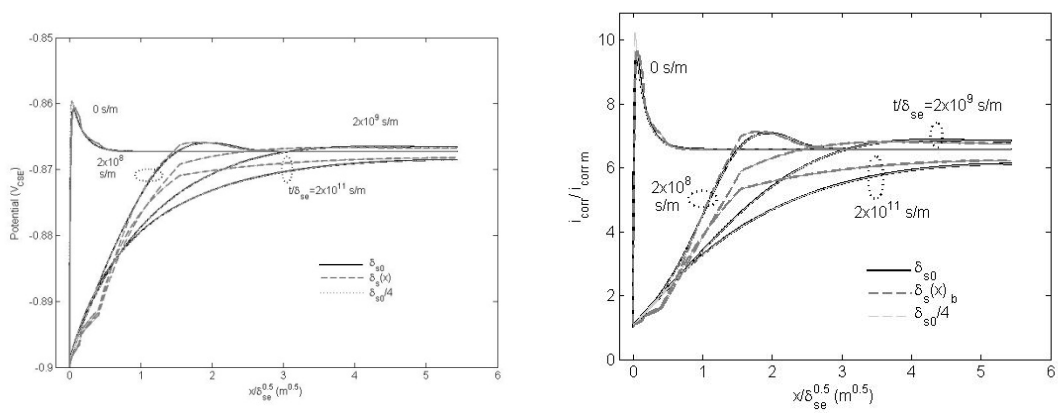

(a) (b)

Figure 2-23. Similar to Figure 2-21, but here the scaling plot is for a comparison of (a) crevice potential and (b) corrosion current density.

3.0 PIPELINE INTERNAL CORROSION

3.1 Background

A significant difference in internal corrosion between dry and wet natural gas pipelines is that for dry gas pipelines, a thin stagnant solution layer due to water condensation may form on the pipe surface and can quickly go saturated. A precipitate film may then form and thicken over time, and the corrosion rate decreases. In wet gas pipelines, water may be constantly present and the bulk solution chemistry is relatively stable. Due to continuous mass exchange between the solution boundary layer and the bulk solution, precipitation may or may not occur.

By coupling mass transport, chemical and electrochemical reactions, possible film growth, and the displacement of the moving metal-solution interface as the metal dissolves into solution, this work developed a model based on fundamental principles. This model allows for predicting the variation of solution chemistry over time, the formation and growth of a precipitate film when existent, and the variation of corrosion rate over time under a variety of operating conditions, including the change of gas temperature, pressure, and composition. Following a brief description of the model equations and validation, key model results will be presented and discussed. A more detailed description of the model equations and results can be found in MS #4 appended at the end of this report.

3.2 Model Description

For a porous medium with a dilute solution containing multiple species (see the corrosion system shown in Figure 3-1), mass transport for an arbitrary species in the solution numbered by i may be expressed by

$$\frac{\partial(\varepsilon c_i)}{\partial t} + \nabla \cdot N_i = R_i \tag{3-1}$$

where ε is porosity or pore volume fraction of the aqueous system. ε is 1 when the solution is homogeneous. R_i is the total net volumetric production rate (after consumption deducted) of the ith species.

The flux of the ith species in the dilute solution, N_i, may be written as

$$N_i = -D_i \varepsilon \tau (\nabla \cdot c_i - \tfrac{z_i F}{RT} c_i \nabla \phi) = -D_i \varepsilon^{\frac{3}{2}} (\nabla \cdot c_i - \tfrac{z_i F}{RT} c_i \nabla \phi) \tag{3-2}$$

where D_i and z_i are diffusivity and charge of the ith species, respectively; τ is tortuosity, which can be approximated by $\varepsilon^{0.5}$; F, R and T are Faraday's constant, universal gas constant, and temperature, respectively; and ϕ is electrostatic potential of solution.

For each solution species, each concentration corresponds to a mass transport equation expressed by Equation (3-1). Two other unknowns in the system, potential and porosity, are yet to be solved from two additional equations. These two additional equations are the equation of electroneutrality for potential

$$\sum_i z_i c_i = 0 \tag{3-3}$$

and mass conservation of solids for the precipitate porosity

$$\frac{\partial(1-\varepsilon)}{\partial t} = \sum_m \overline{V}_m r_m \tag{3-4}$$

In Equation (3-4), $\overline{V}_m$ is molar volume of the mth precipitate, or M_m/ρ_m, where M_m and ρ_m are the molar weight and density of a precipitate, respectively, and r_m is the rate of precipitation soon to be described.

To solve these governing equations, the volumetric reaction rates in Equation (3-1) and the boundary conditions must be defined.

3.2.1 Volumetric Reaction Rates

The total net production rate of the ith species in Equation (3-1), R_i, can result from two types of reactions: homogenous reactions and heterogeneous reactions.

<u>Homogenous Reactions</u>: Such a reaction involving i^{th} species and numbered by h may be expressed in the form of

$$\sum_i \nu_{i_r,h} A_{i_r} \leftrightarrow \sum_i \nu_{i_p,h} A_{i_p} \tag{3-5}$$

where the subscripts r and p at the lower right of the symbols signify reactant and product, respectively.

The individual volumetric reaction rate in the solution may be written as

$$r_h = \varepsilon(k_{h_f} \prod_i c_i^{\nu_{i_r,h}} - k_{h_b} \prod_i c_i^{\nu_{i_p,h}}) \tag{3-6}$$

where k_{h_f} and k_{h_b} are the forward and backward reaction rate constants, respectively.

The net production rate of the ith species for all reactions associated with it is

$$R_{i,h} = \sum_h \nu_{i,h} r_h \tag{3-7}$$

Practically, when a reaction is reversible, the reaction rate can be cancelled out when the governing equation for the secondary species is combined into that of the primary species. This has been detailed elsewhere [1-3] and will be used in this work. By that consideration, only irreversible reactions need to be accounted for when Equation (3-7) is used.

Mineral (Precipitation) Reactions: Such a reaction involving the ith species and numbered by m may be written in the form of

$$\sum_i \nu_{i_r,m} A_{i_r} \leftrightarrow \sum_i \nu_{i_s,m} A_{i_s} \tag{3-8}$$

where subscript m at the lower right of the symbols signifies mineral or precipitate and the subscript s signifies a dissolved solution species.

The individual volumetric reaction rate converted from the surface reaction rate may be written as

$$r_m = A_m (k_{m_f} \prod_i c_i^{\nu_{i_r,m}} - k_{m_b} \prod_i c_i^{\nu_{i_s,m}}) \tag{3-9}$$

where A_m is the interfacial surface area of the solid.

The total net production rate of all the mineral reactions involving the ith species may be written as

$$R_{i,m} = \sum_m \nu_{i,m} r_m \tag{3-10}$$

For the system of concern, only two precipitates are possible—$FeCO_3$ and $Fe(OH)_2$,—while precipitation of $Fe(OH)_2$ is only possible when CO_2 partial pressure is very small.

3.2.2 Electrochemical Reaction Rates at the Metal Surface

The reactions at the steel surface are electrochemical, their rates are connected with boundary conditions, and they are not a part of R_i in Equation (3-1).

Such a reaction numbered by e may be expressed in the form of

$$\sum_i \nu_{i_r,e} M_{i_r}^{z_{i,r}} \leftrightarrow \sum_i \nu_{i_p,e} M_{i_p}^{z_{i,p}} + n_e e^- \tag{3-11}$$

where z_i at the upper right of the symbols signifies the charge carried by the metallic species M_i.

Charge balance for Equation (3-11) dictates that

$$\sum_e \nu_{i,e} z_i - n_e = 0 \tag{3-12}$$

where $\nu_{i,e}$ and n_e are stoichiometric coefficient of the ith species and the number of electrons transferred during the eth electrochemical half-cell reaction, respectively.

The total net production rate of all the electrochemical reactions involving the ith species is

$$R_{i,e} = s_e \sum_e \nu_{i,e} r_{i,e} = s_e \sum_e \frac{\nu_{i,e} i_{i,e}}{n_e F} \tag{3-13}$$

where s_e is the interfacial area of the electrochemically active surface in the system.

For the system of interest here, the electrochemical reactions occur only at the steel surface and the current density of the eth electrochemical reaction may be expressed by the Butler-Volmer equation. [4]

$$i_e = i^0_{e_ref} \left(\prod_i \left(\frac{c_i}{c_{i_ref}}\right)^{\nu_{i_r,e}} \exp\left(\frac{\alpha_{a_e} F}{RT} \eta_e\right) - \prod_i \left(\frac{c_i}{c_{i_ref}}\right)^{\nu_{i_p,j}} \exp\left(-\frac{\alpha_{c_e} F}{RT} \eta_e\right) \right. \tag{3-14}$$

Equation (3-14) may be reduced to Tafel equations for all anodic and cathodic reactions.

In Equation (3-14), the overpotential, η_e, is defined as [4-5]

$$\eta_e = \psi - \phi_s - U_{e_ref} = E_s - U_{e_ref} \tag{3-15}$$

where ψ and ϕ_s are, at the metal-solution interface, the electrostatic potentials of the metal and the solution, respectively. U_{e_ref} can be treated as the electrode potential at a reference condition corresponding to the exchange current density $i^0_{i_ref}$ at the concentration of the ith species c_{i_ref}. U_{e_ref} can also be treated as the equilibrium potential when i_0 and c_i are measured at a given condition of the same system.

$E_s = \psi - \phi_s$ is electrode potential measured with the reference electrode placed very near the metal surface. The electrode potential measured with the reference electrode placed anywhere in solution E is

$$E = \psi - \phi = E_s + \phi_s - \phi \tag{3-16}$$

When there is no externally applied current to and from the metal surface, the electrode potential is the open circuit potential (OCP), E_{corr},

$$E_s = E_{corr} \tag{3-17}$$

and the OCP can be determined from

$$\sum_k i_{a,k} + \sum_l i_{c,l} = 0 \tag{3-18}$$

where i_a and i_c are anodic and cathodic current densities, respectively.

When an external current is applied, either the potential in the bulk solution E_b or the external current density $i_{applied}$ must be provided for a complete solution of the system. When E_b is given, by setting the electrostatic potential in the bulk solution as zero, E_s in Equation (3-16) is

$$E_s = E_b - \phi_s \tag{3-19a}$$

Likewise, if the electrostatic potential at the steel surface is set as zero, the following equation is obtained

$$E_s = E_b + \phi_b \tag{3-19b}$$

where ϕ_b is the solution potential at the interface between the boundary layer and bulk solution.

Either Equation (3-19a) or (3-19b) can be substituted into Equation (3-14) as a boundary condition for potential at the steel surface. This boundary condition contains only the variables to be solved for in the governing equations.

When an externally applied current density i_{net} is given, E_s can be solved for from

$$\sum_k i_{a,k} + \sum_l i_{c,l} = i_{net} \tag{3-20}$$

By substituting E_s into Equation (3-14), the boundary condition for potential at the steel surface is defined. Such a boundary condition contains only the variables to be solved for in the governing equations.

For the system of concern, the anodic reaction is iron oxidation. The cathodic reactions are hydrogen ion reduction, carbonic acid reduction, and water reaction.

3.3 Reaction Rates and Boundary Conditions for the System of Concern

For pipeline internal corrosion with solution containing dissolved CO_2, O_2, and NaCl, if the solution primary species are chosen arbitrarily as the underlined:

(1) $\underline{Na^+}$, (2) $\underline{Cl^-}$, (3) $\underline{Fe^{2+}}$, (4) $\underline{H^+}$, (5) OH^-, (6) $FeOH^+$, (7) $\underline{CO_2(aq)}$, (8) $\underline{O_2(aq)}$, (9) $\underline{CO_3^{2-}}$, (10) HCO_3^+, (11) H_2CO_3, (12) $FeHCO_3^+$, (13) $\underline{H_2(aq)}$, (14) $\underline{H_2O}$, (15) $\underline{Fe}$, (16) $\underline{FeCO_3(s)}$, (17) $\underline{Fe(OH)_2(s)}$.

the concentrations of the secondary species can be calculated from the concentrations of the primary species following their equilibrium relations. The concentrations of the solid species, such as $FeCO_3$ and $Fe(OH)_2$, and the species of H_2 (aq) and H_2O are treated as constants.

3.3.1 Volumetric Reaction Rates

The only irreversible homogeneous reaction in the system of concern is carbon dioxide hydration

$$CO_2(aq) + H_2O \rightarrow H_2CO_3 \tag{3-21}$$

and the reaction rate can be expressed by [6-7]

$$r_{CO_2} = \varepsilon(k_f c_7 - k_b c_{11}) \tag{3-22}$$

where k_f and k_b are the forward and backward reaction rate constants of CO_2 hydration, respectively.

The mineral reactions in the system of concern are precipitations of $FeCO_3(s)$ and $Fe(OH)_2(s)$

$$Fe^{2+} + CO_3^{2-} \rightarrow FeCO_3 \tag{3-23}$$

and

$$Fe^{2+} + 2OH^- \rightarrow Fe(OH)_2 \tag{3-24}$$

while Equation (3-24) occurs only when CO_2 partial pressure is very low and the pH is high.

The corresponding reaction rates of Equations (3-23) and (3-24) are

$$r_{p_1} = k_{f_{FeCO_3}} \sigma_1 K_{sp_{FeCO_3}} (S_{FeCO_3} - 1) \tag{3-25}$$

and

$$r_{p_2} = k_{f_{Fe(OH)_2}} \sigma_2 K_{sp_{Fe(OH)_2}} (S_{Fe(OH)_2} - 1) \tag{3-26}$$

where r_{pj} (j=1,2) is the rate of precipitation; k and K_{sp} are precipitation rate constant and solubility product, respectively; S is the ratio of relevant ionic concentration products to K_{sp} and measures the level of saturation or supersaturation of the solution; and σ_1 or σ_2 is specific area (or the ratio of surface area over the volume of a precipitate).

3.3.2 Initial and Boundary Conditions

For pipeline internal corrosion in wet gas lines, a boundary layer is assumed to be constantly present on the pipe surface and its thickness depends on the flow velocity. The bulk concentration of any species may be considered to be constant over time. No boundary condition is needed for Equation (3-4), because this equation is dimension independent.

Unlike wet gas pipelines, in a dry gas pipeline, the solution boundary layer formed by water condensation can be thin, and at the gas-solution interface, the CO_2 (or O_2 gas if present) may be considered to be in equilibrium with its dissolved species, $CO_2(aq)$ (or $O_2(aq)$). The flux of all other dissolved species, such as H_2CO_3 and ions, is zero at this boundary.

Irrespective of wet and dry gas pipelines, at the steel surface only corrosion reactions occur. When the effective reactive surface area fraction is treated the same as porosity ε, the Tafel equation for iron oxidation may be expressed by

$$i_{corr} = \varepsilon i^0_{Feref} 10^{\frac{E_s - E_{Fe}^{Eqref}}{b_{Fea}}} \tag{3-27}$$

where ref shown as either a subscript or superscript in Equation (3-27), as well as in Equations (3-28) through (3-30), is referred as a reference condition whereby the corresponding exchange current density i^0, bulk concentration c_i (i=3, 4, 5, 14), and equilibrium potential E^{Eq} are known or given. b is Tafel slope.

For reductions of hydrogen ion, water, and carbonic acid, the Tafel equations are

$$i_H = -\varepsilon i^0{}_{Href} \frac{c_{4s}}{c_{4ref}} 10^{\frac{-(E_s - E_H^{Eqref})}{b_H}} \tag{3-28}$$

$$i_{H_2O} = -\varepsilon i^0{}_{H_2Oref} 10^{\frac{-(E_s - E_{H_2O}^{Eqref})}{b_{H_2O}}} \tag{3-29}$$

$$i_{H_2CO_3} = -\varepsilon i^0{}_{H_2CO_3ref} \frac{c_{11s}}{c_{11ref}} \left(\frac{c_{4s}}{c_{4ref}}\right)^{-0.5} 10^{\frac{-(E_s - E_{H_2CO_3}^{Eqref})}{b_{H_2CO_3}}} \tag{3-30}$$

where c_{4s} and c_{11s} are the concentrations of hydrogen ion and carbonic acid at the steel surface respectively.

3.3.3 Moving Boundary Condition for a Dry Gas System

For a dry gas system, when a boundary layer is maintained at the steel surface with the rate of water condensation equal to the rate of evaporation, the total mass of water of this boundary layer does not vary over time. The precipitate film and the boundary layer thickness, however, vary over time because the densities and molar weights of the steel and precipitate differ.

The total mass of the dissolved Na^+ in the system is conserved

$$\int_{x_S}^{x_M} \varepsilon c_1 dx = c_{01}\delta_0 \tag{3-31}$$

Derivation of Equation (3-31) over time t yields

$$\varepsilon_M c_{1M} \frac{\partial x_M}{\partial t} + \int_{x_S}^{x_M} \frac{\partial(\varepsilon c_1)}{\partial t} dx - \varepsilon_S c_{1S} \frac{\partial x_S}{\partial t} = 0 \tag{3-32}$$

The middle term is zero because there is no net loss or gain in mass of Na^+ at the two boundaries. With this constraint, Equation (3-32) may be rearranged as

$$\frac{\partial x_M}{\partial t} - \frac{\partial x_S}{\partial t} = \frac{\varepsilon_s c_{1s} - \varepsilon_M c_{1M}}{\varepsilon_s c_{1s}} \frac{\partial x_M}{\partial t} \tag{3-33}$$

The moving velocity of the steel surface relative to the solution surface as the reference is

$$\frac{\partial x_M}{\partial t} - \frac{\partial x_S}{\partial t} = (1 - \frac{\varepsilon_M c_{1M}}{\varepsilon_s c_{1s}}) \frac{i_{corr}}{\beta} \tag{3-34}$$

where β is a unit conversion factor, which for steel is 2.686×10^{10} $A\cdot s/m^3$.

3.4 Model Validation with Lab and Field Data

Laboratory and field data are available from tests simulating oil and gas production systems similar to conditions in a wet gas pipeline where abundant water is present. Because the same fundamentals for corrosion hold in both wet and dry gas pipelines and in production pipes, the model validation for a wet gas system can be considered applicable to the model for a dry gas system. For the model validation using data obtained for production systems, the variation at the steel boundary due to metal dissolution or formation of deposits is not considered by assuming this effect being insignificant. The values of the model parameters used for modeling the corrosion process are detailed in MS #4 appended at the end of this report.

Figure 3-2 shows a comparison of the predicted corrosion rates with experimental data [8-9]; the initial solution contained little or no ferrous ion and the flow velocity in a pipe loop with an 8-cm inner diameter was 20 m/s. The experimental data were acquired *in situ* by monitoring the activity decrease resulting from the metal loss of neutron-activated steel coupons with Fe59 as the main radioactive isotope. Scintillation counters, placed outside the loop pipe, monitored the activity levels in 1000-second intervals with an accuracy of approximately 0.2%.

The predicted maximum corrosion rate in Figure 3-2 (dashed curve) is the rate when corrosion begins. The steel surface is fresh, and the solution pH at the steel surface is low. Soon after corrosion starts, the pH at the steel surface rapidly elevates by the electrochemical reductions of hydrogen ions and carbonic acid and by the formation of ferrous ions during corrosion. The boundary layer thickness at the condition of the experimental test is determined to be 10 μm based on the diameter of the test tubing and flow velocity. The predicted results show that it takes time for the corrosion process to reach steady state, and at steady state, no precipitation occurs (the predicted porosity at the steel surface is 1).

The predicted steady-state corrosion rates (solid curve) are compared with measured corrosion rates. Except for one point, all experimental data fall slightly below the predicted corrosion rates, suggesting that the predicted steady-state corrosion rates are slightly more conservative or greater than the measured rates.

Figure 3-3 shows the measured corrosion rates at 51 °C in a solution that was initially saturated with ferrous carbonate.[10] The corrosion rates appeared to be measured by using the linear polarization resistance (LPR) method (not clearly stated in the literature). The predicted corrosion rate decreases over time due to an increase of solution pH and formation of solid precipitate at the steel surface. The formation of solid precipitate decreases the system porosity and the active corroding area at the steel surface. Overall, the predicted corrosion rates are shown to be slightly greater than the experimental data.

Similar to Figure 3-3, Figure 3-4 shows the time-dependent corrosion rates measured in a lab at 35 °C in a solution initially saturated by ferrous carbonate.[10] The experimental data were measured possibly by using the LPR method and are shown to be slightly less than and similar to the predicted rates. The formation of precipitate film at the steel surface and the decreasing porosity by solid precipitates may be responsible for the corrosion rate decrease.

Figure 3-5 shows the model-predicted maximum (or initial) corrosion rates and those at the fifth hour in a solution initially saturated by ferrous carbonate. The temperature is 90 °C. These predicted results are compared with experimental data measured in a high pressure flow loop connected to an autoclave at 90 °C.[10] The solution was initially saturated by ferrous carbonate. The CO_2 partial pressure varies between 1.5 and 6 bars at a flow rate of 20 m/s.

Because corrosion rate varies with time as shown in Figures 3-3 and 3-4, depending on the time of measurement the corrosion rate can be different. The time and the methods of the corrosion rate measurements are not clearly stated in the literature.[10]. The predicted corrosion rates at the fifth hour are slightly greater than the measured rates.

Figure 3-6 shows data measured in lab testing with the same facilities used for measuring the data shown in Figures 3-1 through 3-4, and the data were possibly measured by the LPR method.[8,11] In the figure, field corrosion rates reported elsewhere[12] are included. The temperature was 25 °C. The lab and field data are compared with the model-predicted results. The flow velocity is shown to have a significant effect on the corrosion rate. Some corrosion rates measured in lab testing are significantly greater than the predicted steady-state corrosion rates and even greater than the predicted maximum corrosion rates. It is possible that the corrosion rates measured in the lab were affected by the erosion processes, which the model does not cover. It is also possible that the model parameters may not all be fully consistent with the test condition. For this model, the role of flow velocity is treated as reducing the boundary layer thickness only. Because the predicted corrosion rate is greater than the field-estimated corrosion rate, it appears that the predicted corrosion rates are more conservative than the long-term corrosion rate in field conditions.

Similar results are shown in Figure 3-7 for the temperature range of 50-60 °C.[8,11] The data came from the same sources as, and were measured similarly to, the data in Figure 3-6. The difference is that none of the lab data exceed the predicted maximum corrosion rates. The predicted steady-state corrosion rates are less than the lab rates but greater than the field corrosion rates.[12]

Note that not only can experimental data contain errors, but also the model itself has its limitations. The values of the model parameters came from different sources, and each may be associated with errors. Thus, discrepancy between the model predictions and experimental or field data can be expected. A sensitivity analysis of some model parameters is given in MS #4 appended at the end of this report.

3.5 Results

Figure 3-8 shows the predicted corrosion rate, pH, and porosity at the steel surface for a wet gas pipeline. A significant drop of corrosion rate over time is shown shortly after the corrosion process begins. This decrease in corrosion rate is accompanied a pH increase at the steel surface. Because the porosity at the steel surface is unity consistently, this suggests that no solid precipitation is predicted at the steel surface.

The corrosion rate and the porosity at the steel surface are shown for a dry gas system in Figure 3-9. The initial variation of corrosion rate with time is similar to that in the wet gas system (Figure 3-8) before the porosity at the steel surface starts to decrease. This decrease in corrosion rate is consistent with the increase of pH at the steel surface. Afterwards, as the corrosion rate becomes steady for some time, the concentration of ferrous ions in the solution increases and the solution becomes saturated with iron carbonate. The formation of solid $FeCO_3$ in the dry gas system begins almost simultaneously in the entire boundary layer, revealed by the decrease of porosity both at the steel surface and at the gas-solution interface. This decrease in porosity at the steel surface leads to a decreasing corrosion rate because of the total available steel surface area for corrosion (not covered by the precipitate) is reduced. The more significant decrease in porosity at the steel surface than at the gas-solution interface is the result of mass transport (of ferrous ion in the boundary layer from the steel surface) limitation.

Figure 3-10 shows the predicted corrosion rates in both wet and dry gas systems when the solution layer is saturated at time zero. The initial corrosion rates are much smaller than those for the unsaturated condition (shown in Figures 3-8 and 3-9) because of a higher initial pH elevated by the saturation of $FeCO_3$ in the solution. The corrosion rates for both wet and dry gas systems are similar, although the rate in the wet gas system is slightly greater than in the dry gas system. This similarity in corrosion rate is consistent with the porosity values for both systems, which are similar in magnitude, as shown in Figure 3-11. For the wet gas system, the porosity at the bulk boundary is maintained at 1, while at the steel it becomes smaller (a smaller average corrosion rate results).

The corrosion rate in the wet gas system is greater overall because ferrous ions formed from the corrosion process can transport across the boundary layer into the bulk solution. This leads to a slower rate of precipitation and a slower change of porosity compared to a dry gas system where no ferrous ion can escape the solution boundary layer.

3.6 Model Simplification

The model results presented in Section 3.4 can be simplified by neglecting the ionic migration term in the flux equation or by neglecting the effect of the voltage drop across the

solution boundary at the steel surface. The validity of this model simplification has been discussed qualitatively in other works.[7, 13] A quantitative validation of this model simplification will be presented later in this work.

This model simplification implies that Equation (3-2), or the flux of the ith species in a dilute solution, Ni, can be reduced to

$$N_i = -D_i \varepsilon^{\frac{3}{2}} \nabla c_i \tag{3-35}$$

This change of model equations can significantly reduce the difficulties in numerical modeling to solve the differential equations. This change has led to the nonlinear differential equations becoming linear.

Figure 3-12 shows a comparison of the model results obtained when the voltage drop across the boundary layer is and is not included, or Equations (3-2) and (3-35) are respectively used for the model. Clearly, there is no distinction in the model results regardless of whether Equation (3-2) or (3-35) is used, verifying the validity of Equation (3-35).

3.7 Effect of H_2S and O_2 on CO_2 Corrosion

The NACE report (in preparation by a number of experts in modeling CO_2 corrosion with and without H_2S in the system)[14] advises exercising care when using existing CO_2 corrosion models (a total of 17 models have been compiled in the report) for situations with more than a few mbar H_2S, implying the existing CO_2 corrosion models do not apply to corrosion predictions in a CO_2 corrosion system containing H_2S.

Even in the presence of a small amount of H_2S in a CO_2 corrosion system, the corrosion products tend to be iron sulfide rather than iron carbonate, because iron sulfide is much less soluble and precipitates more rapidly than iron carbonate. Thus, existing CO_2 models developed based on the formation of protective iron carbonate films cannot be used for situations where iron sulfide films are dominant. SwRI developed a formula that allows for predicting the type of dominant precipitate at the steel surface based on the molar ratio of CO_2 to H_2S in the gas phase.[13]

$$\frac{p_{H_2S}}{p_{CO_2}} = \frac{H_{CO_2} K_{spFeS} K_{1H_2CO_3} K_{2H_2CO_3}}{H_{H_2S} K_{1H_2S} K_{2H_2S} K_{spFeCO_3}} \tag{3-36}$$

Figure 3-13 developed by others[15] based on the same formula demonstrates the regions of precipitates at two different pHs of the solution. The effect of temperature on this ratio of partial pressures is shown in Figure 3-14. The boundaries can be used to determine the regions where the CO_2 corrosion model is applicable.

In the case where the corrosion product is mackinawite (FeS), the rate-controlling step is found to be dissolution of mackinawite. Mackinawite forms under conditions where the Fe^{2+} and H_2S concentrations in the bulk solution are low enough that FeS is undersaturated and is still soluble. A visible tarnish film can exist when the FeS formation reaction is fast and the

dissolution step is slow. The reaction rate for the dissolution of mackinawite can be expressed as [14]

$$\text{Rate} = k \times 10^{-pH} \times [FeS] \quad (3\text{-}37)$$

where k = the reaction rate constant (which is a function of temperature) and [FeS]= the molar concentration of solid FeS (which is defined as 1 for a solid species).

Tewari and Campbell[16] measured the iron ion release rate from a dissolving mackinawite surface in a series of experiments at various flow rates and two temperatures. The data were extrapolated to infinite flow rate to remove any consideration of iron ion complex diffusion. This allowed values for k to be determined at two temperatures as well as the activation energy and rate constant for the reaction. Tewari's testing was limited in that it could not provide the type of data required to model fluid flow in a manner as has been studied for CO_2 corrosion.

Corrosion rate in an oxygen-containing environment is often limited by oxygen diffusion, and it could be predicted by an empirical equation developed by Pisigan and Singly[17]

$$MPY = (TDS)\ 0.253 \times (DO)0.82 \times (10\ SI)\ 0.876 \times (Day)\ 0.373 \quad (3\text{-}38)$$

where TDS is total dissolved solids in mg/L, DO is dissolved oxygen in mg/L, SI is the Langelier scale index, and Day is exposure period in days.

Oxygen in water obeys Henry's law following

$$p_{O2} = K_{O2} \times x_{O2} \quad (3\text{-}39)$$

where p_{O2} is the partial pressure of oxygen in torr, x_{O2} is the mole fraction of oxygen in oxygen-saturated water, K_{O2} is the Henry's law constant for oxygen in water (about 3.30 × 107 K/torr for oxygen at 298 K).[18]

To determine saturated dissolved O_2 concentration (DO) in mg O_2/L water, the following two empirical equations may be used

$$0°C < t < 30°C \qquad DO = (P\text{-}p) \times 0.678/35 + t \quad (3\text{-}40a)$$
$$30°C < t < 50°C \qquad DO = (P\text{-}p) \times 0.827/49 + t \quad (3\text{-}40b)$$

These equations apply to oxygen in distilled water at a barometric pressure of P (in torr), at a temperature of t (°C), and with a water vapor pressure of p (in torr).[19]

The mechanistic nature of oxygen effect on CO_2 corrosion rate was modeled by researchers at University of Toronto, which accounted for the dual effects of oxygen on the corrosion rate. [20] In an acidic solution containing dissolved CO_2, oxygen reduction at the steel surface increases the corrosion rate by working as a cathodic reaction. On the other hand, as it is being reduced, hydroxyls form and the solution pH is elevated, thus, reducing the corrosion rate. This model is publicly available, and Figure 3-15 shows the model results.

3.8 Summary

A comprehensive CO_2 corrosion model considering both transport and migration of ionic species in solution was developed and validated with a significant amount of data in a wide range of conditions.

This model was used to predict corrosion rates in both wet and dry gas systems. The prediction results show that in a dry gas system, ferrous ions cannot escape the solution boundary layer and precipitation will occur. The reduced porosity at the steel surface by the precipitate leads to a reduced corrosion rate.

For wet gas systems where precipitates can dissolve and transport out of the boundary layer into the bulk solution, precipitation may or may not occur at the steel surface depending on the balance between the rates of formation and dissolution of a solid precipitate.

With a smaller porosity of the precipitate in dry gas corrosion systems, the corrosion rate in a dry gas system is less than in a wet gas system for the same conditions.

The model can be simplified by neglecting the voltage drop across the solution boundary layer (the ionic migration term in the flux equation). By this simplification, the challenges in numerical solution of the differential equations can be greatly reduced.

3.9 Practical Implications of the Model Results

3.9.1 Understanding the Difference in Corrosion Rate Between Wet and Dry Gas Systems

The pipeline industry has been using models developed for oil production systems to predict internal corrosion rates of both wet and dry gas pipelines. Such model prediction is reasonable for wet gas systems where abundant water is present; however, this prediction may significantly overestimate the internal corrosion rate for dry gas systems. In a dry gas pipeline, liquid water may be present condensation, and such a water layer can be thin and easily saturated. As a solid precipitates, both mass transport and the metal surface area available for corrosion are reduced, and thus a smaller corrosion rate is possible. This effect of solid formation on corrosion rate is modeled. The predictions show that the internal corrosion rate in a dry gas system can be significantly smaller than in wet gas systems.

The model has been validated by comparing the model results with lab and field data. The model has been simplified to reduce the challenges in numerically solving the differential equations. By neglecting the effect of the voltage drop in the boundary layer, the model differential equations can be reduced from nonlinear to linear. The complexity of the model can be significantly reduced.

When an internal corrosion rate in dry gas systems is predicted, the fact that the corrosion rate is less than in a wet gas system should be taken into account.

3.9.2 The Effect of H_2S and O_2 on Pipeline Internal Corrosion Rate

The effect of H_2S on CO_2 corrosion rate has been studied for several decades, and it is still challengeing to predict this effect. Charts are provided in this work to show the conditions where $FeCO_3$ (vs. FeS) is dominant and the CO_2 corrosion model is applicable. This provides guidelines for the use of the CO_2 corrosion model.

The effect of O_2 on CO_2 corrosion rate is twofold. The electrochemical reduction of oxygen increases corrosion rate. In the meantime, this reaction generates hydroxyls and decreases the corrosion rate. This interactive effect of O_2 on CO_2 corrosion rate leads to a situation where oxygen diffusion does not entirely controloxygen corrosion. In practice, the additive total of CO_2 corrosion rate without O_2 and the rate of oxygen corrosion controlled by diffusion overestimates the actual corrosion rate.

3.10 References

[1] F.M. Song, N. Sridhar, Corrosion Science 50(1) (2008) 70-83.
[2] F.M. Song, Electrochimica Acta 56 (2011) 6789-6803.
[3] F.M. Song, Corrosion Science 51 (2009) 2657-2674.
[4] J. Newman, K.E. Thomas-Alyea, Electrochemical Systems, 3rd edition, John Wiley and Sons, Inc. (2004) 209-214.
[5] K. Kumaresan, Y. Mikhaylik, R.E. White, J. Electrochem. Soc. 155 (2008) A576-A582.
[6] F.M. Song, D.W. Kirk, J.W. Graydon, D.E. Cormack, Corrosion 60(8) (2004) 736-748.
[7] F.M. Song, Electrochimica Acta 55 (2010) 689-700.
[8] C. de Waard, D.E. Milliams, Corrosion 31 (1975) 177.
[9] K. Videm, A. Dugstad, Materials Performance, March (1989) 63.
[10] K. Videm, A. Dugstad, Materials Performance, April (1989) 46.
[11] A. Dugstad, L. Lunde, K. Videm, "Parametric Study of CO_2 Corrosion of Carbon Steel," (NACE, 1994) Paper 14.
[12] C. de Waard, U. Lotz, "Prediction of CO_2 Corrosion of Carbon Steel" (NACE, 1993) Paper 69.
[13] F.M. Song, N. Sridhar, "An Approach to Determining Reassessment Intervals through Corrosion," DOT Contract No. DTRS56-04-T-0002, Final Report submitted in October 2006.
[13] NACE TG 076, "Prediction of Environmental Agressiveness in Oilfield Systems from System Conditions," draft report, 2011.
[15] R. Woollam, K. Tummala, J. Vera, S. Hernandez, "Thermodynamic Prediction of $FeCO_3$, FeS Corrosion Product Films", (NACE 2011), Paper 11076.
[16] P.H. Tewari, A.B. Campbell, Canadian J. Chemistry 57 (1979) 188-196.
[17] R.A. Pisigan, J.E. Singly, Materials Performance, April 1985.
[18] Z. Szklarska-Smialowska, Pitting Corrosion of Metals (NACE,1986) 302.
[19] P.W. Atkins, Physical Chemistry, 6th ed., Oxford University Press (1998) 174.
[20] F.M. Song, D.W. Kirk, J.W. Graydon, D.E. Cormack, Journal of the Electrochemical Society, 149(11) (2002) B479-B486.

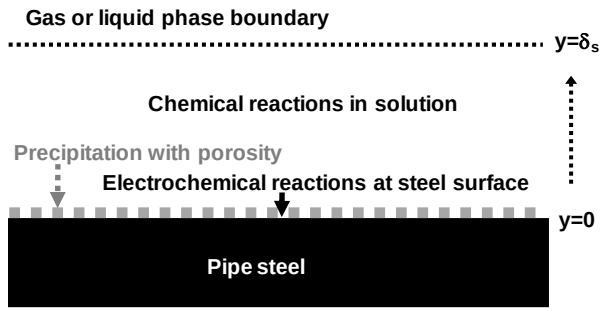

Figure 3-1. Schematic diagram showing the chemical, electrochemical, and mineral (precipitation) reactions that may occur in a boundary layer or at pipe steel surface.

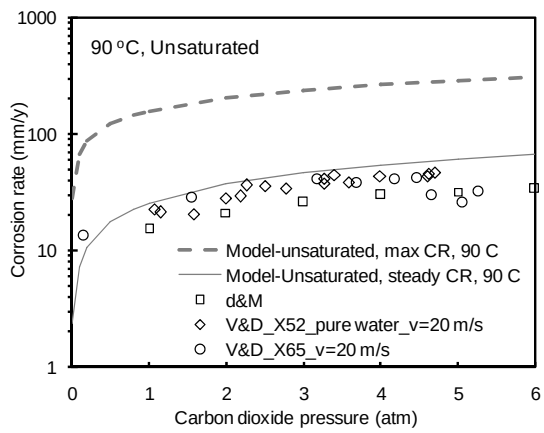

Figure 3-2. Model-predicted maximum (or initial) and steady-state corrosion rates vs. experimental data measured in an unsaturated solution at 90 °C in a flowing system [8,9].

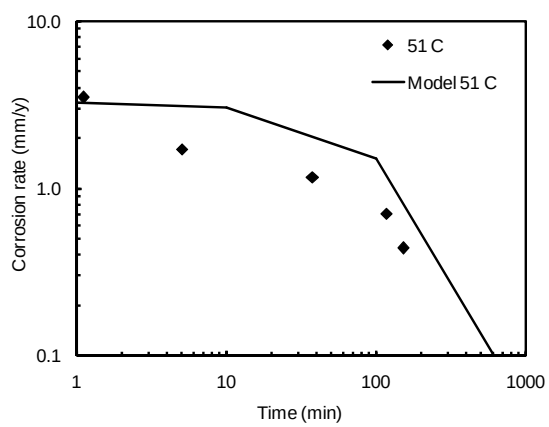

Figure 3-3. Model-predicted time-dependent corrosion rates vs. experimental data measured in a solution initially saturated by ferrous carbonate at 51 °C [10].

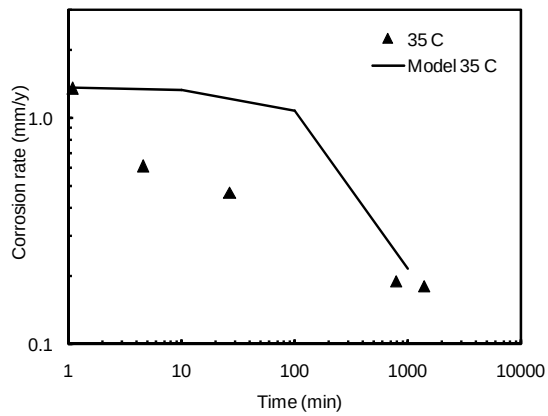

Figure 3-4. Model-predicted time-dependent corrosion rates vs. experimental data measured in a solution initially saturated by ferrous carbonate at 35 °C. [10]

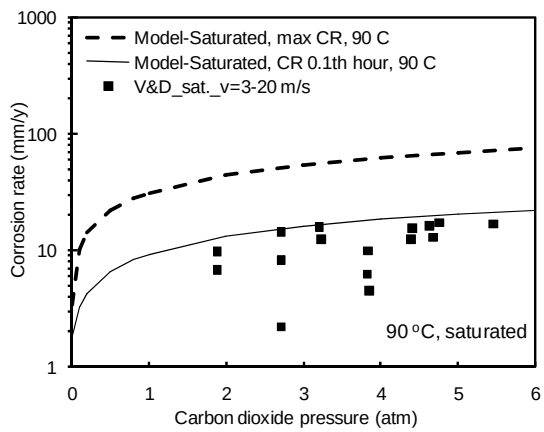

Figure 3-5. Model-predicted maximum (or initial) and at 0.1th hour instant corrosion rates vs. experimental data measured in a saturated solution at 90 °C. [10]

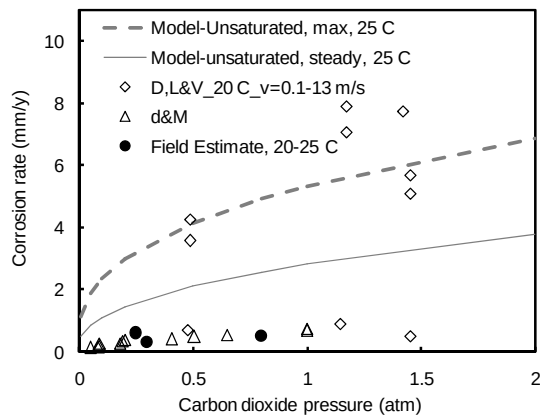

Figure 3-6. Model-predicted maximum (or initial) and steady-state corrosion rates vs. experimental data measured in lab [8,11] and estimated from field [12] in an unsaturated solution at 25 °C with flow.

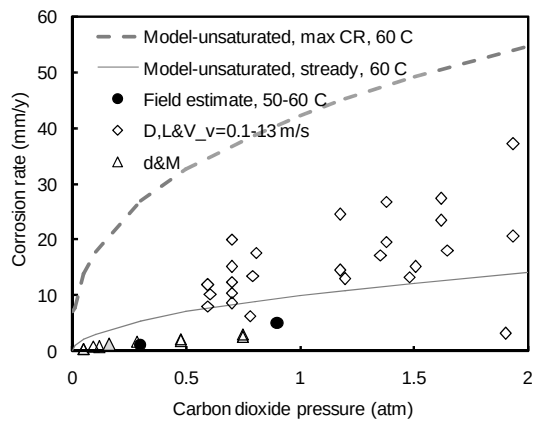

Figure 3-7. Model-predicted maximum (or initial) and steady-state corrosion rates vs. experimental data measured in lab [11] and estimated from field [12] in an unsaturated solution at 60 °C with flow.

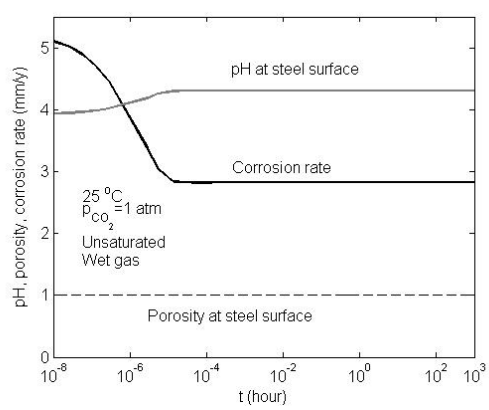

Figure 3-8. Model-predicted corrosion rates for both wet and dry gas systems at 25 °C and p_{CO2}=1 atm. The boundary layer thickness is 10 μm and initially contains negligible ferrous ion.

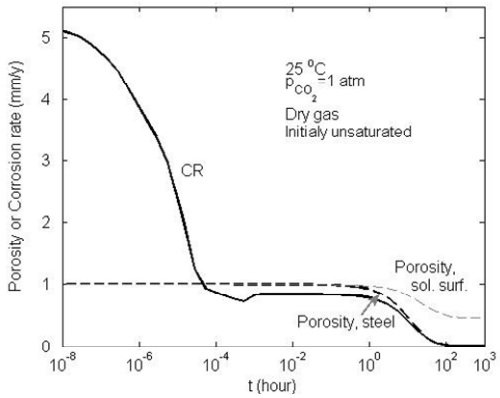

Figure 3-9. Predicted corrosion rates and porosity for only the dry gas system at the same condition of Figure 3-8.

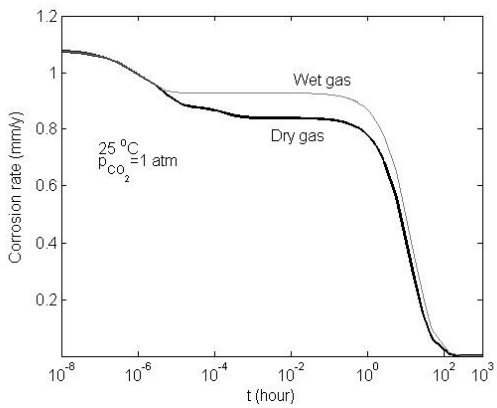

Figure 3-10. Model-predicted corrosion rates for both wet and dry gas systems at 25 °C and p_{CO2}=1 atm. The boundary layer thickness is 10 μm, and it is initially saturated with ferrous carbonate. For wet gas, the bulk solution is also saturated with ferrous carbonate.

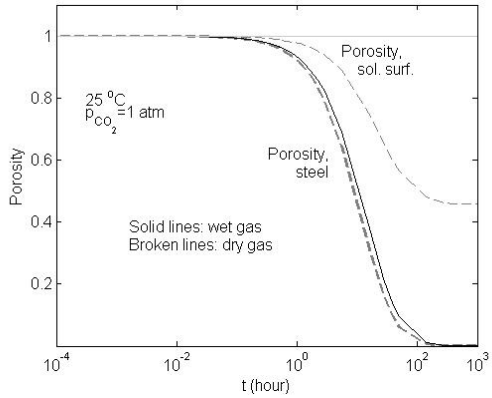

Figure 3-11. For the same conditions of Figure 3-10, the porosity variations with time for both wet and dry gas systems.

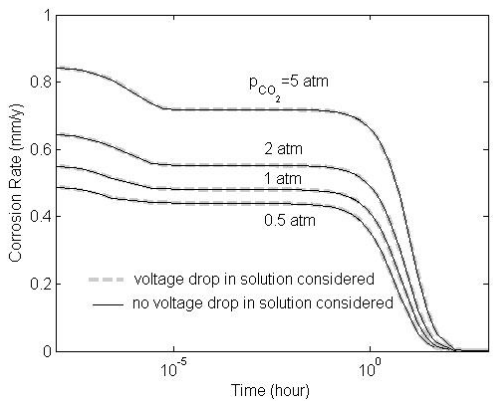

Figure 3-12. Verification of model simplification by comparison of corrosion rates obtained from the model by considering and not considering the voltage drops in the boundary layer.

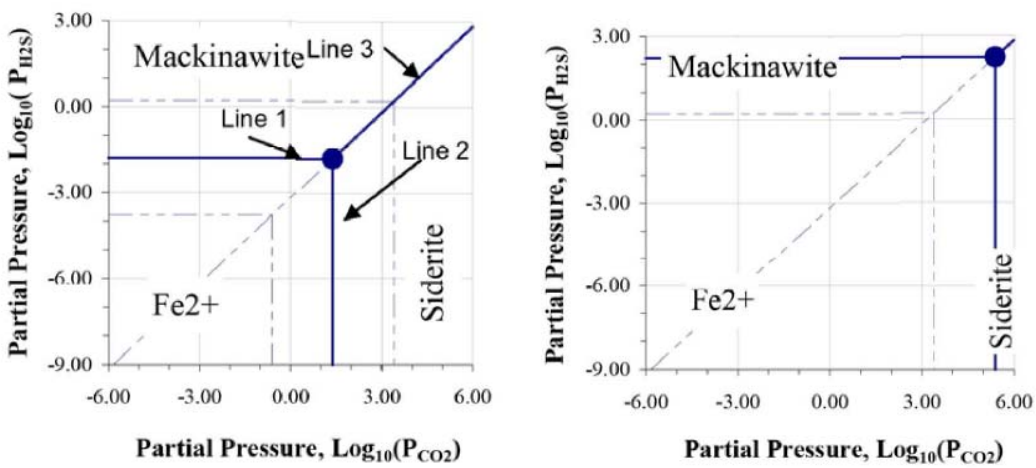

(a) (b)

Figure 3-13. Region of a dominant precipitate: Siderite ($FeCO_3$) or Mackinawite (FeS), determined based on Equation (3-36), when $[Fe^{2+}]=10^{-6}$ mol/liter and the solution pH is (a) pH=6 and (b) pH=4.[15]

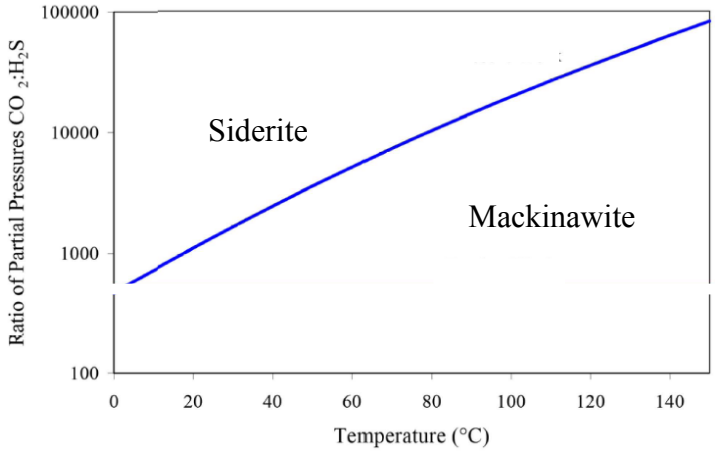

Figure 3-14. Siderite-Mackinawite boundary determined based on Equation (3-36) for varying temperatures and the ratio of partial pressure.[15]

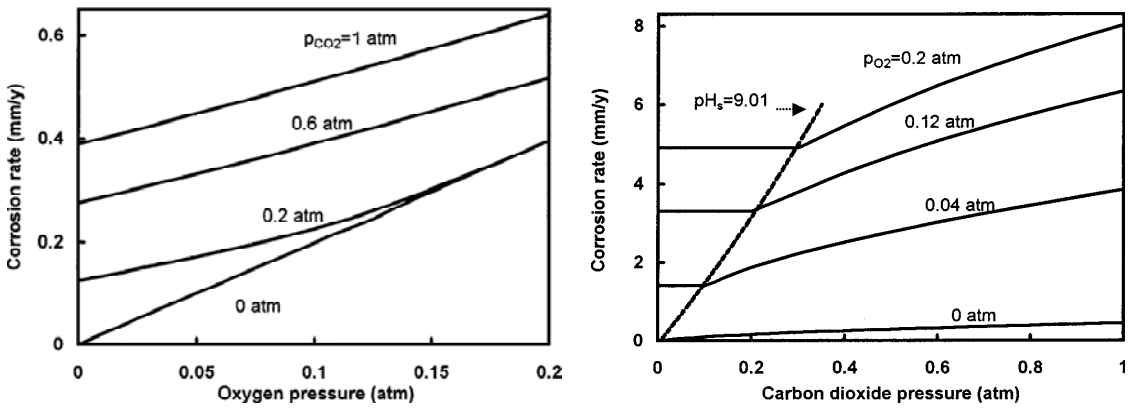

Figure 3-15. The interactive effect of CO_2 and oxygen on steel corrosion.[20]

4.0 CONCLUSIONS AND RECOMMENDATIONS

4.1 Conclusions

4.1.1 Pipeline External Corrosion

A model is developed that enables prediction of the chemistry and corrosion rate in a coating-disbonded region for the following conditions: (1) gap of the disbondment varies with location, (2) different CP levels at the holiday, and (3) the effect of coating permeability to CP and oxygen or carbon dioxide.

The model-predicted results are qualitatively consistent with laboratory test results and with field observations in terms of pH, Cl^- concentration, and steel potentials measured in simulated coating-disbonded regions.

Unlike conventional crevice corrosion often associated with a large cathode-to-anode area ratio, the area ratio for the pipeline corrosion under a disbonded coating is rather small. Irrespective of CP levels, the pH in the disbonded region falls in the neutral or alkaline range as long as the soil is not acidic. Predicted corrosion rate is, in this case, not significant. Pitting, microbiologically induced corrosion, and corrosion due to alternative current or direct current interferences are not studied in this work.

When the pipe surface at a holiday is maintained with CP (e.g., -850 mV or -900 mV vs. copper/copper sulfate (CSE)), the pH in the coating-disbonded region increases over time and the corrosion rate decreases. With time, the pH in the disbonded region may exceed that near the holiday. In the absence of CP and in aerated soil, the overall pH in the disbonded region decreases over time and can fall below that near the holiday.

CP shielding is only partially true. In the presence of CP, the increase of pH over time in coating-disbonded regions and the shift of potential in a more negative direction reduces the local corrosion rate over time. Corrosion may happen when the soil is aerated and wet and the CP is either lacking or inadequate.

The variation of gap with location in a coating-disbonded region appears to have an insignificant effect on the solution chemistry and corrosion rate (relative to a disbondment of uniform gap). The gap effect on the solution chemistry, such as sodium ion (Na^+) concentration if present, may be described by using an analogy to flow effect. Assuming the total diffusion rate of Na^+ (equivalent to flow rate) at the gap-narrowing location is approximately the same, its diffusion flux (equivalent to flow velocity) is different due to the change of cross-section area by the change of gap. With CP, as the gap narrows (away from the holiday), Na^+ tends to accumulate and its concentration increases. Conversely, as the gap expands, the Na^+ diffusion flux decreases and it tends to dissipate out, leading to a reduced concentration.

A permeable coating behaves like a membrane, which, under cathodic polarization at the holiday, tends to raise the cation (e.g. Na^+) concentration and pH more rapidly (relative to an impermeable coating). The Na^+ concentration and the pH may exceed those at the holiday, and

subsequently, the mass transport across the coating starts to reverse to the opposite direction. At a holiday potential of -900 mV_{CSE}, the cathodic current appears to be able to sufficiently suppress corrosion caused by either O_2 or CO_2 (combination not studied) if it penetrates into the disbonded region from both the holiday and the coating. The practical implication is that in the presence of sufficient CP, a permeable coating, when disbonded, can still be capable of protecting the substrate steel from corrosion attack.

The model can be scaled with respect to time and geometry of the coating-disbonded region (gap and length). For a disbonded region of uniform gap, such scaling has been verified by model simulations and is useful for reducing model computations and, when needed, scaling experiments. The geometry scaling factor is found to be L^2/δ_0 (or $L/\sqrt{\delta_0}$), and the time-scaling factor is t/δ_0, where L is the disbondment length, δ_0 is gap, and t is time.

4.1.2 Pipeline Internal Corrosion

For pipeline internal corrosion, a comprehensive CO_2 corrosion model was developed and validated with laboratory and field data in a wide range of conditions. This model considers both diffusion and migration of ionic species in solution. The general fundamentals of the model are the same for both wet and dry natural gas pipelines. Nevertheless, the corroding conditions of these two systems are different such as the different amount of water present in these systems, and thus the predicted corrosion rates are different.

In dry gas pipelines, ferrous ions as corrosion products cannot escape the solution boundary layer at the pipe wall, and thus precipitation will occur. The precipitate reduces mass transport and the exposed metal surface area for corrosion and leads to a reduced corrosion rate compared to a wet gas system. For wet gas systems where precipitates can dissolve and transport out of the boundary layer into the bulk solution, precipitation may or may not occur at the steel surface depending on the balance between the formation rate of a precipitate and the dissolution rate of this precipitate. This model result suggests that when an internal corrosion rate in a dry gas system is predicted, the fact that the corrosion rate in this dry gas system is smaller than in a wet gas system should be considered.

The model can be simplified by neglecting ionic migration across the solution boundary layer to yield the same results. This simplification can greatly reduce the challenges in numerical solution of the differential equations, from nonlinear to linear equations.

Predicting the effect of H_2S on CO_2 corrosion rate is still a challenge. In this work, charts are provided to show conditions where $FeCO_3$ is dominant over FeS (and vice versa) and the CO_2 corrosion model is applicable. O_2 in a CO_2 corrosion system can increase the corrosion rate by diffusion. In the meantime, the generated hydroxyls from O_2 reduction reduce the corrosion rate. This interactive effect of O_2 on CO_2 corrosion rate leads to a situation where oxygen diffusion does not entirely contribute to CO_2 corrosion. In practical prediction of pipeline internal corrosion, it should be considered that the additive total of CO_2 corrosion rate without O_2 and O_2 corrosion rate (controlled by its diffusion) overestimates the actual corrosion rate.

4.2 Recommendations

4.2.1 Pipeline External Corrosion

It is recommended that an industrial survey and field data analysis (a correlation of soil condition, CP level, sample results of chemistry and corrosion in coating-disbonded regions) be performed to understand the conditions where both CP works and fails for a shielding coating. This helps to explain the root causes of pipeline external corrosion.

The effect of solid precipitation on pipeline external corrosion in a coating-disbonded region needs to be studied. It is possible that calcareous deposits formed at the holiday block the pathway of CP penetration into the disbonded region.

4.2.2 Pipeline Internal Corrosion

The effects of H_2S and O_2 on CO_2 corrosion need to be further understood experimentally before a reliable mechanistic model can be developed for field use.

APPENDIX A

DERIVATION OF EQUATION (2-1) AS A MODEL GOVERNING EQUATION

The crevice gap can vary over distance and, when the metal depletion or formation precipitations are considered, the gap can also vary with time. For a two-dimensional (2D) crevice (longitudinal x direction and y direction perpendicular to the steel surface), the mass transport equation for the ith dissolved species in the solution may be written as

$$\frac{\partial(\delta_s c_i)}{\partial t} + \frac{\partial(\delta_s \Gamma_{ix})}{\partial x} + \frac{\partial \Gamma_{iy}}{\partial y} = \delta_s R_i \qquad \text{(A-1)}$$

where c_i is concentration of the ith species; R_i is the total net volumetric production rate (after consumption deducted) of the ith species; subscripts x and y refer to x and y coordinators (e.g., see Figure 2-1a); δ_s is gap at distance x and varies with x and time t. The variation of δ_s with t can be the result of depletion of the metal by corrosion. Γ_i is flux including the convective flow.

When the 2D crevice is simplified as one-dimensional (1D) in the x direction, integration of Equation (A-1) across the gap yields

$$\frac{\partial(\delta_s c_i)}{\partial t} + \frac{\partial}{\partial x}(\delta_s \overline{\Gamma}_{ix}) + \Gamma_{iyc} = \delta_s R_i + R_{si} \qquad \text{(A-2)}$$

where R_{si} is the total reaction rate at the steel surface, which equals the total flux leaving the steel surface, and $\overline{\Gamma}_{ix}$ is average flux across the gap and

$$\overline{\Gamma}_{ix} = \overline{v}_x c_i + N_{ix} = \overline{v}_x c_i - D_j \frac{\partial c_j}{\partial x} - \frac{z_j D_j F}{RT} c_j \frac{\partial \varphi}{\partial x} \qquad \text{(A-3)}$$

where N_{ix} is the flux due to diffusion and migration only, or

$$N_{ix} = -D_j \frac{\partial c_j}{\partial x} - \frac{z_j D_j F}{RT} c_j \frac{\partial \varphi}{\partial x} \qquad \text{(A-4)}$$

N_{ix} differs from $\overline{\Gamma}_{ix}$ by neglecting the convective flow. In the y direction, no flow goes across the coating and the transport of the ith species through the coating is a controlling step. Thus,

$$\Gamma_{iyc} = N_{iyc} = -D_{jc} \frac{c_{j0} - c_j}{\delta_c} - \frac{z_j D_{jc} F}{RT} c_j \frac{\varphi_0 - \varphi}{\delta_c} \qquad \text{(A-5)}$$

The velocity term in Equation (A-3) results from depletion of the metal surface by corrosion. At x, the mass flowing across the gap for a unit time equals the total change of the mass in the disbondment between x and L (disbondment tip). Because there is no mass exchange through the disbondment end, the mass balance can be expressed by

$$\rho_x \bar{v}_x \delta_s = \int_x^L \rho_\chi \frac{\partial \delta_s}{\partial t} d\chi \tag{A-6}$$

When the liquid density variation between x and L can be neglected due to dilute solution, Equation (A-6) becomes

$$\frac{\partial(\bar{v}_x \delta_s)}{\partial x} + \frac{\partial \delta_s}{\partial t} = 0 \tag{A-7}$$

Taking the coating surface as a reference plane, the gap change equals the corrosion velocity

$$\frac{\partial \delta_s}{\partial t} = \beta r_{Fe} \tag{A-8}$$

Substituting Equations (A-3) and (A-7) into Equation (A-2) yields

$$\delta_s \frac{\partial c_i}{\partial t} + \bar{v}_x \delta_s \frac{\partial c_i}{\partial x} + \frac{\partial}{\partial x}(\delta_s N_{ix}) + N_{iyc} = \delta_s R_i + R_{si} \tag{A-9}$$

In Equation (A-9) the average velocity can be determined from Equation (A-6), or

$$\bar{v}_x = \delta_s^{-1} \beta \int_x^L r_{Fe} dx \tag{A-10}$$

When the change of gap vs. time due to metal depletion by corrosion can be neglected, the velocity term can be set as zero and Equation (A-9) becomes

$$\delta_s \frac{\partial c_i}{\partial t} + \frac{\partial}{\partial x}(\delta_s N_{ix}) + N_{iyc} = \delta_s R_i + R_{si} \tag{A-11}$$

APPENDIX B

REVERSIBLE AND IRREVERSIBLE HOMOGENEOUS AND HETEROGENEOUS REACTIONS, CHEMICAL EQUILIBRIUM FORMULA, AND KINETIC RATES IN THE CREVICE CORROSION SYSTEM WITHOUT CO_2

The reversible reactions in the crevice without CO_2 are

$$H_2O - H^+ \leftrightarrow OH^- \quad (H_2O \leftrightarrow H^+ + OH^-),\ c_4c_5 = K_w \tag{B-1}$$

$$Fe(OH)_2 + 2H^+ \leftrightarrow Fe^{2+} + 2H_2O \quad (Fe(OH)_2 \leftrightarrow Fe^{2+} + 2OH^-),\ c_3c_5^2 = K_{SP} \tag{B-2}$$

$$Fe(OH)_2 + H^+ \leftrightarrow FeOH^+ + H_2O \ (Fe^{2+} + H_2O \leftrightarrow FeOH^+ + H^+),\ \frac{c_4c_6}{c_3} = K_1 \tag{B-3}$$

The reactions in the parentheses are equivalent reactions but show more clearly the equilibrium relations among reactants and products. The concentrations of all the secondary species can be expressed by those of the primary species.

The electrochemical reactions are

$$Fe \rightarrow Fe^{2+} + 2e^- \qquad r_{Fe}^e \tag{B-4}$$

$$H^+ + e^- \rightarrow 0.5H_2 \qquad r_H^e \tag{B-5}$$

$$H^+ + e^- \rightarrow 0.5H_2 \qquad r_{H_2O}^e \tag{B-6}$$
$$(H_2O + e^- \rightarrow 0.5H_2 + OH^-)$$

$$4H^+ + O_2 + 4e^- \rightarrow 2H_2O \qquad r_{O_2}^e \tag{B-7}$$

When the concentrations of Na^+ and Cl^- are the same, the electroneutrality ($\sum_j z_j c_j = 0$) allows each concentration to be determined analytically. For the system of concern, the equation of electroneutrality can be written as

$$2K_{sp} + (K_w + \frac{K_1K_{sp}}{K_w})c_5 - c_5^3 = 0 \tag{B-8}$$

The solution of Equation (B-8) is

$$c_5 = \frac{2^{\frac{1}{3}}(k_w + \frac{K_1K_{sp}}{K_w})}{\lambda_2} + \frac{\lambda_2}{3 \cdot 2^{\frac{1}{3}}} \tag{B-9}$$

where $\lambda_1 = 6\sqrt{81k_{sp}^2 - 3(k_w + \frac{K_1K_{sp}}{K_w})^3}$ and $\lambda_2 = (\lambda_1 + 54k_{sp})^{\frac{1}{3}}$.

For a more general case where the charges of Na^+ and Cl^- may or may not balance out, the following equation may be used

$$z_1c_1 + z_2c_2 + z_3\frac{K_{sp}}{c_5^2} + z_4\frac{K_w}{c_5} + z_5c_5 + z_6\frac{K_1K_{sp}}{K_wc_5} = 0 \qquad \text{(B-10)}$$

Alternatively, Equation (B-10) is written as

$$z_5c_5^3 + p_1c_5^2 + p_{10}c_5 + z_3K_{sp} = 0 \qquad \text{(B-11)}$$

where $p_{10} = (z_4K_w + z_6\frac{K_1K_{sp}}{K_w})/z_5$, and $p_{20} = z_3K_{sp}/z_5$.

The solution of Equation (B-11) is

$$c_5 = -\frac{p_1}{3} - \frac{2^{\frac{1}{3}}p_2}{3p_5} + \frac{p_5}{2^{\frac{1}{3}}3} = \frac{p_5^2 - 2^{\frac{1}{3}}p_1p_5 - 2^{\frac{2}{3}}p_2}{2^{\frac{1}{3}}3p_5} \qquad \text{(B-12)}$$

where

$$p_5 = (p_3 + p_4)^{\frac{1}{3}} \qquad \text{(B-13a)}$$

$$p_4 = \sqrt{4p_2^3 + p_3^2}\,, \qquad \text{(B-13b)}$$

$$p_3 = -2p_1^3 + 9p_{10}p_1 - 27p_{20}\,, \qquad \text{(B-13c)}$$

$$p_2 = -p_1^2 + 3p_{10}\,, \qquad \text{(B-13d)}$$

$$p_1 = (z_1c_1 + z_2c_2)/z_5\,. \qquad \text{(B-13e)}$$

With Equation (B-9) or (B-12), the concentrations of other species may be calculated from

$$c_4 = \frac{k_w}{c_5}\,,\ c_3 = \frac{K_{sp}}{c_5^2}\,,\ c_6 = \frac{K_1K_{sp}}{K_wc_5} \qquad \text{(B-14)}$$

APPENDIX C

CREVICE CORROSION CONSIDERING THE EFFECT OF FLOW INDUCED BY GAP VARYING WITH METAL DISSOLUTION

The effect of gap variation over time due to metal dissolution or accumulation of corrosion product in the crevice has not been quantitatively investigated. The time-dependent variation of gap can change the cross-sectional area of the crevice for mass transport and induce a tiny fluid flow. The effect of this fluid flow caused by the corrosion itself is studied in this work.

The condition to be studied is where no CP applied to the crevice or the crevice mouth potential is fixed at -0.8071 V. In this condition, the crevice corrosion rate is greater than in the presence of CP and the effect of this fluid flow on the crevice corrosion is greater. The crevice geometry used for the modeling is Figure 2-1(b).

Figure C-1 shows the gap change vs. the crevice length for different times. At the holiday, the potential and chemistry are fixed as boundary conditions, and thus the corrosion rate at the holiday is a constant and it is expected that the gap increases linearly over time. Without CP at the holiday, driven by an oxygen concentration cell, both the crevice corrosion rate and the gap change are greatest at the holiday.

Because the overall corrosion rate in the crevice is small, only the gap variation near the holiday is seen to be obvious at 10^7 s. At 10^8 s, the gap at the holiday expands to more than 1.5 times its size. The gap change inside the crevice is small after the 100th gap from the holiday.

Figure C-2 shows the corrosion current density in the crevice. The sharp variation of corrosion current density at time zero near the holiday results from the modeling settings. The concentrations at the holiday are different from those initially found in the crevice and the gap has abrupt changes at several locations in the crevice. With initial concentrations uniform in the crevice, essentially Laplace's equation is solved for potential and, thus corrosion current density. This figure provides a comparison of the model results when the gap variation over time is and is not considered.

Prior to 10^7 s (steady state is reached for the crevice without considering gap variation over time), the results obtained from both crevices (with and without considering the gap variation over time) are nearly identical. After 10^7 s or at 10^8 s, the corrosion rate for the crevice considering gap variation over time still increases continuously over time and the curve departs from the curve at 10^7 s. This result suggests that the use of the crevice without considering gap variation over time to approximate the crevice considering the gap variation is valid prior to the steady state for the former crevice (10^7 s).

The fluid flow velocity induced in the crevice by the time-variation of gap caused by metal dissolution is shown in Figure C-3. Because no fluid flows across the tip of the crevice, the velocity there is always zero. Mass conservation dictates that the flow rate at any location in the crevice equals the accumulated volume displaced by metal loss per a unit time between this point

and the crevice tip, or the integration of corrosion rate (in unit m/s) over distance between this location and the crevice tip. This relation is clearly demonstrated by Equation (2-3).

Deep inside the crevice, Figure C-3 shows that the velocity is linear over distance because the corrosion rate is relatively uniform. Close to the crevice tip, the difference in velocity at different times up to 10^8 s is nearly invisible. Moving toward the mouth or as the accumulated fluid volume (per time unit) increases, the flow velocity tends to increase (prior to 10^7 s). For the regions with a narrowed gap, the velocity is significantly greater because of the apparently much smaller cross-sectional area relative to a similar magnitude of flow rate across the edges of these regions. The closer to the mouth, the more significant the flow velocity.

Following Equation (2-3), the flow velocity can increase with increasing corrosion rate over time but can also decrease with increasing gap over time. At 10^8 s, the gap expansion with time near the holiday becomes more dominant and a decrease in flow velocity is seen. Because the overall flow velocity is extremely small, on the order of 10^{-12} m/s, its effect on corrosion by this flow is perhaps smaller than diffusion. Thus, the consideration of this fluid flow in this model yields nearly no benefit. However, when the corrosion rate is significant and it varies significantly along distance in the crevice, this flow effect may dominate over diffusion, a scenario not included in this work.

Because the fluid flow effect is negligible on the corrosion rate, this effect on the crevice chemistry is not expected to be significant. This is demonstrated in Figure C-4 for (a) Na^+ and (b) Cl^- concentrations.

Other than at 10^8 s, the Na^+ and Cl^- concentrations at different times overlap for crevices both with and without considering gap variation over time. After 10^7 s, corrosion in the crevice considering gap variation over time is still in the unsteady state, while the crevice without considering gap variation over time is already in steady state. Thus, the concentrations in the two crevices depart from each other over time.

For the crevice considering gap variation over time, as the crevice gap expands over time, the oxygen transport into the crevice from the holiday increases, the oxygen concentration cell becomes stronger, and the positive current flow from inside the crevice to nearby the mouth increases. Hence, the Na^+ concentration at 10^8 s near the mouth in the crevice considering gap variation over time is greater than for the crevice without considering the gap variation (steady state). For Cl^-, steady state does not seem to be reached in either crevice at 10^8 s; the Cl^- concentration in the crevice considering gap variation over time is smaller than in the crevice without considering gap variation over time.

The charge balance between the Na^+ and Cl^- concentrations in the crevice determines the pH in the crevice as shown in Figure C-5. For the two crevices with and without considering the gap variation over time, the pHs overlap for all times except at 10^8 s. At 10^8 s, steady-state corrosion has not yet bben reached for the crevice considering gap variation over time. The charge balance between Na^+ and Cl^- is positive in the crevice with considering gap variation with time. Thus, relative to the crevice without considering gap variation over time, this positive charge has to be balanced by OH^- and the pH is greater wherever Na^+ is greater.

The potential variation in the crevices at different times is shown in Figure C-6. This variation is similar to that of corrosion current density (as shown in Figure C-2) because of an exponential Tafel relationship.

Although not reported in this work, the gap can decrease over time due to accumulation of corrosion products. However, similar results would be expected before the gap becomes very small. The effect from considering the gap reducing over time is expected to be insignificant unless the corrosion rate is significant; then the induced flow becomes significant.

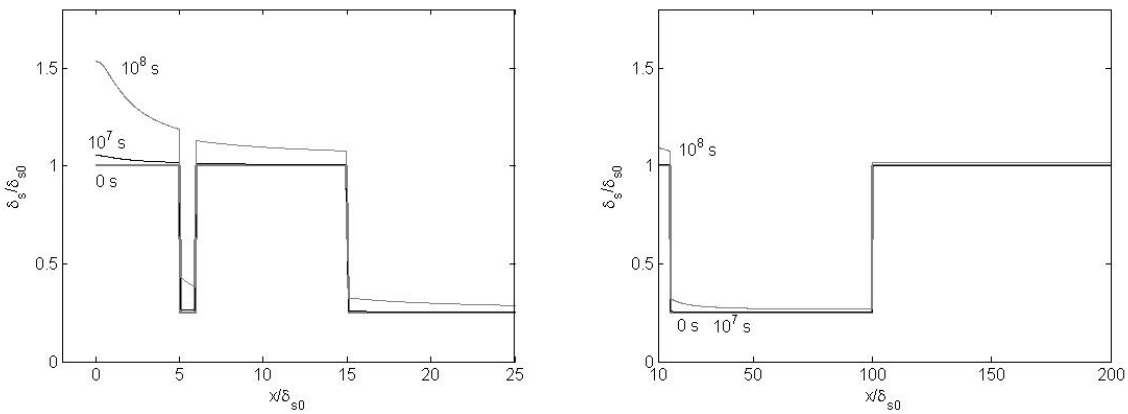

Figure C-1. At a fixed mouth potential of -0.8071 V, the variation, by metal depletion, of the crevice gap vs. distance at different times: (a) near the mouth and (b) away from the mouth.

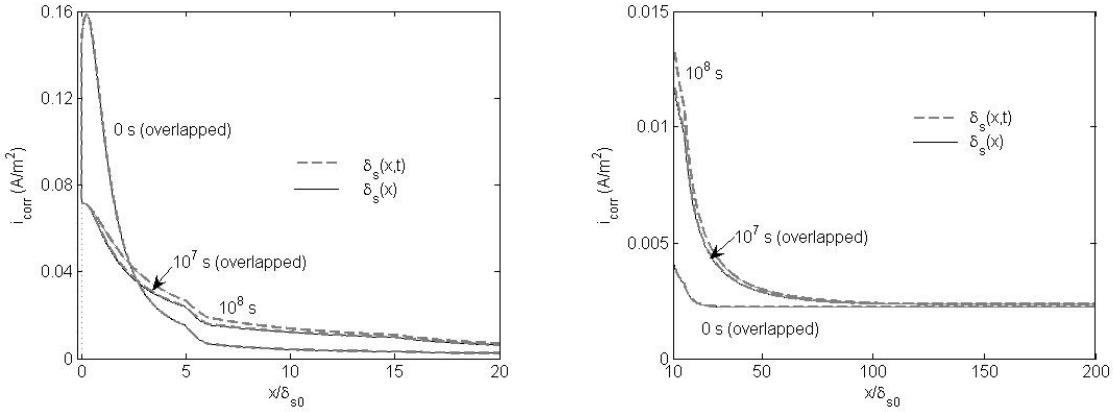

Figure C-2. Same as Figure C-1, but here for the corrosion current density due to time variation of gap: (a) near the mouth and (b) away from the crevice mouth.

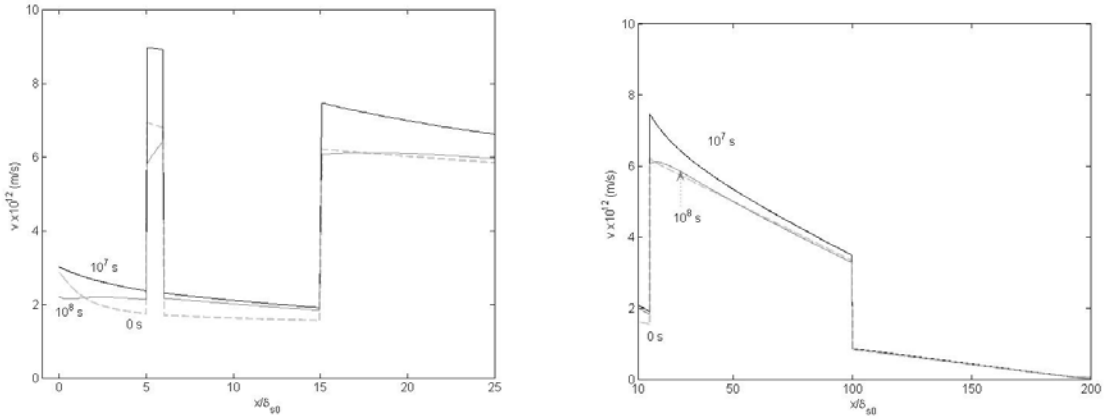

Figure C-3. Same as Figure C-1, but here for the velocity due to time variation of gap: (a) near the mouth and (b) away from the crevice mouth.

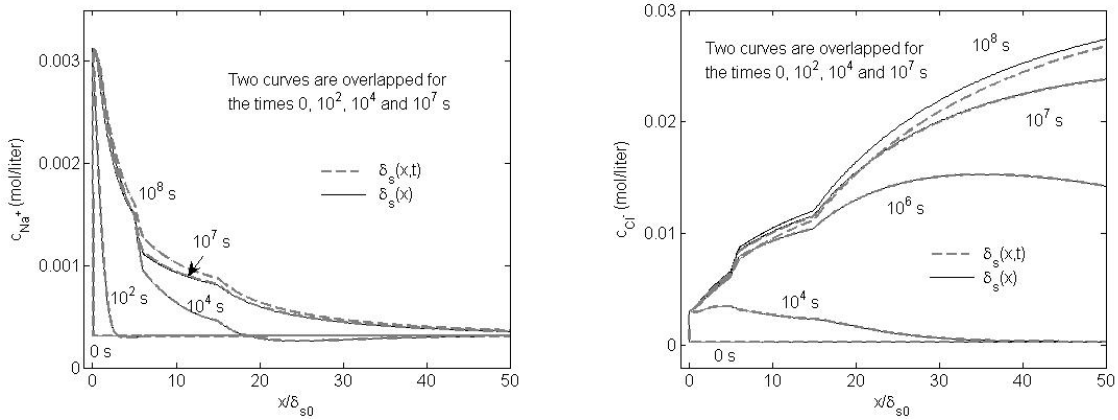

Figure C-4. Same as Figure C-1, but here for the variation near the mouth of (a) Na^+ concentration and (b) Cl^- concentration.

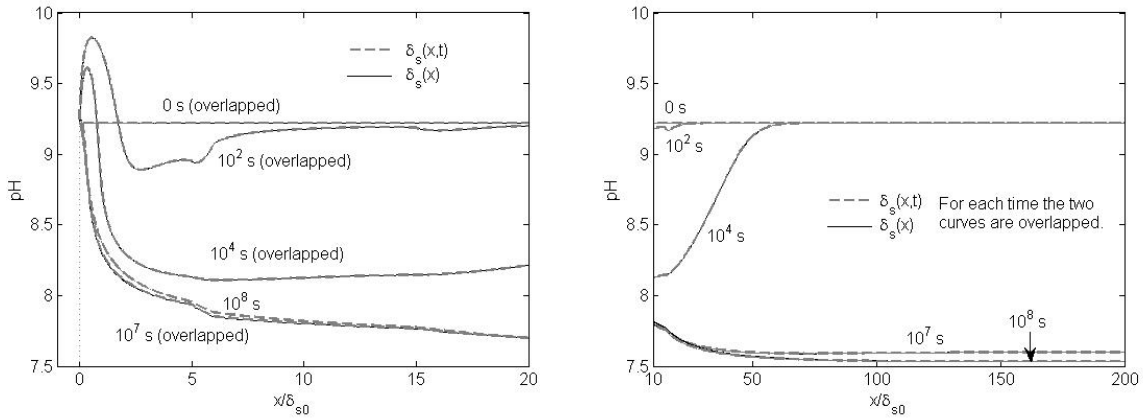

Figure C-5. Same as Figure C-1, but here for the crevice solution pH: (a) near the mouth and (b) away from the crevice mouth.

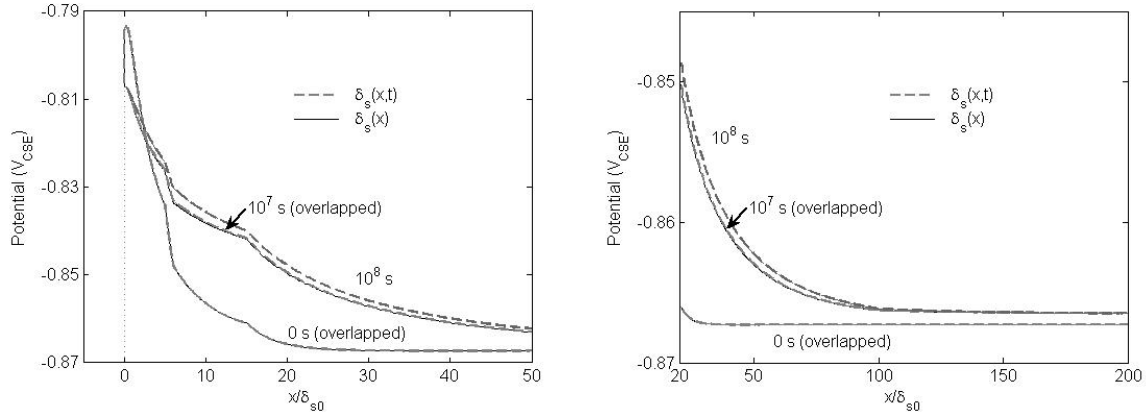

Figure C-6. Same as Figure C-1, but here for the crevice potential: (a) near the mouth and (b) away from the crevice mouth.

APPENDIX D

DERIVATION OF MODEL GOVERNING EQUATIONS WITH CO_2 IN CREVICE

For a crevice solution containing dilute NaCl and CO_2 gas, the solution species include (1) $\underline{Na^+}$, (2) $\underline{Cl^-}$, (3) $\underline{Fe^{2+}}$, (4) $\underline{H^+}$, (5) OH^-, (6) $Fe(OH)^+$, (7) $\underline{CO_2}$, (8) $FeHCO_3^+$, (9) $\underline{CO_3^{2-}}$, (10) HCO_3^-, (11) H_2CO_3, (12) $\underline{H_2(aq)}$, (13) $\underline{FeCO_3}$, (13) $\underline{Fe}$, and (14) $\underline{H_2O}$, where the underlined species are defined as the primary species for this work. Their concentrations can be either given for the initial and boundary conditions, as those shown in Table 2-2 or known, such as for species (11) through (13). The concentrations of the primary species can be used to determine the concentrations of the secondary species based on the equilibrium relationship between the primary and the secondary species.

In this system, the only irreversible chemical reaction considered is CO_2 hydration, a slow step in the CO_2 chain reactions. The precipitation reaction considered is the formation of $FeCO_3$, although porosity due to the precipitation is neglected in this first attempt. This work considers CO_2 both permeable and impermeable to the coating.

By cancelling out the reversible reaction rates, the governing equations for the problem of interest are

$$\frac{\partial c_1}{\partial t} + \frac{\partial}{\partial x} N_{1x} = 0 \qquad \text{(D-1)}$$

$$\frac{\partial c_2}{\partial t} + \frac{\partial}{\partial x} N_{2x} = 0 \qquad \text{(D-2)}$$

$$\frac{\partial (c_3 + c_6 + c_8)}{\partial t} + \nabla (N_3 + N_6 + N_8) = -r_{pc} + \delta_s^{-1} r_{Fe}^e \qquad \text{(D-3)}$$

$$\frac{\partial (c_4 - c_5 - c_6 + c_8 + c_{10} + 2c_{11})}{\partial t} + \nabla (N_4 - N_5 - N_6 + N_8 + N_{10} + 2N_{11}) = 2r_{CO_2} + \delta_s^{-1} (r_H^e + r_{H_2O}^e + 4r_{H_2CO_3}^e)$$

(2-D.4)

$$\frac{\partial c_7}{\partial t} + \nabla N_7 = -r_{CO_2} + \delta_s^{-1} R_{CO_2} \qquad \text{(D-5)}$$

$$\frac{\partial (c_9 + c_8 + c_{10} + c_{11})}{\partial t} + \nabla (N_9 + N_8 + N_{10} + N_{11}) = -r_{pc} + r_{CO_2} \qquad \text{(D-6)}$$

$$\sum_1^6 z_j c_j = 0 \qquad \text{(D-7)}$$

Equation (D-7) may be alternatively written as

$$\frac{\partial}{\partial x} \left(\sum_1^{10} z_j N_{jx} \right) = 2r_{Fe}^e + r_H^e + r_{H_2O}^e + 4r_{H_2CO_3}^e \qquad \text{(D.8)}$$

where t is time and z_j, c_j, and N_j are the charge, concentration, and flux of the jth species, respectively. δ_s is the boundary layer thickness. r^e represents the electrochemical (anodic or cathodic) reaction rate, with a key element involving the reaction shown in the subscript of the r term. r_{pc} is rate of precipitation of ferrous carbonate, r_{CO2} is rate of CO_2 hydration, and R_{CO2} is diffusion rate of CO_2 through the coating.

The rate of ferrous carbonate precipitation may be expressed by

$$r_{p_1} = k_{f_{FeCO_3}} \sigma_1 K_{sp_{FeCO_3}} (S_{FeCO_3} - 1) \tag{D-9}$$

where k and K_{sp} are precipitation rate constant and solubility product, respectively. S is the ratio of relevant ionic concentration products to K_{sp}, which measures the level of saturation or super-saturation of the solution. σ_1 or σ_2 is specific area or the ratio of surface area over the volume of a precipitate. Without specific knowledge, it is assumed $\sigma_1 = 10^4$.

The expression for the rate constants, $k_{f_{FeCO_3}}$, follows

$$k_p = k_{f_{FeCO_3}} = k_{f_{Fe(OH)_2}} = \exp(28.2 - \tfrac{64851.4}{RT}) \tag{D-10}$$

When the precipitation process is considered to be irreversible (or dissolution of the precipitation into solution is neglected), the precipitation rate can be written as

$$r_{p_j} = \max(0, r_{p_1}) \tag{D-11}$$

The irreversible volumetric rate of CO_2 hydration may be written as

$$r_{CO_2} = k_f c_7 - k_b c_{11} \tag{D-12}$$

where k_f and k_b are the forward and backward reaction rate constants of CO_2 hydration, respectively.

Similar equations are shown in Chapter 3 where modeling pipe internal corrosion is addressed.

The initial and boundary conditions for solving the governing equations of the pipeline external corrosion appear in Section 2.3.2.

APPENDIX E

RESULTS OF CREVICE CORROSION CONSIDERING PASSIVITY OF STEEL AT pH 10.5 OR GREATER

It has been argued that when the pH is high, passive film may develop on a steel surface and corrosion slows down. For this model, pH 10.5 is set as the boundary that separates the active and passive states of the steel surface. In both states, Tafel equations are assumed to apply for all cathodic reactions, while Tafel equation applies for steel dissolution only in the active region. In the passive region, the current density on steel is fixed at 10^{-3} A/m^2. For all calculations in this appendix, the crevice geometry of Figure 2-1(a) is used, and the crevice concentrations at the mouth are set to be the same as those in the initial condition and the same as the initial concentrations (see Table 2-1). With these assumptions, the model is used to investigate how steel passivity may affect the predicted crevice chemistry and potential and whether it affects time and dimension scaling.

The Effect of Passivity on Crevice Chemistry and Corrosion

The crevice used in this investigation assumes a uniform gap of 0.5 mm and length of 10 cm. The computational chemistry and corrosion potential and rate are compared when the steel surface is assumed to be active and passive, respectively, and when solution pHs are at or greater than 10.5. The mouth potential is fixed at -0.900 V_{CSE}.

Figure E-1 shows (1) Na^+ and (2) Cl^- concentrations computed at times of 0, 10^4, 10^5, 5×10^5, 10^6, and 10^8 s when the steel is and is not treated to be passive at pH 10.5 and greater. Irrespective of these different treatments of the steel surface, the results are the same at 0 and 10^4 s. This is because the pH in the entire crevice has not yet reached 10.5, as shown in Figure E-2, and the steel passivity has not yet been taken into account.

At 10^5 s, the pH in only a portion of the crevice exceeds 10.5 (Figure E-2), and when this portion of steel is treated as being passive, a reduced constant corrosion current density is used for the modeling. By this treatment, Figure E-1 shows that a different concentration of Na^+ and Cl^- yields from the metal surface if it is treated as active.

For this portion of the crevice, Figure E-2 shows that the pH is slightly greater if the steel surface is treated as being rather passive than active. Moving farther into the crevice, the magnitude of pH is reversed when the pH considering steel passive drops below that whereby the steel is treated as being active. The drop of pH has a small effect on the Na^+ and Cl^- concentrations shown in Figure E-1. Although the decrease in Na^+ concentration close tothe crevice tip is not obvious, the equivalent increase of Cl^- concentration is obvious. With this increase of Cl^- concentration whose charge is balanced by ferrous ions, the pH near the crevice tip is smaller than if the metal surface is treated as being active.

Figure E-2 shows that the overall crevice pH increases over time irrespective of the steel surface being passive or active because, in either case, CP tends to pump Na^+ into and draw Cl^- out of the crevice. This increase in pH tends to increase the size of crevice region with pH at or

greater than 10.5. At time 10^6 s and greater, the pH in most of the crevice other than near the mouth is greater than 10.5 and levels off.

For the portion of the crevice with pH greater than 10.5, the corrosion current density is reduced to a fixed value by the model definition shown in Figure E-3. This step change does not occur until after 10^4 s.

The corresponding crevice potentials are shown in Figure E-3b. For 0 s and 10^4 s (not shown), the potentials obtained from treating the metal surface as active and passive overlap. For 10^5 s and 5×10^5 s, a peak potential is shown in the crevice with the steel surface treated as passive and the potential toward the tip is more positive than if the steel surface is treated as being active. Near the crevice tip, the pH is still below 10.5 and the Tafel relationship between the corrosion density and potential still holds, with more positive potential resulting from a higher corrosion current density. As time increases, the peak potential moves toward the crevice tip until the peak disappears. The potential in the crevice with a passive metal surface is overall more positive than in the crevice with an active metal surface, such as 10^6 s. Because this shift of potential in the crevice with a passive metal surface is faster than that in the crevice with an active metal surface, the difference in potential between the two crevices shrinks toward the steady-state condition. Steady state is reached prior to 10^8 s, and this difference in potential does not change any more.

The Effect of Passivity on Time and Dimension Scaling

Two crevices of uniform gaps, δ_0 and $\delta_0/4$, are used to examine the scaling theory. The metal surface is assumed to be passive when the pH is at or greater than 10.5.

Figure E-4 is a scaling plot showing (a) Na^+ and (b) Cl^- concentrations at different times, where the x coordinator is scaling distance $\frac{x}{\sqrt{\delta_{s0}}}$ and the scaling time $\frac{t}{\delta_{s0}}$ is labeled aside each curve. The time scales at $\frac{t}{\delta_{s0}}$=0, 2×10^7, 2×10^8, 10^9, 2×10^9, and 2×10^{11} s/m correspond with actual times of the crevice of larger gap (δ_{s0}=0.5 mm) at 0, 10^4, 10^5, 5×10^5, 10^6, and 10^8 s, respectively. For the crevice of smaller gap at 0.5/4 mm, the actual times correspond to a quarter more than the actual times described previously.

Figure E-4 shows that for each scaling time, the Na^+ or Cl^- concentrations obtained from the two crevices of different gaps are the same for any given scaling distance, proving that the scaling theory still works, even though the corrosion rate is a step function due to passivity consideration.

Figure E-5 shows the scaling plot for pH. All corresponding curves obtained for the two crevices of different gaps overlap each other. Where the pH is predicted to be at or greater than 10.5, Figure E-6(a) shows that the corrosion current density is exhibited as a flat line at 10^{-3} A/m^2 by definition. For both crevices of uniform gaps, the results at the same scaling time and scaling distance are the same.

Figure E-6(b) shows the scaling plot for crevice potential. It is not surprising that the corresponding curves for the two crevices of uniform gaps overlap, proving again the scaling theory works.

For crevice corrosion of passive alloys, it is important to understand the onset location of pitting. However, by theory L^2/δ_{s0} is the fundamental scaling factor, not L_p at the active-passive transition potential or L_c at the peak potential. Due to the relatively small area of pitting or small length a cross the pit relative to the length L, and because the metal surface away from the pitting area is passive and the passive current density is often constant over distance, it is possible that the scaling by L_p and L_c may work. However, between these two L_c is perhaps more reasonable because it is located in the peak potential and the derivation of potential or current is zero, satisfying approximately the zero current boundary condition at the crevice tip, a condition to be met with the scaling theory.

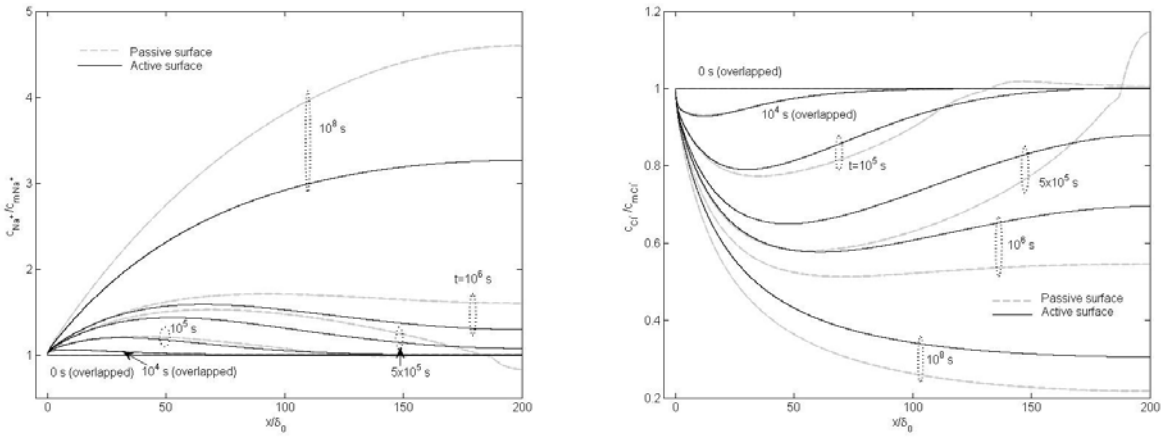

Figure E-1. At a fixed mouth potential of -0.9 V_{CSE}, a comparison of (a) Na^+ and (b) Cl^- concentrations predicted for a crevice of uniform gap when the steel surface is considered passive and active at pHs greater than 10.5.

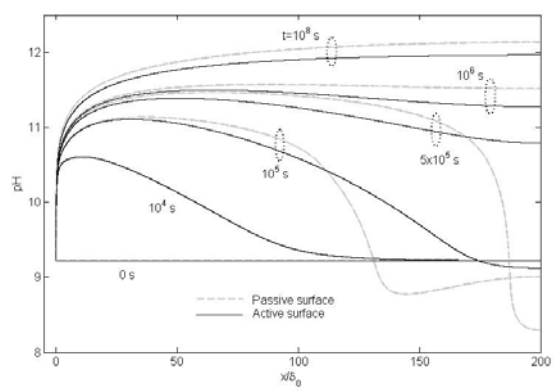

Figure E-2. Similar to Figure E.1, but for a comparison of solution pHs when the steel surface is considered passive and active at pH greater than 10.5.

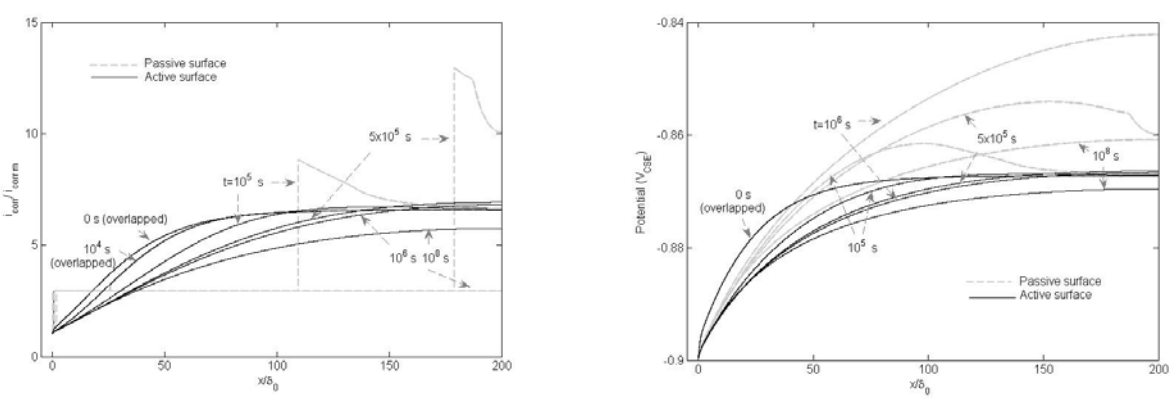

Figure E-3. Similar to Figure E.1, but for a comparison of (a) corrosion current density and (b) crevice potential when the steel surface is considered passive and active at pH greater than 10.5.

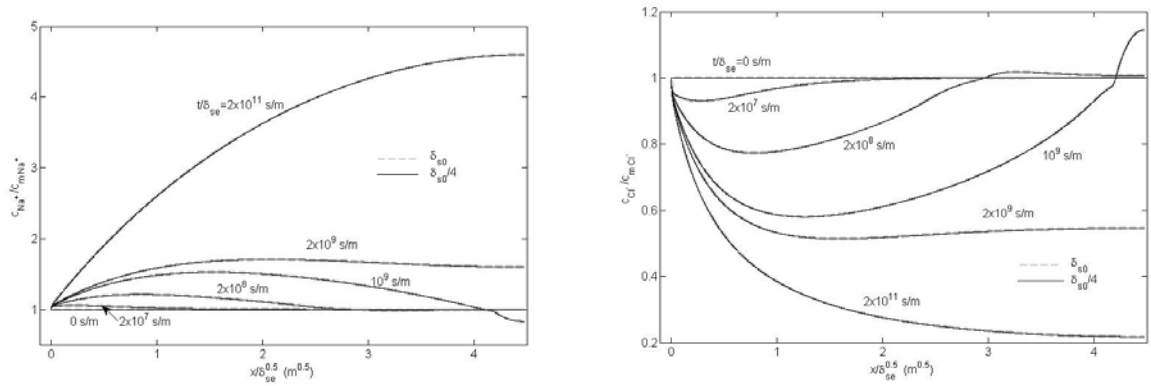

Figure E-4. At a fixed mouth potential of -0.9 V_{CSE}, a scaling plot for (a) Na^+ and (b) Cl^- concentrations in the two crevices of uniform gaps: constant gap of δ_{s0} (gray broken lines) and constant but reduced to a quarter of the gap or $\delta_{s0}/4$ (black solid lines).

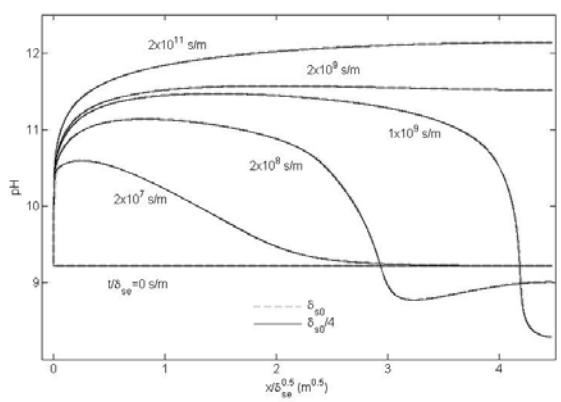

Figure E-5. Similar to Figure E.4, but the scaling plot is for solution pH in the two crevices of uniform gaps.

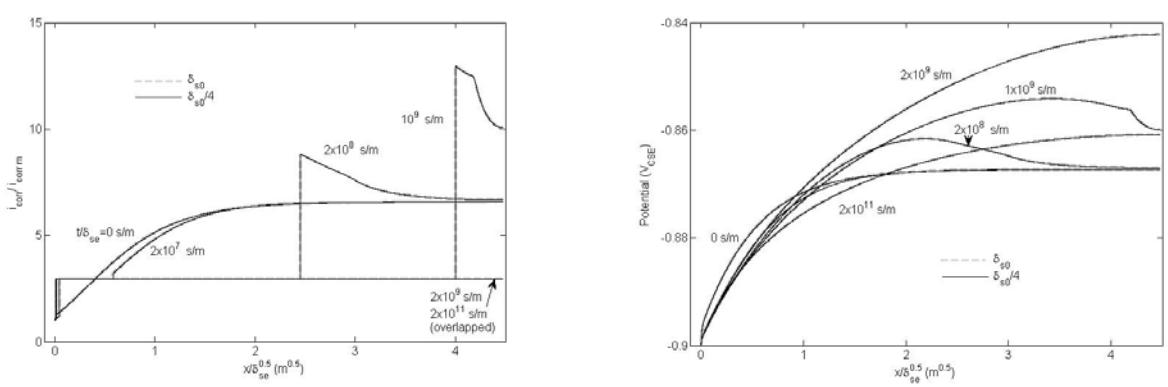

Figure E-6. Similar to Figure E-4, but the scaling plot is for (a) corrosion current density and (b) crevice potential in the two crevices of uniform gaps.

MS #1

A mathematical model developed to predict the chemistry and corrosion rate in a crevice of variable gap

ABSTRACT

A model is developed to predict the chemistry, corrosion potential and rate of pipeline steels in a crevice formed when a coating disbonds from a pipe surface. The gap of the coating disbonded region is assumed to vary with distance from the mouth. The effect of this gap variation on the chemistry and corrosion rate in the coating disbonded region is investigated in this study through modeling. The preliminary model results suggest that overall, the variation of the disbondment gap with distance has an insignificant effect on the pH, corrosion potential and rate in the coating disbonded region. Unlike some conventional crevice corrosion often associated with a large cathode-to-anode area ratio, the area ratio here is rather relatively small and the pH commonly falls in the neutral or alkaline range. Within this pH range, even if the pH varies within a few units across the crevice length, the variation of the crevice corrosion rate is not significant. This paper reports on and discusses the fundamental principles used for the model, some key model results, and the practical implications of the results.

Keywords: pipeline, crevice corrosion, modeling, cathodic protection, steel

1. Introduction

Significant research has been performed in the past to understand the mechanisms of external corrosion of underground pipelines under disbonded coatings with or without a holiday (mouth of a crevice) [1-25]. In both laboratory tests [4,17-24] and mathematical modeling [5-13], often is a crevice of uniform gap used. In reality, this gap rarely is a constant. It can vary in the longitudinal direction of the crevice. In addition, ionic current or oxygen diffusion through a permeable disbonded coating is often not included in such crevice corrosion tests, although models were reported that consider the effect of current or oxygen permeation through the coating [7,13,26,27]. A goal of this work is to understand from a fundamental perspective, by mathematical modeling, the effect of variable crevice gap. The effect of a holidayed permeable coating on the crevice corrosion rate has been investigated and will be reported in a later publication

2. The mathematical model

2.1. The model geometry

The crevice geometries used in the model of this work are schematically shown in Figure 1. These crevices form when a coating disbonds from the pipe surface and the holiday or the crevice mouth is located at the left edge of the disbonded region. The crevice corrosion can be treated as onedimensional (1D) because the crevice width (dimension perpendicular to the surface of Figure 1) is significantly greater than the size of the gap and the properties (except oxygen concentration) can be considered uniform across the gap. For oxygen, because its transport is controlled by diffusion, a higher concentration and a lower gradient near the interior coating surface relative to those near the steel surface are expected. Thus, oxygen transport has been specially treated as already described in earlier work [8,13,27]. Later in this paper, this special treatment will be described further.

For the crevice geometry shown in Figure 1a with a uniform crevice gap, the author and coworkers [13] extensively modeled the temporal and spatial variation of the crevice chemistry and corrosion potential and rate. Corrosion of a crevice with its gap varying with distance from the holiday, as shown in Figures 1b and 1c, has not been investigated; its effect on the evolution of crevice chemistry and corrosion is unknown.

Figure 1b is an extreme case where the gap changes abruptly at $\frac{x}{\delta_{s0}} = 5$, 6, 15, and 100; x is an arbitrary distance from the holiday and δ_{s0} is the gap at the holiday edge. Such a sharp variation of gap is expected to yield a more significant impact on the crevice corrosion than if the gap varies more gradually, as shown in Figure 1c, or is constant, as shown in Figure 1a.

The crevice gap variation in Figure 1b may be expressed by

$\frac{\delta_s}{\delta_{s0}} = 1$ when $\frac{x}{\delta_{s0}} =$ 0-5, 6-15, 100-200, and

$\frac{\delta_s}{\delta_{s0}} = \frac{1}{4}$ when $\frac{x}{\delta_{s0}} =$ 5-6, 15-100,

where δ_s is the gap at variable distance x in the crevice. The previous discrete equations may be combined and written as

$$\frac{\delta_s}{\delta_{s0}} = 1 + \theta_1[-\tfrac{3}{4}(\tfrac{x}{\delta_{s0}} > 5) + \tfrac{3}{4}(\tfrac{x}{\delta_{s0}} > 6) - \tfrac{3}{4}(\tfrac{x}{\delta_{s0}} > 15) + \tfrac{3}{4}(\tfrac{x}{\delta_{s0}} > 100)] \quad (1)$$

where θ_1 serves as a switch in the computer code. θ_1=0 represents a constant crevice gap, and θ_1=1 represents a variable crevice gap, as shown in Figure 1b.

The gap variation for Figure 1c follows:

$\frac{\delta_s}{\delta_{s0}} = 1$ when $\frac{x}{\delta_{s0}} =$ 0-5, 6-15, 100-200,

$\frac{\delta_s}{\delta_{s0}} = \frac{1}{4}$ when $\frac{x}{\delta_{s0}} =$ 5-6, 30-70,

$\frac{\delta_s}{\delta_{s0}} = 1 - \frac{3}{4} \cdot \frac{x\text{-}15}{15}$ when $\frac{x}{\delta_{s0}} =$ 15-30, and

$\frac{\delta_s}{\delta_{s0}} = \frac{1}{4} + \frac{3}{4} \cdot \frac{x\text{-}70}{30}$ when $\frac{x}{\delta_{s0}} =$ 70-100, or

The previous discrete equations may be combined to yield

$$\begin{aligned}\frac{\delta_s}{\delta_{s0}} = 1 + \theta_2[&-\tfrac{3}{4}(\tfrac{x}{\delta_{s0}} > 5) + \tfrac{3}{4}(\tfrac{x}{\delta_{s0}} > 6) - \tfrac{3}{4} \cdot \frac{\frac{x}{\delta_{s0}} - 15}{15}(\tfrac{x}{\delta_{s0}} > 15)(\tfrac{x}{\delta_{s0}} \le 30) - \tfrac{3}{4}(\tfrac{x}{\delta_{s0}} > 30) \\ &+ \tfrac{3}{4} \cdot \frac{\frac{x}{\delta_{s0}} - 70}{30}(\tfrac{x}{\delta_{s0}} > 70)(\tfrac{x}{\delta_{s0}} \le 100) + \tfrac{3}{4}(\tfrac{x}{\delta_{s0}} > 100)]\end{aligned} \quad (2)$$

Like θ_1, θ_2 also serves as a switch. θ_2=0 represents a constant crevice gap. θ_2=1 represents a variable crevice gap, as shown in Figure 1c. The gap varies with "x" linearly in $\frac{x}{\delta_{s0}} = 15 \sim 30$ and in $\frac{x}{\delta_{s0}} = 70 \sim 100$.

The gap is designed to have abrupt variations at x/δ_{s0}= 5 and 6 because past work [5-13] showed that the change of variables would occur most strongly within the first 10 gaps from the mouth. Abrupt or gradual changes of gap are designed to also occur in intermediate (x/δ_{s0}= 15) and longer (x/δ_{s0}= 100) distances to understand how gap changes at these locations would have an effect on the corrosion (relative to the corrosion in a crevice of constant gap).

2.2. Model conditions

The crevice solution used in this modeling is a dilute aerated sodium chloride solution simulating soil ground water. The crevice solution is assumed to be saturated by ferrous hydroxide, which is only sparsely soluble in water. In the presence of oxygen, the formation of ferric oxide suspension in solution may reduce the corrosion rate by consuming oxygen (which otherwise may contribute to corrosion). On the other hand, the formation of iron oxide may also enhance localized pitting when this oxide adheres to the steel surface. Because pitting in a crevice will not be addressed in this work and the reduction of corrosion rate by ferrous ion oxidation is not significant as demonstrated elsewhere [27,28], the effect of ferrous ion oxidation on the crevice corrosion will likewise not be addressed in this work. Ferrous ion oxidation occurs near the holiday only for an impermeable coating. Oxygen cannot penetrate far into the crevice from the holiday before it is completely reduced at the steel surface [27].

The crevice corrosion contains the following species: Na^+ --(1), Cl^- --(2), Fe^{2+} --(3), H^+ --(4), OH^- --(5), $Fe(OH)^+$ --(6), O_2 --(7), $H_2(aq)$ --(8), $Fe(OH)_2$ --(9), and H_2O --(10). The underlined species are defined as the

primary species. Their concentrations can either be approximated or known, such as species (8)-(10). The concentrations of the secondary species, or species (3), (5), and (6), can be determined from the concentrations of the primary species through their equilibrium equations given in Appendix A.

It is assumed that the coating disbonds before a holiday is formed in the coating. Water vapor and oxygen can permeate through the coating to cause the pipe corrosion underneath. Depending on the type, thickness, and degree of coating deterioration, the permeability of oxygen through the coating varies. Two conditions of a coating are considered based on its permeability to oxygen and/or ionic current: (1) the coating is impermeable to either oxygen or cathodic protection (CP) current and (2) the coating is permeable to either or both of oxygen and CP current. The permeability is determined by the effective area of the coating that allows the penetration of oxygen or/and CP current through the disbonded coating.

Regardless of the magnitude of the coating permeability to oxygen and/or CP current, water vapor can permeate through the disbonded coating. Before formation of a holiday, corrosion may have reached a steady-state condition. The chemistry in the crevice can be different from that in soil and can be saturated by the sparsely soluble ferrous hydroxide.

When the pipe surface contains limited contaminant salts before the coating is applied in the mill, the soluble species may dissolve in the solution in the disbonded region. The model considers a dilute NaCl solution in the coating disbonded region, more dilute than in the bulk soil. This disbonded chemistry may have been stable before the disbonded coating is breached and a holiday is created. When the disbonded coating is breached or a holiday formed, the direct transport of oxygen and solution ionic species (or CP current) through the holiday solution will modify the conditions in the coating disbonded region. This work assumes that the stable solution in the disbonded region is more dilute than in the bulk soil before the holiday is created.

The effect of variable crevice gap vs. distance, and/or the permeation of oxygen and/or CP through the crevice holiday and/or the disbonded coating are investigated. For the purpose of this paper, only the results on the effect of gap variation in a crevice of variable gap over distance are reported. The primary goal is to understand the temporal and spatial variation of crevice chemistry and corrosion rate.

The scenario to be modeled may also apply to a condition where the coating holiday is created before a disbonded region forms. Then, it is possible that the entire disbonded region and the holiday may, at some point, experience a dryout with complete loss of CP. When the soil becomes wet and CP starts to function again, the solution in the disbonded region may or may not be more dilute than in the soil ground water. In this scenario, the model results may be different from those where the holiday is formed after disbondment of the coating. Nevertheless, the method and the procedure by which the model is used for computations are the same.

Aside from the practical significance of the cases being investigated, this model is also significant from a fundamental perspective in that it solves challenging problems that have not been explored before.

The model will be developed under the conditions that the steel surface is active in all conditions; its possible passivity at high pH or possible coverage by deposit, if existing, will not be considered. As stated earlier, the model does not consider the effect of ferrous ion oxidation on crevice corrosion.

Although the model described in Section 2.3 is capable of treating complex conditions including (1) gap varying with distance and (2) a coating permeable by oxygen and ions, Section 3 will only show the computational results of this paper for the condition where the crevice gap varies with distance.

2.3. Model governing equations

By considering all the possible reversible and irreversible chemical and electrochemical reactions in the crevice corrosion system and using the equilibrium relations for reversible reactions given in Appendix A, the mass transport equation for each primary species and the equation of electroneutrality can be written as follows:

$$\delta_s \frac{\partial c_1}{\partial t} + \frac{\partial}{\partial x}(\delta_s N_{1x}) + N_{1yc} = 0 \qquad (3)$$

$$\delta_s \frac{\partial c_2}{\partial t} + \frac{\partial}{\partial x}(\delta_s N_{2x}) + N_{2yc} = 0 \tag{4}$$

$$\delta_s \frac{\partial}{\partial t}(\sum_3^6 z_j c_j) + \frac{\partial}{\partial x}(\delta_s \sum_3^6 z_j N_{jx}) + \sum_3^6 z_j N_{jyc} - (2r_{Fe}^e + r_H^e + r_{H_2O}^e + 4r_{O_2}^e) = 0 \tag{5}$$

$$\sum_1^6 z_j c_j = 0 \tag{6}$$

$$\delta_s \frac{\partial \bar{c}_7}{\partial t} + \frac{\partial}{\partial x}(\delta_s N_{7x}) = \frac{2D_{O_2}[3m(\pi+2)c_7^0 - 6(m+\pi+m\pi)\bar{c}_7]}{\delta_s(4m+12+\pi m+4\pi)} \tag{7}$$

where t is time and z_j, c_j, and N_j are the charge, concentration, and flux of the jth species, respectively. δ_s is the boundary layer thickness. Subscript "x" refers to the "x" direction in the crevice geometry, and subscript "yc" refers to the "y" direction across the coating. r^e represents the electrochemical (anodic or cathodic) reaction rate, with a key element involving the reaction shown in the subscript of the "r" term. These electrochemical reactions and the "r" expressions are given in Appendix A and will also be presented in the main text later.

Equation (7) depicts O_2 transport that already accounts for the fact that O_2 in solution in the disbonded region tends to have a higher concentration and a lower concentration gradient near the interior coating surface than that near the steel surface. This non-uniform distribution of O_2 concentration across the gap was successfully treated in 1D by using a parabolic O_2 concentration vs. y across the gap for each point along "x" [12]. It yields the same result as if a full 2D model was solved and this parabolic relation was imposed only at the holiday mouth (x=0). Because this treatment in the past was cumbersome, it is reorganized and more concisely presented in Appendix B. In Equation (7), $\bar{c}_7$ and c_7^0 are O_2 concentration averaged across the crevice gap and that in bulk soil or at the holiday adjacent to the coating, respectively; D_{O_2} is oxygen diffusion coefficient in solution; and m and π are terms that are defined in Appendix B. $m = \frac{D_{O_2c}/\delta_c}{D_{O_2}/\delta_s}$, a ratio of the coating permeability to that of the solution layer; D_{O2c} and δ_c are O_2 diffusivity in coating and the coating thickness, respectively. Both m and π will be described further later.

In the previous equations, the flux of the jth species in the crevice solution in the longitudinal direction N_{jx} may be written as

$$N_{jx} = -D_j \frac{\partial c_j}{\partial x} - \frac{z_j D_j F}{RT} c_j \frac{\partial \varphi}{\partial x} \tag{8}$$

where the first and second terms to the right of the equal sign are the diffusion and migration components of the jth species in the "x" direction. F, R, and T are Faraday's constant, universal gas constant, and temperature in K, respectively. φ is electrostatic potential of the solution.

The flux in the "y" direction shown by N_{jyc} represents the transport of the jth species through the coating, and it is one component of the ionic current flow passing through the disbonded coating. Due to the significantly low permeability of the coating (to O_2 and CP current) relative to that of solution, a linear gradient of the concentration and the electrostatic potential of the solution is assumed across the coating and thus, N_{jyc} has the form

$$N_{jyc} = \theta_3(-D_j \frac{c_{j0} - c_j}{\delta_c} - \frac{z_j D_j F}{RT} \frac{c_{j0} + c_j}{2} \frac{\varphi_0 - \varphi}{\delta_c}) \tag{9}$$

For O_2, its diffusion through the coating has been incorporated in the term to the right of the equal sign in Equation (7). Like θ_1 and θ_2 in Equations (1) and (2) respectively, θ_3 serves as a switch in the computer code. $\theta_3 = 0$ represents an impermeable coating so that no CP current can penetrate through the coating. Conversely,

$\theta_3 = 1$ represents a permeable coating so that CP current can penetrate through the coating. In the last term on the right side of Equation (9), the concentration in the coating is approximated by the average across the coating, or $0.5(c_j+c_{j0})$.

The derivation of Equation (7) has been given in Appendix B. The term to the right of the equal sign has already included oxygen transport through the coating, embedded in the "m" parameter. When D_{O2c} is set to be zero, m=0, and thus, the O_2 diffusion rate through the coating is automatically eliminated.

Equation (6) may alternatively be replaced by

$$\delta_s \frac{\partial}{\partial x}\left(\sum_1^6 z_j N_{jx}\right) + \sum_1^6 z_j N_{jyc} - \left(2r_{Fe}^e + r_H^e + r_{H_2O}^e + 4r_{O_2}^e\right) = 0 \tag{10}$$

The electrochemical reaction rates can be converted from the corresponding current density following Faraday's law:

$$r_l^e = \frac{i_l}{n_l F} \tag{11}$$

where l represents Fe, H^+, H_2O, and O_2. n is the number of electrons of charge transfer in an elemental half cell reaction.

The corrosion or iron oxidation current density (i_{Fe}) is assumed to follow the Tafel equation:

$$i_{Fe} = i_{Feref}^0 10^{\frac{E-E_{Fe}^{Eqref}}{b_{Fea}}} \tag{12}$$

where E is the electrode/pipe potential with respect to an arbitrary reference electrode, which is in this work is consistently referred to as the saturated $Cu/CuSO_4$ electrode (CSE). "ref" in either subscript or superscript is referred to as a reference condition whereby the corresponding exchange current density i^0, concentration c_j (j=3, 4), and equilibrium potential E^{Eq} are known. "b" is Tafel slope. It is cautioned that Equation (12) derived for active dissolution of a metal may become impractical when the solution shifts to become highly alkaline so that a passive film develops on the steel surface.

For reductions of hydrogen ion and water, their Tafel equations are, respectively,

$$i_H = -i^0{}_{Href} \frac{c_4}{c_{4ref}} 10^{\frac{-(E-E_H^{Eqref})}{b_H}} \tag{13}$$

and

$$i_{H_2O} = -i^0{}_{H_2Oref} 10^{\frac{-(E-E_{H_2O}^{Eqref})}{b_{H_2O}}} \tag{14}$$

For O_2 reduction, the Tafel equation in terms of O_2 surface concentration c_{7s} is

$$i_{O_2s} = -i_{O_2ref}^0 \frac{c_{7s}}{c_{7ref}} 10^{\frac{-(E-E_{O_2}^{Eqref})}{b_{O_2}}} \tag{15}$$

When the reference condition is taken at the holiday mouth, the electrostatic potential of solution at the holiday may be set as φ_m=0. With the electrode potential at the holiday expressed by E_m, the electrode potential anywhere inside the crevice E can be expressed by the electrostatic potential of the solution φ as

$$\varphi = E_m - E \tag{16}$$

Thus, the Tafel equations for the anodic and cathodic half cell reactions may be written as

$$i_{Fe} = i_{Fem} 10^{\frac{-\varphi}{b_{Fe}}} \tag{17}$$

where subscript "m" is referred to as the quantity at the holiday mouth.

For reductions of hydrogen ion and water, their Tafel equations may be expressed, respectively, as

$$i_H = i_{Hm} \frac{c_4}{c_{4m}} 10^{\frac{\varphi}{b_H}} \tag{18}$$

and

$$i_{H_2O} = i_{H_2Om} 10^{\frac{\varphi}{b_{H_2O}}} \tag{19}$$

For O_2 reduction, the Tafel equation of Equation (15) can be written as

$$i_{O_2s} = i_{O_2sm} \frac{c_{7s}}{c_{7sm}} 10^{\frac{\varphi}{b_{O_2}}} \tag{20}$$

where $i_{O_2sm} = -i^0_{O_2ref} \frac{c_{sm}}{c_{ref}} 10^{\frac{-(E_m - E^{Eqref}_{O_2})}{b_{O_2}}}$. The derivation given in Appendix B considering O_2 transport through coating and replacing O_2 concentrations at the steel surface with its average across the gap ($\bar{c}_7$) and its concentration in soil (c^0_7) yields the following expression:

$$r_{O_2s} = -\frac{D_{O_2}\pi[6(m+2)\bar{c}_7 - 2mc^0_7]}{\delta_s(4m+12+\pi m+4\pi)} \tag{21}$$

2.4. Model initial and boundary conditions

The initial and boundary conditions for solving the previous equations are given in Table 1, where only concentrations of the primary species are given with the realization that the concentrations of the secondary species can be calculated from the concentrations of the primary species by using the formula given in Appendix A.

As discussed earlier, the concentrations of Na^+ and Cl^- at the holiday or in soil can be and are assumed to be greater than those at time zero in the disbonded region (initial condition). The solution is saturated by $Fe(OH)_2$ with the pH of approximately 9.2 at time zero both at the mouth and in the disbonded region. When the Na^+ and Cl^- concentrations are given, the electroneutrality ($\sum_j z_j c_j = 0$) and the saturation of the solution by $Fe(OH)_2$ can allow all other species to be determined. The equations for this calculation are also given in Appendix A.

The boundary conditions at the crevice mouth are that the concentrations of all solution species are constant and invariant with time. The applied potential at the mouth can be either determined, in the case of no CP, or it is given as a fixed value when CP is present. The boundary conditions at the crevice tip are zero flux for each species; due to the coating, they are impermeable to ionic and molecular species.

2.5. Methods of solving the model equations

Equations (3-7) can be solved simultaneously to obtain all concentrations of the independent species (c_1, c_2, c_4, and c_7) and the potential (ϕ or E), where Equation (6) can be replaced by Equation (10). The values of the model parameters used for this work are given in Table 2 [29-38].

A commercial finite element method code, Comsol 3.5a, was used to solve the previous equations. This code allows for flexible meshing of the model geometry and flexible setting of time steps. Because the gradients of concentrations and that of the potential are very large near the crevice mouth, the mesh there is very dense. The time steps near time zero are designed to be very small.

Once the concentrations of the primary species are computed, by substituting them into the equilibrium equations given in Appendix A, the concentrations of the secondary species can be determined.

Only the shaded scenarios shown in Table 3 are presented for the current paper, although all scenarios in the table have been investigated. This paper focuses on the effect on crevice chemistry and corrosion potential and rate by the change of crevice gap vs. distance (x). The first scenario in the table was investigated extensively earlier [13], while the condition with different initial concentrations between the holiday and the disbonded region was not. The model results of the latter condition are presented first.

3. Computational results

3.1. Uniform Crevice Gap

3.1.1. Mouth Potential Fixed at -0.8071 V_{CSE} (Negligible CP)

This condition or Case No. 1 in Table 3 was previously studied extensively. In this condition, the mouth boundary concentrations and the initial concentrations are the same [13]. These concentrations are shown in the last row of Table 1. The tail boundary condition is shown one row above.

As discussed earlier, when the holiday is created after the coating is disbonded, the Na^+ and Cl^- concentrations in the crevice may initially be smaller than those at the mouth or in soil. It would be useful to understand how this difference in concentrations of Na^+ and Cl^- would affect the evolution of the crevice chemistry and corrosion potential and rate. In this study, the Na^+ and Cl^- concentrations are assumed to be uniform initially in the entire crevice and are equal in value. Their initial concentrations are one-tenth of their concentrations at the mouth. With a slightly different pH from the initial condition used in the previous work [13], the initial condition used in this study is given in the second row from the top of Table 1. The mouth boundary condition is shown in the third row for the presence of CP with a fixed mouth potential or the fourth row when CP is absent. The crevice tail boundary condition is shown in the third row from the bottom of Table 1: zero flux for each species and zero current flow.

Note that in Table 1, the pH (or c_4) at the mouth used in this work (third row from the top of Table 1) is only slightly different from the previous work [13] (last row), and thus, the results of the previous work can be reproduced approximately by the current model when the Na^+ and Cl^- initial concentrations are set to be the same as their concentrations at the mouth. Throughout this section, the reproduced results are results of previous work.

Figure 2a shows the Na^+ and Cl^- concentrations in the crevice obtained in the previous work. The fixed mouth potential of -0.8071 V_{CSE} was used at the mouth to represent a condition with negligible cathodic polarization. In previous work and as shown later in this work, at this mouth potential the cathodic current that flows into the crevice through the mouth is negligibly small. The mouth boundary condition used here is the third row from the top of Table 1.

The presence of O_2 and the cathodic reduction of O_2, which occurs only near the mouth, makes the steel potential at and near the mouth more positive than inside the crevice. This oxygen reduction near the mouth functions as an imposed anodic polarization if the solution were anaerobic and the mouth potential were applied at -0.8071 V_{CSE}, which draws Na^+ out of and pumps Cl^- into the crevice. Because the mouth and the initial chemistries

are the same, this equivalent anodic polarization has led to a decreasing Na^+ concentration, or increasing Cl^- concentration, inside the crevice as time progresses (Figure 2a).

When the Na^+ and Cl^- concentrations at the mouth are set in the model as 10 times those initially in the crevice, the change of their concentrations vs. x is shown in Figures 2b and c. This change at the mouth is sharp at time zero for both Na^+ and Cl^- concentrations due to the given boundary condition at the mouth. This sharp change of concentrations leads to a large diffusion rate from the mouth into the crevice for both Na^+ and Cl^-.

Unlike in Figure 2a where the Na^+ concentration in the crevice decreases over time, Figure 2b shows that the Na^+ concentration in the crevice increases over time, powered by its diffusion from the mouth. Although Na^+ migration controlled by the potential gradient imposed by the equivalent anodic polarization depresses the Na^+ concentration in the crevice, this effect is less significant than the diffusion near the mouth. The effect of Na^+ migration can first be seen on the curve of 10^4 s, where the Na^+ concentration deep in the crevice drops below its initial concentration. Although the Na^+ migration can occur immediately after time zero, the slow Na^+ diffusion cannot. The Na^+ diffusion would not occur deep in the crevice until after quite some time when a concentration gradient is created by the Na^+ migration and corrosion reactions.

Due to the different initial conditions used to obtain Figures 2a and b, the Na^+ concentration in the crevice varies differently. In Figure 2a, the Na^+ concentration tends to decrease over time controlled by migration, while in Figure 2b, Na^+ concentration changes in an opposite direction due to its diffusion from the mouth. Nevertheless, overall the Na^+ concentration decreases from the mouth into the crevice for both conditions. At 10^7 s, when the corrosion process approximately reaches steady state, the two curves in both conditions overlap as shown in Figure 2b, verifying that the steady-state condition of the corrosion process is not affected by the different initial conditions. At steady state, the driving force caused by Na^+ diffusion, which forces Na^+ to move into the crevice, is counterbalanced by the driving force caused by Na^+ migration (due to the equivalent anodic polarization), which tends to draw Na^+ out from inside the crevice.

Unlike Na^+, Figure 2c shows that by carrying a negative charge, the diffusion and migration of Cl^- both tend to increase its concentration over time in the crevice. Diffusion is more dominant initially near the mouth, and migration becomes increasingly more significant over time inside the crevice. With time when the in-crevice Cl^- concentration becomes close to or greater than that at the mouth, the diffusion to increase Cl^- concentration in the crevice diminishes. Rather reversely, Cl^- starts to diffuse to the mouth from inside the crevice, and this reverse diffusion increases over time. Eventually, this reverse Cl^- diffusion has to be counterbalanced by the Cl^- migration into the crevice for the steady-state condition to be approached.

With an initial disadvantage of a lower concentration than in the previous work, the Cl^- concentration keeps getting smaller, as shown by the pair of curves at 10^5 s and 10^6 s. This situation continues until steady state is reached at 10^7 s when the pair of curves overlap. Due to the presence of oxygen at the mouth (equivalent to anodic polarization at the mouth in the deaerated condition), the Cl^- concentration in the crevice is greater than at the mouth.

Even though the initial and mouth pHs are initially the same for both this model and the previous model as shown in Figure 3, due to the previously described variation of Na^+ and Cl^- concentrations, which simultaneously affect or are affected by the concentrations of other secondary species including Fe^{2+}, the variations of pHs are different as shown. Nevertheless, this difference eventually diminishes at steady state at 10^7 s, shown by the overlapped curve. These modeling results for the temporal and spatial variations of crevice pH are qualitatively consistent with experimental results [19–22,39]. Under external anodic polarizations, experimental work [19–22,39] showed that the overall crevice pH decreases with time and the decrease deep in the crevice is slower at first. With a fixed concentration at the mouth, the pH deep in the crevice eventually surpasses that near the holiday.

Figure 4a shows the corrosion potential and corrosion current density in the crevice at different times obtained in the previous work. Overall, their variations at the steady-state condition are not significantly different from those at their initial condition. With oxygen being the main driving force for the corrosion process, the corrosion current density decreases from the holiday into the crevice and the corrosion potential correspondingly shifts in the more negative direction.

The difference between this model and the previous model is mainly shown at time zero in Figure 4b for potential and in Figure 4c for corrosion current density. This difference results from the sharp change of the solution chemistry at the mouth immediately after time zero. This requires a significant change of crevice potential and correspondingly corrosion current density to compensate for the sudden change of chemistry at the mouth. With time, this difference is shown to decrease quickly as the chemistry becomes smoother in the crevice. By about 10^5 s, this difference nearly vanishes from the scales of the charts.

By fixing the mouth potential at -0.8071 V_{CSE} as modeled earlier, it is assumed that the variation of the mouth potential with time due to variation of chemistry can be neglected. The validity of this assumption can be verified as described next.

3.1.2. Time-Varying Mouth Potential at Truly No CP

When there is truly no CP, the mouth potential can vary with time due to a variation of the chemistry inside the crevice. The only difference between modeling this no CP condition and modeling the condition with a fixed mouth potential is the mouth boundary condition for potential. All other boundary conditions at the mouth, the initial condition, and the crevice tail boundary condition remain the same. The no CP mouth boundary condition corresponds to the fourth row of Table 1 (current passing through the mouth is zero). The model results obtained in these two conditions are compared. The variation of the mouth potential with time at the condition of truly no CP is presented first.

Figure 5 shows the variation of the crevice mouth potential vs. time when there is truly no CP applied. The mouth potential varies within a small range: -0.7929 ~ -0.8087 V_{CSE}. In this semi-log diagram, although some variation is shown near time zero, the seemingly more significant potential drop occurs after approximately 5 s. The total potential drop within 10^7 s is less than 16 mV, caused by the change over time of the solution chemistry in the crevice. The mouth potential of -0.8071 V_{CSE} used in the previous section falls within this narrow window of mouth potential. This result verifies that the use of a fixed mouth potential at -0.8071 V_{CSE} provides a good approximation to the truly no CP condition. Figures 6-7 further demonstrate this verification as described next.

Figure 6 shows a comparison of the Na^+ concentration and pH obtained with truly no CP and with a fixed mouth potential at -0.8071 V_{CSE}. For the different times given in the charts, nearly no difference can be seen with the Na^+ concentration or a small difference in pH only at 10^2 s .

Although an obvious difference is shown at time zero for the crevice potential in Figure 7a and for the corrosion current density in Figure 7b, the difference then decreases and becomes invisible from 10^5 s onward.

3.1.3. Fixed Mouth Potential at -0.9 V_{CSE}

The crevice chemistry and corrosion potential and rate at the mouth potential of -0.9 V_{CSE} was investigated in detail elsewhere when the mouth chemistry was the same as the initial in the crevice [13]. At this potential, the crevice mouth is cathodically polarized.

Figure 8a shows the Na^+ and Cl^- concentrations obtained in previous work [13] with the mouth potential of -0.9 V_{CSE}. The Na^+ and Cl^- concentrations are shown to change with time in the opposite direction; Na^+ concentration in the crevice increases over time while that of Cl^- decreases.

Figure 8b shows the Na^+ concentration obtained in this work with the mouth chemistry different from that initially in the crevice. The synergistic diffusion and migration of Na^+ into the crevice leads to an increase of Na^+ concentration over time in the crevice. Although the Na^+ concentration obtained in this model is overall smaller than that obtained in the previous work due to a smaller initial concentration with this model, the difference in Na^+ concentration decreases over time and nearly disappears at 10^7 s. This variation of Na^+ concentration is rather similar to the variation of Cl^- concentration shown in Figure 2c with the mouth potential of -0.8071 V_{CSE}, because these two ions have opposite signs of charge and the correspondingly external polarizations between the two cases are opposite. These two factors cancel each other in the migration term of the flux equation. Under cathodic polarization, the more negative potential at the holiday relative to that in the crevice creates a driving force that pumps Na^+ into the crevice. When the Na^+ concentration in the crevice becomes greater than at the holiday, its

diffusion direction reverses, changing from initially diffusing into the crevice to diffusing outside the crevice. At steady state, the Na^+ migration into the crevice has to counterbalance its diffusion.

Figure 9 shows a comparison of crevice pHs obtained from this model and the previous model. Both crevice pHs increase over time. For the times shown in the figure, the largest difference between these two pHs is shown at 10^4 s. At 10^7 s, steady state is approached and the two curves are overlapped. The model-predicted variation in time and space of the crevice pH under CP is also in qualitative agreement with experimental data reported in earlier papers [19–22,25,39].

Figure 10 shows a comparison of the crevice potential and current density at different times obtained from this model and reported in previous work [13]. The significant difference at time zero results from the sudden change of the mouth chemistry after time zero, similar to what was explained for Figure 4 earlier. At 10^7 s, the two curves are merged irrespective of their different initial conditions.

3.2. Crevice Gap Varying with Distance (x)

In the field, a rectangular crevice with a uniform gap as shown in Figure 1a is rarely seen, even though such geometry has been most frequently used in crevice corrosion studies. The real crevice gap always varies with distance in the longitudinal direction, and each crevice has a unique geometry. To understand the effect on the crevice chemistry and corrosion by the crevice geometries, a sharp change of the gap with distance (Figure 1b) and a smoother change of the gap (Figure 1c) in the crevice longitudinal direction are used in the model. In this work, Figure 1b is chosen to be the focus of the modeling because its sharp variation of gap would yield the greatest effect on crevice corrosion.

The following sections describe the effect of the gap variation on the crevice chemistry, potential and corrosion current density. The effect with nearly no CP is presented first, followed by the effect with substantial CP imposed at the crevice mouth.

3.2.1. Mouth Potential at -0.8071 V_{CSE} (Figures 1a and 1b)

With (approximately) no CP at the crevice mouth, Figure 11a shows the Na^+ concentrations obtained near the mouth for the two crevice geometries shown in Figures 1a and 1b. The concentrations obtained from these two crevices are shown to be the same until after 10^2 s when the change of gap at $\frac{x}{\delta_{s0}}$=5 is reached. At 10^4 s and 10^7 s, a steeper decrease of Na^+ concentration is seen in the region of narrowed gap with $\frac{x}{\delta_{s0}}$=5-6. Compared to the Na^+ concentration obtained for the crevice of constant gap, the Na^+ concentration in the crevice of variable gap is greater around $\frac{x}{\delta_{s0}}$=5 but is smaller around $\frac{x}{\delta_{s0}}$=6. This effect may be explained by treating Na^+ diffusion in the crevice as flow and treating the Na^+ diffusion flux as velocity. The total rates of Na^+ diffusion (equivalent to flow rate) are approximately the same across the edges of the gap-narrowed region. However, the diffusion fluxes of Na^+ (equivalent to flow velocity) are significantly different immediately before and after the edge, because these fluxes are inversely proportional to the cross-sectional area or the gap size. For this reason, the diffusion flux, reflected by the slope on the Na^+ concentration curve, is shown to be greater in the gap-narrowed region. Around the left edge of the gap-narrowed region ($\frac{x}{\delta_{s0}}$=5), the mass of Na^+ tends to squeeze into the gap-narrowed region. When the gap suddenly expands at $\frac{x}{\delta_{s0}}$=6, the Na^+ diffusion flux decreases and Na^+ tends to dissipate out from the gap-narrowed region, leading to a decrease of Na^+ concentration relative to that in the crevice of constant gap. For the special condition at 10^7 s when the system approximately reaches steady state, the net flux consisting of diffusion and migration of Na^+ or Cl^- is zero, or the diffusion and migration terms are balanced each other with $N_{jx} = 0$ where j=1 or 2. This leads to the condition $-\frac{D_j}{c_j}\frac{\partial c_j}{\partial x} = \frac{z_j D_j F}{RT}\frac{\partial \varphi}{\partial x}$ or $-\frac{1}{z_j c_j}\frac{\partial c_j}{\partial x} = \frac{F}{RT}\frac{\partial \varphi}{\partial x}$. When the total electrical current $\delta_s \frac{F}{RT}\frac{\partial \varphi}{\partial x}$ (the term to the right of the equal sign) can be treated as being continuous before and after an edge of the gap-narrowed region, the total diffusion rate $-\delta_s D_j \frac{\partial c_j}{\partial x}$ (assuming a unit width of the crevice in the direction perpendicular to the geometry) is correspondingly continuous or the same before and after an edge. With the ratio of

diffusion rate to diffusion flux inversely proportional to the ratio of crevice gap, a greater diffusion flux (equivalent to the slope of the curve) in the gap-narrowed region should be expected rather than in the adjacent regions of larger gap.

The previously described variation of Na^+ concentration across the first gap-narrowed region is also similarly shown in Figure 11b across the second gap-narrowed region in $\frac{x}{\delta_{s0}}$=15-100. In Figure 11b, the y axis was scaled up because the difference in Na^+ concentration deep in the crevice is smaller and would otherwise not be seen clearly if plotted together with Figure 11a.

The change of Na^+ concentration in the range of $\frac{x}{\delta_{s0}}$=5-6 is shown to be greater than in the range of $\frac{x}{\delta_{s0}}$=15-100 because the Na^+ concentration gradient is greater near the mouth, and the impact on this gradient by the sharp change of gap is also greater. Even with a steeper change of Na^+ concentration due to the sharp change of gap (relative to a constant crevice gap), the Na^+ concentration obtained from the two different geometries (Figures 1a and b) are overall not significantly different. Within these two regions of narrowed gap ($\frac{x}{\delta_{s0}}$=5-6 and 15-100), the change of Na^+ concentration at 10^7 s is smoother or less steep than at 10^4 s because more time is needed for the transport of Na^+ from the mouth.

Overall, Figure 11a and b suggests that the effect of variable gap for the case studied here is not significant. It is however expected that this effect would be greater if the gap-narrowed region near the mouth is expanded or greater.

Figures 12a and b shows a comparison of the crevice pHs at different times for the two crevice geometries shown in Figures 1a and b. Although the sharp change of the crevice gap has resulted in a different pH relative to that obtained with a constant crevice gap, the overall difference between the pHs obtained from these two crevice geometries is shown to be insignificant. The difference in the pHs occurs mainly around and within the two regions of narrowed gap in $\frac{x}{\delta_{s0}}$=5-6 and 15-100.

The results from Figures 11 and 12 suggest that the difference in the crevice geometries of Figures 1a and b does not significantly affect crevice chemistry. Thus, it is expected that this effect on the crevice potential and corrosion rate would not be significant either.

Figure 13 shows a comparison of the crevice potentials obtained with the two crevice geometries shown in Figures 1a and b. Although the sharp change of gap clearly changes the potential near the mouth (relative to the potential in the crevice of constant gap), deep in the crevice at $\frac{x}{\delta_{s0}}$=100 the effect by the sharp change of the gap is seen to be insignificant. Because this effect is local (only at or near the regions of narrowed gap), the overall difference in potential is shown to be small.

The variation of crevice corrosion current density is similar to that of the crevice potential and shown in Figure 14a near the mouth and in Figure 14b deeper inside the crevice. Even though the difference between corrosion current densities obtained from these two crevice geometries is shown to be more significant at 10^7 s than at time zero, the difference is, in general, small.

3.2.2. Mouth Potential at -0.9 V_{CSE} (Figures 1a-1c)

Figure 15 shows Na^+ concentrations obtained by using all three crevice geometries shown in Figure 1. Figure 15a shows the results in the entire crevice, and Figure 15b shows only the results near the mouth. Overall, the difference in Na^+ concentration in the entire crevice for the three different crevice geometries is insignificant. At 10^8 s, the Na^+ concentration deeper in the crevice of constant gap is shown to be smaller than in the two crevices of variable gap, while it is slightly greater near the holiday. In the crevices with variable gap, 10^8 s is required for the crevice corrosion to reach steady state. This time is longer than for the crevice of constant gap, which requires only 10^7 s for its corrosion to reach steady state.

Figure 15b shows that across the gap-narrowed region ($\frac{x}{\delta_{s0}}$=5~6), the Na^+ concentration overall has a steeper variation with distance compared to the crevice of constant gap. The sharp change of Na^+ concentration occurs at the points of gap change. The more gradual gap variation in $\frac{x}{\delta_{s0}}$=15-100 associated with Figure 1c shows a more gradual variation of Na^+ concentration relative to the variation associated with Figure 1b.

For the first region of narrowed gap in $\frac{x}{\delta_{s0}}$=5~6, Figure 15b shows that at 10^3 s, Na^+ transport just passes through this region and has not yet reached the second gap-narrowed region in $\frac{x}{\delta_{s0}}$=15~100. When $\frac{x}{\delta_{s0}}$<15, the geometry of the two crevices shown in Figures 1b and c is the same; the Na^+ concentrations in these two crevices overlap. The Na^+ concentration in these crevices around the left edge of the narrowed region ($\frac{x}{\delta_{s0}}$=5) is shown to be greater than that in the crevice of constant gap. This difference in Na^+ concentration among the crevices is consistent with the significant increase of the Na^+ flux caused by the sudden reduction of the crevice gap at $\frac{x}{\delta_{s0}}$=5. This increased flux leads to accumulation of Na^+ around the left edge of the narrowed gap. By contrast, at the sudden expansion of the gap at $\frac{x}{\delta_{s0}}$=6, a reverse effect dominates. Na^+ easily transports out from the gap-narrowed region, and the Na^+ concentration after the right edge of the gap-narrowed region becomes smaller (relative to the crevice of constant gap).

The increase of Na^+ concentration with the crevice of Figure 1b occurs at the left edge of the second gap-narrowed region ($\frac{x}{\delta_{s0}}$=15) at 10^4 s. By contrast, with a gradual decrease of gap for the crevice in Figure 1c, the Na^+ concentration does not become greater than in the crevice of constant gap until after $\frac{x}{\delta_{s0}}$=20. This more gradual increase of Na^+ concentration can be attributed to the reduced Na^+ concentration around the right edge of the first gap-narrowed region. This Na^+ concentration in the crevice with gradual a gap reduction eventually exceeds the concentration in the crevice of constant gap because of the gradually increasing Na^+ flux as the gap continues to narrow down.

At 10^5 s, the Na^+ transport still does not pass though the right edge of the second gap-narrowed region as shown in Figure 15a, where at $\frac{x}{\delta_{s0}}$=100, the Na^+ concentration is still approximately the same as that in the initial condition. Due to accumulation of Na^+ in the crevice of variable gap before the right edge of the second gap-narrowed region (Na^+ transport limited by the narrowed gap), the Na^+ concentration in the crevices with a gap-narrowed region is overall greater than in the crevice of constant gap.

Once the Na^+ transport passes across the right edge of the second gap-narrowed region, the Na^+ concentration gradient in the crevice becomes smoother over time. At time 10^6 s, limited by the narrowed gap, Na^+ still accumulates in the crevices of variable gap near the mouth, but the Na^+ concentration deeper inside these crevices is smaller than in the crevice of constant gap. At 10^6 s, Na^+ concentration near the holiday becomes slightly greater than at the holiday, suggesting that Na^+ tends to diffuse out. Meanwhile, the external CP tends to force Na^+ to migrate into the crevice. Due to the dominance of the CP-driven migration over diffusion deeper in the crevice, the Na^+ concentration in the crevice continues to increase over time until a steady state is reached.

The previous analysis suggests that with CP, the narrowing of crevice gap forces Na^+ into the region of narrowed gap, while expanding of the gap b draws out Na^+ concentration from the region of narrowed gap. This effect is stronger near the mouth because of a greater flux.

The crevice with a narrowed gap appears to behave like a longer crevice of constant gap. Thus, a longer time is needed for the crevices with narrowed gaps to reach steady state than the crevice of constant gap. For the crevice of constant gap, 10^7 s is needed, while for the crevices of variable gap, 10^8 s is required. At 10^8 s, Figure 15a shows that the Na^+ concentration in the crevice of variable gap eventually becomes greater than in the crevice of constant gap. The crevice of Figure 1b also has a higher Na^+ concentration than the crevice of Figure 1c.

Figure 16 shows a comparison of the pHs in the previously described three crevices at different times. Similar to the variation of Na^+ concentration, pH sharply changes at the edges of gap change; however, this cannot

be clearly seen in the first gap-narrowed region in $\frac{x}{\delta_{s0}}$=5-6 because the overall pH change there is steep (even in the crevice of constant gap). The steeper change of pH in the crevice of variable gap (relative to the crevice of constant gap) is more clearly shown in the second gap-narrowed region associated with the crevice of Figure 1b at $\frac{x}{\delta_{s0}}$=15 and 100 where the gap sharply narrows. With a more gradual variation of gap in Figure 1c, at 10^6 s the pH variation is shown to be smoother relative to the crevice with a sharp change of gap shown in Figure 1b. Overall, the effect of variable gap on the crevice pH is not significant for the conditions studied.

Figure 17 shows (a) crevice potentials and (b) corrosion current densities at different times for the three crevices. In general, the effect of variable gap on these two parameters is not significant.

4. Conclusions

A comprehensive mathematical model is developed that allows for predicting the evolution of chemistry and corrosion in a crevice which may have a boundary chemistry different from the initial chemistry. Additionally, the crevice gap may vary along the crevice longitudinal direction.

Due to the specific crevice geometry used in this modeling (a crevice mouth with a small area), the overall temporal and spatial change of the solution chemistry and the corrosion potential and rate in the crevice of varying gap is not significantly different from the corresponding change in a crevice of uniform gap. This is shown for conditions with or without cathodic polarization at the mouth.

Regardless of the variation of crevice gap over distance, the model results show that when a holiday is protected with cathodic polarization, the pH in the crevice increases over time and the corrosion rate decreases. Given a sufficient time and with the cathodic polarization continuously maintained at the mouth, this pH increase can go farther into the disbonded region and becomes even greater than at the mouth. Conversely, in the absence of external polarization but in the presence of oxygen, a situation equivalent to external anodic polarization at the mouth occurs in a deaerated condition. In this situation, the overall pH in the crevice decreases with time and this decrease picks up more slowly as it moves into the crevice, but eventually the pH deeper in the crevice becomes smaller than near the mouth. These model-predicted results with or without external polarization are shown to be qualitatively consistent with experimental findings in the literature.

In a crevice of variable gap, the effect of gap change on the crevice chemistry may be treated as similar to the effect of flow. The total diffusion rate of an ion transport (equivalent to flow rate) is approximately the same across an edge of the gap-narrowed region. However, the diffusion flux of the ion (equivalent to flow velocity) is significantly different immediately before or after an edge, because the fluxes are inversely proportional to the gap size. Approaching to the gap-narrowing edge from the mouth, the ion tends to accumulate and the diffusion flux increases. Conversely, as the gap expands, the diffusion flux decreases and the ion tends to dissipate out from the gap-narrowed region, leading to a decrease of Na^+ concentration relative to that in the crevice of constant gap.

5. Practical Aspects of the Model Results

Due to the insignificant effect of a variable gap on crevice corrosion, the model result suggests that the field techniques developed earlier [40] for evaluating the CP penetration limit and for estimating the distributions of corrosion potential and rate in a pipeline crevice of constant gap can be applied to crevices of variable gap. In using the field methods, the values of the variable gap may need to be averaged approximately.

With a small crevice mouth area, when sufficient CP is imposed at the mouth, this crevice corrosion is insignificant if sufficient time is given for the crevice chemistry to develop to become alkaline. In the absence of CP or with insufficient CP, the aerated mouth area serves as the cathode and the broader coating disbonded region serves as the anode. This small cathode-to-anode area ratio is different from the traditional crevice corrosion of a passive alloy, which is often driven by a large cathode-to-anode ratio. For this reason, an aggressive acidic solution is unlikely to develop in a coating disbonded region on pipelines even in the absence or with insufficient levels of CP. When an aggressive acidic solution exists in the coating disbonded region, it is likely that the local soil chemistry itself is aggressive and CP is not functioning well or the time of CP application is inadequate. In a complex corrosion system, such as in a pipe disbonded region, many other factors may also contribute to generating

an acidic solution such as anodic dissolution by stray currents, galvanic coupling, or other factors, which are all beyond the scope of this work.

Acknowledgments

This work was sponsored by the U.S. Department of Transportation, Pipeline and Hazardous Materials Safety Administration (Mr. James Merritt, Program Manager), under the contract DTPH56-08-T-0003. It was co-funded by Pipeline Research Council International (Mr. Mark Piazza, Senior Program Manager) and CenterPoint Energy, New Orleans, Louisiana (Mr. Rickey Payne, Direct Assessment Manager).

This paper was revised from paper no. 31316, presented at the 8th International Pipeline Conference held in Calgary, Canada, on September 28-October 1, 2010,.

References

1. H. Leidheiser, W. Wang, L. Igetoft, Progress in Organic Coatings 11 (1983) 19-40.
2. C.G. Munger, Corrosion Prevention by Protective Coatings (NACE, 1984) 47-61.
3. J.M. Leeds, Pipe Line & Gas Industries, March (1995) 21-26.
4. M. Meyer, X. Campaignolle, F. Coeuille, M.E.R. Shanahan, "Impact of Aging Processes on Anticorrosion properties of Thick Polymer Coatings for Steel Pipelines," in Proceedings of the Corrosion/2004 Research Topical Symposium: Corrosion Modeling for Assessing the Condition of Oil and Gas Pipelines, F. King and J. Beavers (eds.) (NACE, 2004) 93-146.
5. F.M. Song, Corrosion 66(9) (2010) 095004.
6. F.M. Song, D.W. Kirk, D.E. Cormack, D. Wong, Materials Performance 44(4) (2005) 26-29.
7. F.M. Song, D.W. Kirk, D.E. Cormack, D. Wong, Materials Performance 42(9) (2003) 24-26.
8. F.M. Song, D.W. Kirk, J.W. Graydon, D.E. Cormack, Corrosion 58(12) (2002) 1015-1024.
9. F.M. Song, D.W. Kirk, J.W. Graydon, D.E. Cormack, Corrosion 59(1) (2003) 42-49.
10. F.M. Song, D.A. Jones, D.W. Kirk, Corrosion, 60(2) (2005) 145-154.
11. F.M. Song, N. Sridhar, Corrosion 62(8) (2006) 676-686.
12. F.M. Song, N. Sridhar, Corrosion 62(10) (2006) 873-882.
13. F.M. Song, N. Sridhar, Corrosion Science 50(1) (2008) 70-83.
14. N. Sridhar, D.S. Dunn, M. Seth, Corrosion 57 (7) (2001) 598-613.
15. N. Sridhar, "Modeling the Conditions under Disbonded Coating Crevices—A Review," in Proceedings of the Corrosion/2004 Research Topical Symposium: Corrosion Modeling for Assessing the Condition of Oil and Gas Pipelines, F. King and J. Beavers (eds.) (NACE, 2004) 53-92.
16. M.E. Orazem, D.P. Reimer, C. Qiu, K. Allahar, "Computer Simulations for Cathodic Protection of Pipelines," in Proceedings of the Corrosion/2004 Research Topical Symposium: Corrosion Modeling for Assessing the Condition of Oil and Gas Pipelines, F. King and J. Beavers (eds.) (NACE, 2004) 25-52.
17. R.R. Fessler, A.J. Markworth, R.N. Parkins, Corrosion 39(1) (1983) 20-25.
18. T.R. Jack, G.V. Boven, M. Wilmott, R.L. Sutherby, R.G. Worthingham, Materials Performance (8) (1994) 17-21.
19. A. Turnbull, A.T. May, Materials Performance 22 (1983) 34.
20. J.J. Perdomo, I. Song, Corrosion Science 42 (2000) 1389.
21. M.H. Peterson, T.J. Lennox, Jr., Corrosion 29 (1973) 406.
22. A.C. Toncre, N. Ahmad, Materials Performance 19(6) (1980) 39.
23. M.D. Orton, Materials Performance 24(6) (1985) 17.
24. F. Gan, Z.-W. Sun, G. Sabde, D.-T. Chin, Corrosion 50(10) (1994) 804.
25. R. Brousseau, S. Qian, Corrosion 50(12) (1994) 907-911.
26. F. King, T. Jack, M. Kolar, R. Worthingham, "A Permeable Coating Model for Predicting the Environment at the Pipe Surface under CP-Compatible Coatings," (NACE, 2004) paper no. 04158.
27. F.M. Song, Corrosion Science 50 (2008) 3287-3295.
28. F.M. Song, D.W. Kirk, J.W. Graydon, D.E. Cormack, Corrosion 58(2) (2002) 145-155.
29. R. Parsons, Handbook of Electrochemical Constants (London: Butterworths Scientific Publications, 1959) 47 and 66.
30. D. Tromans, Corrosion 55 (1999) 942.

31. J. Newman, K.E. Thomas-Alyea, Electrochemical Systems, 3rd ed. (Englewood Cliffs, NJ: Prentice Hall, 1991).
32. J. Kvarekval, "A Kinetic Model for Calculating Concentration Profiles and Fluxes of CO_2-Related Species across the Nernst Diffusion Layer," (NACE, 1997) Paper no. 5.
33. V. Jovancicevic, J. O'M. Bockris, J. Electrochem. Soc. 133 (1986) 1797.
34. S. Nesic, J. Postlethwaite, S. Olsen, Corrosion 52 (1996) 280.
35. J.O'M. Bockris, D. Drazic, A.R. Despic, Electrochimica Acta 4 (1961) 325.
36. J.G.N. Thomas, T.J. Nurse, R. Walker, Br. Corros. J. 5 (1970) 87.
37. C.M. Shepherd, S. Schuldiner, J. Electrochem. Soc. 115 (1968) 1124.
38. M. Stern, R.M. Roth, J. Electrochem. Soc. 104 (1957) 390.
39. R.N. Parkins, Y. Liu, Effects of Dynamic Strain on Crack Tip Chemistry, Vol. 1: Tests Using a Segmented Artificial Crevice, Final Report to Electric Power Research Institute, EPRI RD-4649, June 1986.
40. F.M. Song, Corrosion 66(3) (2010) 035005.

Appendix A. Reversible and irreversible homogeneous and heterogeneous reactions in the system, chemical equilibrium formula, and kinetic rates in the crevice corrosion system

The reversible reactions in the crevice solution are listed next. The reactions in the parentheses are equivalent reactions but show more clearly the equilibrium relationships among reactants and products. The concentrations of all the secondary species can be expressed by those of the primary species as shown.

$$H_2O - H^+ \leftrightarrow OH^- \quad (H_2O \leftrightarrow H^+ + OH^-),\ c_4c_5 = K_w$$
(A.1)

$$Fe(OH)_2 + 2H^+ \leftrightarrow Fe^{2+} + 2H_2O \quad (Fe(OH)_2 \leftrightarrow Fe^{2+} + 2OH^-),\ c_3c_5^2 = K_{SP}$$
(A.2)

$$Fe(OH)_2 + H^+ \leftrightarrow FeOH^+ + H_2O \quad (Fe^{2+} + H_2O \leftrightarrow FeOH^+ + H^+),\ \frac{c_4c_6}{c_3} = K_1$$
(A.3)

The electrochemical reactions at the steel surface are

$$Fe \rightarrow Fe^{2+} + 2e^- \qquad r^e_{Fe}$$
(A.4)

$$H^+ + e^- \rightarrow 0.5H_2 \qquad r^e_H$$
(A.5)

$$H^+ + e^- \rightarrow 0.5H_2 \quad (H_2O + e^- \rightarrow 0.5H_2 + OH^-) \qquad r^e_{H_2O}$$
(A.6)

$$4H^+ + O_2 + 4e^- \rightarrow 2H_2O \qquad r^e_{O_2} \qquad \text{(A.7)}$$

When the concentrations of Na^+ and Cl^- are same, the electroneutrality ($\sum_j z_j c_j = 0$) and the previous equations allow each concentration to be determined analytically.

The equation of electroneutrality is

$$2K_{sp} + (K_w + \frac{K_1 K_{sp}}{K_w})c_5 - c_5^3 = 0 \tag{A.8}$$

The solution of Equation (A.8) is

$$c_5 = \frac{2^{\frac{1}{3}}(k_w + \frac{K_1 K_{sp}}{K_w})}{\lambda_2} + \frac{\lambda_2}{3 \cdot 2^{\frac{1}{3}}} \tag{A.9}$$

where $\lambda_1 = 6\sqrt{81k_{sp}^2 - 3(k_w + \frac{K_1 K_{sp}}{K_w})^3}$ and $\lambda_2 = (\lambda_1 + 54k_{sp})^{\frac{1}{3}}$.

For a more general case where the charges of Na^+ and Cl^- may or may not balance out, the following equation may be used:

$$z_1 c_1 + z_2 c_2 + z_3 \frac{K_{sp}}{c_5^2} + z_4 \frac{K_w}{c_5} + z_5 c_5 + z_6 \frac{K_1 K_{sp}}{K_w c_5} = 0 \tag{A.10}$$

Alternatively, it is written as

$$z_5 c_5^3 + p_1 c_5^2 + p_{10} c_5 + z_3 K_{sp} = 0 \tag{A.11}$$

where $p_{10} = (z_4 K_w + z_6 \frac{K_1 K_{sp}}{K_w}) / z_5$, and $p_{20} = z_3 K_{sp} / z_5$.

The solution of Equation (A.11) is

$$c_5 = -\frac{p_1}{3} - \frac{2^{\frac{1}{3}} p_2}{3p_5} + \frac{p_5}{2^{\frac{1}{3}} 3} = \frac{p_5^2 - 2^{\frac{1}{3}} p_1 p_5 - 2^{\frac{2}{3}} p_2}{2^{\frac{1}{3}} 3 p_5} \tag{A.12}$$

where

$$p_5 = (p_3 + p_4)^{\frac{1}{3}}, \tag{A.13a}$$

$$p_4 = \sqrt{4p_2^3 + p_3^2}, \tag{A.13b}$$

$$p_3 = -2p_1^3 + 9p_{10}p_1 - 27p_{20}, \tag{A.13c}$$

$$p_2 = -p_1^2 + 3p_{10}, \text{ and} \tag{A.13d}$$

$$p_1 = (z_1 c_1 + z_2 c_2) / z_5. \tag{A.13e}$$

With Equation (A.9) or (A.12), the concentrations of other species may be calculated from

$$c_4 = \frac{k_w}{c_5},\ c_3 = \frac{K_{sp}}{c_5^2},\ c_6 = \frac{K_1 K_{sp}}{K_w c_5} \tag{A.14}$$

Appendix B. Simplification of 2D O_2 transport by using a parabolic relationship

A parabolic relationship may be used to express the oxygen concentration c vs. y across the gap shown in Figures 1a, b, or c:

$$c = \alpha_1 y^2 + \beta_1 y + c_s \tag{B.1}$$

For a permeable coating, the boundary condition at the coating inner surface may be approximated by

$$\left.\frac{\partial c}{\partial y}\right|_{y=\delta_s} = \frac{D_{O_2c}(c^0 - c_c)}{D_{O_2}\delta_c} = \frac{m(c^0 - c_c)}{\delta_s} \tag{B.2}$$

where $m = \frac{\delta_s D_{O_2c}}{D_{O_2}\delta_c}$; δ_c is the coating thickness; D_{O_2} and D_{O_2c} are O_2 diffusivity in solution and coating, respectively; and c^0 and c_c are O_2 concentrations in solution located at the outer and inner surfaces of the coating, respectively.

When the boundary condition at the steel surface

$$-D_{O_2}\left.\frac{\partial c}{\partial y}\right|_{y=0} = r_{O_2} \tag{B.3}$$

is used ($r_{O_2} \le 0$), because the first derivative of Equation (B.1) over y is

$$\frac{\partial c}{\partial y} = 2\alpha_1 y + \beta_1 \tag{B.4}$$

the following equations are obtained:

$$\beta_1 = -\frac{r_{O_2}}{D_{O_2}} \tag{B.5a}$$

and

$$\alpha_1 = \frac{m(c^0 - c_c)}{2\delta_s^2} - \frac{\beta_1}{2\delta_s} \tag{B.5b}$$

Because $c_c = \alpha_1\delta_s^2 + \beta_1\delta_s + c_s$ at the coating inner surface, by substitution of (B.5a) and (B.5b) and reorganization, the following is obtained:

$$c_c = \frac{mc^0 + \beta_1\delta_s + 2c_s}{m+2} \tag{B.6}$$

Substitute Equations (21-22) into Equation (B.5a) to yield

$$\beta_1 = \frac{\pi}{\delta_s} c_s \tag{B.7}$$

where

$$\pi = -\frac{\delta_s i_{O_2sm} 10^{\frac{\varphi}{b_{O_2}}}}{n_{O_2} F D_{O_2} c_{sm}} = -\frac{\delta_s^2}{\lambda} 10^{\frac{\varphi}{b_{O_2}}} \tag{B.7a}$$

if it is ordered that $\lambda = -\frac{\delta_s n_{O_2} F D_{O_2} c_{ref}}{i^0_{O_2 ref} 10^{\frac{-(E_m - E^{Eqref}_{O_2})}{b_{O_2}}}}$.

Substitute Equation (B.7) into (B.6) to yield

$$c_c = \frac{mc^0 + (2+\pi)c_s}{m+2} \tag{B.8}$$

Substituting (B.7-B.8) into (B.5b) yields

$$\alpha_1 = \frac{mc^0 - (m+\pi+m\pi)c_s}{\delta_s^2 (m+2)} \tag{B.9}$$

By averaging O_2 concentration in (B.1) and by using Equations (B.7) and (B.9) the following equation is obtained:

$$\bar{c} = \frac{a^2\alpha_1}{3} + \frac{a\beta_1}{2} + c_s = \frac{mc^0}{3(m+2)} + \frac{4m+12+\pi m+4\pi}{6(m+2)} c_s$$

or

$$c_s = \frac{6(m+2)\bar{c} - 2mc^0}{4m+12+\pi m+4\pi} \tag{B.10}$$

Substitute (B.10) into (B.8) and (B.5a) to yield, respectively,

$$c_c = \frac{6(\pi+2)\bar{c} + m(\pi+4)c^0}{4m+12+\pi m+4\pi} \tag{B.11}$$

and

$$r_{O_2} = -D_{O_2} \frac{\pi}{\delta_s} c_s = -\frac{D_{O_2}\pi[6(m+2)\bar{c} - 2mc^0]}{\delta_s (4m+12+\pi m+4\pi)} \tag{B.12}$$

The overall mass transport equation of oxygen can now be expressed by

$$\frac{\partial(\bar{c}\delta_s)}{\partial t} - \frac{\partial}{\partial x}\left(D_{O_2}\delta_s \frac{\partial \bar{c}}{\partial x}\right) = D_{O_2}\left(\frac{m(c^0 - c_c)}{\delta_s} + \frac{r_{O_2}}{D_{O_2}}\right) = \frac{2D_{O_2}[3m(\pi+2)c^0 - 6(m+\pi+m\pi)\bar{c}]}{\delta_s (4m+12+\pi m+4\pi)} \tag{B.13}$$

At the mouth, $\varphi=0$ and Equation (B.7a) becomes

$$\pi_m = -\frac{\delta_s i_{O_2 sm}}{n_{O_2} F D_{O_2} c_{sm}} = -\frac{\delta_s^2}{\lambda} \tag{B.14}$$

where π_m is π at the crevice mouth.

With $c_c = c^0$ at the mouth, Equation (B.8) at the mouth becomes

$$c^0 = \frac{mc^0 + (2+\pi_m)c_{sm}}{m+2} \tag{B.15}$$

or

$$c_{sm} = \frac{2c^0}{2+\pi_m} = \frac{2\lambda c^0}{2\lambda - \delta_s^2} \tag{B.16}$$

If applied at the mouth, with $c_c = c^0$, Equation (B.11) becomes

$$\bar{c}_m = \frac{2(3\lambda - \delta_s^2)c^0}{3(2\lambda - \delta_s^2)} \tag{B.17}$$

or

$$\lambda = \frac{\delta_s^2}{6}\frac{2c^0 - 3\bar{c}_m}{c^0 - \bar{c}_m} \tag{B.17a}$$

Substitute Equation (B.17a) into Equations (B.16) and (B.12) to yield, respectively,

$$c_{sm} = \frac{3\lambda \bar{c}_m}{(3\lambda - \delta_s^2)} \tag{B.18}$$

and

$$r_{O_2 m} = -D_{O_2}\frac{\pi_m}{\delta_s}c_{sm} = \frac{3D_{O_2}\delta_s \bar{c}_m}{3\lambda - \delta_s^2} \tag{B.19}$$

When approximation is applied for $r_{O_2 m}$ by assuming oxygen diffusion controls so that $\lambda >> \delta_s^2$, Equations (B.17) and (B.19) become, respectively,

$$\bar{c}_m = \frac{2c^0}{3} \tag{B.20a}$$

and

$$r_{O_2 m} \cong -\frac{3D_{O_2}\bar{c}_m}{\delta_s} \cong -\frac{2D_{O_2}c^0}{\delta_s} \tag{B.20b}$$

Table 1: Initial and Boundary Conditions in This and a Previous Work [13]

Condition	c_1 *(mol/m³)*	c_2 *(mol/m³)*	c_4 *(mol/m³)*	c_7^0 *(mol/m³)*	ϕ *or* $i_{totx} = \sum_1^6 z_j F N_{jx}$ *(V)* *(A/m²)*
Initial	0.3128	0.3128	6.014×10^{-7}	0*	
Mouth with CP	3.128	3.128	6.014×10^{-7}	0.2601	ϕ=0
Mouth with no CP	3.128	3.128	6.014×10^{-7}	0.2601	i_{totx}=0
Condition	N_{1x} (mol/m²·s)	N_{2x} (mol/m²·s)	$\sum_1^6 z_j N_{jx}$ (mol/m²·s)	N_{7x} (mol/m²·s)	i_{totx} (A/m²)
Crevice tail	0	0	0	0	0
Previous work [13]	c_1 *(mol/m³)*	c_2 *(mol/m³)*	c_4 *(mol/m³)*	c_7^0 *(mol/m³)*	ϕ *(V)*
Initial and mouth	0.3128	0.3128	6.31×10^{-7}	0.2601	0

** This value may also be determined from O_2 diffusion via coating at steady state (prior to holiday formation).*

Table 2: Constants and Values of Parameters Used for the Modeling

Symbol	*Value*	*Units*	*Explanation*	*Ref*
Physical parameters				
T	298.15	K	System temperature	
Constants				
F	96485	C/mol	Faraday's constant	29
R	8.3143	J/mol·K	Gas constant	29
Thermodynamic constants				
K_w	10^{-8}	$(mol/m^3)^2$	Water ionic product	29
K_1	3.16×10^{-7}	mol/m^3	Equilibrium constant for $Fe^{2+}+H_2O\rightarrow Fe(OH)^+ + H^+$	#
Ksp	1.82×10^{-6}	$(mol/m^3)^3$	Solubility product of $Fe(OH)_2$	29
H_{O_2}	0.8074	$atm\cdot m^3/mol$	Henry's law constant for O_2	30
Diffusion coefficients				
D_{Na^+}	1.334×10^{-9}	m^2/s	Na^+	31
D_{Cl^-}	2.032×10^{-9}	m^2/s	Cl^-	31
$D_{Fe^{2+}}$	0.72×10^{-9}	m^2/s	Fe^{2+}	32
D_{H^+}	9.312×10^{-9}	m^2/s	H^+	31
D_{OH^-}	5.26×10^{-9}	m^2/s	OH^-	31
$D_{Fe(OH)^+}$	0.5×10^{-9}	m^2/s	$Fe(OH)^+$	##
D_{O_2}	1.96×10^{-9}	m^2/s	O_2	30
Standard potentials (vs. $Cu/CuSO_4$)				
E_{Fe}^0	-0.756	V	Iron oxidation	29
$E_{H_2O}^0$ (pH=14)	-1.144	V	H_2O reduction	29
$E_{H^+}^0$ (pH=0)	-0.316	V	H^+ reduction	29
$E_{O_2}^0$ (pH=14)	0.085	V	O_2 reduction	29
Number of electrons transferred				

n_{Fe}	2		Iron oxidation	33
n_{H_2O}	1		H_2O reduction	29
n_{H^+}	1		H^+ reduction	29
n_{O_2}	4		O_2 reduction	33
Exchange current densities				
i_{Fe}^0	0.0002	A/m^2	Iron oxidation	34-38
$i_{H_2O}^0$	0.002	A/m^2	H_2O reduction	34
$i_{H^+ref}^0$	0.001	A/m^2	H_2O reduction	34
(c_{H^+ref}=0.1 mol/m^3)				
$i_{O_2 Ref}^0$	4.0×10^{-9} A/m^2		O_2 reduction	33
(pH=9, $p_{O_2 ref}$=1atm)				
Tafel slopes				
b_{Fe}	0.04	V/decade	Iron oxidation	30; 34
b_{H_2O}	0.12	V/decade	H_2O reduction	34
b_{H^+}	0.12	V/decade	H^+ reduction	34
b_{O_2} (pH=9)	0.12	V/decade	O_2 reduction	33

Based on parameters in OLI software
Estimated

Table 3: Parameters and Their Values Used for Switching On or Off One or More Conditions in the Modeling

No.	*Switch*	θ_1	θ_2	θ_3	D_{7c}
i	Constant gap vs. x and t, no current & no O_2 penetration via coating	0	0	0	0
ii	Variable gap vs. x (Fig. 1b), no current & no O_2 penetration via coating	1	0	0	0
iii	Variable gap vs. x (Fig. 1c), no current & no O_2 penetration via coating	0	1	0	0
iv	Variable gap vs. x (Fig. 1b), no current but O_2 penetration via coating	1	0	0	1
v	Variable gap vs. x (Fig. 1b), current but no O_2 penetration via coating	1	0	1	0
vi	Variable gap vs. x (Fig. 1b), current & O_2 penetration via coating	1	0	1	1

θ_1 corresponds to variable gap vs. x shown by Figure 1b, θ_2 to variable gap vs. x shown by Figure 1c (gap vs. x), and θ_3 to current penetration through coating.

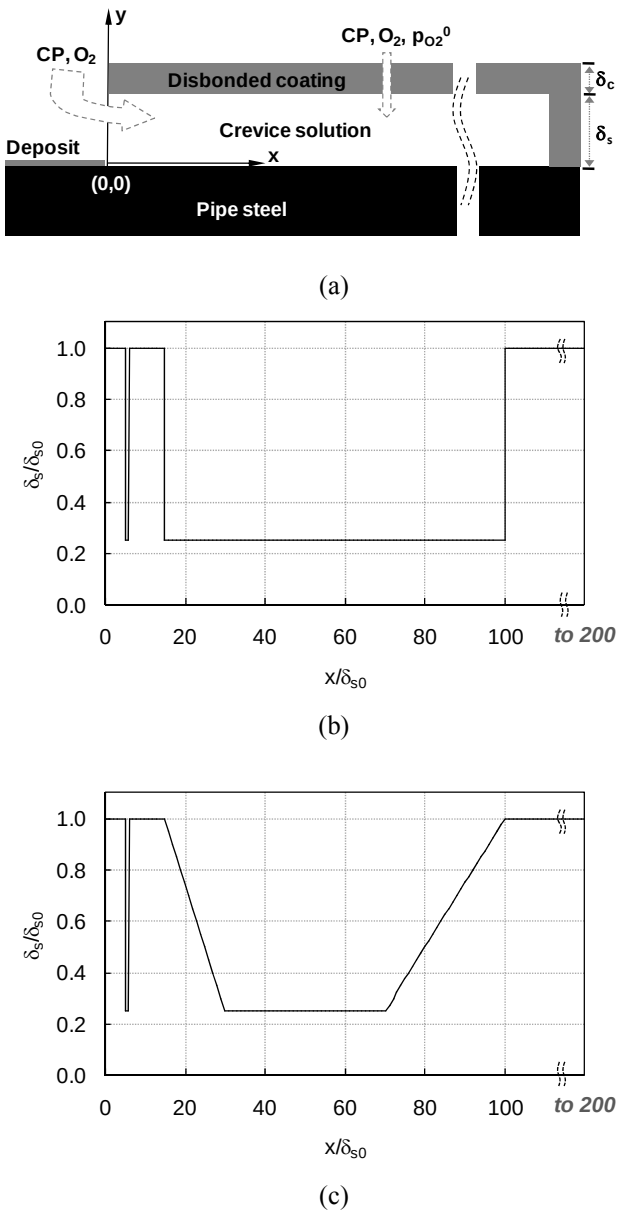

Figure 1. Model crevice geometry showing the coordinators and dimensions of the crevice and transport of CP current and O_2 into the crevice through the disbonded coating.

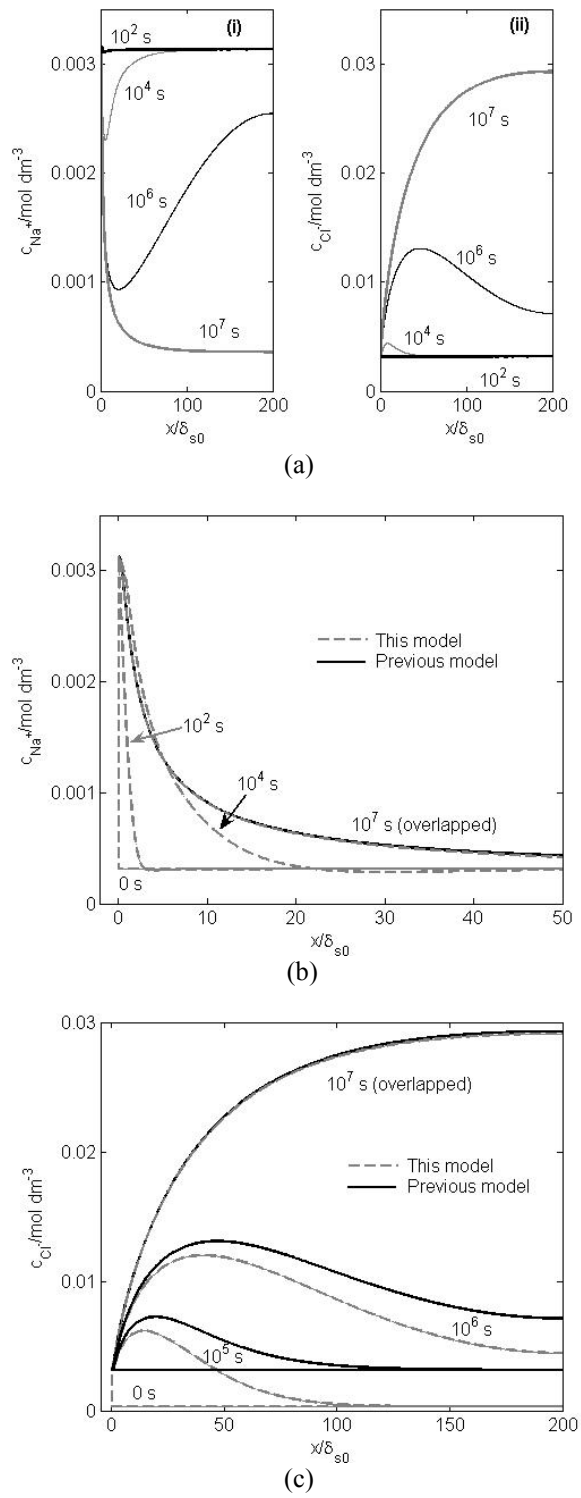

Figure 2. At a fixed mouth potential of -0.8071 V_{CSE}, with negligible or low initial CP, (a) evolution of Na^+ and Cl^- concentrations with time in previous work with crevice Figure 1a where the initial and mouth chemistry are the same, (b) Na^+ concentration vs. time in this work with the initial concentrations different from the mouth concentrations of Na^+ and Cl^- (gray lines), overlaying with the Na^+ concentration in previous work at 10^7 s (dark line), and (c) similar to (b) but for Cl^-.

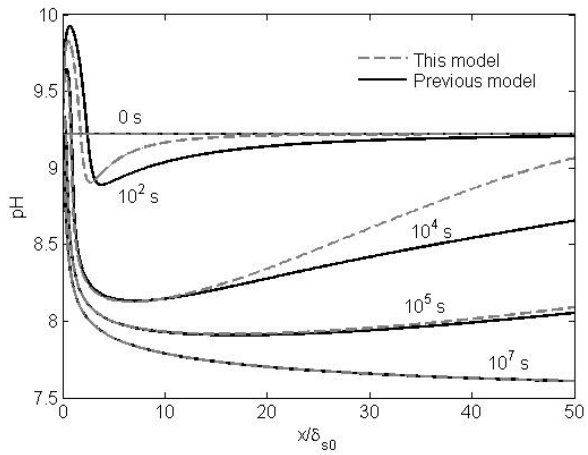

Figure 3. At a fixed mouth potential of -0.8071 V_{CSE}, with negligible or low initial CP, pH variation in crevice at different times; a comparison of the results obtained in this work with those in previous work.

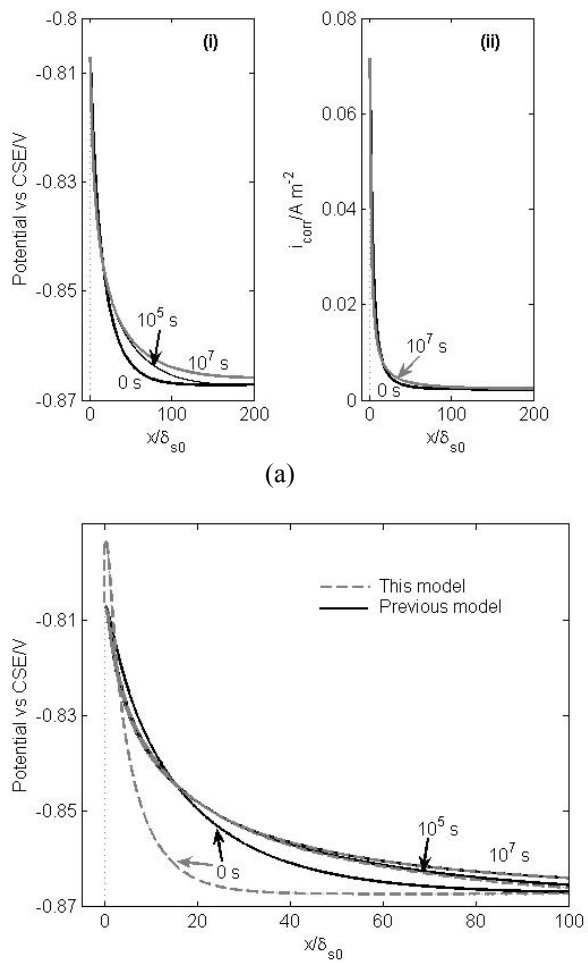

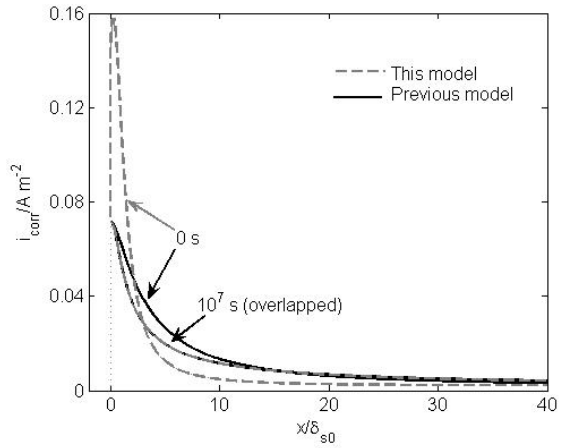

(c)

Figure 4. At a fixed mouth potential of -0.8071 V_{CSE}, with negligible or low initial CP, (a) variation of crevice potential and corrosion current density at different times obtained in previous work where the initial and mouth chemistry are the same, (b) variation of crevice potential at different times obtained in this work with the initial concentrations different from the mouth concentrations of Na^+ and Cl^- (gray lines) in comparison with the potential in previous work at 10^7 s (dark line), and (c) similar to (b) but with crevice corrosion current density.

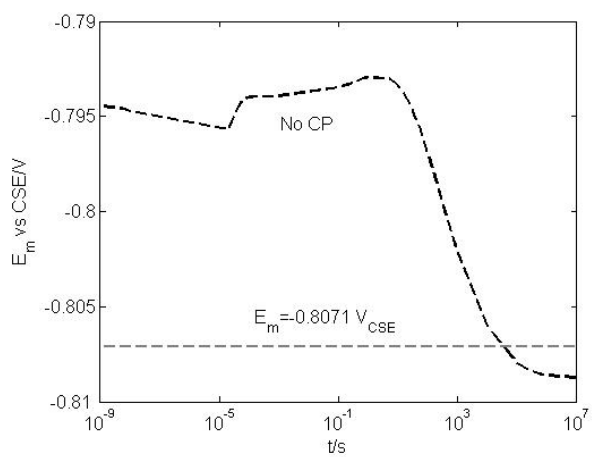

Figure 5. Variation of the crevice mouth potential with time during the corrosion process with no CP.

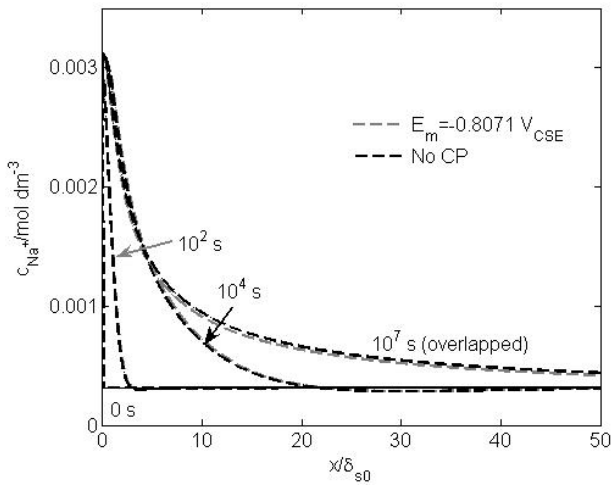

(a)

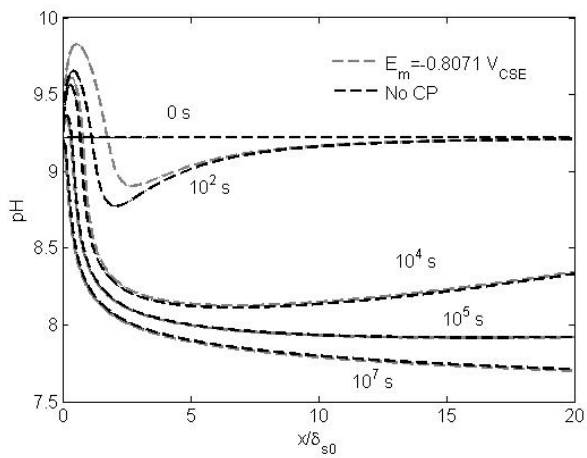

(b)

Figure 6. A comparison of (a) Na^+ concentration and (b) pH in the crevice at different times between the crevice corrosion with no CP (dark lines) and low CP at a fixed potential of -0.8071 V_{CSE} (gray lines).

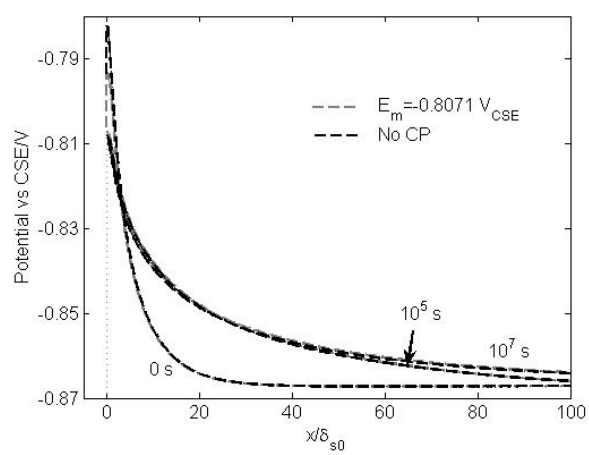

(a)

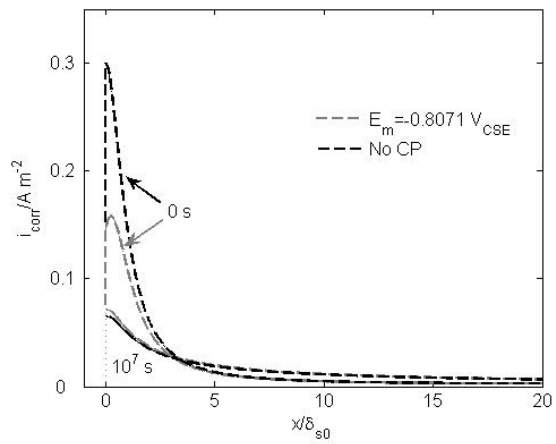

(b)

Figure 7. A comparison of (a) potential and (b) corrosion current density in the crevice at different times between the crevice corrosion with no CP (dark lines) and low CP at a fixed potential of -0.8071 V_{CSE} (gray lines).

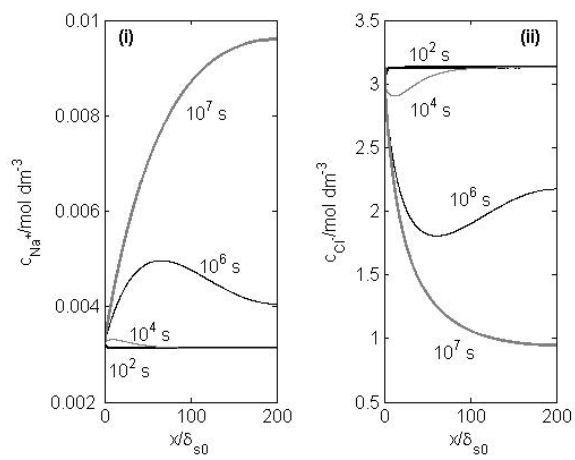

(a)

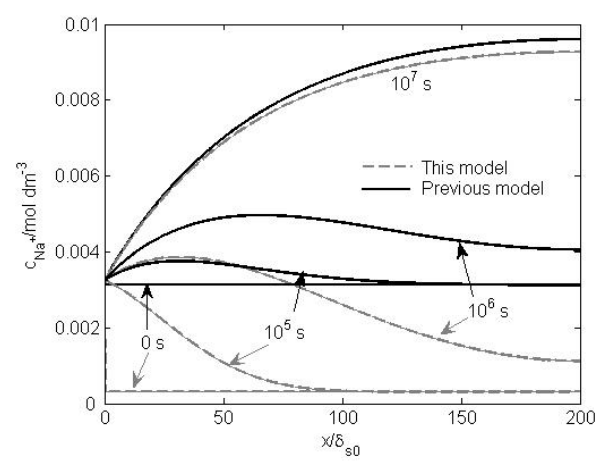

(b)

Figure 8. Similar to Figure 2, but here the mouth potential is fixed at -0.9 V_{CSE}.

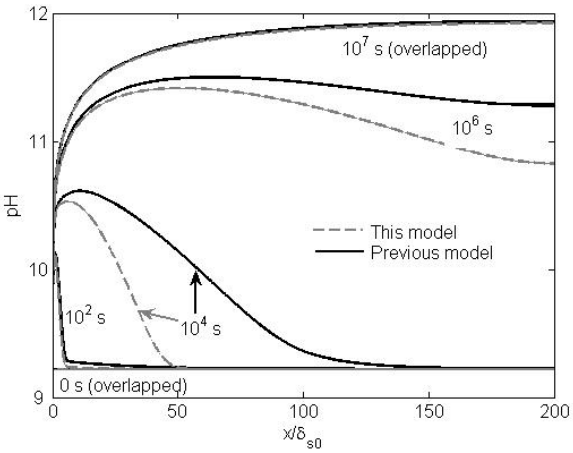

Figure 9. Similar to Figure 3, but here the mouth potential is fixed at -0.9 V_{CSE}.

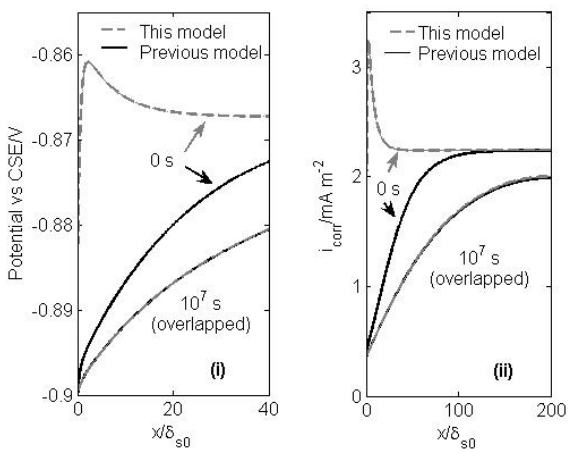

Figure 10. Similar to Figure 4, but here the mouth potential is fixed at -0.9 V_{CSE}.

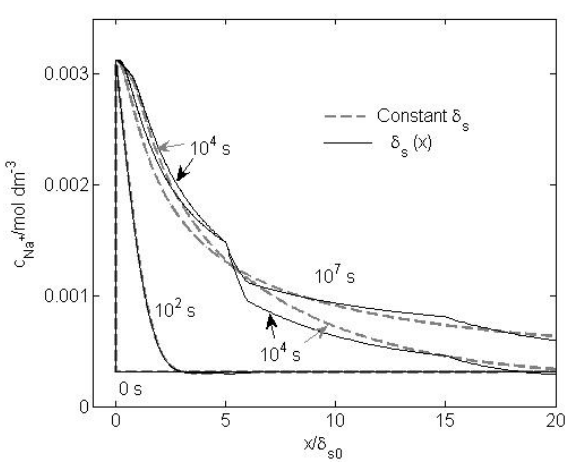

(a)

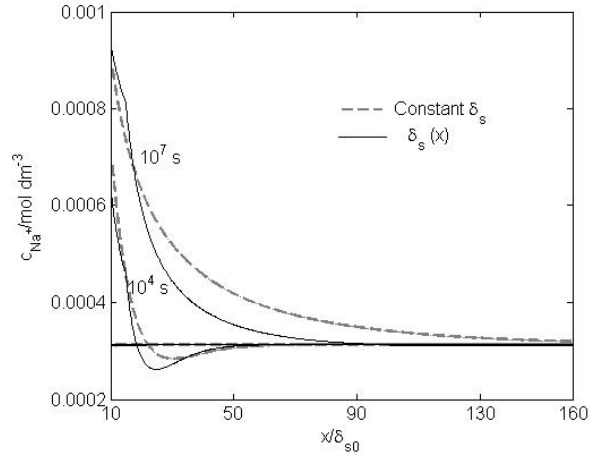

(b)

Figure 11. At a fixed mouth potential of -0.8071 V_{CSE}, a comparison of Na^+ concentrations in two crevices at different times between a constant gap shown by Figure 1a (gray lines) and a variable gap vs. x shown by Figure 1b (dark lines) (a) near the mouth and (b) away from the crevice mouth.

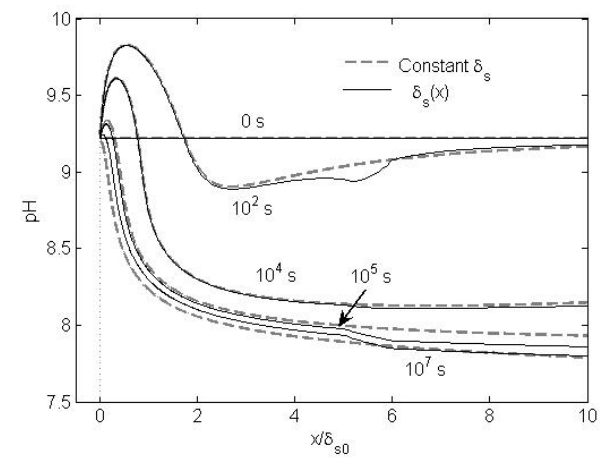

(a)

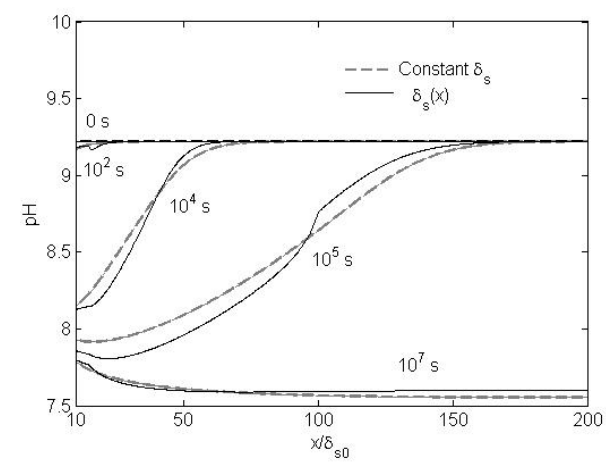

(b)

Figure 12. Similar to Figure 11, but here crevice pHs are compared (a) near the mouth and (b) away from the crevice mouth.

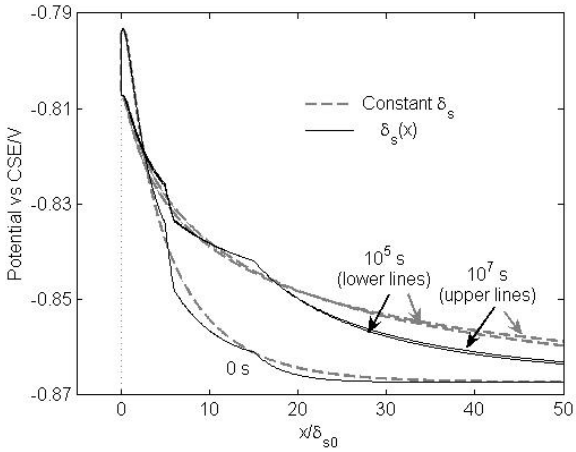

(a)

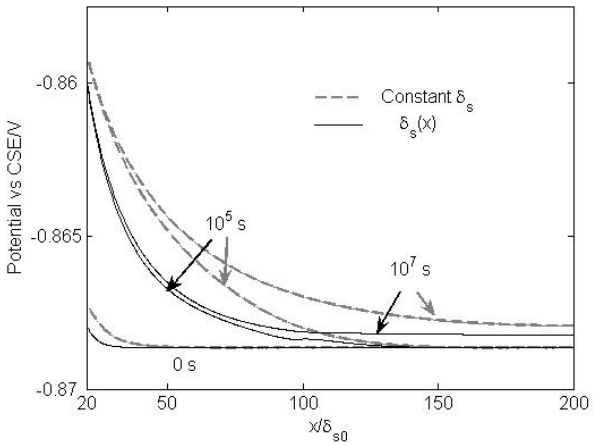

(b)

Figure 13. Similar to Figure 11, but here crevice potentials are compared (a) near the mouth and (b) away from the crevice mouth [note the reduced scale of potential from (a)].

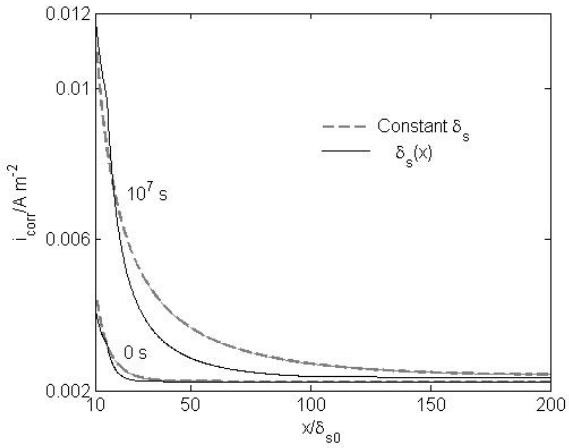

(b)

Figure 14. Similar to Figure 11, but here crevice corrosion current densities are compared (a) near the mouth and (b) away from the crevice mouth [note the reduced scale of i_{corr} from (a)].

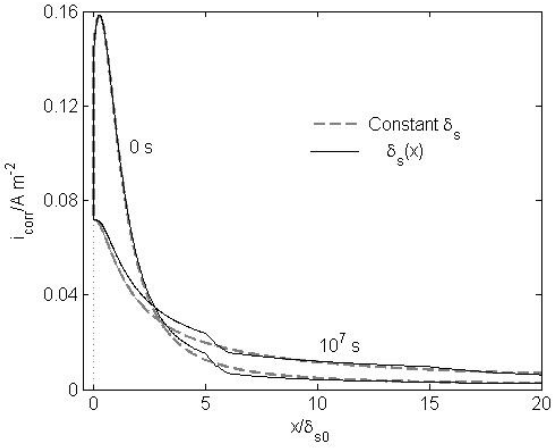

(a)

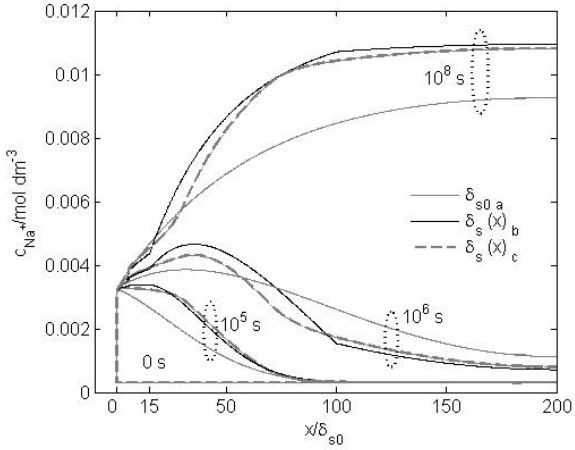

(a)

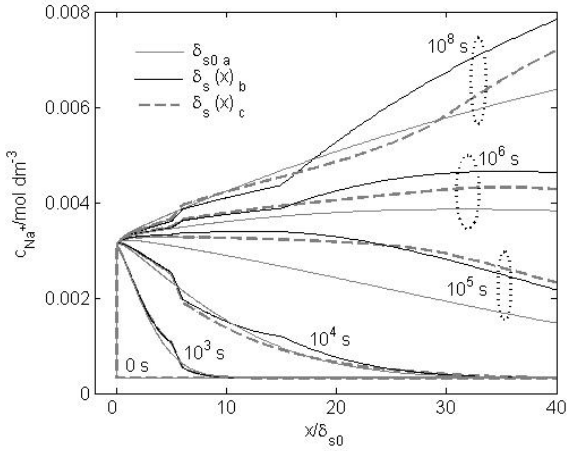

(b)

Figure 15. At a fixed mouth potential of -0.9 V_{CSE}, a comparison of Na^+ concentrations in the three crevices in Figure 1 at different times: constant gap of Figure 1a (gray solid lines), variable gap vs. x of Figure 1b (black solid lines), and variable gap vs. x of Figure 1c (gray broken lines): (a) the entire crevice and (b) near the mouth. In the legend, δ_{s0}, $\delta_s(x)_b$, and $\delta_s(x)_c$ refer to crevices shown in Figures 1a, b, and c, respectively.

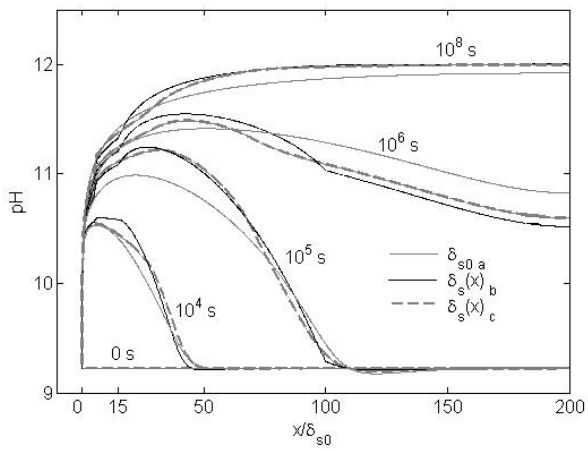

Figure 16. Similar to Figure 15, but here crevice pHs are compared.

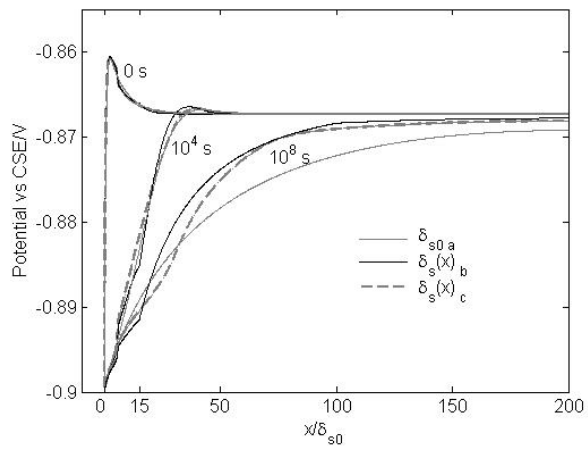

(a)

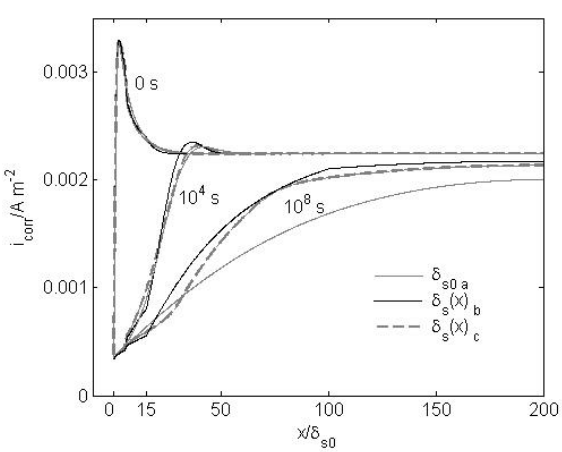

(b)

Figure 17. Similar to Figure 15, but here (a) crevice potentials and (b) crevice corrosion current densities are compared.

MS #2

Predicting the chemistry, corrosion potential, and rate in a crevice formed between substrate steel and a disbonded permeable coating with a mouth

ABSTRACT

A model developed in an earlier work was used in this work to investigate the effect of coating permeability on the evolution of solution chemistry, corrosion potential, and rate in a crevice formed between a steel surface and a coating disbonded from it. The crevice gap varies along distance from the mouth, and the coating is permeable to ions and/or oxygen (O_2). The earlier work focused specifically on modeling the effect of variable gap (on crevice corrosion) with the coating impermeable to either ions or O_2. In both works, the crevice chemistry was an aerated, diluted sodium chloride solution, which at the mouth was set to be different from that initially in the crevice. The results of this work show that a permeable coating behaves like a membrane, which, under a cathodic polarization at the crevice mouth, tends to raise the in-crevice sodium ion concentration and pH more rapidly relative to an impermeable coating. Later, as the sodium ion concentration and pH in the crevice become greater than at the mouth, the permeable coating tends to reverse the transport direction for ions. At a mouth potential of -0.900 V vs. saturated $Cu/CuSO_4$, the cathodic current is sufficient to suppress all O_2 penetrating the crevice both from the mouth and through the coating. The practical implication is that in the presence of sufficient cathodic polarization, a permeable coating, when disbonded, can still be capable of protecting the substrate steel from corrosion attack.

Keywords: A. steel, polymer coatings; B. modeling studies; C. crevice corrosion, cathodic protection

6. Introduction

Significant research has been performed to understand the mechanisms of the external corrosion of underground steel pipelines under disbonded coatings with or without a holiday (crevice mouth) [1-25]. To expand these studies where a crevice of uniform gap was often used, modeling was performed to study the effect of a variable gap on the crevice corrosion [26]. In that modeling study and also this present work, the crevice gap was intentionally designed to sharply vary over distance to demonstrate the most dramatic effect of the gap variation. The earlier study [26] was performed for conditions with and without cathodic protection (CP) applied at the mouth. The crevice chemistry was an aerated, diluted sodium chloride solution simulating soil groundwater. The model results showed that under the conditions investigated, the variation of the crevice gap with distance from the mouth had rather an insignificant effect on the crevice potential and corrosion rate due to the small cathode-to-anode area ratio of the crevice studied. Within the pH ranges studied (varying from neutral to alkaline), even if the pH varies within a few units across the crevice length, the variation of the crevice corrosion rate was not significant. The practical implication of the results was that unless the soil solution itself was aggressive with a low pH or contained carbon dioxide, an aggressive acidic solution may not likely develop in a coating disbonded region on buried steel pipelines even in the absence or with inadequate levels of CP.

The earlier study [26] assimilated the effect of gap variation on the crevice solution chemistry to the effect of flow, with the total diffusion rate of an ion (e.g., Na^+) analogous to flow rate and the diffusion flux to flow velocity. Maintaining approximately the same diffusion rate of an ion across a crevice edge with a sharp gap change, the diffusion flux of the ion can vary dramatically. In the presence of CP, this diffusion flux for Na^+ increases when the gap narrows and decreases when the gap expands.

The earlier study [26] also noted the lack of studies to understand the effect of coating permeability to ions and/or to molecular corrosive species, such as O_2 and carbon dioxide, on crevice corrosion. Although few studies were performed [7,27], none considers a coating that both is permeable and contains a mouth. This present work attempts to investigate, through mathematical modeling, the effect of coating permeability on crevice corrosion with a fixed potential applied at the crevice mouth. The crevice gap varies with distance, and the mouth chemistry is different from initially in the crevice. An understanding of the magnitude of coating permeability to CP current relative to the permeability to O_2 may provide insight into the corrosion protectiveness of the coating and the coating compatibility with CP.

It is often believed that an impermeable coating, when disbonded, may not allow CP current to pass through quickly enough to protect against local corrosion in the coating disbonded region. On the other hand, a

permeable coating (to ions) may provide such protection, although the degree of protection is yet to be understood. The degree of corrosion protection can be evaluated by comparing the relative coating permeability to ions vs. permeability to molecular species, such as O_2 and carbon dioxide, and the effect of the coating permeability on corrosion. The permeability of a new coating has been shown to have little effect on crevice corrosion [28]. This work investigates the effect of the coating permeability (to ions and/or O_2) on the crevice corrosion. The effect of carbon dioxide permeation through the coating will be explored in the future.

7. The mathematical model

2.1. The model geometry

The crevice geometry used in the model of this work is schematically shown in Figure 1, where the crevice gap δ_s varies along distance x, and δ_{s0} is δ_s at the crevice mouth, which is located at the left edge of the crevice. The crevice forms when a coating disbonds from a steel pipe surface. The crevice corrosion is treated as one dimensional (1D) with the properties considered uniform across the gap except for O_2. Special treatment of O_2 concentration and its diffusion in two dimensions was detailed elsewhere [8,13,26,29], and the result will be used here. O_2 diffusion cannot be directly treated in 1D, because it is slower than reduction, resulting in a higher concentration and lower gradient near the coating inner surface (facing to steel) and a low concentration and high gradient near the steel surface.

In Figure 1, the sharp gap changes occur at $\frac{x}{\delta_{s0}} = 5$, 6, 15, and 100. Such a sharp gap change is expected to yield a dramatic impact on the crevice corrosion process. The gap variation in Figure 1 may be expressed by

$\frac{\delta_s}{\delta_{s0}} = 1$ when $\frac{x}{\delta_{s0}} =$ 0-5, 6-15, and 100-200 and

$\frac{\delta_s}{\delta_{s0}} = \frac{1}{4}$ when $\frac{x}{\delta_{s0}} =$ 5-6 and 15-100.

Or,

$$\frac{\delta_s}{\delta_{s0}} = 1 - \frac{3}{4}\left(\frac{x}{\delta_{s0}} > 5\right) + \frac{3}{4}\left(\frac{x}{\delta_{s0}} > 6\right) - \frac{3}{4}\left(\frac{x}{\delta_{s0}} > 15\right) + \frac{3}{4}\left(\frac{x}{\delta_{s0}} > 100\right) \quad (1)$$

The gap is designed to have abrupt variations at x/δ_{s0}= 5 and 6 because past work [5-13] showed that the most significant variable change would occur within the first few gaps from the mouth.

2.2. Model conditions

The crevice solution used in this modeling work is an aerated, dilute sodium chloride solution simulating soil groundwater. The crevice solution is assumed to be saturated by ferrous hydroxide ($Fe(OH)_2$), which is only sparsely soluble in water. The crevice solution contains the following species: (1) $\underline{Na^+}$, (2) $\underline{Cl^-}$, (3) Fe^{2+}, (4) $\underline{H^+}$, (5) OH^-, (6) $Fe(OH)^+$, (7) $\underline{O_2}$, (8) $\underline{H_2(aq)}$, (9) $\underline{Fe(OH)_2}$, and (10) $\underline{H_2O}$, where the underlined species are defined as the primary species. Their concentrations can either be approximated or known, such as species (8)-(10). The concentrations of the secondary species, or species (3), (5), and (6), can be computed from the concentrations of the primary species through their equilibrium equations as described elsewhere [13,26].

When the coating is impermeable to ions or O_2, the results were reported for both a crevice of uniform gap [13] and a crevice of variable gap [26]. This paper investigates the crevice corrosion when the coating is permeable to either, both, or neither of O_2 and ions. The permeability of a coating is defined here as the porosity of the coating, which is the area percentage of the micropores in the coating. The goal is to understand the temporal and spatial variation of crevice chemistry and corrosion rate due to the coating permeability and how the results relate to a practical coating design in terms of coating compatibility to CP.

2.3. Model-governing equations

The detailed model equations have been given elsewhere, including the effect of coating permeability to ions and O_2 [26]. The equations provided in this section are general in nature and focus on the coating permeation to ions and O_2.

The general mass transport equation for any dissolved species in solution may be written as

$$\delta_s \frac{\partial c_j}{\partial t} + \frac{\partial}{\partial x}(\delta_s N_{jx}) + N_{jyc} = \delta_s R_j + R_{sj} \tag{2}$$

where c_j is concentration of the jth dissolved species in solution, t is time, δ_s is crevice gap varying with distance x, R_j is the total net volumetric production rate (after consumption deducted) of the jth species, R_{sj} is the total surface reaction rate of the jth species including corrosion reactions, N_j is flux of the jth species, subscript "x" refers to the longitudinal direction from the mouth in Figure 1, and subscript "yc" refers to the vertical direction from the steel surface and the coating boundary in Figure 1.

In Equation (2), the flux of the jth species N_{jx} may be written as

$$N_{jx} = -D_j \frac{\partial c_j}{\partial x} - \frac{z_j D_j F}{RT} c_j \frac{\partial \varphi}{\partial x} \tag{3}$$

where the first and second terms to the right of the equal sign are the diffusion and migration components, respectively, of the jth species in the "x" direction; F, R, and T are Faraday's constant, universal gas constant, and temperature in K, respectively; φ is electrostatic potential of the solution; and Z_j and D_j are the charge and diffusivity, respectively, in solution of the jth species.

The flux in the "y" direction N_{jyc} represents the flux of the jth species through the coating. Due to the significantly low permeability of the coating to O_2 and ions relative to their corresponding diffusivity in solution, linear gradients of concentrations and the electrostatic potential of the solution are assumed across the coating, and thus N_{jyc} has the form

$$N_{jyc} = \varepsilon_c\left(-D_j \frac{c_{j0} - c_j}{\delta_c} - \frac{z_j D_j F}{RT} \frac{c_{j0} + c_j}{2} \frac{\varphi_0 - \varphi}{\delta_c}\right) \tag{4}$$

where δ_c is coating thickness; c_{j0} and φ_0 are the concentration of the jth species and the solution electrostatic potential at the coating outer surface (facing to soil), respectively; ε_c represents porosity of the coating with $\varepsilon_c = 0$ representing an impermeable coating; and $\varepsilon_c = 1$ represents absence of coating. In the last term on the right side of Equation (4), the concentration in the coating is approximated by the average across the coating or $0.5(c_j+c_{j0})$.

To solve for all system variables, including concentrations of all species and the corrosion potential, the equation of electroneutrality is needed

$$\sum_{1}^{6} z_j c_j = 0 \tag{5}$$

For the system of concern, the effect of ferrous hydroxide precipitation (a mineral reaction) on the crevice corrosion is neglected. Only reversible reactions, such as water dissociation, occur as the homogenous reactions, and the reversible reaction rates (R_j) can be cancelled out when the governing equations for the secondary species are merged into those of the primary species. This treatment has been detailed elsewhere [13,26] and will be shown later in this section.

The surface reactions contributing to R_{sj} in Equation (2) occur only at the steel surface. They are electrochemical half-cell reactions consisting of anodic reaction (iron oxidation) and cathodic reactions (hydrogen

ion reduction, water reduction, and O_2 reduction). Their reaction rates can be converted from their respective current densities following Faraday's law

$$r^{e}_{j,l} = \frac{i_{j,l}}{n_{j,l}F} \tag{6}$$

where l represents Fe, H^+, H_2O, and O_2; each is a key element in the related electrochemical half-cell reaction. n is the number of electrons of charge transfer in an elemental half-cell reaction.

The corrosion or iron oxidation current density (i_{Fe}) is assumed to follow the Tafel equation

$$i_{Fe} = i^{0}_{Feref} 10^{\frac{E_m - \varphi - E^{Eqref}_{Fe}}{b_{Fe}}} \tag{7}$$

where E is crevice potential with respect to an arbitrary reference electrode (in this work the reference electrode is consistently referred to as the saturated $Cu/CuSO_4$ electrode (CSE), which is 0.316 V relative to the standard hydrogen electrode); E_m is E at the mouth where the electrostatic potential is defined as zero for reference; "ref" in either subscript or superscript is a reference condition whereby the corresponding exchange current density i^0, concentration if applicable c_j (j=4,7), and equilibrium potential E^{Eq} are known; and "b" is Tafel slope.

Tafel equations for reductions of hydrogen ion and water, respectively, are

$$i_H = -i^{0}{}_{Href} \frac{c_4}{c_{4ref}} 10^{\frac{-(E_m - \varphi - E^{Eqref}_{H})}{b_H}} \tag{8}$$

and

$$i_{H_2O} = -i^{0}{}_{H_2Oref} 10^{\frac{-(E_m - \varphi - E^{Eqref}_{H_2O})}{b_{H_2O}}} \tag{9}$$

For O_2 reduction, the Tafel equation is

$$i_{O_2} = -i^{0}_{O_2ref} \frac{c_{7s}}{c_{7ref}} 10^{\frac{-(E_m - \varphi - E^{Eqref}_{O_2})}{b_{O_2}}} \tag{10}$$

where c_{7s} is O_2 concentration at the steel surface.

The total surface reaction rate of the jth species, R_{sj}, may be written as

$$R_{sj} = \sum_{l} \nu_{j,l} r^{e}_{j,l} \tag{11}$$

where ν is the stoichiometric coefficient of species j in a relevant reaction, which will be explained later.

For Na^+ and Cl^-, R_{sj}=0. Applying Equation (2) for Na^+ or Cl^- yields

$$\delta_s \frac{\partial c_j}{\partial t} + \frac{\partial}{\partial x}(\delta_s N_{jx}) = -N_{jyc} \tag{12}$$

where j=1 and 2.

Applying Equations (2) and (10) for O_2 yields

$$\delta_s \frac{\partial \bar{c}_7}{\partial t} + \frac{\partial}{\partial x}(\delta_s N_{7x}) = \frac{2D_{O_2}[3m(\pi+2)c_7^0 - 6(m+\pi+m\pi)\bar{c}_7]}{\delta_s(4m+12+\pi m+4\pi)} \tag{13}$$

where the term on the right of the equal sign consists of both O_2 permeation rate through the coating and O_2 reduction rate at the steel surface, $N_{7x} = -D_{O_2}\frac{\partial \bar{c}_7}{\partial x}$, and $\bar{c}_7$ is average O_2 concentration across the crevice gap including the effect of O_2 permeation through the coating. The detailed derivation of Equation (13) can be found elsewhere [26], which considers two-dimensional diffusion of O_2 in the crevice. Unlike other dissolved species in solution, O_2 diffusion is slow relative to its reduction, and thus the O_2 concentration gradient in the "y" direction across the gap should not be neglected.

In Equation (13), c_7^0 is O_2 concentration in soil. $m = \frac{D_{O_2c}/\delta_c}{D_{O_2}/\delta_s}$ and $\pi = \frac{\delta_s}{\beta}10^{\frac{\varphi}{b_{O_2}}}$. m=0 represents an impermeable coating. D_{O2c} is O_2 diffusion coefficient in the coating considering coating porosity, or $D_{O2c} = D_{O2}\varepsilon_c$. β is a constant depending only on the crevice mouth potential.

Applying Equation (2) for hydrogen ion with all reversible reaction rates cancelled out yields

$$\delta_s \frac{\partial}{\partial t}(\sum_3^6 z_j c_j) + \frac{\partial}{\partial x}(\delta_s \sum_3^6 z_j N_{jx}) = -\sum_3^6 z_j N_{jyc} + 2r_{Fe}^e + r_H^e + r_{H_2O}^e + 4r_{O_2}^e \tag{14}$$

where $\nu_{H^+,H^+}=1$, $\nu_{H^+,H_2O}=1$, and $\nu_{H^+,O_2}=4$, which follow the stoichiometric coefficients of hydrogen ion reduction ($H^+ + e^- \rightarrow 0.5H_2$), water reduction ($H_2O + e^- \rightarrow 0.5H_2 + OH^-$) and O_2 reduction ($O_2 + 4H^+ + 4e^- \rightarrow 2H_2O$), respectively. Because Fe^{2+} is treated as a secondary species in this crevice corrosion system, following the stoichiometric coefficient of the equilibrium relation $Fe^{2+} + H_2O \leftrightarrow Fe(OH)_2 + 2H^+$, $\nu_{H^+,Fe}=2$.

Equation (5) may be replaced with

$$\delta_s \frac{\partial}{\partial x}(\sum_1^6 z_j N_{jx}) = -\sum_1^6 z_j N_{jyc} + 2r_{Fe}^e + r_H^e + r_{H_2O}^e + 4r_{O_2}^e \tag{15}$$

2.4. Model initial and boundary conditions

The initial and boundary conditions for solving the model equations are given in Table 1, where only concentrations of the primary species are given with the realization that the concentrations of the secondary species can be calculated from the concentrations of the primary species by using their equilibrium relations [13,26].

In this work, the concentrations of Na^+ and Cl^- at the mouth are given to be greater than their respective values at time zero inside the crevice (initial condition). The boundary conditions at the crevice mouth are constant concentrations for all solution species, and the applied potential at the mouth is fixed at -0.900 V_{CSE}. The boundary conditions at the crevice tip are zero flux for each species.

8. Computational results

The effect of gap variation on the crevice chemistry, corrosion potential, and rate when the coating is impermeable to ions and O_2 has been presented elsewhere [26]. This paper reports the effect of coating permeability to ions, O_2, both, or neither.

3.1. Coating permeable to ions only

Although an intact coating on buried pipes is generally not permeable to ions or CP current, some coatings are considered permeable when deteriorated, such as fusion-bonded epoxy or asphalt. Virtually all coatings have defects, while the sizes of the defects may vary. All coatings deteriorate. Therefore, to a certain degree, every coating has a certain permeability to ions, while for an intact coating, particularly those with very high dielectric resistance, CP current or ion penetration may be considered negligible. When the coating becomes permeable, the quantitative effect of CP penetration through the disbonded coating on the steel corrosion rate is not well understood. It is unclear how much CP is required to protect the steel surface in the coating-disbonded region, or how this CP penetration through the coating interacts with CP from the mouth and how this interaction may affect the steel corrosion rate in the coating-disbonded region. This section attempts to address this issue by modeling.

It is assumed that the potential measured in soil near the coating surface can be approximated to be the same as at the mouth. Although a CP permeable coating is always permeable to O_2, for the scenario being studied in this section, this O_2 permeability is temporally ignored. The combined effect of CP and O_2 penetration through the coating will be discussed in the next section.

It is known that in the presence of CP, the chemistry at the mouth is expected to become alkaline due to formation of hydroxyls from the electrochemical reduction of water. Away from the mouth outside the disbonded region, the chemistry in the soil can be different, particularly when the movement of the ground water in soil is considered. A neutral pH groundwater containing equal Na^+ and Cl^- concentrations is assumed to maintain at the coating outer surface (Table 1), and this chemistry does not vary over time.

Three conditions are compared to understand the effect of CP penetration through the coating on the crevice corrosion: (1) a coating impermeable to ions, which has been investigated elsewhere [26]; (2) a coating with a given ion permeability (coating porosity of 2×10^{-4}); and (3) a coating with a larger ion permeability or at coating porosity of 10^{-3}.

Using the crevice geometry shown in Figure 1, the crevice chemistry, corrosion potential, and current density can be computed. For all computations performed in this work, the transport of Fe^{2+} and $Fe(OH)^+$ through the coating is neglected because (1) Fe^{2+} and $Fe(OH)^+$ have much smaller concentrations than Na^+ in the entire system, and their concentrations at the coating outer surface can be considered to be zero and (2) the presence of CP forces cations to pass through the coating to move into the crevice. With a very low concentration in the coating disbonded region, it is expected that little permeation of these two ions occurs through the coating. Although not shown, model results have proven that with or without considering the transport of these two ions through the coating, nearly exactly the same results were obtained at all times between 0 s and 10^8 s.

Figure 2 shows Na^+ concentration in the crevice at three different times. CP is applied at the crevice mouth. Starting from a higher mouth concentration than that initially inside the crevice, both diffusion and CP-driven migration force Na^+ to move into the crevice from the mouth. When the coating is permeable to CP, the higher Na^+ concentration outside the crevice and the positive potential gradient across the coating from outside to inside of the crevice both drive Na^+ to pass into the crevice through the coating. The Na^+ concentration in the crevice increases over time, as demonstrated by the higher Na^+ concentration at time 10^5 s relative to that initially at time 0 s. At 10^5 s, the Na^+ concentration is greater with a CP permeable coating than with an impermeable coating, and a coating with a higher CP permeability (10^{-3} porosity relative to 10^{-4}) gives a greater Na^+ concentration. The more dramatic changes of the Na^+ concentration at $\frac{x}{\delta_{s0}} = 15$ and 100 with the permeable coatings result from the sharp change of the crevice gap at these two locations. With a narrowed gap (or a smaller solution volume per unit length) between these two locations, for approximately the same total transport flux of Na^+ through the coating, the Na^+ concentration in this region of the crevice increases faster than in the regions with a larger gap (or a greater solution volume per unit length). This is also true within the gap-narrowed region in $\frac{x}{\delta_{s0}} = 5\text{-}6$. In this region close to the mouth, the Na^+ concentration is much more significantly affected by the Na^+ transport from the mouth than across the coating. For the impermeable coating, the increase of Na^+ concentration in the crevice is entirely the result of Na^+ transport from the mouth.

At 10^8 s, when the crevice corrosion reaches steady state, the magnitude of the Na^+ concentration in the three crevices is shown to be in reverse order relative to that at 10^5 s; a higher permeable coating now corresponds to a smaller Na^+ concentration. This phenomenon may be explained as follows. For a coating with a higher CP permeability, the Na^+ concentration in the crevice increases faster initially. However, as the Na^+ concentration in the crevice increases and becomes greater than its concentration outside the coating, a reverse Na^+ concentration gradient is set up across the coating. This leads to a diffusion flux that counters Na^+ migration and tends to push Na^+ out of the crevice through the coating. When the net result is Na^+ leaking out from inside the crevice, the Na^+ concentration in the crevice with a permeable coating still increases due to transport from the mouth, but this increase becomes increasingly slower than in the crevice with an impermeable coating. With Na^+ concentration inside the crevice greater than at the mouth, opposite to its direction of diffusion at earlier times, Na^+ now tends to diffuse out through the mouth. For a crevice with an impermeable coating, eventually the rate of Na^+ pumping in by CP from the mouth (migration) has to dynamically balance the total rate of Na^+ diffusing out for steady state to establish. In a crevice with a permeable coating, steady state can be reached only when Na^+ transport, including migration and diffusion through the mouth, and its transport through the coating are balanced. With the coating leaking out of Na^+, the eventual concentration of Na^+ in the crevice is smaller than in the crevice with an impermeable coating, and the higher the permeability of a coating, the smaller the Na^+ concentration in the crevice.

For the crevice with an impermeable coating, at the locations with dramatic gap changes, the Na^+ concentration has a sharper change. This sharper change of Na^+ concentration was detailed in an earlier paper [26] and assimilated to the effect of flow. The Na^+ concentration gradient (slope of the curve) is proportional to its diffusion flux, analogous to flow velocity. For the same diffusion rate, analogous to flow rate across an edge of a gap-narrowed region, the Na^+ concentration gradient (analogous to flow velocity) is greater in the gap-narrowed region.

Figure 3 shows the variation of Cl^- concentration in the crevice. Its initial distribution in the crevice is uniform irrespective of the coating being permeable to CP. Unlike Na^+, CP draws out Cl^- from inside the crevice through both the mouth and the coating. Countering this driving force, with a higher concentration both at the mouth and outside the coating (or in soil), Cl^- tends to diffuse into the crevice through both the mouth and the coating, similar to Na^+. The balance between the two forces is the net flux of Cl^- entering the crevice. The sharp increase of Cl^- concentration near the mouth suggests that near the mouth Cl^- diffusion is dominant over migration and this dominance decreases over time. This dominance of Cl^- diffusion over migration determines that the Cl^- concentration in the crevice increases over time, irrespective of the magnitude of the coating permeability. At 10^4 s, the Cl^- concentration in the crevice with a more permeable coating is greater. The Cl^- concentration is greater in the regions of narrowed gap, or $\frac{x}{\delta_{s0}} = 15\text{-}100$, than in the regions of larger gap, because the Cl^- concentration in the former region rises faster with a smaller solution volume per length (given a similar diffusion flux of Cl^- through the coating).

As Cl^- continuously diffuses into the crevice both from the mouth and through the coating, its concentration in the crevice increases over time, and the increase in Cl^- concentration in the crevice creates a decrease in its concentration gradient or the driving force for diffusion. When the diffusion flux balances out with the migration flux driven by the potential gradient provided by CP, steady state is established, as shown by the curves at 10^8 s. Because CP tends to draw out Cl^- from inside the crevice, the Cl^- concentration in the crevice cannot surpass its concentration at the mouth or outside the crevice.

Figure 4 shows the pH distribution in the crevice. The pH at the mouth and inside the crevice is uniform at time 0, and it is greater than the pH in soil or at the coating outer surface. Because H^+ carries a positive charge (like Na^+), with CP, H^+ migrates into the crevice both from the mouth and through the coating if permeable. Interestingly, at 10^5 s, the pH in the crevice with a permeable coating is greater than in the crevice with impermeable coating, and the greater the coating permeability, the greater the pH. This counter-intuitive pH distribution results from the increased rates of cathodic reactions at the steel surface, including hydrogen ion and water reductions, which consume hydrogen ions or generate hydroxyls equally. O_2 reduction also generates hydroxyls.

When the coating is permeable to CP, even if the initial chemistry and the boundary conditions are the same as those with an impermeable coating, the initial potential distributions determined for the two different types of coatings are different. Figure 5(a) shows that the potential in the crevice with a permeable coating is more negative,

and the more permeable the coating, the more negative the potential. A more negative potential means greater reduction rates of hydrogen ions and water; both generate OH^- equivalently. When the rate of OH^- generation overbalances the H^+ flux across the coating due to mass transport, the pH in the crevice would be greater with a greater permeable coating.

Figure 4 also shows that at 10^8 s, a reverse order of the pH distributions is shown: the greater the coating permeability, the smaller the pH in the crevice. With time, as the pH in the crevice increases, the diffusion of H^+ across the coating becomes more significant over time. Meanwhile, the potential (as shown by Figure 5(a)) shifts in the more negative direction (less potential gradient across the coating), and the H^+ migration across the coating into the crevice becomes less significant over time. Note that a smaller pH is equivalent to a smaller concentration of OH^-, and the overall H^+ transport into the crevice through the coating is similar to a decrease of OH^- concentration if neutralization is considered to take place instantaneously. This decrease in OH^- concentration by mass transport to the mouth must be balanced by the formation of hydroxyls at the steel surface for the steady-state corrosion to arrive. Due to the net transport of H^+ into the crevice across the coating, at steady state, the pH in a crevice with a higher permeable coating must be lower.

Figure 5(a) shows that the potential in the crevice shifts in the more negative direction when the coating is permeable to CP. Because CP penetration through the coating tends to depress CP penetration from the mouth, compared to the potential peak at time zero with the crevice of impermeable coating, very near the mouth the potential peak with a permeable coating is further squeezed or narrowed. The potential peak with the crevice of impermeable coating is the result of the initial sharp change of the solution chemistry at the mouth. With time, as the chemistry in the crevice becomes smoother, the potential peaks expand and then disappear. Due to the Tafel relation between potential and corrosion current density, the distribution of corrosion current density in Figure 5(b) is similar to that of the crevice potential.

3.2. Coating permeable to either O_2 or ions, both, or neither

Any organic coating (e.g., fusion-bonded epoxy, high density polyethylene (HDPE) and asphalt) used on buried steel pipelines is permeable to O_2. The coating becomes permeable to ions when they deteriorate, and the coating's permeability varies depending on its type. Given a coating porosity of 0.001, the overall ionic permeability through the coating may be treated as 0.1% of its diffusivity in water. Because a coating is more permeable to molecules (such as O_2) than ions, a much larger coating porosity for O_2 is used. This larger porosity will cover O_2 transport through both the deteriorated coating matrix and the still good coating matrix (good coating matrix is often impermeable to ions). The O_2 diffusion coefficient in a new HDPE coating is 1.1×10^{-11} m^2/s. Twenty times this permeability is used for this coating of interest, which yields a permeability of 2.2×10^{-10} m^2/s, equivalent to 11% of O_2 diffusivity in water (1.96×10^{-9} m^2/s) (i.e., the porosity of coating for O_2 is 0.11). The different treatments for coating permeability to ions and O_2 are used for the model computations.

The initial condition for O_2 concentration in the crevice can be the equation used in an earlier work for an impermeable coating [26]. That is

$$\bar{c}_7 = c_7^0 \exp(-\tfrac{x\sqrt{3}}{\delta_{s0}}) \tag{16}$$

For a permeable coating, O_2 diffuses through the coating over time until steady state is reached.

Figure 6 shows the ratio of average O_2 concentration in the crevice to that at the mouth for a coating that is permeable to O_2. At the mouth (x=0), the O_2 concentration ratio should be unity by definition. At time zero, following Equation (16), the O_2 concentration decreases rapidly from the mouth into the crevice. With time, as O_2 permeates through the coating, the O_2 concentration in the crevice increases over time until steady state is reached, shown to be at or greater than 300 s. The O_2 concentration inside the crevice varies with distance due to the variation of crevice gap. Even though the O_2 concentration is affected by the gap variation, the overall O_2 diffusion flux to the steel surface, which is controlled by its diffusion through the coating, is approximately the same irrespective of the gap variation. This O_2 diffusion flux to the steel surface across the crevice solution can be approximated by [29]

$$J_{O_2} = \frac{c_{7c} - c_{7s}}{\delta_s} \approx \frac{3\bar{c}_7}{2\delta_s} \quad (17)$$

where c_{7c} and c_{7s} are oxygen concentrations inside the crevice at the coating and at the steel surface, respectively. The O_2 concentration at the steel surface is assumed to be zero.

Equation (17) suggests that for the same J_{O2}, a larger δ_s corresponds to a greater average O_2 concentration as shown in Figure 6. Near the mouth, O_2 transport is mainly controlled by its diffusion through the mouth.

Figure 7 shows a comparison of (1) steel potential and (2) corrosion current density for the four cases with the penetration of either O_2 or current, neither, or both. At time zero, when no O_2 diffusion through the coating is considered, the initial corrosion potential and current density is only affected by CP penetration through the coating. Thus, the two dark curves without current penetration through the coating overlap, and similarly, the two gray curves with current penetration overlap.

At 10^8 s, the corrosion process reaches steady state. The effect of O_2 diffusion through the coating is clearly demonstrated. With no current penetration through the coating, the steel potential with O_2 diffusion through the coating is more positive and the corrosion current density is greater (dark dashed curve) than if no O_2 diffuses through the coating (dark solid curve). This same effect of O_2 diffusion through the coating also applies when CP current penetrates the coating. From without to with O_2 penetration through the coating, the steel potential shifts in the more positive direction, and the corrosion current density is greater.

By comparing the two conditions (1) neither current nor O_2 permeation through the coating (dark solid curve) and (2) both current and O_2 permeation through the coating (gray dashed curve)), Figure 7 shows that the corrosion current density inside the crevice is smaller for the latter. This result can have significant implications for coating design and for an understanding of the protectiveness of a coating once it disbonds and becomes permeable. Even though a much larger (100 times more) overall porosity of the coating was used for O_2 than for ions, the CP can still adequately suppress the increased corrosion current density by O_2 diffusion through the coating, suggesting that in the field, a permeable coating, when disbonded, can still allow adequate CP current to pass through and protect the steel pipe from corrosion attack, despite O_2 permeation through the coating. The CP penetration through the coating can still be effective, despite a much greater permeability of the coating to O_2 than to ions, because the current penetration can be driven by the potential gradient across the coating, which does not occur with O_2.

Figure 8 shows a comparison of the crevice chemistry for all four cases. The initial conditions are the same, and all curves for the four cases overlap at time zero for each figure. At steady state (10^8 s), the effect of O_2 or/and current penetration through the coating is clearly exhibited. Irrespective of current penetration through the coating, O_2 diffusing through the coating is electrochemically reduced at the steel surface. This reduction of O_2 generates hydroxyls which attract cations such as Na^+ and repel anions such as Cl^-. This effect, superimposed by additional generation of hydroxyls from CP as well as by the potential-driven ionic migration, leads to an increased Na^+ concentration in the crevice, a decreased Cl^- concentration, and correspondingly to an increased crevice pH.

Because the mass transport of any ion through the coating is much slower than through the solution, the pumping effect by CP through the coating is less significant than through the mouth. The chemistry change in the crevice is mainly attributed to the ionic transport from the mouth. Although CP tends to pump Na^+ into the crevice across the coating (controlled by migration), with a higher concentration inside the crevice Na^+ tends to diffuse out across the coating, and this diffusion is more dominant than migration. Thus, a CP-permeable coating functions like a membrane. The Na^+ concentration in the crevice is smaller than if the coating is impermeable to CP. Conversely, the Cl^- concentration in the crevice with a CP permeable coating is greater than in the crevice with an impermeable coating to CP. Due to the decrease in Na^+ concentration, the solution pH in the crevice with a CP-permeable coating is smaller. The interactions of Na^+ concentration, Cl^- concentration and pH have also been discussed elsewhere [5,13,26,30].

9. Conclusions

A comprehensive mathematical model is developed that allows for predicting the evolution of chemistry, corrosion potential, and rate in a crevice of variable gap, mouth chemistry different from that initially in the crevice, and the coating permeable to ions and/or O_2.

CP tends to pump Na^+ into the crevice both from the mouth and through a permeable coating, increasing the solution pH in the crevice and reducing the corrosion rate. Cl^- is conversely drawn out by CP from inside the crevice. In the gap-narrowed regions of the crevice, the change of Na^+ concentration or Cl^- concentration is more drastic due to a smaller solution volume per unit length relative to the regions with a larger gap.

A permeable coating behaves like a membrane. Relative to an impermeable coating, the permeable coating tends to raise the in-crevice Na^+ concentration and pH more rapidly at the beginning of the crevice corrosion, and the more permeable the coating, the more rapid the increase of the Na^+ concentration and pH. When the Na^+ concentration becomes greater in the crevice than at the mouth, it tends to diffuse out through the coating and counter the potential-driven migration, leading to a smaller in-crevice Na^+ concentration over time.

When a coating is permeable to both O_2 and CP current, even if the overall coating porosity to O_2 is set to be 100 times more than that of ions, the CP current penetration through the coating can still be effective in suppressing corrosion raised by O_2 diffusion through the coating. Mechanistically, this results from the potential-driven migration of ions, which does not occur with O_2. Practically, this result suggests that in the field, a permeable coating, when disbonded, still can provide adequate CP current to protect the steel pipe surface from corrosion, despite O_2 permeation through the coating.

Acknowledgments

This work was sponsored by the U.S. Department of Transportation, Pipeline and Hazardous Materials Safety Administration (Mr. James Merritt, Program Manager), under the contract DTPH56-08-T-0003. It was co-funded by Pipeline Research Council International (Mr. Mark Piazza, Senior Program Manager) and CenterPoint Energy, New Orleans, Louisiana (Mr. Rickey Payne, Direct Assessment Manager).

This paper was revised from paper no. 11322, presented at the 2011 NACE International Conference on March 13-17, 2011 in Houston, Texas, U.S.A.

References

41. H. Leidheiser, W. Wang, L. Igetoft, Progress in Organic Coatings 11 (1983) 19-40.
42. C.G. Munger, Corrosion Prevention by Protective Coatings (NACE, 1984) 47-61.
43. J.M. Leeds, Pipe Line & Gas Industries, March (1995) 21-26.
44. M. Meyer, X. Campaignolle, F. Coeuille, M.E.R. Shanahan, "Impact of Aging Processes on Anticorrosion properties of Thick Polymer Coatings for Steel Pipelines," in Proceedings of the Corrosion/2004 Research topical Symposium: Corrosion Modeling for Assessing the Condition of Oil and Gas Pipelines, F. King and J. Beavers (eds.), Houston, TX: NACE/2004, 93-146.
45. F.M. Song, Corrosion 66(9) (2010) 095004.
46. F.M. Song, D.W. Kirk, D.E. Cormack, D. Wong, Materials Performance, 44(4) (2005) 26-29.
47. F.M. Song, D.W. Kirk, D.E. Cormack, D. Wong, Materials Performance, 42(9) (2003) 24-26.
48. F.M. Song, D.W. Kirk, J.W. Graydon, D.E. Cormack, Corrosion 58(12) (2002) 1015-1024.
49. F.M. Song, D.W. Kirk, J.W. Graydon, D.E. Cormack, Corrosion 59(1) (2003) 42-49.
50. F.M. Song, D.A. Jones, D.W. Kirk, Corrosion, 60(2) (2005) 145-154.
51. F.M. Song, N. Sridhar, Corrosion 62(8) (2006) 676-686.
52. F.M. Song, N. Sridhar, Corrosion 62(10) (2006) 873-882.
53. F.M. Song, N. Sridhar, Corrosion Science 50(1) (2008) 70-83.
54. N. Sridhar, D.S. Dunn, M. Seth, 2001, Corrosion 57 (7) 598-613.
55. K.N. Allahar, M.E. Orazem, Corrosion Science 51 (2009) 962-970.
56. M.E. Orazem, D.P. Reimer, C. Qiu, K. Allahar, "Computer Simulations for Cathodic Protection of Pipelines," in Proceedings of the Corrosion/2004 Research Topical Symposium: Corrosion Modeling for

Assessing the Condition of Oil and Gas Pipelines, F. King and J. Beavers (eds.), Houston, TX: NACE/2004, 25-52.
57. R.R. Fessler, A.J. Markworth, R.N. Parkins, Corrosion 39(1) (1983) 20-25.
58. T.R. Jack, G.V. Boven, M. Wilmott, R.L. Sutherby, R.G. Worthingham, MP (8) (1994) 17-21.
59. A. Turnbull, A.T. May, Materials Performance, 22 (1983) 34.
60. J.J. Perdomo, I. Song, Corrosion Science 42 (2000) 1389.
61. M.H. Peterson, T.J. Lennox, Jr., Corrosion 29 (1973) 406.
62. A.C. Toncre, N. Ahmad, Materials Performance 19(6) (1980) 39.
63. M.D. Orton, Materials Performance 24(6) (1985) 17.
64. F. Gan, Z.-W. Sun, G. Sabde, D.-T. Chin, Corrosion 50(10) (1994) 804.
65. R. Brousseau, S. Qian, Corrosion 50(12) (1994) 907-911.
66. F.M. Song, Electrochimica Acta 56 (2011) 6789-6803.
67. F. King, T. Jack, M. Kolar, R. Worthingham, "A Permeable Coating Model for Predicting the Environment at the Pipe Surface under CP-Compatible Coatings," NACE/04, paper no. 04158.
68. F.M. Song, D.W. Kirk, D.E. Cormack, D. Wong, Materials Performance 44 (2005) 26-29.
69. F.M. Song, Corrosion Science 50 (2008) 3287-3295.
70. F.M. Song, Corrosion Science 51 (2009) 2657-2674.

TABLE 1: INITIAL AND BOUNDARY CONDITIONS

Condition	c_1 *(mol/m³)*	c_2 *(mol/m³)*	c_4 *(mol/m³)*	c_7^0 *(mol/m³)*	ϕ *or* $i_{totx} = \sum_1^6 z_j F N_{jx}$ *(V)* *(A/m²)*
Initial	0.3128	0.3128	6.014×10^{-7}	0	
Mouth with CP	3.128	3.128	6.014×10^{-7}	0.2601	ϕ=0 and E_m=-0.9 V_{CSE}
Soil outside coating	3.128	3.128	10^{-4}	0.2601	ϕ=0 and E_m=-0.9 V_{CSE}
Condition	N_{1x} (mol/m²·s)	N_{2x} (mol/m²·s)	$\sum_3^6 z_j N_{jx}$ (mol/m²·s)	N_{2x} (mol/m²·s)	i_{totx} (A/m²)
Crevice tail	0	0	0	0	0

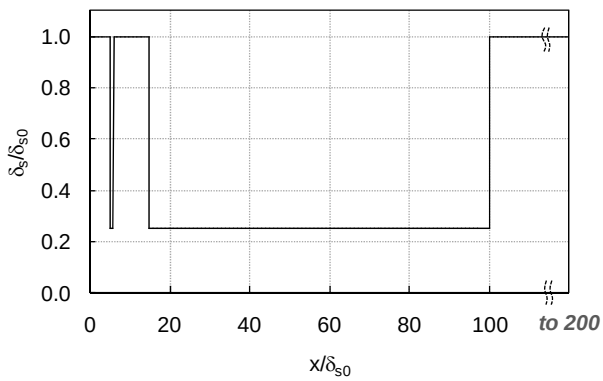

Figure 1. Model crevice gap variation (δ_s) with distance from the mouth into the crevice (x), where δ_{s0} is the gap size at the mouth on the left edge of the crevice.

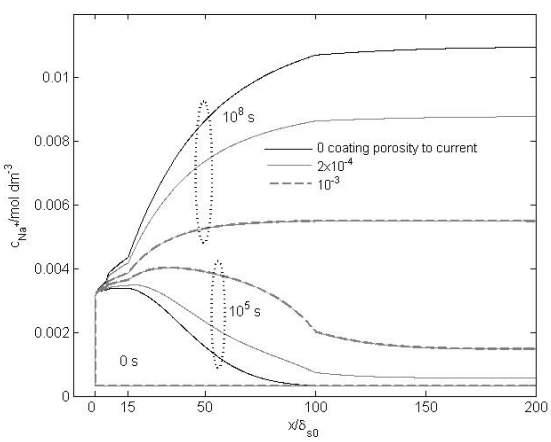

Figure 2. At a fixed mouth potential of -0.9 V_{CSE}, a comparison of computed Na^+ concentrations in a crevice at different times, when the coating has different permeability to current, reflected by different area percentage of pores in the coating.

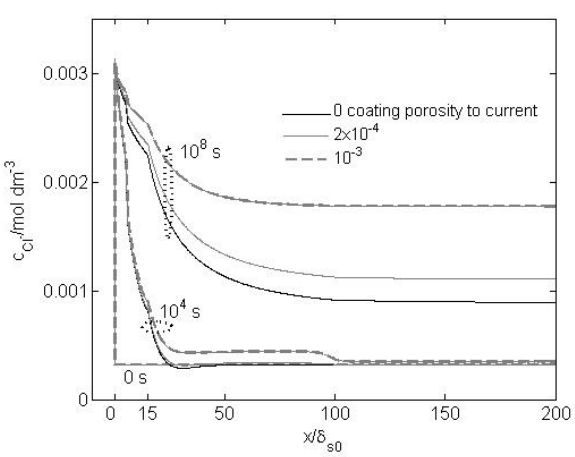

Figure 3. Similar to Figure 2, but the results are for Cl^- concentrations in the crevice.

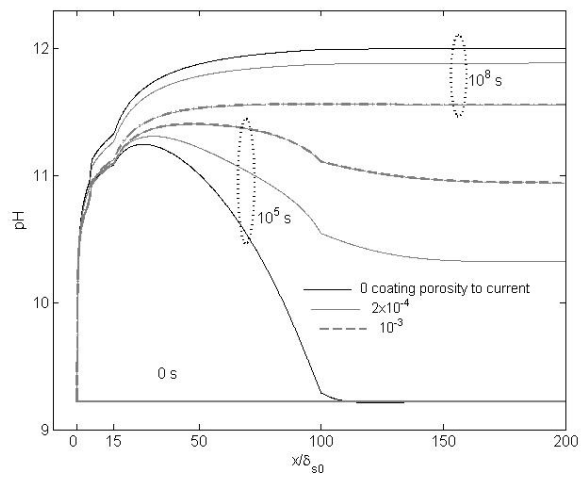

Figure 4. Similar to Figure 2, but the results are for the solution pH in the crevice.

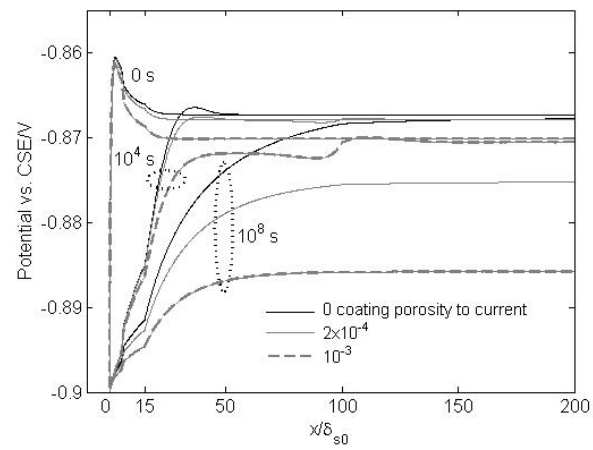

(a)

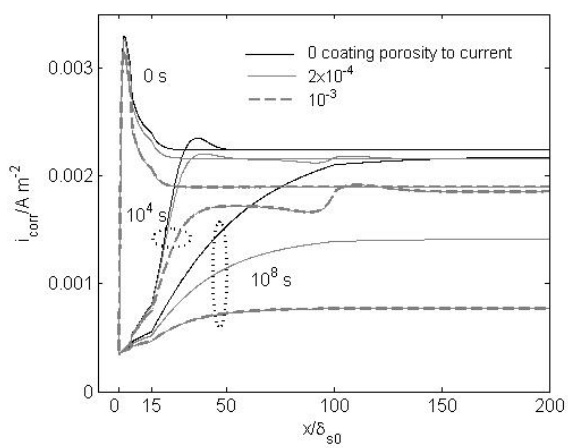

(b)

Figure 5. Similar to Figure 2, but the results are for (a) the crevice potential and (b) crevice corrosion density.

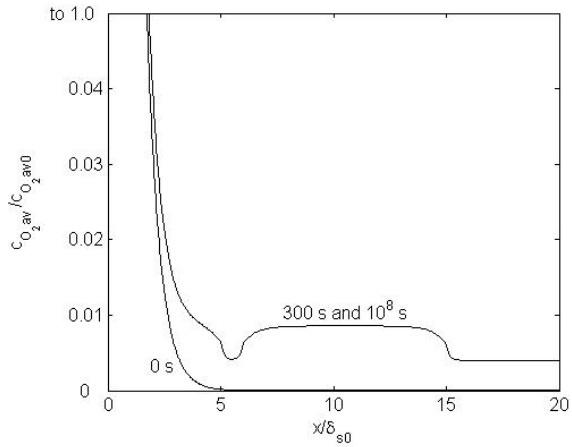

Figure 6. At a fixed mouth potential of -0.9 V_{CSE}, the O_2 concentration in a crevice with a permeable coating to O_2. The concentration ratio at the mouth is 1 by definition.

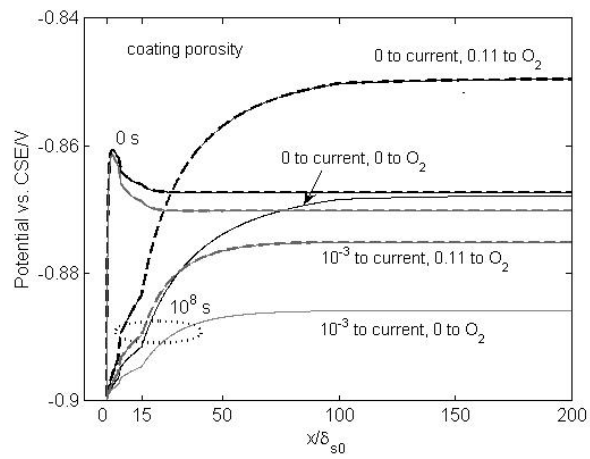

(a)

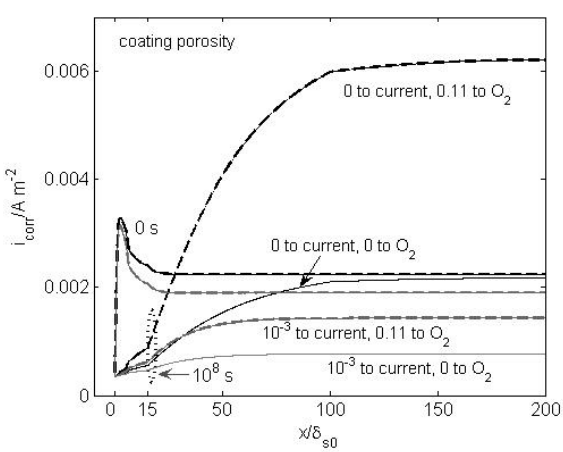

(b)

Figure 7. At a fixed mouth potential of -0.9 V_{CSE}, a comparison of the model results for four cases studied at both the initial and steady-state conditions: (a) crevice potential and (b) corrosion current density.

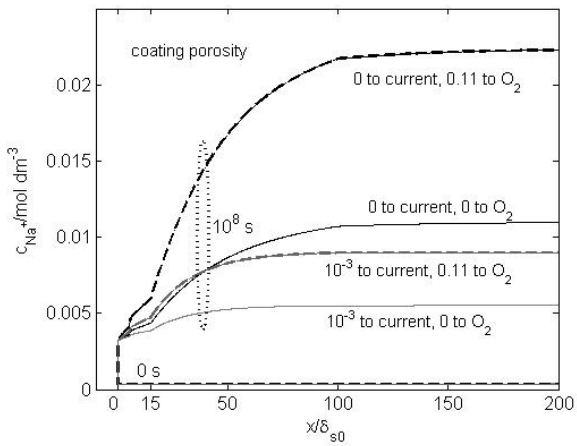

(a)

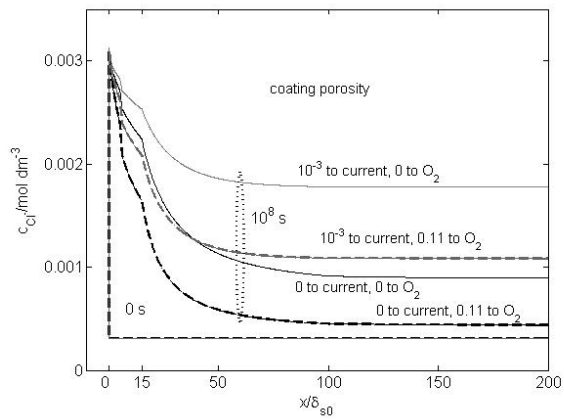

(b)

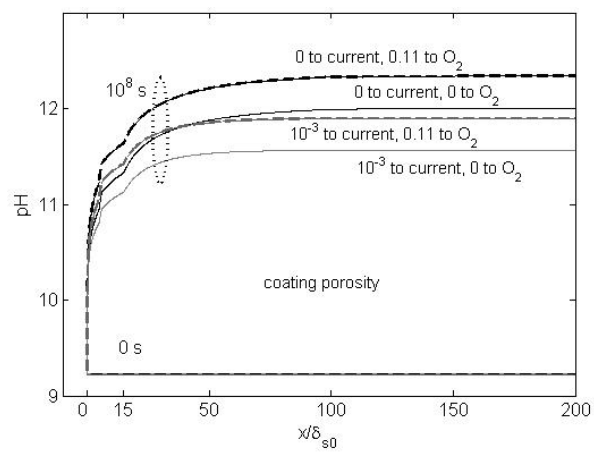

(c)

Figure 8. Similar to Figure 9 but for crevice chemistry: (a) Na^+ concentration, (b) Cl^- concentration, and (c) pH in the crevice.

MS #3

Theoretical investigation into time and dimension scaling for crevice corrosion

ABSTRACT

Geometry scaling for crevice corrosion has been broadly studied, and past studies focus on steady-state analysis for a crevice of uniform gap. The scaling factor has been reported to be L^2/δ_0 (or $L/\sqrt{\delta_0}$) or L/δ_0, where L is crevice length and δ_0 is crevice gap. Time scaling for unsteady-state crevice corrosion has not been reported. For geometry scaling, the underlying fundamentals can be more generally treated by dimension scaling with the scaling variable $x/\sqrt{\delta_0}$, where x is the dimension of a one-dimensional crevice. This paper is aimed at discussing the theory behind dimension and time scaling for a crevice of uniform gap, verifying the scaling theory with model simulation results, and understanding how biased the scaling is when applied to a crevice of variable gap. The scaling theory suggests that geometry scaling for a crevice of uniform gap should follow L^2/δ_0 or $L/\sqrt{\delta_0}$ and time scaling follows t/δ_0, where t is time.

Keywords: A. steel; B. modeling studies, scaling method; C. crevice corrosion, cathodic protection

1. Introduction

The evolution, over time and distance, of the chemistry, corrosion rate, and potential in a crevice can depend upon the crevice geometry, such as the crevice gap and length. In crevice corrosion modeling, the effect of the geometrical parameters may, under some conditions, be combined with the model independent variables, such as time t and distance x, to reduce the number of model variables and potentially alleviate the load of model computations with respect to the various effects of the crevice geometrical parameters and time. One chart plotted with scaling variables can cover information that otherwise must be obtained by multiple charts due to the variation of the crevice geometrical parameters (e.g., length and gap) and time. Geometry scaling has been used for scaling up experiments (crevice length and gap) to overcome challenges with tests associated with extremely small crevice geometries.

A literature review was performed in this work, and the results are summarized. For the active metal surfaces, geometrical scaling for a crack of uniform width (or for a crevice of uniform gap) was reported to follow L^2/δ_0, where L is the entire crack (or crevice) length and δ_0 is half-crack width (or crevice gap) [1-2]. The scaling factor L^2/δ_0 was derived based on modeling analysis under steady-state conditions. The scaling works when a crack has a uniform width (or a crevice has a uniform gap); the fluxes at the crack or crevice tip as boundary conditions, as is often the case, can be treated as zero; and the reactions in solution are fast or can be treated as being in thermodynamic equilibrium. For a passive metal surface, analysis of experimental data also confirmed the scaling factor of L^2/δ_0 [3]. Modeling and experimental results yielded a scaling factor L_p^2/δ_0 for passive metals, where L_p is the distance from the mouth to the location where active corrosion occurs [4-6]. Experimental results obtained with crevice gaps at or greater than 0.1 mm exhibited a scaling factor of L_p/δ_0 [6], explained to be applicable when the passive current density is much smaller than the active current density. Recent experimental results obtained from so-called "rigorously controlled" tight crevices (gaps as small as 7 μm) confirmed a slightly different scaling factor: L_{crit}^2/δ_0 in a Ni/H_2SO_4 crevice system, where L_{crit} is the distance between the crevice mouth and the location of peak active current density [7]. It was also found that this scaling factor was invalid when the crevice-gap-to-length ratio exceeded 0.02 [7-8].

Geometry scaling for corrosion in a crevice of constant gap has been studied broadly, but time scaling for crevice potential and chemistry under unsteady-state conditions has never been reported. In addition, the underlying fundamentals of geometry scaling can be more broadly explored through dimension scaling, whereas past geometry scaling focused only on the reaction terms in the mass transport equations [1-2]. This work aims at investigating both dimension scaling and time scaling for crevice corrosion of steel undergoing active dissolution as one case, and transient active and passive dissolution as another. The effect on the dimension and time scaling of crevice gap variation over distance was also studied.

2. *Scaling theory for crevice corrosion*

For a dilute solution containing multiple species in a one-dimensional crevice, mass transport for an arbitrary species in the solution numbered by i may be written as

$$\delta_s \frac{\partial c_i}{\partial t} + \frac{\partial}{\partial x}(\delta_s N_{ix}) + N_{iyc} = \delta_s R_i + R_{si} \tag{1}$$

where c_i is concentration in solution of the ith species; R_i is total net volumetric production rate (after consumption deducted) of the ith species; R_{si} is the total surface reaction rate of the ith species including corrosion reactions; δ_s is gap size, which may vary with distance x; subscript x refers to the x direction in the crevice geometry; subscript yc refers to the y direction across the coating. Figure 1a shows an example crevice to be used in this study. The crevice may form when the coating on a steel pipe surface disbonds from a large holiday (or mouth), as seen in Figure 1a on the left edge of the crevice.

In Equation (1), N_{ix} is the flux of the ith species and can be expressed by

$$N_i = -D_i\left(\frac{\partial c_i}{\partial x} - \frac{z_i F}{RT} c_i \frac{\partial \varphi}{\partial x}\right) \tag{2}$$

where D_i and z_i are, respectively, diffusion coefficient and charge of the ith species; F, R, and T are, respectively, Faraday's constant, universal gas constant, and temperature; φ is the electrostatic potential of the solution.

Due to the significantly low permeability of the coating relative to that of a liquid solution, a linear concentration gradient and a linear gradient of the electrostatic potential of the solution may be assumed across the coating. Thus, N_{iyc} has the form

$$N_{iyc} = \varepsilon_c\left(-D_i \frac{c_{i0} - c_i}{\delta_c} - \frac{z_i D_i F}{RT} \frac{c_{i0} + c_i}{2} \frac{\varphi_0 - \varphi}{\delta_c}\right) \tag{3}$$

where δ_c is coating thickness; c_{i0} and φ_0 are concentration of the ith species and the solution electrostatic potential at the coating outer surface, respectively. In the last term on the right side of Equation (3), the concentration in the coating is approximated by the average across the coating, or $0.5(c_i+c_{i0})$. ε_c represents porosity of the coating, with $\varepsilon_c = 0$ representing an impermeable coating; $\varepsilon_c = 1$ representing the absence of coating. The pores are assumed to be uniformly distributed in the coating.

Equations (1) and (2) may alternatively be written, respectively, as

$$\frac{\partial c_i}{\partial (t/\delta_s)} + \delta_s \frac{\partial N_{ix}}{\partial x} = \delta_s R_i + R_{si} - N_{iyc} - N_{ix} \frac{\partial \delta_s}{\partial x} \tag{4}$$

and

$$\delta_s \frac{\partial N_{ix}}{\partial x} = \left[-D_i \frac{\partial^2 c_i}{\partial (x/\sqrt{\delta_{s0}})^2} - \frac{z_i D_i F}{RT} \frac{\partial}{\partial (x/\sqrt{\delta_{s0}})}\left(c_i \frac{\partial \varphi}{\partial (x/\sqrt{\delta_{s0}})}\right)\right](\delta_s \delta_{s0}^{-1}) \tag{5}$$

The total net production rate of the ith species in Equation (1) or (4), R_i, can result from homogenous reactions and/or precipitation reactions in solution, and these reactions can be reversible or irreversible. For a reversible reaction such as water (H_2O) dissociation, others have stated R_i has no effect on scaling [1-2]. This noneffect will also be explained in this work. For an irreversible reaction, such as carbon dioxide hydration if present, its rate R_i can make the dimension scaling invalid; this will also be explained later.

The surface reactions contributing to R_{si} in Equation (1) or (4) can occur only at the metal surface. They may consist of an anodic reaction and cathodic reactions. The rate of such a half-cell reaction can be converted from its corresponding current density following Faraday's law

$$r^{e}_{i,l} = \frac{i_{i,l}}{n_{i,l}F}$$
(6)

where subscript l represents the half-cell reaction involving the ith species; n is the number of electrons of charge transfer in the half-cell reaction.

If the reference point for the electrostatic potential of the solution is set at the crevice mouth so that φ=0 there, the metal potential measured in the crevice with respect to an arbitrary reference electrode is $E=E_m-\varphi$, where E_m is E at the crevice mouth. Throughout this work, a saturated $Cu/CuSO_4$ electrode (CSE) is used as the reference electrode, which is 0.316 V relative to the standard hydrogen electrode. CSE is most commonly used in the field to measure potentials of buried or immersed steel pipelines.

For steel corrosion in an aqueous solution, the anodic reaction is iron oxidation and the common cathodic reactions are hydrogen ion (H^+) reduction, H_2O reduction, and oxygen (O_2) reduction. The Tafel equation can be used to express the current density of a half-cell reaction, which for iron oxidation is

$$i_{Fe} = i^{0}_{Feref} 10^{\frac{E_m-\varphi-E^{Eqref}_{Fe}}{b_{Fe}}} \tag{7}$$

where ref in either subscript or superscript is referred to as a reference condition where the corresponding exchange current density i^0, concentration c_i if involved, and equilibrium potential E^{Eq} are known; b is Tafel slope; i_{Fe} is anodic or corrosion current density.

When the steel is in passive state due to exposure in a solution with a high pH, a constant passive current density may be used for i_{Fe} to replace Equation (7). This will be described in the results when steel passivity is considered.

For reductions of H^+ and H_2O, their Tafel equations are, respectively,

$$i_H = -i^{0}_{Href} \frac{c_{H^+}}{c_{H^+ref}} 10^{\frac{-(E_m-\varphi-E^{Eqref}_{H})}{b_H}} \tag{8}$$

and

$$i_{H_2O} = -i^{0}_{H_2Oref} 10^{\frac{-(E_m-\varphi-E^{Eqref}_{H_2O})}{b_{H_2O}}} \tag{9}$$

The O_2 reduction current density can be expressed by

$$i_{O_2} = -i^{0}_{O_2ref} \frac{c_{O_2s}}{c_{O_2ref}} 10^{\frac{-(E_m-\varphi-E^{Eqref}_{O_2})}{b_{O_2}}} = \frac{-3D_{O_2}\pi\bar{c}_{O_2}}{\delta_s(\pi+3)} \tag{10}$$

where c_{O2s} and $\bar{c}_{o_2}$ are O_2 concentration at the steel surface and its average across the gap, respectively. The detailed derivation of Equation (10) can be found elsewhere [9-13], which considers two-dimensional diffusion of O_2 in the crevice. Unlike other dissolved species in solution, O_2 diffusion is slow relative to its reduction, and its concentration gradient in the y direction across the gap should not be neglected. In Equation (10), $\pi = \frac{\delta_s}{\beta} 10^{\frac{\varphi}{b_{O_2}}}$ and β is a constant depending only on the crevice mouth potential.

The total surface reaction rate of the ith species, R_{si}, may be written as

$$R_{si} = \sum_{l} \nu_{i,l} r^{e}_{i,l} \tag{11}$$

where $\nu_{i,l}$ is the stoichiometric coefficient of a related surface reaction involving species i. An example will be demonstrated in the next section.

R_{si} and N_{iyc} in Equation (4) are only functions of concentration and potential, not an explicit function of t and δ_s, except for i_{O2}. Equations (4) and (5) suggest that for a crevice of uniform gap ($d\delta_s/dx=0$ and $\delta_s\delta_{s0}^{-1}=1$), in a deaerated condition ($i_{O2}=0$), the time t and distance x can be scaled, respectively, as $\frac{t}{\delta_{s0}}$ and $\frac{x}{\sqrt{\delta_{s0}}}$ (treated as new variables to replace t and x, respectively) and still yield the same results. Scaling x to $\frac{x}{\sqrt{\delta_{s0}}}$ implies that the geometry scaling factor, L^2/δ_{s0}, is theoretically valid with a few exceptions.

The dimension scaling $\frac{x}{\sqrt{\delta_{s0}}}$ can fail when the crevice gap is not uniform and the non-uniformity has a significant effect on the crevice corrosion process. The scaling can also fail when the mass transport cannot be treated as being one dimensional (as with the case of O_2). When irreversible homogeneous or precipitation reactions in the crevice cannot be ignored, the dimension scaling can also fail because δ_s and R_i are tied together in Equation (4). The failure of dimension scaling for a crevice of non-uniform gap may imply that dimension scaling, initially valid with a crevice of uniform gap, may become invalid over time when the crevice gap changes due to metal depletion from corrosion and/or due to precipitation of solid reaction products.

The initial condition is not related to either dimension scaling or time scaling. As for boundary conditions, a fixed concentration, a fixed potential, or a zero flux does not affect either dimension scaling or time scaling. When a flux boundary condition is not zero, such as at a crack or crevice tip, by theory the dimension scaling is not valid. In reality, the tip boundary generally has little effect on the mass transport due to the much smaller area of the tip relative to the crack walls [1]. The effect of tip boundary on scaling can be practically neglected if the flux is not zero but not significant.

3. Scaling theory demonstrated with specific crevice corrosion

The crevice corrosion that is of interest in this work is schematically shown in Figure 1. It is assumed that the substrate steel surface is exposed to a dilute aerated sodium chloride solution under a disbonded coating with a large holiday on the left (crevice mouth). This solution simulates soil water and contains the following dissolved species: $\underline{Na^+}$ --(1), $\underline{Cl^-}$ --(2), Fe^{2+} --(3), $\underline{H^+}$ --(4), OH^- --(5), $Fe(OH)^+$ --(6), $\underline{O_2}$ --(7), $\underline{H_2(aq)}$ --(8), $\underline{Fe(OH)_2}$ --(9) and $\underline{H_2O}$ --(10). The underlined species are defined as the primary species. Their concentrations can either be given, such as species 1, 2 and 4, or known, such as species 8-10. The concentrations of the secondary species, or species 3, 5 and 6, can be calculated from the concentrations of the primary species through their equilibrium relations.

Table 1 shows the solution chemistry at the mouth (only the primary species), which is set to be different from that initially in the crevice, with the latter more dilute and having a lower pH. It is assumed that the solution in the crevice is saturated by the sparsely soluble ferrous hydroxide, and the effect of the homogeneous ferrous ion oxidation on the crevice corrosion can be neglected by justifications given elsewhere [10,14].

Two crevice corrosion scenarios are considered: (1) uniform crevice gap and (2) gap varying with distance. By properly scaling the crevice length, the modeling results will be compared. All parameters used for the modeling, including diffusivity, exchange current density, and Tafel slope, can be found elsewhere [10]. The modeling condition is 25 °C and the total pressure is 1 atm.

For a crevice with a uniform gap shown in Figure 1a ($d\delta_s/dx=0$ and $\delta_s = \delta_{s0}$), applying Equation (4) for Na^+ yields

$$\frac{\partial c_1}{\partial(t/\delta_s)} + \delta_s \frac{\partial N_{1x}}{\partial x} = -N_{1yc} \tag{12}$$

where N_{1yc} does not contain δ_s. Following Equations (4-5), both time scaling and dimension scaling ($\frac{t}{\delta_{s0}}$ and $\frac{x}{\sqrt{\delta_{s0}}}$) are applicable to Na^+. Likewise, the scaling also applies to Cl^-. With no gap involved, the scaling also applies to the equation of electroneutrality ($\sum_{j=1}^{6} z_j c_j = 0$) as a governing equation.

Applying Equation (4) for O_2 yields

$$\delta_s \frac{\partial \bar{c}_7}{\partial t} + \frac{\partial}{\partial x}(\delta_s N_{7x}) = \frac{2D_{O_2}[3m(\pi+2)c_7^0 - 6(m+\pi+m\pi)\bar{c}_7]}{\delta_s(4m+12+\pi m+4\pi)} \tag{13}$$

where the term on the right of the equal sign consists of the O_2 permeation rate through the coating and the O_2 reduction rate at the steel surface. $N_{7x} = -D_{O_2}\frac{\partial \bar{c}_7}{\partial x}$, and c_7^0 and $\bar{c}_7$ are, respectively, O_2 concentration in soil and its average across the gap including the effect of O_2 permeation through the coating. $m = \frac{D_{O_2c}/\delta_c}{D_{O_2}/\delta_s}$, and D_{O2c} is O_2 diffusion coefficient in the coating considering the coating porosity, or $D_{O2c} = D_{O2}\varepsilon_c$. m=0 represents an impermeable coating.

Although the O_2 permeation rate through the coating is not a function of δ_s, the O_2 reduction rate is a function of δ_s, as shown by Equation (10). This leads to the dependence on δ_s of the term on the right hand side of Equation (13). Due to this dependence on δ_s, dimension scaling should not theoretically apply to Equation (13) or to the mass transport of O_2 in the crevice. Fortunately, O_2 can only exist in the crevice very near the mouth and its overall effect on the scaling for the entire crevice is insignificant [9,10,13]. For that reason, the effect on dimension scaling by O_2 can be neglected as a first approximation; this effect will be discussed only when the effect becomes obvious.

Applying Equation (4) for H^+ yields

$$\frac{\partial}{\partial(t/\delta_s)}\left(\sum_3^6 z_j c_j\right) + \frac{\partial}{\partial x}\left(\delta_s \sum_3^6 z_j N_{jx}\right) = -\sum_3^6 z_j N_{jyc} + (2r_{Fe}^e + r_H^e + r_{H_2O}^e + 4r_{O_2}^e) \tag{14}$$

where all associated reversible reaction rates are cancelled out. The coefficients to r_l^e with subscript l=Fe, H, H_2O, and O_2 are reaction stoichiometric coefficients for H^+. ν_{H^+,H^+}=1, ν_{H^+,H_2O}=1, and ν_{H^+,O_2}=4 follow, respectively, the stoichiometric coefficients of the H^+ reduction ($H^+ + e^- \rightarrow 0.5H_2$), H_2O reduction ($H_2O + e^- \rightarrow 0.5H_2 + OH^-$) and O_2 reduction ($O_2 + 4H^+ + 4e^- \rightarrow 2H_2O$). Because Fe^{2+} is a secondary species defined in this system, following the stoichiometric coefficient of the equilibrium relation $Fe^{2+} + H_2O \leftrightarrow Fe(OH)_2 + 2H^+$, $\nu_{H^+,Fe}$=2. The stoichiometric coefficients are discussed elsewhere [9,10].

In Equation (14), N_{jyc} (j=3-6) and r_l^e (subscript l=Fe, H and H_2O) do not contain δ_s. Thus, for a deaerated condition with $r_{O_2}^e = 0$, both time scaling and dimension scaling ($\frac{t}{\delta_{s0}}$ and $\frac{x}{\sqrt{\delta_{s0}}}$) are completely applicable to H^+. For the aerated condition, dimension scaling does not fully apply to O_2, because $r_{O_2}^e$ contains δ_s. However, as mentioned earlier, the effect of O_2 on dimension scaling only occurs near the mouth and has an insignificant effect on the overall crevice scaling.

For a crevice of variable gap (δ_s varies with x), an equivalent uniform gap δ_{se} to account for the varying gap will be defined in the next section. With no irreversible reaction associated with Na^+, applying δ_{se} and Equation (4) for Na^+ yields

$$\frac{\partial c_1}{\partial(t/\delta_{se})} + \delta_{se}\frac{\partial N_{1x}}{\partial x} = -\frac{\delta_{se}}{\delta_s}N_{1yc} - N_{1x}\frac{\delta_{se}}{\delta_s}\frac{\partial \delta_s}{\partial x} \quad (15)$$

If the coating is impermeable, Equation (15) becomes

$$\frac{\partial c_1}{\partial(t/\delta_{se})} + \delta_{se}\frac{\partial N_{1x}}{\partial x} = -N_{1x}\frac{\delta_{se}}{\delta_s}\frac{\partial \delta_s}{\partial x} \quad (16)$$

The term on the right hand side of Equation (16) is analogous to an irreversible reaction source term. When this term is zero, both time and dimension scaling would apply. Otherwise, this term is equivalent to generating Na^+ in the system if it has a positive value. Conversely, this term would be equivalent to consuming Na^+ if it has a negative value.

4. Computational results and discussion

Three crevices of different gaps are investigated to understand and verify the dimension- and time-scaling method. Two of the crevices have uniform gaps as shown in Figure 1(a): one gap is δ_{s0} and the other is $\delta_{s0}/4$. The third crevice has a variable gap shown in Figure 1(b), where the gap $\delta_s=\delta_{s0}$, except at x=5-6 and 15-100, where $\delta_s=\delta_{s0}/4$. In solving the model equations, the commercial software code COMSOL 3.5a was used as was done elsewhere [9,10].

To maintain the same total scaling length $\frac{L}{\sqrt{\delta_s}}$ for the two crevices of uniform gaps with a gap ratio of four, the total length of the crevice with the larger gap, L_L, is set to be twice the length of the smaller gap, L_S (or $L_L=2L_S$). For the crevice of variable gap, its scaling-equivalent total length is $L_v = \sum_i \Delta L_i \sqrt{\frac{\delta_{s0}}{\delta_{sj}}}$ relative to the crevices of uniform gaps.

When $L_V=200\delta_{s0}$, the equivalent length for the crevice with a uniform gap of δ_{s0} is $L_L=243\delta_{s0}$ (or $L_L=1.215L_V$). The equivalent length for the crevice with a uniform gap of $\delta_{s0}/4$ follows $L_S=121.5\delta_{s0}$. For the crevice of variable gap, to satisfy its scaling length, its equivalent gap δ_{se} relative to the crevice with the larger uniform gap is $\delta_{se} = (\frac{L_V}{L_L})^2\delta_{s0} = 0.6774\delta_{s0}$.

Following the mass transport equations (Equations (4-5)), to maintain a constant scaling time $\frac{t}{\delta_s}$, a smaller crevice gap requires a smaller time to retain the same crevice condition. The time needed for the crevice with a smaller uniform gap should be only one-quarter of the time for the crevice of a larger uniform gap, or $t_S=0.25t_L$. For the variable crevice, the equivalent time is $t_v = \frac{\delta_{se}}{\delta_{s0}}t_L = 0.6774t_L$.

These crevice dimensions are used in the model computations. The initial and boundary conditions used for all three crevices are the same. They are given in Table 1. For any given crevice, the Na^+ and Cl^- concentrations at the mouth are equal and each is 10 times its value in the initial condition. The pH at the mouth is the same as its initial value. Two conditions, one with substantial cathodic protection (CP) and the other with negligible CP, are examined next.

4.1. Mouth potential at -0.9 V_{CSE} (significant CP)

Figure 2 is a scaling plot showing Na^+ concentration computed for different times for the three crevices. In this figure, the x coordinate is plotted as scaling distance $\frac{x}{\sqrt{\delta_{se}}}$, where δ_{se} is the equivalent gap applicable to all three crevices. Next to each curve, the scale time $\frac{t}{\delta_{se}}$ is labeled. For the crevice of uniform and larger gap with $\delta_{se}=\delta_{s0}=0.5$ mm, the time scales at 0, 2×10^8, 2×10^9, 2×10^{10}, and 2×10^{11} s/m correspond with actual times of 0, 10^5, 10^6, 10^7, and 10^8 s, respectively. For the crevice with a uniform but smaller gap at 0.5/4 mm, the actual times correspond to a

quarter the above actual times. Likewise, for the crevice of variable gap, the same scale time represents 0.6774 multiplied by those actual times.

For the two crevices with uniform gaps, their Na^+ concentrations overlap for each of the same scale times. They are, however, different from the Na^+ concentration in the crevice of variable gap. This difference is greatest at the intermediate times, such as 2×10^{10} s/m. At steady state (e.g., at the scale time of 2×10^{11} s/m), this difference in Na^+ concentration is smaller but still obvious.

The model results verify that for crevices of uniform gaps, both time scaling and dimension scaling are valid, while for the crevice of variable gap, the scaling method is not valid.

Figure 2 shows that starting from the same initial concentration, prior to or at the scale time of 2×10^{8} s/m, the Na^+ concentration in the crevice of variable gap increases faster and is greater than in the crevices of uniform gaps. This result is attributed to the term on the right hand of Equation (16), which is analogous to a "reaction" source term. Initially, both the concentration-driven diffusion flux and the voltage-driven migration flux of Na^+ are greater than zero. When the gap decreases at the scale distance ($\frac{x}{\sqrt{\delta_{se}}}$) about 0.4 $m^{0.5}$, the right-hand term of Equation (16) is greater than zero, like creating Na^+ and increasing the local Na^+ concentration. Thus, the Na^+ concentration in the gap-narrowed region ($\frac{x}{\sqrt{\delta_{se}}}$=0.4~1.5 $m^{0.5}$) is greater than in the crevices of uniform gaps.

As the Na^+ transport passes the location of the last gap change (gap expansion) at $\frac{x}{\sqrt{\delta_{se}}}$=1.5 $m^{0.5}$, the gap expansion behaves as consuming Na^+ and the Na^+ concentration becomes smaller than in the crevices of uniform gaps. With increasing time, this effect of gap expansion on Na^+ concentration increases. At the scale time of 2×10^{9} s/m, the Na^+ concentration in nearly the entire crevice of variable gap becomes smaller than in the crevices of uniform gaps, and this difference is even greater at 2×10^{10} s/m.

This difference, however, shrinks as steady state is approached because the value of the "reaction" source term becomes smaller and eventually becomes zero at steady state. At steady state, the Na^+ flux is zero and the "reaction" term becomes zero. Thus, Equation (16) has the same form as the Na^+ transport equation for crevices of uniform gaps, and close results are expected between the crevice of variable gap and crevices of uniform gaps.

At the scale time 2×10^{11} s/m (steady state for Na^+ transport), the Na^+ concentration in the crevice of variable gap is still different from that in the crevices of uniform gaps because, for H^+, its flux at steady state is not zero across the crevice and affects the Na^+ concentration distribution in the crevice. In the gap-narrowed region, the Na^+ concentration gradient is greater than in the regions with a larger gap. An analogy to flow was used to describe this effect [10]. The diffusion rate (analogous to flow rate) is the same across the edges of the gap-narrowed region, but the diffusion flux of Na^+ (analogous to flow velocity) can change significantly, reflected by the slope of the curve in Figure 2.

Figure 3 shows a comparison of the pHs predicted for the three crevices. The curves for the two crevices of uniform gaps overlap for each scale time, while they are different from the corresponding curves with the crevice of variable gap except at time zero. At time zero, the same initial conditions were given for all three crevices set by the model.

The variation of solution pH can be evaluated based on the variation of Na^+ concentration. As detailed elsewhere for such an evaluation [9-10], in the presence of CP, a higher Na^+ concentration corresponds to a lower Cl^- concentration; their difference in charge, which is positive, has to be balanced by hydroxyls; and a higher pH results.

Figure 4 shows (1) crevice potentials and (2) corrosion current densities predicted for the three crevices. In general, the curves with the two crevices of uniform gaps approximately overlap for each scale time except very near the mouth. This discrepancy near the mouth is small and results from the presence of O_2 in the crevice. The O_2 exists only near the mouth, and its mass transport equation cannot be scaled in the same way as other dissolved species. This difference in dimension scaling with respect to O_2 was briefly discussed in the previous section and

will be examined in more detail in the next section. The two curves for the crevices of uniform gaps are clearly different from those in the crevice of variable gap, and this difference increases over time. This, again, suggests that dimension scaling does not apply to the crevice of variable gap.

4.2. Mouth potential at -0.8071 V_{CSE} (negligible CP)

This is a condition that was previously determined to have negligible CP [10], or nearly zero external current flowing into the crevice through the mouth.

Figure 5 shows Na^+ concentrations in the three crevices at scale times of 0, 2×10^7, 2×10^9, and 2×10^{11} s/m. With the same initial condition, the Na^+ concentration at time zero is the same for all three crevices. At the mouth, the Na^+ concentration is 10 times that initially inside the crevice. Steady state is reached at the scale time of 2×10^9 s/m (the results overlap that at 2×10^{11} s/m).

For all scale times, the Na^+ concentrations in the crevices of uniform gaps overlap each other, suggesting that both time scaling and dimension scaling apply to crevices of uniform gaps. By contrast, the Na^+ concentration in the crevice of variable gap differs from that in the crevices of uniform gaps and this difference initially increases over time and then decreases. At steady state, this difference becomes small.

Figure 6(a) shows the pH in the three crevices, which is the same both at the mouth and initially in each crevice. The pHs in the two crevices of uniform gaps overlap for each scale time and these pHs are slightly different from that in the crevice of variable gap. This difference is greatest at the intermediate times. Figure 6(b) is an expansion of Figure 6(a) near the mouth. The pH in the two crevices of uniform gaps is different near the mouth but merges deeper into the crevices. This discrepancy results from O_2 in the crevice, which exists only near the mouth and cannot be scaled in the same way as other dissolved species. If O_2 is absent, Figure 6(c) shows that for each scale time, the pHs in the two crevices of uniform gaps fully overlap, although they are still different from the pH in the crevice of variable gap. This is totally attributed to the gap variation along the crevice.

Figure 7(a) shows O_2 concentration at steady state in the crevice. The discrepancy in O_2 concentration in the two crevices of uniform gaps is obvious, implying inapplicability of dimension scaling for O_2 Concentration.

Earlier work [9-10] shows that O_2 is present only near the mouth and steady state can be achieved rapidly. When the coating is impermeable to O_2, Equation (13) for O_2 in a crevice of uniform gap at steady state may be written as

$$\frac{\partial^2 \bar{c}_7}{\partial (x/\delta_s)^2} = \frac{-3\pi \bar{c}_7}{3+\pi} \approx -3\bar{c}_7 \tag{17}$$

Derivation of Equation (17) can be found elsewhere [13]. Equation (17) suggests that O_2 concentration should be properly scaled as x/δ_s, not $x/\delta_s^{0.5}$. By scaling with x/δ_s, Figure 7(b) shows that all curves in the three crevices are merged as one curve, although for the crevice of variable gap, this overlap is a coincidence because O_2 diffusion from the mouth cannot reach the location of the first variation of the gap. Otherwise, the overlap with O_2 concentration could not occur with the crevice of variable gap.

Figure 8(a) shows the crevice potentials at the scale times of 0 and 2×10^{11} s/m. The potentials in the two crevices of uniform gaps approximately overlap except near the mouth. These potentials are slightly different from the potential in the crevice of variable gap. Figure 8(b) is a blowup of Figure 8(a), only near the mouth. The small difference in potential between the two crevices of uniform gaps is more clearly seen for scale time zero, but it disappears at the scale time of 2×10^{11} s/m. This small difference at time zero results from the fact that O_2 mass transport cannot be scaled in the same way as other concentrations. If O_2 is absent, Figure 8(c) shows that the potentials in the two crevices of uniform gaps fully overlap. The difference in potential between the crevices of uniform gaps and the crevice of variable gap is attributed to gap variation, suggesting again that the scaling method is not applicable to a crevice of variable gap.

Figure 9 shows the computed corrosion current densities in the three crevices. Similar to Figure 8, the difference between the two crevices of uniform gaps occurs very near the mouth and it results from the presence of

O_2 in the system. The difference in corrosion current density between the crevices of uniform gaps and the crevice of variable gap is attributed to gap variation.

4.3. Consideration of steel passivity

It has been argued that when the crevice solution pH is high, passive film may develop and corrosion slows down. Solely for the purpose of investigating crevice scaling, a pH of 10.5 is set in this model as the boundary that separates the steel active and passive regions. In reality, this boundary can vary and depends on many factors, which are beyond the scope of this work. In both active and passive states for steel, Tafel equations are assumed to apply for all cathodic reactions, while the Tafel equation is only used in the active region for steel dissolution. When a local solution pH is greater than 10.5, a constant passive current density on steel at 10^{-3} A/m^2 is used for this theoretical investigation. For all calculations to follow, only the two crevices of uniform gaps are considered. The concentrations at the mouth are set to be the same as those in the initial condition. A cathodic potential of -0.900 V_{CSE} is fixed at the mouth. Under those conditions, the model is used to investigate whether time scaling and dimension scaling still work when the steel surface experiences transitions between active and passive states.

Figure 10 is a scaling plot showing (1) Na^+ and (2) Cl^- concentrations at different times computed for the two crevices of uniform gaps. For each scale time, the Na^+ or Cl^- concentrations obtained from the two crevices overlap, proving that both time scaling and dimension scaling are still valid.

Figure 11 shows the scaling plot for pH. All curves obtained for the two crevices overlap for the same scale time. Where the pH exceeds 10.5, the corrosion current density is exhibited as a flat line in Figure 12(a), set by the model.

Figure 12(b) shows the scaling plot for crevice potential. For the same scale time, the potentials in the two crevices overlap, proving again that both time scaling and dimension scaling are valid when a steel surface experiences active and passive transitions.

For crevice corrosion of passive alloys, by theory the geometry scaling factor should be L^2/δ_{s0} because at the crevice tip all fluxes are zero, not either L_p at the active-passive transition potential or L_c at the peak potential as others reported [6-7]. Because the length of the active pitting area is often much smaller than the crevice total length L and the pitting current density is much smaller than the passive current density, it is possible that the scaling length of either L_p or L_c can work, while L_c is probably more reasonable. At $x=L_c$, with a peak potential the total current is zero, approximately satisfying the zero total flux boundary condition for potential—one of the zero flux boundary conditions required for dimension scaling. It was shown experimentally that the scaling with L_p or L_c works only within a limited range of conditions [7].

5. Conclusions

A general theory of dimension scaling and time scaling for crevice corrosion is presented. By theory, the geometry scaling factor should be L^2/δ_0 (or $L/\sqrt{\delta_0}$) because the fluxes at the crevice tip are zero. L is crevice total length and δ_0 is crevice gap. The time scaling factor is t/δ_0, where t is time.

Modeling was performed for two crevices of uniform gaps with a fixed value of $L/\sqrt{\delta_0}$. The model simulation was performed for steel corrosion in a crevice formed when a coating disbands from the steel surface. For a steel surface experiencing either active dissolution or transient active and passive dissolution, the model results confirm the validity of the time scaling and dimension scaling methods.

Dimension scaling has limitations. It may fail if the volumetric reactions are irreversible and the rates cannot be neglected, if the crevice gap varies with distance, or if the crevice corrosion cannot be treated as being one dimensional, or the flux at the boundary is not zero and can have a significant effect on the mass transport in the crevice.

Geometry scaling and time scaling of crevice corrosion can be used to scale experiments or reduce model computations when broad ranges of the effects of crevice geometry and time on crevice corrosion are studied.

Acknowledgement

This work was sponsored by the U.S. Department of Transportation, Pipeline and Hazardous Materials Safety Administration (Mr. James Merritt, Program Manager), under the contract DTPH56-08-T-0003. It was cofunded by Pipeline Research Council International (Mr. Mark Piazza, Senior Program Manager) and CenterPoint Energy, New Orleans, Louisiana (Mr. Rickey Payne, Direct Assessment Manager).

References

[1] A. Turnbull and J.G.N. Thomas, J. Electrochem. Soc. 129 (1982) 1412-1422.
[2] M.J. Psaila-Dombrowski, "Modeling of Crack and Crevice Chemistry in Light Water Environments," Massachusetts Institute of Technology, Doctor of Philosophy in Nuclear Engineering Dissertation. Boston, Massachusetts (1990).
[3] G.F. Kennell and R.W. Evitts, Electrochimica Acta 54 (2009) 4696-4703.
[4] J.C. Walton, Corrosion Science 30 (1990) 915-928.
[5] P.O. Gartland, "Modeling of Crevice Processes," Topical Research Symposia Proceedings, National Association of Corrosion Engineers: Houston, Texas (1996) 311-339.
[6] Y. Xu and H.W. Pickering, J. Electrochem. Soc. 140 (1993) 658-668.
[7] J.S. Lee, M.L. Reed, and R.G. Kelly, J. Electrochem. Soc. 151 (2004) B423-433.
[8] M.I. Abdulsalam, and H.W. Pickering, Corrosion Science 41 (1999) 351-372.
[9] F.M. Song and N. Sridhar, Corrosion Science 50(1) (2008) 70-83.
[10] F.M. Song, Electrochimica Acta, 56 (2011) 6789-6803.
[11] F.M. Song, D.W. Kirk, J.W. Graydon, and D.E. Cormack, Corrosion 58 (2002) 1015-1024.
[12] F.M. Song, D.W. Kirk, J.W. Graydon, and D.E. Cormack, Corrosion 59 (2003) 42-49.
[13] F.M. Song, Corrosion Science 50 (2008) 3287-3295.
[14] F.M. Song, D.W. Kirk, J.W. Graydon, and D.E. Cormack, Corrosion 58 (2002) 145-155.

TABLE 1
INITIAL AND BOUNDARY CONDITIONS

Condition	c_1 *(mol/m³)*	c_2 *(mol/m³)*	c_4 *(mol/m³)*	c_7^0 *(mol/m³)*	ϕ *or* i_{totx} $=\sum_1^6 z_j F N_{jx}$ *(V) (A/m²)*
Initial	0.3128	0.3128	6.014×10^{-7}	0	
Mouth with CP	3.128	3.128	6.014×10^{-7}	0.2601	$\phi=0$
Mouth with no CP	3.128	3.128	6.014×10^{-7}	0.2601	$i_{totx}=0$
Condition	N_{1x} (mol/m²·s)	N_{2x} (mol/m²·s)	$\sum_3^6 z_j N_{jx}$ (mol/m²·s)	N_{7x} (mol/m²·s)	i_{totx} (A/m²)
Crevice tail	0	0	0	0	0

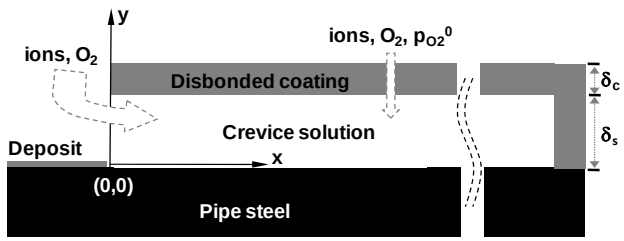

(a)

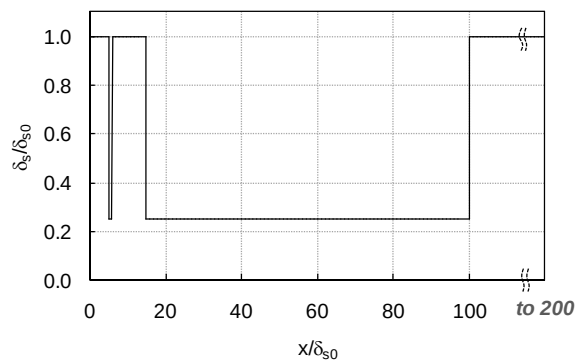

(b)

Figure 1. Model crevice geometry showing the coordinates and dimensions of the crevice and transport of CP current and O_2 into the crevice through the disbonded coating.

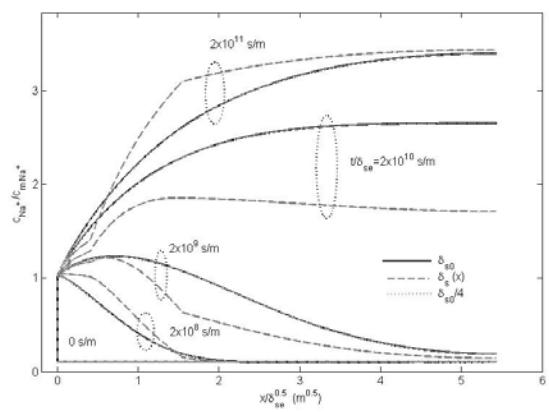

Figure 2. At a fixed mouth potential of -0.9 V_{CSE}, a scaling plot is shown for a comparison of Na^+ concentrations in the three crevices at different times: constant gap of δ_{s0} in Figure 1a (black solid lines), variable gap vs. x of Figure 1b or $\delta_s(x)_b$ (gray solid lines), and constant but reduced to a quarter of the gap or $\delta_{s0}/4$ (gray broken lines).

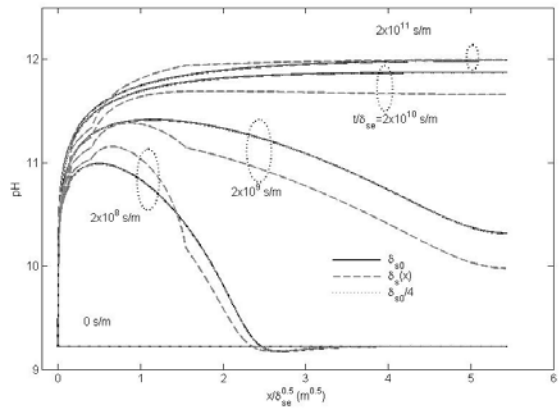

Figure 3. Similar to Figure 2, but here the scaling plot is for a comparison of crevice pH.

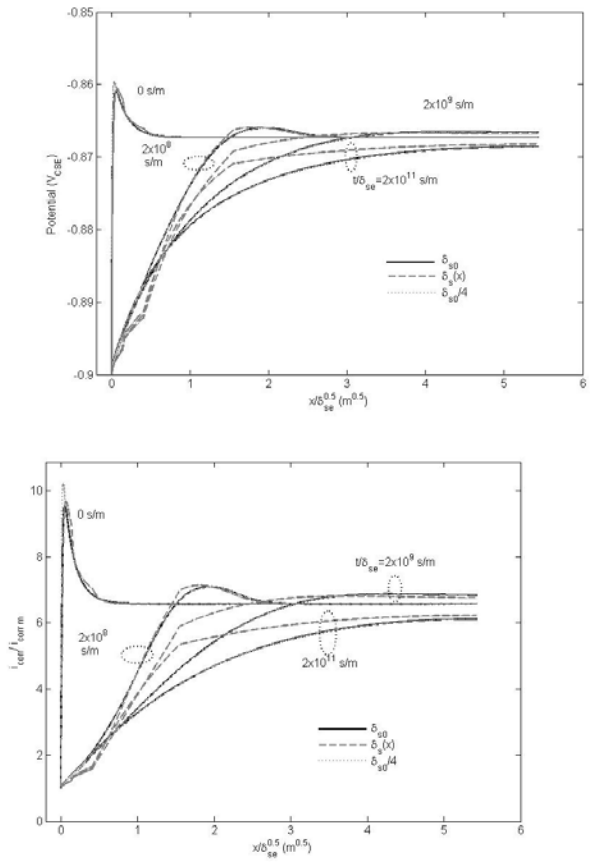

(a) (b)

Figure 4. Similar to Figure 2, but here the scaling plot is for a comparison of (a) crevice potential and (b) corrosion current density.

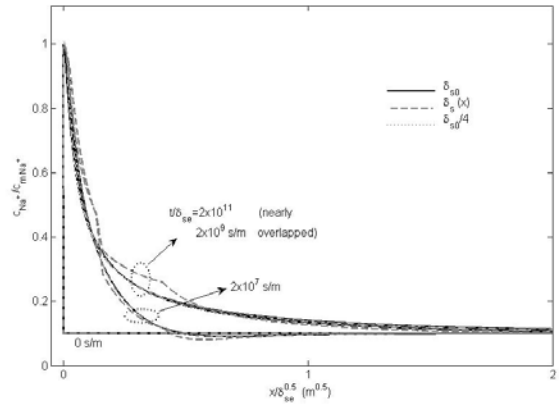

Figure 5. Similar to Figure 3, but here for Na^+ concentration at the mouth potential of -0.8071 V_{CSE}.

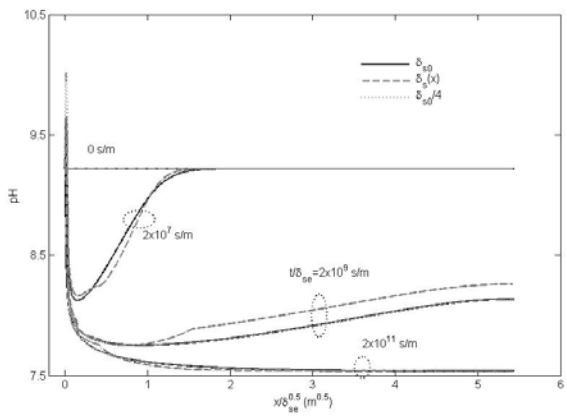

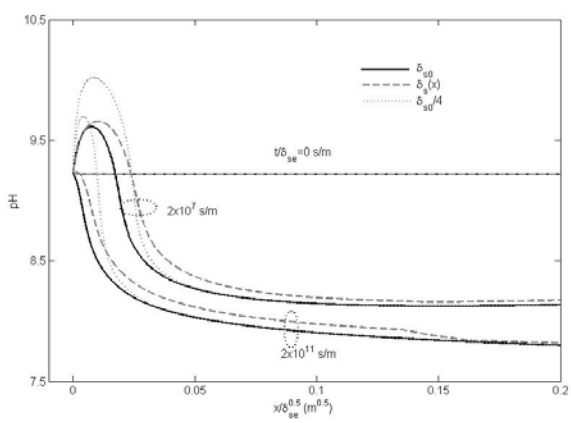

(a) (b)

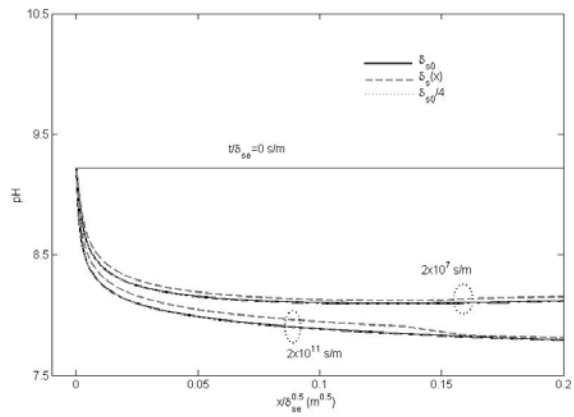

(c)

Figure 6. Similar to Figure 3, but here for crevice pHs at the mouth potential of -0.8071 V_{CSE}: (a) in the entire crevice, (b) near the mouth, and (c) same as (b), but when O_2 is absent.

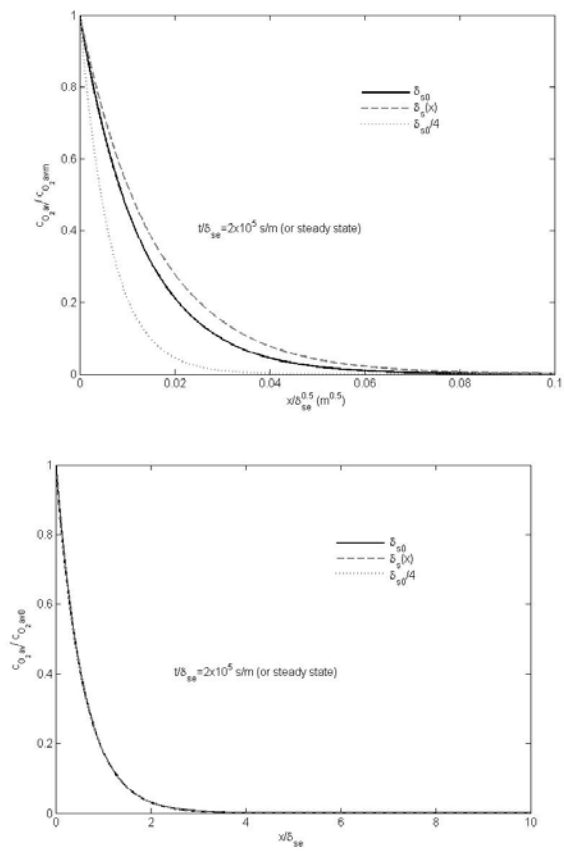

(a) (b)

Figure 7. Similar to Figure 3, but here for O_2 concentration at the mouth potential of -0.8071 V_{CSE}: (a) scaled distance by $x/\delta_s^{0.5}$ and (b) scaled distance by x/δ_s.

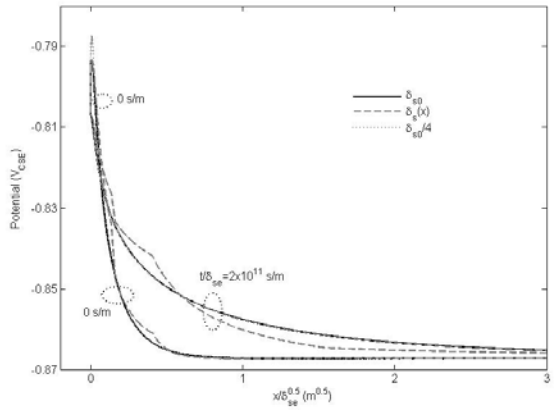

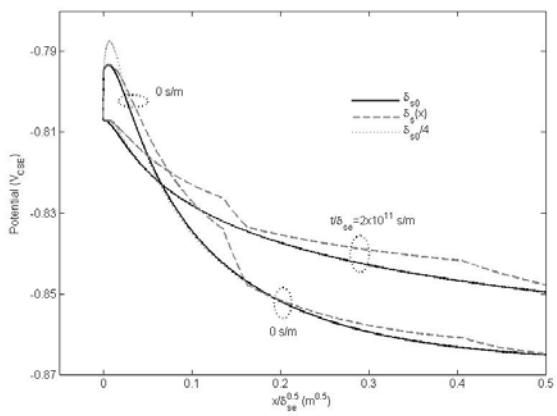

(a) (b)

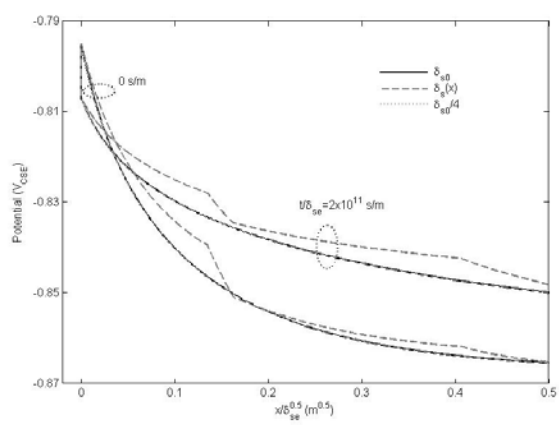

(c)

Figure 8. Similar to Figure 3, but here for crevice potentials at the mouth potential of -0.8071 V_{CSE}: (a) in the entire crevice, (b) near the mouth, and (c) same as (b), but when O_2 is absent.

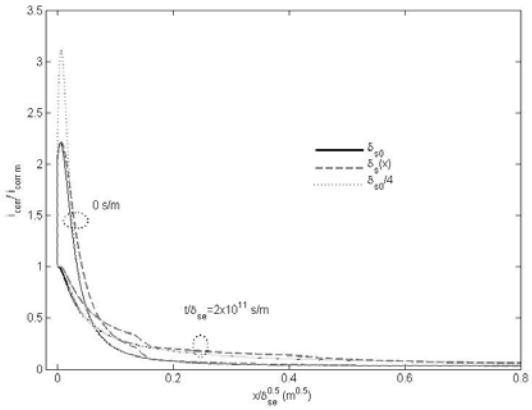

Figure 9. Similar to Figure 9(a), but for corrosion current densities.

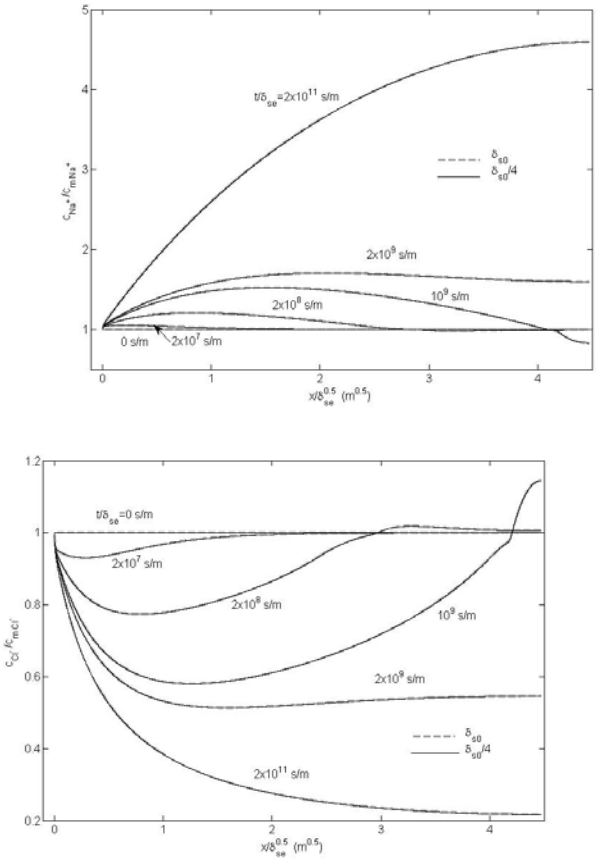

Figure 10. At a fixed mouth potential of -0.9 V_{CSE}, a scaling plot for (a) Na^+ and (b) Cl^- concentrations in the two crevices of uniform gaps: constant gap of δ_{s0} in Figure 1a (gray broken lines) and constant but reduced to a quarter of the gap or $\delta_{s0}/4$ (black solid lines).

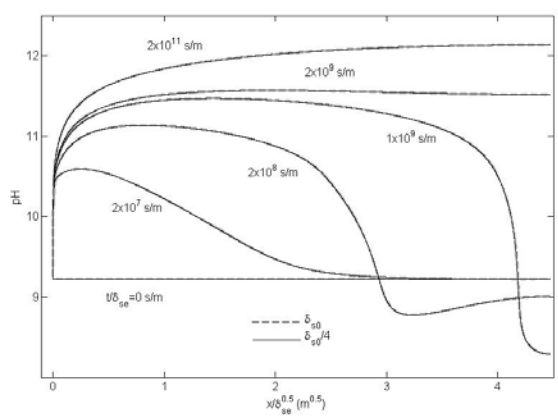

Figure 11. Similar to Figure 10, but the scaling plot is for solution pH in the two crevices of uniform gaps.

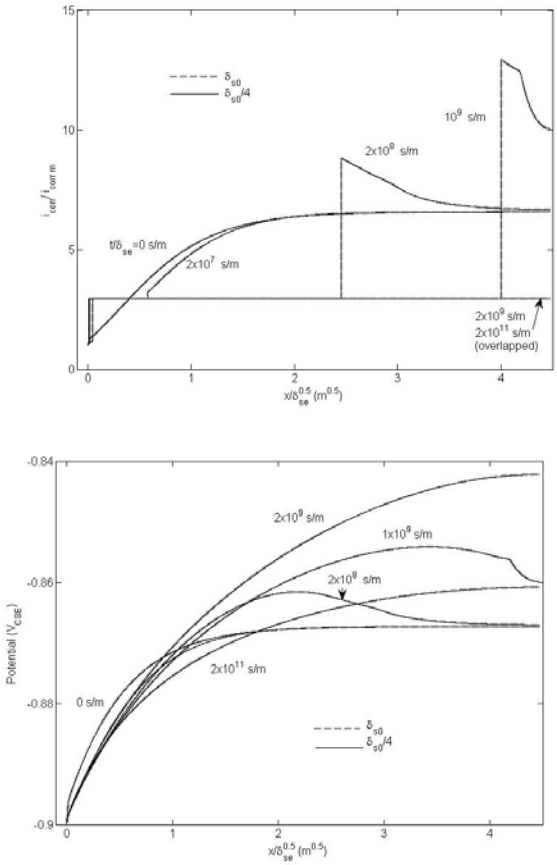

Figure 12. Similar to Figure 10, but the scaling plot is for (a) corrosion current density and (b) crevice potential in the two crevices of uniform gaps.

MS #4

A MODEL DEVELOPED TO PREDICT THE INTERNAL CORROSION RATES OF WET AND DRY GAS PIPELINES

ABSTRACT

A comprehensive mathematical model is developed to predict internal corrosion rates in pipelines that carry wet or dry natural gas. A significant difference in corrosion between the two types of gas pipelines is that for dry gas pipelines, a thin stagnant solution layer due to water condensation may be sitting on the pipe surface and can quickly go saturated. A precipitate film then forms and thickens over time, which reduces the corrosion rate. In wet gas pipelines, water may be constantly present on the pipe surface and the bulk solution chemistry may not change over time. Due to continuous mass exchange between the boundary layer and the bulk solution, precipitate may or may not be able to form.

By coupling mass transport, chemical and electrochemical reactions, possible film growth and the displacement of the moving metal-solution interface due to metal dissolution, a fundamental model is developed. This model can allow for predicting the variation of solution chemistry over time, the formation and growth of a precipitate film and the corrosion rate under various operating conditions, including temperature, pressure and gas composition. Following a presentation of the fundamentals of the model, a validation of the model is provided and key model results are reported and discussed.

Keywords: corrosion, carbon dioxide, modeling, steel, pipeline, oil and gas

INTRODUCTION

Significant research has been performed in the area of CO_2 corrosion for oil and gas production systems.[1-27] It considers a large volume of liquid water flowing inside the pipe and the liquid often contains concentrated salts. This same condition can also exist in wet gas pipelines, such as gathering lines. Even though production or wet gas system are significantly different from a dry gas system often referred to as transmission or distribution lines, the models developed for the former system are frequently used to predict the corrosion rate in the latter system. Models developed specifically for the latter system are lacking. For dry gas systems, the presence of liquid water is an infrequent event. When it occurs due to condensation, the water film may be thin and may not initially contain salts. Such a thin film may not flow along the pipe surface.

The models for the production systems are often developed first for the worst case scenarios, and the effect of film growth (at temperatures often above 60 °C) is then included by some by multiplying a correction factor to the rate.[3,7] In the current industrial practice in America, for dry gas systems, this correction factor is commonly neglected and thus, the corrosion rate predicted from these worst case models can be excessively conservative (greater than the actual rates), particularly if the water film is thin. With a limited thickness, the solution layer at the steel surface can quickly be saturated by corrosion products and the precipitate then builds up to limit mass transport required for the corrosion process to proceed.

This effect of water film thickness on the pipe internal corrosion rate in dry gas systems has been modeled and significant effect was shown[28]. Such a model was developed for proprietary use and an examination of the model appears to show flaws in the equations of boundary conditions defined for the model. When the solution is treated to be dilute, the fundamental equations for either dry or wet gas pipelines are the same, although the boundary conditions at the bulk solution boundary for wet gas or at the gas-liquid interface for dry gas differ. The model to be described in this work is one based on fundamentals, validated with broad lab and/or field data, and can provide a broad examination of the effect of limited water volume.

This paper reports a general CO_2 corrosion rate model that is developed broadly applicable to both oil and gas production and transportation systems. For oil and gas production system and for wet gas pipe system, the corrosion mechanisms and the model needed for corrosion rate prediction are the same while they are treated differently when applied for dry gas pipe system. The difference between wet and dry gas pipe systems is only at the boundary opposite to the steel surface (in Figure 1, $y=\delta_s$). For the dry gas system, this boundary can be the gas-liquid interface, where no mass transfer takes place with the ionic and some dissolved species, such as carbonic acid. By contrast, for a flowing system with a significant amount of solution, water may be constantly flowing in the system with the chemistry at the interface between the bulk solution and the boundary layer consistently refreshed. This difference in boundary condition can be easily handled in a computer code when the model equations are solved. A switch may be used to turn on only the desired boundary condition and automatically turn off the undesired one.

THE MATHEMATICAL MODEL

General Equations of Mass Transport

For a porous medium with a dilute solution containing multiple species, mass balance for an arbitrary species in the solution numbered by i may be written as:

$$\frac{\partial(\varepsilon c_i)}{\partial t} + \nabla \cdot N_i = R_i \tag{1}$$

where ε is porosity or pore volume fraction of the aqueous system. R_i is the total net volumetric production rate (after consumption deducted) of the ith species.

The flux of the ith species in the dilute solution, N_i, may be written as:

$$N_i = -D_i \varepsilon \tau (\nabla \cdot c_i - \frac{z_i F}{RT} c_i \nabla \phi) = -D_i \varepsilon^{\frac{3}{2}} (\nabla \cdot c_i - \frac{z_i F}{RT} c_i \nabla \phi) \tag{2}$$

where D_i and z_i are respectively diffusion coefficient in solution and charge of the ith species, τ is tortuosity approximated by $\varepsilon^{0.5}$. F, R and T are respectively Faraday's constant, universal gas constant and temperature. ϕ is the electrostatic potential of solution.

Volumetric Reaction Rates

In Equation (1), the total net production rate of the ith species, R_i, can result from three types of reactions.

<u>Homogenous Reactions</u>: For such a reaction numbered by h, in the form of:

$$\sum_i \nu_{i_r,h} A_{i_r} \leftrightarrow \sum_i \nu_{i_p,h} A_{i_p} \tag{3}$$

where the subscripts r and p represent reactant and product respectively, the individual volumetric reaction rate in the aqueous solution may be written as:[29]

$$r_h = \varepsilon (k_{h_f} \prod_i c_i^{\nu_{i_r,h}} - k_{h_b} \prod_i c_i^{\nu_{i_p,h}}) \tag{4}$$

where k_{h_f} and k_{h_b} are the forward and backward reaction rate constants respectively.

The net production rate of the ith species for all reactions associated with it is:

$$R_{i,h} = \sum_h \nu_{i,h} r_h \tag{5}$$

Practically, when a reaction goes fast in both directions relative to other reactions, such a reaction may be considered in chemical equilibrium. Only the slow or irreversible reactions (they are the rate-controlling reactions) need to be accounted for when treating Equation (5).

Mineral (Precipitation) Reactions: For such a reaction numbered by m, in the form of:

$$\sum_i \nu_{i_r,m} A_{i_r} \leftrightarrow \sum_i \nu_{i_s,m} A_{i_s} \,, \tag{6}$$

where subscript "m" means mineral, and subscript "s" means dissolved solution species, the individual volumetric reaction rate converted from the surface reaction rate may be written as:

$$r_m = A_m (k_{m_f} \prod_i c_i^{\nu_{i_r,m}} - k_{m_b} \prod_i c_i^{\nu_{i_s,m}}) \tag{7}$$

where A_m is the interfacial surface area of the solid.

If the solid volume fraction of the mth precipitate is defined as ε_m, its variation with time follows:[29]

$$\frac{\partial \varepsilon_m}{\partial t} = \overline{V}_m r_m \tag{8}$$

where $\overline{V}_m$ is molar volume of the mth precipitate.

Porosity is related to the solid volume fractions by:

$$\varepsilon = 1 - \sum_m \varepsilon_m \tag{9}$$

The total net production rate of all the mineral reactions involving the ith species may be written as:

$$R_{i,m} = \sum_m \nu_{i,m} r_m \tag{10}$$

Boundary Reaction Rates

The reactions at the steel surface are the electrochemical reactions. The rates of these electrochemical reactions are connected to boundary conditions. They are not part of R_i in Equation (1).

For such a reaction numbered by e, in the form of:

$$\sum_i \nu_{i_r,e} M_{i_r}^{z_{i,r}} \leftrightarrow \sum_i \nu_{i_p,e} M_{i_p}^{z_{i,p}} + n_e e^- \tag{11}$$

(where z_i represents charge carried by the metallic species M_i), the following charge balance must be met:

$$\sum_e \nu_{i,e} z_i - n_e = 0 \tag{12}$$

where $\nu_{i,e}$ and n_e are respectively the stoichiometric coefficient of the ith species and the number of electrons transferred during the eth electrochemical half-cell reaction.

The total net production rate of all the electrochemical reactions involving the ith species is:

$$R_{i,e} = s_e \sum_e \nu_{i,e} r_{i,e} = s_e \sum_e \frac{\nu_{i,e} i_{i,e}}{n_e F} \tag{13}$$

where s_e is the interfacial area of the electrochemically active surface in the system.

For the system of interest here, the electrochemical reactions occur only at the metal surface and thus they are applicable only when the boundary conditions are defined. The current density of the eth electrochemical reaction may be written by the Butler-Volmer equation as:[30]

$$i_e = i^0_{e_ref} \left(\prod_i \left(\frac{c_i}{c_{i_ref}}\right)^{\nu_{i_r,e}} \exp\left(\frac{\alpha_{a_e} F}{RT} \eta_e\right) - \prod_i \left(\frac{c_i}{c_{i_ref}}\right)^{\nu_{i_p,j}} \exp\left(-\frac{\alpha_{c_e} F}{RT} \eta_e\right) \right. \tag{14}$$

or simplified by the Tafel equations to be specified later when the boundary conditions are specifically described.

In Equation (14), the over-potential is often expressed by:[29,30]

$$\eta_e = \psi - \phi_s - U_{e_ref} \tag{15}$$

where ψ and ϕ_s are respectively the electrostatic potentials of the metal and the solution at the metal-solution interface. Their difference $\psi - \phi_s$ is the electrode potential measured with the reference electrode placed very near the metal surface, or,

$$E_s = \psi - \phi_s \tag{16}$$

where E_s is electrode potential measured by a reference electrode placed in solution at the steel surface.

When the reference electrode is placed in solution but not at the steel surface, the electrode potential measured relative to that at the steel surface is the difference: ϕ-ϕ_s. Thus,

$$E = \psi - \phi \tag{16a}$$

where E is electrode potential measured by a reference electrode placed in an arbitrary location in solution, where the local electrostatic potential of the solution is ϕ.

U_{e_ref} in Equation (15) can be treated as electrode potential at a reference condition corresponding to the exchange current density $i^0_{j_ref}$ at the concentration of the ith species c_{i_ref}. U_{e_ref} can also be treated as the equilibrium potential when i_0 and c_i are referred to as those measured in a given condition of the same system.

When there is no external current flowing to and from the metal surface, the electrode potential is the free corrosion potential or the open circuit potential, a case that is of particular interest here, or

$$E_s = E_{corr} \tag{17}$$

where E_{corr} is the open circuit potential of the same system.

Mass Transport Equations for the CO_2 Corrosion System

For pipeline internal corrosion with the solution containing dissolved CO_2, O_2 and NaCl, if the solution primary species are chosen arbitrarily as underlined below:

$\underline{Na^+}$ --(1), $\underline{Cl^-}$ --(2), $\underline{Fe^{2+}}$ --(3), $\underline{H^+}$ --(4), OH^- --(5), $FeOH^+$ --(6), $\underline{CO_2(aq)}$ --(7), $\underline{O_2(aq)}$ --(8), $\underline{CO_3^{2-}}$ --(9), HCO_3^+ --(10), H_2CO_3 ---(11), $FeHCO_3^+$ --(12), $H_2(aq)$ --(13), H_2O --(14), Fe --(15), $FeCO_3(s)$ --(16), $Fe(OH)_2(s)$ --(17)

the concentrations of the secondary species (not underlined) can be determined by those of the primary species following their equilibrium relations given in Appendix A and summarized in Table 1 (the very left column). Appendix A lists all the reversible and irreversible homogeneous and heterogeneous reactions involved in this system, including all the electrochemical reactions. The equilibrium relations for the reversible reactions and the kinetic rates for the irreversible reactions are also given. The concentrations of the mineral or solid species and the solution species of H_2 (aq) and H_2O are treated to be constant.

In this corrosion system, it is known that some reactions proceed much faster than others and these fast reactions can be considered in equilibrium. For instance, relative to CO_2 hydration (a slow step in the CO_2 chain reactions), the dissociation reactions of carbonic acid to bicarbonate and carbonate ions can be considered to be reversible.

By cancelling out the reversible reaction rates, the mass transport equations of the secondary species can be combined into those of the primary species and the following equations result:

$$\frac{\partial(\varepsilon c_1)}{\partial t} + \nabla \cdot N_1 = 0 \tag{18}$$

$$\frac{\partial(\varepsilon c_2)}{\partial t} + \nabla \cdot N_2 = 0 \tag{19}$$

$$\frac{\partial[\varepsilon(c_3 + c_6 + c_{12})]}{\partial t} + \nabla \cdot (N_3 + N_6 + N_{12}) = -(r_{p_1} + r_{p_2}) \tag{20}$$

$$\frac{\partial[\varepsilon(c_4 - c_5 - c_6 + c_{10} + 2c_{11} + c_{12})]}{\partial t} + \nabla \cdot (N_4 - N_5 - N_6 + N_{10} + 2N_{11} + N_{12}) = 2(r_{CO_2} + r_{p_2}) \tag{21}$$

$$\frac{\partial \varepsilon c_7}{\partial t} + \nabla \cdot N_7 = -r_{CO_2} \tag{22}$$

$$\frac{\partial \varepsilon c_8}{\partial t} + \nabla \cdot N_8 = 0 \tag{23}$$

$$\frac{\partial[\varepsilon(c_9 + c_{10} + c_{11} + c_{12})]}{\partial t} + \nabla \cdot (N_9 + N_{10} + N_{11} + N_{12}) = (-r_{p_1} + r_{CO_2}) \tag{24}$$

The time-dependent terms in Equations (20), (21) and (24) can be reorganized to be expressed by the concentrations of the primary species only. These are shown in Appendix B and Table 1 (the bottom four rows). The reorganization of the time-dependent terms is useful when these equations are incorporated into the computer code to be solved.

The general mathematical treatments to yield Equations (20), (21) and (24) have been given in detail elsewhere.[31-33] The above equations involve the rate of precipitation r_{pj} and the rate of CO_2 hydration (irreversible), which will be explained soon.

To solve for the electrode potential as an independent variable, one of the following two methods can be used.

When the equation of electroneutrality:

$$\sum_j z_j c_j = 0, \tag{25}$$

is used, the combination of Equations (18-24) yields:

$$\sum_j z_j N_j = 0 \tag{26}$$

where j=1, 2, 3, 4, 5, 6, 9, 10 and 12, the ionic species in solution. This equation suggests that no current flows through solution in the direction parallel with the metal surface (Figure 1). The use of Equation (26) and the equilibrium equations given in Appendix A may yield an analytical solution to express the concentration of one primary species with those of others, such as shown in Appendix C. The use of the analytical equations reduces the total number of equations to be solved and facilitates the numerical solution of the model.

The second method, alternative to the equation of electroneutrality, is the Possion's equation below:[28,30]

$$\nabla \cdot (\xi \varepsilon \tau \nabla \cdot \phi) = -F\varepsilon \sum z_j c_j \tag{27}$$

where the charge density $\sum z_j c_j$ may not necessarily be zero.

In the system of porous media, the system porosity is also a variable that must be solved for in order to gain the complete solution of the mass transport equations.

For the system of interest, two precipitates: $FeCO_3$ and $Fe(OH)_2$, are of concern. The variation with time of their solid volumetric fractions may, for any space in the system, be expressed as:

$$\frac{\partial \varepsilon_{m1}}{\partial t} = \frac{M_{FeCO_3}}{\rho_{FeCO_3}} r_{p_1} \tag{28}$$

and

$$\frac{\partial \varepsilon_{m2}}{\partial t} = \frac{M_{Fe(OH)_2}}{\rho_{Fe(OH)_2}} r_{p_2} \tag{29}$$

where ε_{m1} and ε_{m2} are the solid volume fractions of $FeCO_3$ and $Fe(OH)_2$ respectively. M and ρ are respectively the molar weight and density of a precipitate; their ratio is molar volume. r_{pj} (j=1,2) is the rate of precipitation which can be expressed by:[29]

$$r_{p_1} = k_{f_{FeCO_3}} \sigma_1 K_{sp_{FeCO_3}} (S_{FeCO_3} - 1) \tag{30}$$

and

$$r_{p_2} = k_{f_{Fe(OH)_2}} \sigma_2 K_{sp_{Fe(OH)_2}} (S_{Fe(OH)_2} - 1) \tag{31}$$

where k and K_{sp} are respectively precipitation rate constant and solubility product. S is the ratio of relevant ionic concentration products to K_{sp}, which measures the level of saturation or supersaturation of the solution. σ_1 or σ_2 is specific area or the ratio of surface area over the volume of a precipitate. Without specific knowledge, it is assumed that σ_1 and σ_2 are the same, and

$$\sigma_1 = \sigma_2 = 10^4 \varepsilon \tag{31a}$$

The expression for the rate constants, $k_{f_{FeCO_3}}$ and $k_{f_{Fe(OH)_2}}$, are assumed to be the same and follow:

$$k_p = k_{f_{FeCO_3}} = k_{f_{Fe(OH)_2}} = \exp(28.2 - \frac{64851.4}{RT}) \tag{31b}$$

Since $1-\varepsilon = \varepsilon_{m1} + \varepsilon_{m2}$, the combination of Equations (28-29) leads to:

$$\frac{\partial(1-\varepsilon)}{\partial t} = \frac{M_{FeCO_3}}{\rho_{FeCO_3}} r_{p_1} + \frac{M_{Fe(OH)_2}}{\rho_{Fe(OH)_2}} r_{p_2} \tag{32}$$

When the precipitation process is considered to be irreversible (or dissolution of the precipitation into solution is neglected), the precipitation rate can be written as:[28]

$$r_{p_j} = \max(0, r_{p_j}) \tag{33}$$

where j=1,2.

The irreversible volumetric rate of CO_2 hydration may be written as:

$$r_{CO_2} = \varepsilon(k_f c_7 - k_b c_{11}) \tag{34}$$

where k_f and k_b are respectively the forward and backward reaction rate constants of CO_2 hydration.

Equations (18-24) and one of Equations (26-27) may be combined with two of the three equations, Equations (28-29, 32), to solve for all the concentrations, the electrode potential and the porosity of the system. This needs to be done by incorporating the initial and boundary conditions of the system to be defined next.

Initial and Boundary Conditions

Two systems of interest are to be dealt with here. For internal corrosion in wet gas lines, a solution layer is constantly present on the pipe surface and the boundary layer thickness can depend on the flow velocity. For this dynamic system, for a fixed flow velocity, there exists a fixed boundary layer thickness and the concentrations at the bulk solution boundary may be considered to be constant over time. These and other boundary conditions are summarized in Table 2, which has also included the initial and boundary conditions for the dry gas system.

For the ordinary differential equations relating to porosity, or Equation (32), they are dimension-independent and require no boundary conditions to be solved.

Unlike wet gas pipelines, in a dry gas system, the solution boundary layer formed by water condensation can be thin. At the gas-solution interface, the CO_2 or O_2 gas if present may be considered to be in equilibrium with its dissolved species, CO_2(aq) or O_2(aq). The flux of all other dissolved species is zero at this boundary.

The boundary conditions at the steel surface are the same irrespective of dry gas or wet gas systems. At this boundary, the fluxes can be defined as shown in Table 2.

Since the problem of interest is time-dependent, the initial conditions for concentrations and porosities must be defined, even though at large times the results are independent of the initial conditions given. The initial conditions are not necessary for Equation (26) or (27) as either equation does not contain any time-dependent term.

The boundary condition for Equation (26) or (27) deserves to be noted. Even though several potentials (electrostatic potentials of metal and solution, electrode potential, open circuit potential) are involved in the system (as also shown in Equations (15-16)), it is the electrode potential that is of practical significance. However, all these potentials are interrelated and interdependent. Their relations must be understood in order to properly define the electrode potential.

Since only the relative difference between the electrostatic potential of the metal, that of the solution and the electrode potential is meaningful, Table 3 summarizes three equivalent ways of defining one of the potentials as a reference (value may be set as zero or a fixed value, with the other two potentials determined by their differences to the reference). This table is explained further in Appendix D when the system is in the open circuit condition. The condition highlighted in gray in Table 3 is used for the modeling in this work. The corresponding boundary conditions are given in Table 2.

For either a dry or wet gas system, the same boundary conditions associated with electrode potential apply for Equation (26) or (27). When the Possion's equation or Equation (27) is used, at one of the boundaries the net current density, with direction being to or from or neutral at the steel surface, must be implemented.

The total or net ionic current density of mass transport in solution may be written as:

$$i_{netT} = F\sum_j z_j N_j = i_{diff} + i_{migr} \tag{35}$$

where j=1-6, 9-10, and 12, and the current density contributed by ionic diffusion only is

$$i_{diff} = -F\varepsilon^{1.5}\sum_j (z_j D_j \tfrac{\partial c_j}{\partial x}), \tag{35a}$$

The solution conductivity is:

$$\kappa = \tfrac{\varepsilon^{1.5}F^2}{RT}\sum_j (z_j^2 D_j c_j) = \varepsilon^{1.5}F^2\sum_j (z_j^2 u_j c_j), \tag{35b}$$

and the current density contributed by ionic migration is

$$i_{migr} = -\kappa\tfrac{\partial\phi}{\partial x}. \tag{35c}$$

The total current density of ion transport, which flows in solution perpendicular to the steel surface, must equal the net current density due to the electrochemical reactions at the steel surface, or

$$i_{netT} = i_{netE} \tag{36}$$

where i_{netE} is net current density resulting from electrochemical reactions. This net current density i_{netE} is the summation of all anodic (positive) and all cathodic (negative) current densities with consideration of the effective surface area of the reactive steel surface:

$$i_{netE} = \sum_j i_{aj} + \sum_k i_{ck} \tag{37}$$

where i_{aj} and i_{ck} are respectively the jth anodic and k^{th} cathodic current densities. The effective surface area can be expressed as a function of ε and it can be embedded in i_{aj} or i_{ck} as will be shown explicitly later.

With the above consideration, the potential gradient as a boundary condition for Equation (27) may be written as:

$$\tfrac{\partial\phi}{\partial x} = \tfrac{-i_{netE} + i_{diff}}{\kappa} \tag{38}$$

Expressed by effective current density, Equation (38) becomes:

$$\xi\varepsilon^{1.5}\tfrac{\partial\phi}{\partial x} = \xi\varepsilon^{1.5}\tfrac{-i_{netE} + i_{diff}}{\kappa} \tag{39}$$

When the effective reactive surface area fraction for the electrochemical reactions at the steel surface is the same in magnitude as porosity ε, written by Tafel equation the anodic and cathodic half cell current densities are given below. The anodic or corrosion current density at the steel surface is:

$$i_{corr} = \varepsilon i^0_{Feref} 10^{\frac{E_s - E_{Fe}^{Eqref}}{b_{Fea}}} \tag{40}$$

where "ref" in the above and below equations shown as either a subscript or superscript is referred as a reference condition whereby the corresponding exchange current density i^0, bulk concentration c_j (j=3, 4, 5, 14) and equilibrium potential E^{Eq} are reported or known. "b" is Tafel slope.

For reductions of hydrogen ion, water and carbonic acid, their Tafel equations respectively are:

$$i_H = -\varepsilon i^0{}_{Href} \frac{c_{4s}}{c_{4ref}} 10^{\frac{-(E_s - E_H^{Eqref})}{b_H}} \tag{41}$$

$$i_{H_2O} = -\varepsilon i^0{}_{H_2Oref} 10^{\frac{-(E_s - E_{H_2O}^{Eqref})}{b_{H_2O}}} \tag{42}$$

$$i_{H_2CO_3} = -\varepsilon i^0{}_{H_2CO_3ref} \frac{c_{11s}}{c_{11ref}} \left(\frac{c_{4s}}{c_{4ref}}\right)^{-0.5} 10^{\frac{-(E_s - E_{H_2CO_3}^{Eqref})}{b_{H_2CO_3}}} \tag{43}$$

where c_{4s} and c_{11s} are respectively the concentrations of hydrogen ion and carbonic acid at the steel surface.

When corrosion is not under open circuit conditions, the electrode potential at the bulk solution surface at the steel surface, or the external (net) current density needs to be known. When the corrosion is under open circuit conditions, there is an analytical solution to the electrode potential E_s, which is a function of concentration at the steel surface. Appendix D shows how E_s is expressed by concentrations analytically. For a known E_s, the anodic and cathodic current densities can be determined from Equations (40-43), which are then used as the boundary conditions shown in Table 3 to solve for Equations (18-25).

With the governing equations and boundary conditions, all concentrations of the primary species, the electrode potential (E) and the system porosity can be determined. This can be accomplished by implementing a commercial finite element method software code: Comsol 3.5. This code allows for flexible meshing of the model geometry and flexible setting of time steps.

Since the gradients of concentrations and that of potential are very large near the boundaries, the local mesh is set to be very dense. The time steps near time zero are made to be very small because the gradients of variables with time are also large near time zero.

When the concentrations of the primary species are determined, by substituting them into the equilibrium equations in Appendix A or Table 1, the concentrations of the secondary species can be calculated.

Simplified Moving Boundary Condition

For a dry gas system, when a boundary layer is maintained at the steel surface with the rate of water condensation equal to the rate of evaporation, the total mass of water in this boundary layer does not change over time. When there is formation of precipitate due to corrosion, the precipitate film may have different density and molar weight from steel. Thus, the solution boundary layer thickness can vary with time as the steel corrodes. Since the total mass of dissolved Na^+ in the solution does not change over time, this may lead to the relation below.

Since:

$$\int_{x_S}^{x_M} \varepsilon c_1 dx = c_{01}\delta_0 \tag{44}$$

The derivative of Equation (44) over t gives:

$$\varepsilon_M c_{1M} \frac{\partial x_M}{\partial t} + \int_{x_S}^{x_M} \frac{\partial(\varepsilon c_1)}{\partial t} dx - \varepsilon_S c_{1S} \frac{\partial x_S}{\partial t} = 0 \tag{45}$$

Rearrangement of Equation (45) yields:

$$\varepsilon_s c_{1s} \left(\frac{\partial x_M}{\partial t} - \frac{\partial x_S}{\partial t}\right) + \left(\varepsilon_M c_{1M} - \varepsilon_s c_{1s}\right) \frac{\partial x_M}{\partial t} + \int_{x_S}^{x_M} \frac{\partial(\varepsilon c_1)}{\partial t} dx = 0 \tag{46}$$

With Equation (18) and its boundary conditions in Table 2, Equation (46) becomes:

$$\frac{\partial x_M}{\partial t} - \frac{\partial x_S}{\partial t} = \frac{\varepsilon_s c_{1s} - \varepsilon_M c_{1M}}{\varepsilon_s c_{1s}} \frac{\partial x_M}{\partial t} \tag{47}$$

The moving velocity of the steel surface relative to the solution surface as the reference is:

$$\frac{\partial x_M}{\partial t} - \frac{\partial x_S}{\partial t} = \left(1 - \frac{\varepsilon_M c_{1M}}{\varepsilon_s c_{1s}}\right) \frac{i_{corr}}{\beta} \tag{48}$$

where β is a unit conversion factor which, for steel, is 2.686×10^{10} $A\cdot s/m^3$.

MODEL VALIDATION WITH LAB AND FIELD DATA

For model validation, the moving boundary condition is not considered with the understanding that this effect may only have a slight effect on the predictions. Also, in this validation, since the lab and field data were obtained in production systems, the model used for validation is one that simulates a boundary layer sandwiched between the bulk solution and the steel surface, unlike a dry gas case where the solution layer is bounded by gas phase and the steel surface.

The model parameters used for the model validation and other computations are given in Table 4. Figure 2 shows a comparison of the predicted corrosion rates with experimental data[1,5] measured in lab testing; the initial solution contained little or no ferrous ion and the flow velocity in a pipe loop of 8cm in inner diameter was 20 m/s. The experimental data were acquired *in situ* by monitoring the activity decrease resulting from the metal loss of neutron activated steel coupons with Fe59 as the main radioactive isotope. Scintillation counters, placed outside the loop pipe, monitored the activity levels in 1000-second intervals with an accuracy of approximately 0.2%.

The predicted maximum corrosion rate in Figure 2 is the rate at the time when corrosion first initiates. This does not depend on the boundary layer thickness. When corrosion just starts, the steel surface is fresh and the solution pH at the steel surface is low relative to that after corrosion has started. Soon after corrosion starts, the pH at the steel surface quickly elevates due to electrochemical reduction of hydrogen ions and carbonic acid and formation of ferrous ion by the corrosion process. The boundary layer thickness used in the model is 10 μm determined from the diameter of the tubing and flow velocity. The predicted results show that it takes some time before the corrosion process reaches steady state. When steady state is reached, there is still no precipitation because the predicted porosity at the steel surface is zero.

Since steady state is soon reached after corrosion starts, this corrosion rate is used to compare with measured corrosion rates. Except one point, all experimental data fall slightly below the predicted corrosion rates, suggesting that the predicted steady state corrosion rate is slightly more conservative or higher than the measured rates.

Figure 3 shows the measured corrosion rates at 51 °C in a solution that was initially saturated with ferrous carbonate.[6] The corrosion rates were measured by the linear polarization resistance method, although this is not clearly stated in the literature. The predicted corrosion rate is shown to decrease over time due to increase of solution pH and formation of solid precipitate at the steel surface. The formation of solid precipitate decreases the system porosity and thus, the active corroding area at the steel surface. Overall, the predicted corrosion rates are shown to be slightly greater than the experimental data.

Similar to Figure 3, Figure 4 shows time-dependent corrosion rates measured in lab at 35 ^{o}C in a solution initially saturated by ferrous carbonate.[6] The experimental data were measured possibly by linear polarization resistance method and are shown to be slightly below and in similar trend to the predicted rates. The formation of precipitate film at the steel surface and the decreasing porosity by the solid precipitate may be responsible for the decrease of corrosion rate.

Figure 5 shows the model-predicted maximum (or initial) corrosion rates and those at the 5th hour for steel in a solution initially saturated by ferrous carbonate. The temperature is 90 ^{o}C. These predicted results are compared with experimental data measured in a high pressure, flow rate loop connected to an autoclave at 90 ^{o}C.[6] The solution was initially saturated by ferrous carbonate. The CO_2 partial pressure varies between 1.5 and 6 bars at a flow rate of 20 m/s.

Since corrosion rate varies with time as shown in Figures 3-4, depending on when it is measured the corrosion rate can be different. The time and the methods of the corrosion rate measurements are not clearly stated in the literature.[6] The predicted corrosion rates at the 5th hour are slightly greater than the measured rates.

Figure 6 shows data[7] measured in lab testing with the same facilities used for measuring the data shown in Figures 1-4 and the data were measured by linear polarization resistance method,[1] although the exact methods of rate measurements were not stated clearly in the reference.[7] The temperature was 20 °C. A flow loop connecting to an autoclave was used to measure the rates of coupons at different velocities and at different CO_2 partial pressures.

Figure 6 also shows estimated field corrosion rates reported elsewhere.[3] The temperature was 25 ^{o}C. The lab and field data are compared to the model-predicted results. It appears that the variation of flow velocity can significantly affect the corrosion rate. Corrosion rates measured in lab testing are shown to be significantly greater than the predicted steady state corrosion rates and the predicted maximum corrosion rates. It is possible that the corrosion rate measured in the lab is affected by the erosion processes, which the model does not cover. It is also possible that the model parameters may not all be appropriate in this condition. For this model, the role of flow velocity is treated as reducing the boundary layer thickness only. Since the predicted corrosion rate is rather greater than field estimated corrosion rate, it appears that the predicted corrosion rates are more conservative than the long-term corrosion rate in field conditions.

Similar results are shown in Figure 7 for the temperature range of 50-60 ^{o}C.[1,7] The data came from the same sources as, and measured similarly to, the data in Figure 6. The difference is that none of the lab data go above the predicted maximum corrosion rates. The lab rates are greater than the predicted steady state corrosion rates and the latter is greater than the field corrosion rates.[3]

It should be recognized that other than errors associated with experimental measurements, the model itself has its limitations. For instance, the values of model parameters come from different sources and each parameter may have associated errors. Thus, discrepancy between the model predictions and experimental or field results can be expected. A sensitivity analysis of some model parameters is to be provided later.

MODEL RESULTS

Corrosion Rate in Dry Gas System vs. in Wet Gas

Figure 8 shows the predicted corrosion rate, pH and porosity at the steel surface for a wet gas system. A significant drop of corrosion rate over time is shown shortly after the corrosion process begins. This drop in corrosion rate is accompanied by the increase of pH at the steel surface. No precipitation is predicted at the steel surface since the porosity at the steel surface is shown to be 1 consistently.

When the system is dry gas, the corrosion rate and porosity at the steel surface are shown in Figure 9. The initial variation of corrosion rate with time is similar to that in the wet gas system shown in Figure 8 before the porosity at the steel surface starts to decrease. The initial decrease of corrosion rate results from the increase of pH at the steel surface. Afterwards, as the corrosion rate becomes steady for some time, the concentration of ferrous ion in the solution increases until saturation of iron carbonate is reached. Then, formation of solid $FeCO_3$ begins almost simultaneously throughout the boundary layer, since the decrease of porosity at the steel surface is shown to decrease even at the gas-solution interface. The more significant decrease of porosity at the steel surface relative to that at the gas-solution interface shows the limitation of mass transport of ferrous ion from the steel surface. This decrease of porosity at the steel surface leads to the decrease of corrosion rate because of the total active steel surface area (not covered by the precipitate) is reduced.

Figure 10 shows the effect of solution chemistry on corrosion rate. Compared to the results of unsaturated condition shown in Figure 8-9, the corrosion rates shown in Figure 10 for both dry and wet gas systems with the boundary layer and the bulk solution saturated are much smaller initially due to a different initial pH. For the saturated solution, the corrosion rates predicted for both the wet and dry gas systems are similar, with the rate in the wet gas system slightly greater than in the dry gas system. This similarity is primarily a function of porosity values at the steel surface for both systems, and the porosities have similar values as shown in Figure 11. For the wet gas system, the bulk boundary is shown to have a porosity of 1 throughout the corrosion process, but the porosity at the steel becomes very small. This leads to a small average corrosion rate.

The corrosion rate in the wet gas system is greater overall because ferrous ions formed from corrosion processes can transport across the boundary layer into the bulk solution. This leads to slower precipitation and slower change of porosity compared to a dry gas system where all ferrous ions formed must stay in the boundary layer in either dissolved or solid state.

Effect of Moving Boundary Condition

In the above computations, the effect of moving boundary condition described by Equation (48) is neglected. This effect is studied below for both wet and dry gas systems at the condition of: 25 ^{o}C and CO_2 partial pressure of 1 atm.

For a wet gas system when the bulk solution is unsaturated, Figure 12 shows that the predicted corrosion rates with or without including the moving boundary condition in the model are the same. This is because there is no precipitation at the steel surface and the boundary layer thickness remains the same.

When a dry gas system is considered, however, Figure 12 shows that inclusion of a moving boundary in the model leads to a smaller corrosion rate. This is because the density of $FeCO_3$ solid is smaller than iron and thus, the solid volume in the system increases over time. This leads to a faster decreasing porosity than if the moving boundary condition is not considered.

Figure 13 shows a sharper decrease of porosity at both surfaces when the moving boundary is considered in the model. With a moving boundary, the entire boundary layer becomes saturated and the porosity decreases. This is not the case with moving boundary not considered, when no precipitation occurs at the bulk solution surface.

Sensitivity Analysis of the Model

The model results can depend on the values of the model parameters taken in the computations. For instance, the boundary layer thickness can depend on flow velocity and the pipe surface condition; the uncertainty associated with the rate constant of $FeCO_3$ precipitation; uncertainty associated with the activation energies used for kinetic parameters such as that for the exchange current density of hydrogen ion reduction. Here, only the results of the effect of boundary layer thickness and that of the rate constant of ferrous carbonate precipitate are presented and discussed.

Figure 14 shows the corrosion rates modeled for a wet gas system with the boundary layer unsaturated at 25 °C and at a CO_2 partial pressure of 1 atm. For the same surface condition, three boundary layer thicknesses are used for modeling and the effect of boundary layer thickness or the flow velocity is shown to be significant. For this system, since no saturation occurs in the boundary layer and the boundary layer thickness does not change, the results with or without including moving boundary condition in the model are the same. The initial corrosion rate is the same irrespective of the boundary layer thickness because the same initial condition is used for the model. Figure 14 shows that a larger boundary layer thickness corresponds to a smaller corrosion rate. This is because the resistance of mass transport is greater, and the pH at the steel surface is correspondingly higher as shown in Figure 15.

Figure 16 shows the modeled corrosion rates for a dry gas system with the boundary layer unsaturated at 25 °C and at a CO_2 partial pressure of 1 atm and when the value of the rate constant of ferrous carbonate precipitation varies by uncertainties associated with the specific surface area of the precipitate solid. A wide range of the rate constant is investigated. The increase of this value from 76.8 to 7.68×10^5 $m^5/mol\cdot s$, four orders of magnitude of change, has led to very little change of the corrosion rate, although the rate associated with the latter values is greater. The porosity variations with time obtained by the use of these two different values are approximately overlapped as shown in Figure 17.

It appears that in Figures 16 and 17 the increase of this parameter from 7.68×10^5 to 7.68×10^7 $m^5/mol\cdot s$ has resulted in obvious decrease of the corrosion rate due to the obvious decrease of porosity at the steel surface.

CONCLUSIONS

A comprehensive CO_2 corrosion model considering both transport and migration of ionic species in solution was developed and validated with significant amount of data in a wide range of conditions.

This model was used to predict corrosion rates in both wet and dry gas systems. The prediction results show that in a dry gas system, ferrous ions cannot escape out of the boundary layer and precipitation will occur. Consequently, the reduced porosity at the steel surface by the precipitate leads to a reduced corrosion rate.

For wet gas systems, precipitation may not occur at the steel surface if the solution in the bulk is unsaturated and the pH is lower.

Due to difference in porosity, the corrosion rate in dry gas systems is lower than in wet gas system for the same modeling conditions.

Although this model is very useful when external current is involved in the corrosion system, it is perhaps overly sophisticated when it is used for corrosion in an open circuit condition. This is because for the latter system, the migration term can be neglected and CO_2 hydration may be the rate controlling step. Therefore, a simpler model that is convenient to use while not losing significant accuracy is more appropriate. The result of this model simplification effort is to be reported later.

Sensitivity analysis of the model is provided to show how uncertainties with the values of some model parameters may have an effect on the model predictions. It is important that the most reliable values of the model parameters be selected for predictions.

ACKNOWLEDGEMENT

This work was sponsored by the US Department of Transportation Pipeline and Hazardous Materials Safety Administration (Mr. James Merritt, Program Manager), under the contract: DTPH56-08-T-0003 and co-funded by the PRCI and CenterPoint Energy, New Orleans, LA.

The author would like to acknowledge advice provided by Prof. John Newman of the University of California, Berkeley on reference conditions of potentials.

REFERENCES

1. C. de Waard, D.E. Milliams, Corrosion 31 (1975) 177.
2. C. de Waard, U. Lotz, D.E. Milliams, Corrosion 47 (1991) 976.
3. C. de Waard, U. Lotz, "Prediction of CO_2 Corrosion of Carbon Steel" (Houston, TX: NACE, 1993) Paper 69.
4. C. de Waard, U. Lotz, A. Dugstad, "Influence of Liquid Flow Velocity on CO_2 Corrosion: A Semi-Empirical Model" (Houston, TX: NACE, 1995) Paper 128.
5. K. Videm, A. Dugstad, Materials Performance, March (1989) 63.
6. K. Videm, A. Dugstad, Materials Performance, April (1989) 46.
7. A. Dugstad, L. Lunde and K. Videm, "Parametric Study of CO_2 Corrosion of Carbon Steel", (Houston, TX: NACE, 1994) Paper 14.
8. W.P. Jepson, C. Kang, M. Gopal, S. Stitzel, "Model for Sweet Corrosion in Horizontal Multiphase Slug Flow" (Houston, TX: NACE, 1997) Paper 11.
9. A. Carlos, T. Palacios, S.A. Corpoven, "Application of Simulation Techniques for Internal Corrosion Prediction" (Houston, TX: NACE, 1997) Paper 2.
10. A.M.K. Halvorsen, T. Sontvedt, "CO_2 Corrosion Model for Carbon Steel Including a Wall Shear Stress Model for Multiphase Flow and Limits for Production Rate to Avoid Mesa Attack" (Houston, TX: NACE, 1999) Paper 42.
11. Y.M. Gunaltun, "Combining Research and Field Data for Corrosion Rate Prediction" (Houston, TX: NACE, 1996) Paper 27.
12. Y.M. Gunaltun, D. Larrey, "Correlation of Cases of Top of Line Corrosion with Calculated Water Condensation Rates" (Houston, TX: NACE, 2000) Paper 71.
13. M.R. Bonis, J.L. Crolet, "Basics of the Prediction of the Risks of CO_2 Corrosion in Oil and Gas Wells" (Houston, TX: NACE, 1989) Paper 466.
14. K.A. Sangita, S. Srinivasan, "An Analytical Model to Experimentally Emulate Flow Effects in Multiphase CO_2/H_2S Systems" (Houston, TX: NACE, 2000) Paper 58.
15. F.M. Song, D.W. Kirk, J.W. Graydon, D.E. Cormack, Corrosion 60 (2004) 736.
16. F.M. Song, D.W. Kirk, J.W. Graydon, D.E. Cormack, J. Electrochem. Soc. 149 (2002) B479-B486.
17. S. Nesic, J. Postlethwaite, S. Olsen, Corrosion 52 (1996) 280.
18. B.F.M. Pots, "Mechanistic Models for the Prediction of CO2 Corrosion Rates under Multi-phase Flow Conditions" (Houston, TX: NACE, 1995) Paper 137.
19. B.F.M. Pots, E.L.J.A. Hendriksen, "CO_2 Corrosion under Scaling Conditions – The Special Case of Top-of-Line Corrosion in Wet Gas Pipelines" (Houston, TX: NACE, 2000) Paper 31.
20. A. Anderko, R.D. Young, "Simulation of CO_2/H_2S Corrosion Using Thermodynamic and Electrochemical Models" (Houston, TX: NACE, 1999) Paper 31.
21. A. Anderko, "Simulation of $FeCO_3$/FeS Scale Formation Using Thermodynamic and Electrochemical Models" (Houston, TX: NACE, 2000) Paper 00102.
22. M. Nordsveen, S. Nesic, R. Nyborg, A. Stangeland, Corrosion 59 (2003) 443.
23. R. Zhang, M. Gopal, W.P. Jepson, "Development of a Mechanistic Model for Predicting Corrosion Rate in Multiphase Oil/Water/Gas Flows" (Houston, TX: NACE, 1997) Paper 601.
24. E. Dayalan, F.D. de Moraes, J.R. Shadley, S.A. Shirazi, S.A. Ribicki, "CO_2 Corrosion Prediction in Pipe Flow under $FeCO_3$ Scale-Forming Conditions" (Houston, TX: NACE, 1998) Paper 51.
25. M.S. High, J. Wagner, S. Natarajan, "Mechanistic Modeling of Mass Transfer in the Laminar Sublayer in Downhole Systems" (Houston, TX: NACE, 2000) Paper 62.
26. M. Sundaram, V. Raman, M.S. High, D.A.Tree, J. Wagner, "Deterministic Modeling of Corrosion in Downhole Environments" (Houston, TX: NACE, 1996) Paper 30.
27. F.M. Song, D.W. Kirk and D.E. Cormack, Electrochimica Acta, 55 (2010) 689–700.
28. F. King, M. Kolar, "A Model for Predicting the Extent of Internal Corrosion of Gas Transmission Pipleines", Final Report to NRTC, 2002.
29. K. Kumaresan, Y. Mikhaylik and R.E. White, J. Electrochem. Soc. 155 (2008) A576-A582.
30. J. Newman, K.E. Thomas-Alyea, Electrochemical Systems, 3rd ed. John Wiley & Sons, New York (2004).
31. F.M. Song, N. Sridhar, J. Been, and F. King, "Predicting Pipeline SCC Conditions through Simulation of Under-Disbondment Chemistry and Potential," International Pipeline Conference held Oct 4-8, 2004, Calgary, Alberta, Canada, Paper 0196.
32. F.M. Song and N. Sridhar, Corrosion Science 50 (1) (2008) 70-83.

33. F.M. Song, "Predicting the Effect of Soil Seasonal Change on Stress Corrosion Cracking Susceptibility of Buried Pipelines at High pH", corrosion, submitted.
34. S. Nesic, J. Postlethwaite, S. Olsen, Corrosion 52 (1996) 280.
35. R. Parsons, Handbook of Electrochemical Constants (London: Butterworths Scientific Publications, 1959) 47 and 66.
36. J. Greenberg, M. Tomson, Appl. Geochem. 7 (1992) 185-190.
37. W. Sun, S. Nesic, R.C. Woollam, Corrosion Science 51(2009) 1273-1276.
38. D.M. Kern, J. Chem. Educ. 37 (1960) 15.
39. Group of Inorganic Chemistry, Inorganic Chemistry (Dalian, China: Butterworths Institute of Dalian Technology Press, 1978) 358.
40. D. Tromans, Corrosion 55 (1999) 942.
41. D.R. Lide, "CRC Handbook of Chemistry and Physics", 75th ed. (New York, NY: CRC Press, 1995).
42. J. Kvarekval, "A Kinetic Model for Calculating Concentration Profiles and Fluxes of CO2-Related Species across the Nernst Diffusion Layer", Corrosion/97, Paper no. 5 (Houston, TX: NACE 1997).
43. R.H. Perry and D. Green, Perry's Chemical Engineers' Handbook, 50th ed. (New York, NY: McGraw-Hill, 1984).
44. W. Sun and S. Nesic, Corrosion 64(4) (2008) 334-346.
45. V. Jovancicevic, J. O'M. Bockris, J. Electrochem. Soc. 133 (1986) 1797.
46. J.O'M. Bockris, D. Drazic, A.R. Despic, Electrochimica Acta 4 (1961) 325.
47. J.G.N. Thomas, T.J. Nurse, R. Walker, Br. Corros. J. 5 (1970) 87.
48. C.M. Shepherd, S. Schuldiner, J. Electrochem. Soc. 115 (1968) 1124.
49. M. Stern, R.M. Roth, J. Electrochem. Soc. 104 (1957) 390.
50. M.D. Koretsky, F. Abooameri, J.C. Westall, Corrosion 55 (1999) 52.
51. F.M. Song, D.W. Kirk, J.W. Graydon, D.E. Cormack, Corrosion 58 (2002) 145.

APPENDIX A

REVERSIBLE AND IRREVERSIBLE HOMOGENEOUS AND HETEROGENEOUS REACTIONS IN THE PIPELINE SYSTEMS: CHEMICAL EQUILIBRIUM FORMULA AND KINETIC RATES FOR A CORROSION SYSTEM IN THE PRESENCE OF DISSOLVED CO_2 AND O_2

All of the reactions below are written such that the secondary species are products and the primary species are reactants. These reactions are written as such to facilitate the derivation of the model governing equations as detailed elsewhere.[32]

The reversible reactions are listed below. The reactions in the parentheses are equivalent ones but show more clearly the thermodynamic relations between concentrations and the equilibrium constants. The concentrations of all the secondary species can be expressed by those of the primary species as shown below:

$$H_2O - H^+ \leftrightarrow OH^- \ (H_2O \leftrightarrow H^+ + OH^-),\ c_4c_{11} = K_w \tag{A.1}$$

$$FeCO_3 - Fe^{2+} \leftrightarrow CO_3^{\ 2-} \ (FeCO_3 \leftrightarrow Fe^{2+} + CO_3^{\ 2-}),\ c_3c_{12} = K_{spFeCO_3} \tag{A.2}$$

$$(HCO_3^- \leftrightarrow H^+ + CO_3^{2-}),\ \frac{c_4c_{12}}{c_{13}} = K_{2H_2CO_3} \tag{A.3}$$

$$FeCO_3 - Fe^{2+} + 2H^+ \leftrightarrow H_2CO_3 \ (H_2CO_3 \leftrightarrow H^+ + HCO_3^-,\ K_{11H2CO3}),\ \frac{c_4c_{13}}{c_{14}} = K_{11H_2CO_3} \tag{A.4a}$$

$$(CO_2(aq) + H_2O \leftrightarrow H^+ + HCO_3^-,\ K_{1H2CO3}),\ K_{11H_2CO_3} = K_{1H_2CO_3} / K_h \tag{A.4b}$$

$$Fe^{2+} + H_2O - H^+ \leftrightarrow FeOH^+ \ (Fe^{2+} + H_2O \leftrightarrow FeOH^+ + H^+),\ \frac{c_4c_{15}}{c_3} = K_1 \tag{A.5}$$

$$FeCO_3 + H^+ \leftrightarrow FeHCO_3^{\ +} \ (FeHCO_3^+ \leftrightarrow Fe^{2+} + HCO_3^-),\ \frac{c_3c_{13}}{c_{16}} = K_{cx1} \tag{A.6}$$

The above equilibrium equations are also summarized in Table 1 (the very left column).

The irreversible reaction is CO_2 hydration:

$$CO_2 + H_2O + Fe^{2+} \leftrightarrow FeCO_3 + 2H^+ \ (CO_2 + H_2O \leftrightarrow H_2CO_3),\ r_{CO2} \tag{A.7}$$

The electrochemical reactions are:

$$Fe \rightarrow Fe^{2+} + 2e^-,\ r_{Fe}^e \tag{A.8}$$

$$H^+ + e^- \rightarrow 0.5H_2,\ r_H^e \tag{A.9}$$

$$H^+ + e^- \rightarrow 0.5H_2 \ (H_2O + e^- \rightarrow 0.5H_2 + OH^-),\ r_{H_2O}^e \tag{A.10}$$

$$4H^+ + O_2 + 4e^- \rightarrow 2H_2O,\ r_{O_2}^e \tag{A.11}$$

$$H^+ + e^- \rightarrow 0.5H_2 \ (H_2CO_3 + e^- \leftrightarrow HCO_3^{\ -} + 0.5H_2),\ r_{H_2CO_3}^e \tag{A.12}$$

APPENDIX B

TRANSFORMATION OF THE TIME DEPENDENT TERMS IN THE GOVERNING EQUATIONS

Since concentrations of the secondary species can be expressed by those of the primary species, the time dependent terms in the governing equations can be expressed by the time gradient of concentrations of the primary species. This rearrangement of the time-dependent terms is necessary when the governing equations are incorporated into the computer code for being solved.

For Equation (20), its time dependent-term can be expressed by:

$$\frac{\partial[\varepsilon(c_3+c_6+c_{12})]}{\partial t} = (c_3+c_6+c_{12})\frac{\partial\varepsilon}{\partial t} + \varepsilon(fc_3\cdot\frac{\partial c_3}{\partial t} + fc_4\cdot\frac{\partial c_4}{\partial t} + fc_9\cdot\frac{\partial c_9}{\partial t}) \quad \text{(B.1)}$$

where:

$$fc_3 = \frac{\partial(c_3+c_6+c_{12})}{\partial c_3} = 1 + \frac{c_6+c_{12}}{c_3}, \quad \text{(B.1a)}$$

$$fc_4 = \frac{\partial(c_3+c_6+c_{12})}{\partial c_4} = \frac{c_{12}-c_6}{c_4}, \quad \text{(B.1b)}$$

$$fc_9 = \frac{\partial(c_3+c_6+c_{12})}{\partial c_9} = \frac{c_{12}}{c_9}. \quad \text{(B.1c)}$$

Similar transformations applied to Equation (21) yields

$$\frac{\partial[\varepsilon(c_4-c_5-c_6+c_{10}+2c_{11}+c_{12})]}{\partial t} = (c_4-c_5-c_6+c_{10}+2c_{11}+c_{12})\frac{\partial\varepsilon}{\partial t} + \varepsilon(gc_3\cdot\frac{\partial c_3}{\partial t} + gc_4\cdot\frac{\partial c_4}{\partial t} + gc_9\cdot\frac{\partial c_9}{\partial t}) \quad \text{(B.2)}$$

where:

$$gc_3 = \frac{\partial(c_4-c_5-c_6+c_{10}+2c_{11}+c_{12})}{\partial c_3} = \frac{c_{12}-c_6}{c_3}, \quad \text{(B.2a)}$$

$$gc_4 = \frac{\partial(c_4-c_5-c_6+c_{10}+2c_{11}+c_{12})}{\partial c_4} = 1 + \frac{c_5+c_6+c_{10}+4c_{11}+c_{12}}{c_4}, \quad \text{(B.2b)}$$

$$gc_9 = \frac{\partial(c_4-c_5-c_6+c_{10}+2c_{11}+c_{12})}{\partial c_9} = \frac{c_{10}+2c_{11}+c_{12}}{c_9}. \quad \text{(B.2c)}$$

Similar transformations as shown above are applied for Equation (24) to yield:

$$\frac{\partial[\varepsilon(c_9+c_{10}+c_{11}+c_{12})]}{\partial t} = (c_9+c_{10}+c_{11}+c_{12})\frac{\partial\varepsilon}{\partial t} + \varepsilon(hc_3\cdot\frac{\partial c_3}{\partial t} + hc_4\cdot\frac{\partial c_4}{\partial t} + hc_9\cdot\frac{\partial c_9}{\partial t}) \quad \text{(B.3)}$$

where:

$$hc_3 = \frac{\partial(c_9+c_{10}+c_{11}+c_{12})}{\partial c_3} = \frac{c_{12}}{c_3}, \tag{B.3a}$$

$$hc_4 = \frac{\partial(c_9+c_{10}+c_{11}+c_{12})}{\partial c_4} = \frac{c_{10}+2c_{11}+c_{12}}{c_4}, \tag{B.3b}$$

$$hc_9 = \frac{\partial(c_9+c_{10}+c_{11}+c_{12})}{\partial c_9} = 1 + \frac{c_{10}+c_{11}+c_{12}}{c_9}. \tag{B.3c}$$

APPENDIX C

ANALYTICAL SOLUTION TO THE EQUATION OF ELECTRONEUTRALITY FOR DIFFERENT CHEMISTRIES

Solution with Dissolved CO_2

In a CO_2-dissolved solution containing Na^+ and Cl^-, when the solution is saturated by $FeCO_3$ and the concentrations of Na^+, Cl^- and Fe^{2+} are given, an analytical solution exists for all other concentrations.

With dissolved CO_2 in solution, the equation of electroneutrality is:

$$\sum_{j=1}^{4} z_j c_j + z_9 \frac{K_{c1true} K_{c2} c_{11}}{c_4^2} + ((z_5 K_w + z_6 K_1 c_3) + (z_{10} + z_{12} \frac{c_3}{K_{cx}}) K_{c1true} c_{11}) \frac{1}{c_4} = 0 \qquad \text{(C.1a)}$$

or

$$c_4^3 + \frac{z_1 c_1 + z_2 c_2 + z_3 c_3}{z_4} c_4^2 + \frac{(z_5 K_w + z_6 K_1 c_3) + (z_{10} + z_{12} \frac{c_3}{K_{cx}}) K_{c1true} c_{11})}{z_4} c_4 + \frac{z_9 K_{c1true} K_{c2} c_{11}}{z_4} = 0 \qquad \text{(C.1b)}$$

A simplification of the above equation yields:

$$c_4^3 + p_1 c_4^2 + p_{10} c_4 + p_{20} = 0 \qquad \text{(C.2)}$$

The solution to the concentration of hydrogen ion is determined to be:

$$c_4 = -\frac{p_1}{3} - \frac{2^{\frac{1}{3}} p_2}{3 p_5} + \frac{p_5}{2^{\frac{1}{3}} 3} = \frac{p_5^2 - 2^{\frac{1}{3}} p_1 p_5 - 2^{\frac{2}{3}} p_2}{2^{\frac{1}{3}} 3 p_5} \qquad \text{(C.3)}$$

where:

$$p_5 = (p_3 + p_4)^{\frac{1}{3}}, \qquad \text{(C.3a)}$$

$$p_4 = \sqrt{4 p_2^3 + p_3^2}, \qquad \text{(C.3b)}$$

$$p_3 = -2 p_1^3 + 9 p_{10} p_1 - 27 p_{20}, \qquad \text{(C.3c)}$$

$$p_2 = -p_1^2 + 3 p_{10}, \qquad \text{(C.3d)}$$

$$p_1 = (z_1 c_1 + z_2 c_2 + z_3 c_3) / z_4, \qquad \text{(C.3e)}$$

$$p_{10} = [(z_5 K_w + z_6 K_1 c_3) + (z_{10} + z_{12} \frac{c_3}{K_{cx}}) K_{c1true} c_{11})] / z_4, \qquad \text{(C.3f)}$$

$$p_{20} = z_9 K_{c1true} K_{c2} c_{11} / z_4 \qquad \text{(C.3g)}$$

When the charge of Na^+, Cl^- and Fe^{2+} are balanced out so that $p_1 = 0$, the equation of electroneutrality can be simplified to:

$$c_4^3 + p_{10} c_4 + p_{20} = 0 \qquad \text{(C.4)}$$

and the analytical solution for the concentration of hydrogen ion is:

$$c_4 = -\frac{(\frac{2}{3})^{\frac{1}{3}} p_{10}}{\lambda} + \frac{\lambda}{18^{\frac{1}{3}}} \tag{C.5}$$

where

$$\lambda = (-9p_{20} + \sqrt{3}\sqrt{4p_{10}^3 + 27p_{20}^2})^{\frac{1}{3}}. \tag{C.6}$$

Solution without Dissolved CO_2

For a simple NaCl solution without dissolved CO_2, the solution can be saturated by $Fe(OH)_2$. When the concentrations of Na^+ and Cl^- are known, the concentration of hydrogen ion can be determined analytically.

The electroneutrality with this solution is:

$$z_1c_1 + z_2c_2 + z_3\frac{K_{sp}}{c_5^2} + z_4\frac{K_w}{c_5} + z_5c_5 + z_6\frac{K_1K_{sp}}{K_wc_5} = 0 \tag{C.7}$$

where $c_6 = K_1\frac{c_3}{c_4}$. Equation (C.7) can be reorganized to become:

$$c_5^3 + p_1c_5^2 + p_{10}c_5 + z_3K_{sp} = 0 \tag{C.8}$$

The analytical solution of Equation (C.8) for concentration of hydroxide ion is:

$$c_5 = -\frac{p_1}{3} - \frac{2^{\frac{1}{3}}p_2}{3p_5} + \frac{p_5}{2^{\frac{1}{3}}3} = \frac{p_5^2 - 2^{\frac{1}{3}}p_1p_5 - 2^{\frac{2}{3}}p_2}{2^{\frac{1}{3}}3p_5} \tag{C.9}$$

where:

$$p_5 = (p_3 + p_4)^{\frac{1}{3}}, \tag{C.9a}$$

$$p_4 = \sqrt{4p_2^3 + p_3^2}, \tag{C.9b}$$

$$p_3 = -2p_1^3 + 9p_{10}p_1 - 27p_{20}, \tag{C.9c}$$

$$p_2 = -p_1^2 + 3p_{10}, \tag{C.9d}$$

$$p_1 = (z_1c_1 + z_2c_2)/z_5, \tag{C.9e}$$

$$p_{10} = (z_4K_w + z_6\frac{K_1K_{sp}}{K_w})/z_5, \tag{C.9f}$$

$$p_{20} = z_3K_{sp}/z_5 \tag{C.9g}$$

With c_5 obtained, the concentrations of other species can be determined as:

$$c_4 = \frac{k_w}{c_5},\ c_3 = \frac{K_{sp}}{c_5^2},\ c_6 = \frac{K_1K_{sp}}{K_wc_5} \tag{C.10}$$

When the solution contains balanced NaCl, the equation of electroneutrality becomes:

$$2c_3 + c_4 + c_6 - c_5 = 0, \tag{C.11a}$$

or

$$2K_{sp} + (K_w + \frac{K_1 K_{sp}}{K_w})c_5 - c_5^3 = 0 \tag{C.11b}$$

The solution for the concentration of hydroxide ion in Equation (71) is:

$$c_5 = \frac{2^{\frac{1}{3}}(k_w + \frac{K_1 K_{sp}}{K_w})}{\lambda_2} + \frac{\lambda_2}{3 \cdot 2^{\frac{1}{3}}} \text{ and } c_3 = \frac{k_{sp}}{c_5^2} \tag{C.12}$$

where:

$$\lambda_1 = 6\sqrt{81k_{sp}^2 - 3(k_w + \frac{K_1 K_{sp}}{K_w})^3}\ , \tag{C.12a}$$

$$\lambda_2 = (\lambda_1 + 54k_{sp})^{\frac{1}{3}}\ . \tag{C.12b}$$

APPENDIX D

ANALYTICAL SOLUTION TO THE OPEN CIRCUIT POTENTIAL

There is an analytical solution to the electrode potential at the steel surface in open circuit condition. The following equation must be satisfied:

$$i_{Fea} + i_{Fec} + i_{H} + i_{H_2O} + i_{H_2CO_3} = 0 \tag{D.1}$$

Let

$$p = 10^{\frac{E_{s0}}{b_H}}. \tag{D.2}$$

Since

$$m = \frac{b_H}{b_{Fea}} = 3, \tag{D.3}$$

substituting Equation (40-43) into Equation (44) yields:

$$i^0_{Feref} p^{(m+1)} 10^{\frac{-E^{Eqref}_{Fe}}{b_{Fea}}} - (i^0_{Href} \frac{c_{04}}{c_{4ref}} 10^{\frac{E^{Eqref}_{H}}{b_H}} + i^0_{H_2Oref} 10^{\frac{E^{Eqref}_{H_2O}}{b_{H_2O}}} + i^0_{H_2CO_3ref} \frac{c_{011}}{c_{11ref}} (\frac{c_{04}}{c_{4ref}})^{-0.5} 10^{\frac{E^{Eqref}_{H_2CO_3}}{b_{H_2CO_3}}}) = 0 \tag{D.4}$$

The solution of p is:

$$p = [\frac{10^{\frac{E^{Eqref}_{Fe}}{b_{Fea}}} i_{ctot}}{i^0_{Feref}}]^{\frac{1}{m+1}} \tag{D.5}$$

where

$$i_{ctot} = i^0_{Href} \frac{c_{04}}{c_{4ref}} 10^{\frac{E^{Eqref}_{H}}{b_H}} + i^0_{H_2Oref} 10^{\frac{E^{Eqref}_{H_2O}}{b_{H_2O}}} + i^0_{H_2CO_3ref} \frac{c_{011}}{c_{11ref}} (\frac{c_{04}}{c_{4ref}})^{-0.5} 10^{\frac{E^{Eqref}_{H_2CO_3}}{b_{H_2CO_3}}} \tag{D.6}$$

With p, the electrode potential at time zero is:

$$E_{s0} = b_H \log_{10}(p) \text{ -0.316 vs. CSE,} \tag{D.7}$$

An alternative but equivalent method to solve for the open circuit potential is given below. This method requires the open circuit potential at time zero, denoted by E_{s0}, to be solved first as is done above in this appendix. With this E_{s0} determined, the electrode potential (E_s) at any arbitrary time may be defined as:

$$E_s = E_{s0} - \varphi_s \tag{D.8}$$

where φ_s simply means the shift of the electrode potential from its value at time zero.

With the initial porosity of 1 everywhere in the boundary layer, the half cell current densities may be expressed by:

$$i_{corr} = \varepsilon i_{corr0} 10^{\frac{-\varphi_s}{b_{Fea}}} \tag{D.9}$$

$$i_H = \varepsilon i_{H0} \frac{c_{4s}}{c_{04}} 10^{\frac{\varphi_s}{b_H}} \tag{D.10}$$

$$i_{H_2O} = \varepsilon i_{H_2O0} 10^{\frac{\varphi_s}{b_{H_2O}}} \tag{D.11}$$

$$i_{H_2CO_3} = -\varepsilon i_{H_2CO_3 0} \frac{c_{11s}}{c_{011}} \left(\frac{c_{4s}}{c_{04}}\right)^{-0.5} 10^{\frac{\varphi_s}{b_{H_2CO_3}}} \tag{D.12}$$

where

$$i_{H0} = -i^0{}_{Href} \frac{c_{4s0}}{c_{4ref}} 10^{\frac{-(E_{s0}-E_H^{Eqref})}{b_H}}, \tag{D.13}$$

$$i_{H_2O0} = -i^0{}_{H_2Oref} 10^{\frac{-(E_{s0}-E_{H_2O}^{Eqref})}{b_{H_2O}}}, \tag{D.14}$$

and

$$i_{H_2CO_3 0} = -i^0{}_{H_2CO_3 ref} \frac{c_{11s0}}{c_{11ref}} \left(\frac{c_{4s0}}{c_{4refCA}}\right)^{-\frac{0.5}{n_{H_2CO_3}}} 10^{\frac{-(E_{s0}-E_{H_2CO_3}^{Eqref})}{b_{H_2CO_3}}}. \tag{D.15}$$

When the corrosion is at the open circuit condition, the following equation must be satisfied:

$$i_{corr} + i_H + i_{H_2O} + i_{H_2CO_3} = 0 \tag{D.16}$$

φ_s is obtained. From the φ_s, the electrode potential E_{s0}-φ_s at any time t can be determined. This is done as presented below.

Let

$$q = 10^{\frac{-\varphi_s}{b_H}}. \tag{D.17}$$

Equation (53) becomes:

$$i_{Fe0} 10^{\frac{-\varphi_s}{b_{Fea}}} + i_{H0} \frac{c_{4s}}{c_{04}} 10^{\frac{\varphi_s}{b_H}} + i_{H_2O0} 10^{\frac{\varphi_s}{b_{H_2O}}} + i_{H_2CO_3 0} \frac{c_{11s}}{c_{011}} \left(\frac{c_{4s}}{c_{04}}\right)^{-0.5} 10^{\frac{\varphi_s}{b_{H_2CO_3}}} = 0 \tag{D.18a}$$

or

$$i_{Fe0a} q^{(m+1)} + i_{H0} \frac{c_{4s}}{c_{04}} + i_{H_2O0} + i_{H_2CO_3 0} \frac{c_{11s}}{c_{011}} \left(\frac{c_{4s}}{c_{04}}\right)^{-0.5} = 0 \tag{D.18b}$$

The solution is:

$$q = \left(-\frac{i_{H0}\frac{c_{4s}}{c_{04}} + i_{H_2O0} + i_{H_2CO_3 0}\frac{c_{11s}}{c_{011}}\left(\frac{c_{4s}}{c_{04}}\right)^{-0.5}}{i_{Fe0a}}\right)^{\frac{1}{m+1}} \tag{D.19a}$$

and

$$\varphi_s = -b_H \log_{10}(q) \tag{D.19b}$$

When ψ is defined as the electrode potential at time zero or $\psi = E_0$, the third way of defining the reference condition as shown in Table 3.

$$\phi_s = \varphi_s \tag{D.20}$$

When q is obtained, φ_s in Equation (D.19b) can determined, which can be substituted into Equations (D9-D12) to determine the anodic and cathodic current densities.

At OCP, $i_{netE} = 0$. A boundary condition for the Possion's equation may be written as:

$$\xi\varepsilon\frac{\partial\varphi}{\partial x} = \xi\frac{i_{diff}}{\kappa} \tag{D.21}$$

TABLE 1
CONCENTRATIONS AND GRADIENTS OF SECONDARY SPECIES
EXPRESSED BY THOSE OF THE PRIMARY

c_j	$\partial c_j / \partial c_3$	$\partial c_j / \partial c_4$	$\partial c_j / \partial c_9$
$c_5 = k_w / c_4$	0	$-c_5 / c_4$	0
$c_6 = k_1 c_3 / c_4$	c_6 / c_3	$-c_6 / c_4$	0
$c_{10} = c_4 c_9 / K_{c2}$	0	c_{10} / c_4	c_{10} / c_9
$c_{11} = c_4^2 c_9 / K_{c1} K_{c2}$	0	$2c_{11} / c_4$	c_{11} / c_9
$c_{12} = c_3 c_4 c_9 / K_{c2} K_{cx}$	c_{12} / c_3	c_{12} / c_4	c_{12} / c_9
$\sum c_j$	$\sum \partial c_j / \partial c_3$	$\sum \partial c_j / \partial c_4$	$\sum \partial c_j / \partial c_9$
$c_3 + c_6 + c_{12}$	$fc_3 = 1 + \frac{c_6 + c_{12}}{c_3}$	$fc_4 = \frac{c_{12} - c_6}{c_4}$	$fc_9 = \frac{c_{12}}{c_9}$
$c_4 - c_5 - c_6 + c_{10} + 2c_{11} + c_{12}$	$gc_3 = \frac{c_{12} - c_6}{c_3}$	$gc_4 = 1 + \frac{c_5 + c_6 + c_{10} + 4c_{11} + c_{12}}{c_4}$	$gc_9 = \frac{c_{10} + 2c_{11} + c_{12}}{c_9}$
$c_9 + c_{10} + c_{11} + c_{12}$	$hc_3 = \frac{c_{12}}{c_3}$	$hc_4 = \frac{c_{10} + 2c_{11} + c_{12}}{c_4}$	$hc_9 = 1 + \frac{c_{10} + c_{11} + c_{12}}{c_9}$

TABLE 2
INITIAL AND BOUNDARY CONDITIONS FOR THE MODEL SYSTEM

Primary Species/Potential		Dynamic system (wet gas)			Static system (dry gas)		
		Initial	Sol. bnd.	Steel boundary	Initial	Sol. bnd.	Steel boundary
Species 1		$c_1 = c_{01}$	$c_1 = c_{11}$	$N_1 = 0$	$c_1 = c_{01}$	$N_1 = 0$	$N_1 = 0$
Species 2		$c_2 = c_{02}$	$c_2 = c_{12}$	$N_2 = 0$	$c_2 = c_{02}$	$N_2 = 0$	$N_2 = 0$
Species 3		$c_3 = c_{03}$	$c_3 = c_{13}$	$N_3 + N_6 + N_{12} = r_{corr}$	$c_3 = c_{03}$	$N_3 + N_6 + N_{12} = 0$	$N_3 + N_6 + N_{12} = r_{corr}$
Species 4		$c_4 = c_{04}$	$c_4 = c_{14}$	$N_4 - N_5 - N_6 + N_{10} + 2N_{11} + N_{12} = r_H + r_{H_2O} + r_{H_2CO_3} + 4r_{O_2}$	$c_4 = c_{04}$	$N_4 - N_5 - N_6 + N_{10} + 2N_{11} + N_{12} = 0$	$N_4 - N_5 - N_6 + N_{10} + 2N_{11} + N_{12} = r_H + r_{H_2O} + r_{H_2CO_3} + 4r_{O_2}$
Species 7		$c_7 = c_{07}$	$c_7 = c_{17}$	$N_7 = 0$	$c_7 = c_{07}$	$c_7 = c_{17}$	$N_7 = 0$
Species 8		$c_8 = c_{08}$	$c_8 = c_{18}$	$N_8 = r_{O_2}$	$c_8 = c_{08}$	$c_8 = c_{18}$	$N_8 = r_{O_2}$
Species 9		$c_9 = c_{09}$	$c_9 = c_{19}$	$N_9 = 0$	$c_9 = c_{09}$	$N_9 = 0$	$N_9 = 0$
Potential	Electroneutrality	/	$\phi_b = 0$	$\sum_j z_j N_j = 2r_{Fe} + r_H + r_{H_2O} + r_{H_2CO_3} + 4r_{O_2}$	/	$\phi_b = 0$	$\sum_j z_j N_j = 2r_{Fe} + r_H + r_{H_2O} + r_{H_2CO_3} + 4r_{O_2}$
	or Poisson's eqn	/	$\phi_b = 0$	$\phi_x = (-i_{net} + i_{diff})/\kappa$	/	$\phi_b = 0$	$\phi_x = (-i_{net} + i_{diff})/\kappa$

TABLE 3

BOUNDARY CONDITIONS FOR ϕ FOR THREE TYPES OF REFERENCE CONDITIONS (POISSON'S EQUATION)

$\phi_s=0$ ($\psi=E_s$, $E_b=E_s-\phi_b$)			$\phi_b=0$ ($\psi=E_b$, $E_s=E_b-\phi_s$)			$\psi=E_0$ ($E_b=E_0-\phi_b$, $E_s=E_0-\phi_s$)		
i_{net} known	E_b given	E_s given	i_{net} known	E_b given	E_s given	i_{net} known	E_b given	E_s given
$\phi_{xb}=(-i_{net}+i_{diffb})/\kappa$	$E_s=E_b+\phi_b$	$\phi_{xb}=(-i_{net}+i_{diffb})/\kappa$	$\phi_{xs}=(-i_{net}+i_{diffs})/\kappa$	$E_s=E_b-\phi_s$	$\phi_{xs}=(-i_{net}+i_{diffs})/\kappa$	$\phi_{xb}=(-i_{net}+i_{diffb})/\kappa$	$\phi_b=E_0-E_b$	$\phi_s=E_0-E_s$
/	$\phi_{xb}=(-i_{net}+i_{diffb})/\kappa$	/	/	$\phi_{xs}=(-i_{net}+i_{diffs})/\kappa$	/	$E_s=E_0-\phi_s$	$E_s=E_0-\phi_s$	$\phi_{xb}=(-i_{net}+i_{diffb})/\kappa$
$E_{corr}=E_s$	/	$E_{corr}=E_s$	$E_{corr}=E_s$	/	$E_{corr}=E_s$	$E_{corr}=E_s$	$\phi_{xs}=(-i_{net}+i_{diffs})/\kappa$	$E_{corr}=E_s$
$E_b=E_s-\phi_b$	$E_{corr}=E_s$	$E_b=E_s-\phi_b$	$E_b=E_s+\phi_s$	$E_{corr}=E_s$	$E_b=E_s+\phi_s$	$E_b=E_0-\phi_b$	$E_{corr}=E_s$	$E_b=E_0-\phi_b$
$E=E_s-\phi$	$E=E_s-\phi$	$E=E_s-\phi$	$E=E_b-\phi$	$E=E_b-\phi$	$E=E_b-\phi$	$E=E_0-\phi$	$E=E_0-\phi$	$E=E_0-\phi$
i_{net}=cons. E_s dtm fr i_{net}	$i_{net}=f(Es)$		i_{net}=cons. E_s dtm fr i_{net}	$i_{net}=f(Es)$		i_{net}=cons. ϕ_s dtm fr i_{net}	$i_{net}=f(Es)$	

TABLE 4
CONSTANTS AND VALUES OF PARAMETERS USED FOR THE MODELING

Parameter	*Value*	*Unit*	*Explanation*	*Reference*
System conditions				
T	given	K	System temperature	
p	given	atm	System pressure	
Tref	298.15	K	Reference temperature	
σ	10^5	m^{-1}	Specific surf. area of precipitate	34
Constants				
F	96485	C/mol	Faraday's constant	35
R	8.3143	J/mol·K	Gas constant	35
Thermodynamic constants				
K_w	$=10^{\frac{-4470.99}{T}+12.0875-0.01706T}$	$(mol/m^3)^2$	Water ionic product	35
K_1	below	mol/m^3	Equilibrium constant for $Fe^{2+}+H_2O \rightarrow Fe(OH)^+ + H^+$	OLI
	$10^{-3}(2.68572\times10^{-8}T^3-2.30864\times10^{-5}T^2+6.6226\times10^{-3}T-0.6338125)$			
K_{c1}	$=10^{\frac{-3404.71}{T}+17.8435-0.032786T}(1+\frac{1}{K_h})$	mol/m^3	First dissociation cons. of H_2CO_3	35
K_{c2}	$=10^{\frac{-2902.39}{T}+9.498-0.02379T}$	mol/m^3	2nd diss. Cons. of H_2CO_3	35
K_{csp}	$=10^{-53.2385-0.041377T-\frac{2.1963}{T}+24.5724\log10(T)}$	$(mol/m^3)^2$	Solubility product of $FeCO_3$	36,37
K_{cx}	below	mol/m^3	Equilibrium constant for $Fe(HCO_3)^+ \rightarrow H^+ + HCO_3^-$	OLI
	$=10^3(1.8253\times10^{-5}T^3-0.018926T^2+6.3421T-669.26)$			
K_{href}	1/600	(/)	CO_2 hydration constant at T_{ref}	38
K_h	$=K_{href}\exp(\frac{-4180}{R}(\frac{1}{T_{ref}}-\frac{1}{T}))$	(/)	CO_2 hydration constant at T	38
K_{spref}	1.82×10^{-6}	$(mol/m^3)^3$	Solubility prod.of $Fe(OH)_2$ at T_{ref}	35

K_{sp} $= K_{spref}\exp(\frac{20600}{R}(\frac{1}{T_{ref}} - \frac{1}{T}))$ $(mol/m^3)^3$ Solubility prod. of $Fe(OH)_2$ at T 39

H_{O_2} below $atm \cdot m^3/mol$ Henry's law constant for O_2 40

$= 10^{-3}\exp(-\frac{0.046T^2 + 203.35T\log_{10}(T/Tref) - (299.378 + 0.092T)(T - Tref) - 20591}{RT})$

H_{CO_2} below $atm \cdot m^3/mol$ Henry's law constant for CO_2 35

$= 0.02941\exp(-\frac{-159.854 + \frac{8741.68}{T} + 21.6694\log_{10}(T) - 0.00110261T}{RT}(1 - \frac{T}{T_{ref}}))$

Solution Properties

μ_{H_2Oref} 8.9×10^{-4} m^2/s water viscosity at T_{ref} 41

$\mu_{H_2O} = \mu_{H_2Oref}10^{(1.3272(T_{ref} - T) - 0.001053(T_{ref} - T)^2)/(T+105)}$ m^2/s water viscosity at T 41

$\rho_{H_2O} = 753.596 + 1.87748T - 0.003564T^2$ kg/m^3 water viscosity 41

ξ_{sol} below m^2/s water dielectric resistance 41

$= \frac{10^{-9}}{36\pi}(249.21 - 0.79069T + 0.0007299T^2)$

Diffusion coefficients

D_{Na^+ref} 1.334×10^{-9} m^2/s diffusivity of Na^+ at T_{ref} 30

D_{Cl^-ref} 2.032×10^{-9} m^2/s diffusivity of Cl^- at T_{ref} 30

$D_{Fe^{2+}ref}$ 0.8×10^{-9} m^2/s diffusivity of Fe^{2+} at T_{ref} 42

D_{H^+ref} 9.312×10^{-9} m^2/s diffusivity of H^+ at T_{ref} 30

D_{OH^-ref} 5.26×10^{-9} m^2/s diffusivity of OH^- at T_{ref} 30

$D_{Fe(OH)^+ref}$ 2.5×10^{-9} m^2/s diffusivity of $Fe(OH)^+$ at T_{ref} #

$D_{CO_3^{2-}ref}$ 10^{-9} m^2/s diffusivity of CO_3^{2-} at T_{ref} 42

$D_{HCO_3^-ref}$ 10^{-9} m^2/s diffusivity of HCO_3^- at T_{ref} 30

$D_{Fe(HCO_3)^+ref}$ 10^{-9} m^2/s diffusivity of $Fe(HCO_3)^+$ at T_{ref} #

$D_{H_2CO_3ref}$	2.00×10^{-9}	m^2/s	diffusivity of H_2CO_3 at T_{ref}	42
D_{CO_2ref}	1.96×10^{-9}	m^2/s	diffusivity of CO_2 at T_{ref}	43
D_j	$D_j = D_{jRef}\frac{T}{T_{Ref}}\frac{\mu_{H_2O\,Ref}}{\mu_{H_2O}}$	m^2/s	diffusivity above species at T	43
D_{O_2}	below	m^2/s	diffusivity of O_2	40

$$=1.363\times10^{-6}\exp\left(\frac{-14277-4.661\times10^{19}\,T^{-6.8132}}{RT}\right)$$

Kinetic Rate Constants

$k_{CO2bref}$	18	(1/s)	CO_2 hydr. back react. cons. at T_{ref}	38
k_{CO2b}	$=18\exp\left(\frac{66880}{RT}\left(\frac{T}{T_{ref}}-1\right)\right)$	(1/s)	CO_2 hydr. back react. cons. at T	39
K_{CO2f}	$k_{CO2b}\times K_h$	(1/s)	CO_2 hydr. back react. cons. at T	38
K_p	$=\exp\left(28.2-\frac{64851.4}{RT}\right)$	(m^4/mol/s)	$FeCO_3$ precipitation rate cons.	44

Precipitate density and molar weight

ρ_{FeCO3}	3900	(Kg/m^3)	$FeCO_3$	44
M_{FeCO3}	0.116	(Kg/mol)	$FeCO_3$	39
$\rho_{Fe(OH)2}$	7800	(Kg/m^3)	$Fe(OH)_2$	##
$M_{Fe(OH)2}$	0.056	(Kg/mol)	$Fe(OH)_2$	39

Standard potentials and enthalpies

E_{Feref}^{0}	-0.756	V_{CSE}	Standard potential of iron oxidation	35
ΔH_{Fe}^{0}	87,800	J/mol	Thermal enthalpy of iron oxidation	39
$E_{H^+ref}^{0}$ (pH=0)	-0 .316	V_{CSE}	Standard potential of H^+ reduction	35
$\Delta H_{H^+}^{0}$	0	J/mol	Thermal enthalpy of H^+ reduction	39
$E_{H_2Oref}^{0}$ (pH=0)	-1.145	V_{CSE}	Standard potential of H_2O reduction	35
$\Delta H_{H_2O}^{0}$	56,000	J/mol	Thermal enthalpy of H_2O reduction	39
$E_{H_2CO_3ref}^{0}$ (pH=0)	-0 .693	V_{CSE}	Standard potential of H_2CO_3 reduction	35

$\Delta H_{H_2CO_3}^{0}$	9396.6	J/mol	Thermal enthalpy of H_2CO_3 reduction	39
$E_{O_2ref}^{0}$ (pH=14)	0.085	V_{CSE}	Standard potential of O_2 reduction	35
$\Delta H_{O_2}^{0}$	-347,800	J/mol	Thermal enthalpy of O_2 reduction	39
$E_j^{0} = \frac{TE_{jref}^{0}}{T_{ref}} - \frac{\Delta H_j^{0}}{n_j F}(1 - \frac{T}{T_{ref}})$		V_{CSE}	Standard potential of O_2 reduction	xx

Number of electrons transferred

n_{Fe}	2	/	No. of electron transfer of iron oxid.	45
n_{H_2O}	1	/	No. of electron transfer of H_2O reduc.	35
n_{H^+}	1	/	No. of electron transfer of H^+ reduc.	35
$n_{H_2CO_3}$	1	/	No. of electron transfer of H_2CO_3 reduc.	34
n_{O_2}	4	/	No. of electron transfer of O_2 reduc.	45

Exchange current densities and enthalpies

$i_{Fe_ref}^{0}$ (c_{3ref}=0.01 mol/m^3)	0.002*	A/m^2	Exchange curr. dens. of iron oxid. at T_{ref}	34,46-49
E_{Fe}	37,500	J/mol	Activation energy of iron oxid. at T_{ref}	34
$i_{H^+ref_ref}^{0}$ (c_{H^+ref}=0.1/200 mol/m^3)*	0.05	A/m^2	Exchange curr. dens. of H^+ red. at T_{ref}	34
E_{H^+}	30,000	J/mol	Activation energy of H^+ redu. at T_{ref}	34
$i_{H_2O_ref}^{0}$	0.002	A/m^2	Exchange curr. dens. of H_2O redu. at T_{ref}	34
E_{H_2O}	35,000	J/mol	Activation energy of H_2O redu. at T_{ref}	#
$i_{H_2CO_3ref_ref}^{0}$ ($c_{H_2CO_3ref}$ =0.1 mol/m^3 and $c_{CA_H^+ref} = c_{H^+ref}$*)	0.06	A/m^2	Exchange curr. dens. of H_2CO_3 redu. at T_{ref}	34 34

$E_{H_2CO_3}$	56,000*	J/mol	Activation energy of H_2CO_3 redu. at T_{ref}	34
$i^0_{O_2ref_ref}$		4.0×10^{-9}	A/m^2 Exchange curr. dens. of O_2 redu. at T_{ref}	45
(pH=9, $p_{O_2\,ref}$ =1atm)				
E_{O_2}	40,000	J/mol	Activation energy of O_2 redu. at T_{ref}	#
i^0_{jref}	$= i^0_{jref} \frac{E_j}{RT}(1-\frac{T}{T_{ref}})$	V_{CSE}	Exchange curr. dens. at T	xx
Tafel slopes				
b_{Feref}	0.04	V/decade	Iron oxidation	34,45,50
b_{Fecref}	0.12	V/decade	Ferrous ion reduction	51
b_{H_2Oref}	0.12	V/decade	H_2O reduction	34
b_{H^+ref}	0.12	V/decade	H^+ reduction	34
b_{O_2ref} (pH=9)	0.12	V/decade	O_2 reduction	45
b_j	$= b_{jref} \frac{T}{T_{ref}}$	V/decade	O_2 reduction	xx

#: estimated, *Modified from original value given elsewhere.

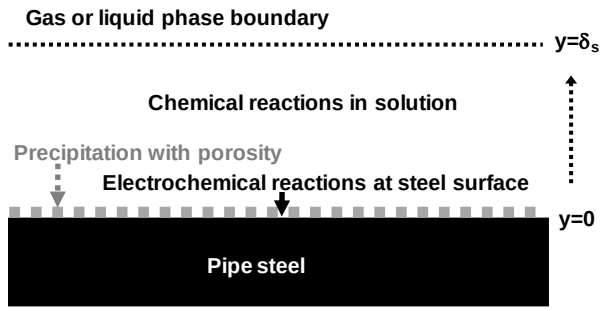

Figure 1. Schematic diagram showing the chemical, electrochemical, mineral (precipitation) reactions that may occur in a boundary layer or at pipe steel surface.

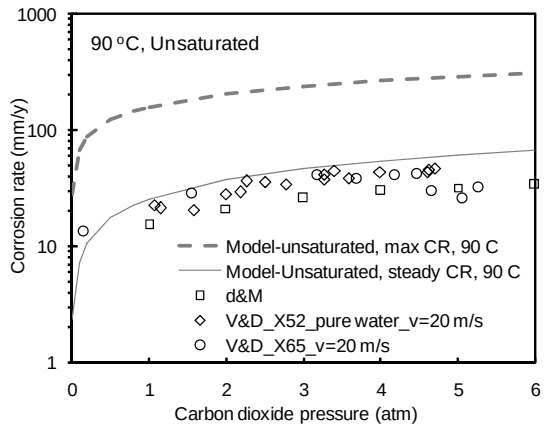

Figure 2. Model-predicted maximum (or initial) and steady state corrosion rates vs. experimental data measured in an unsaturated solution at 90 °C in a flowing system.[1,5]

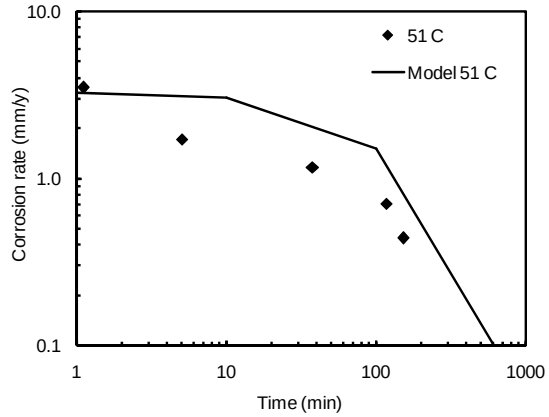

Figure 3. Model predicted time-dependent corrosion rates vs. experimental data measured in a solution initially saturated by ferrous carbonate at 51 °C.[6]

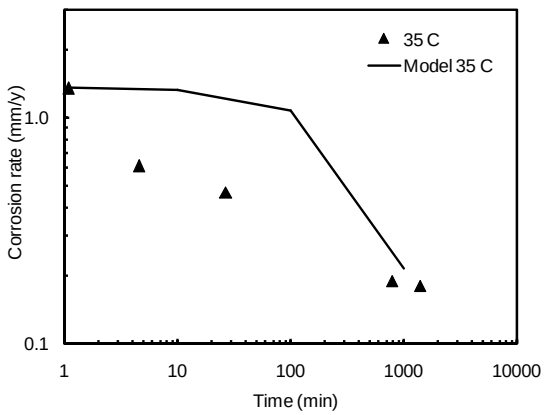

Figure 4. Model predicted time-dependent corrosion rates vs. experimental data measured in a solution initially saturated by ferrous carbonate at 35 °C.[6]

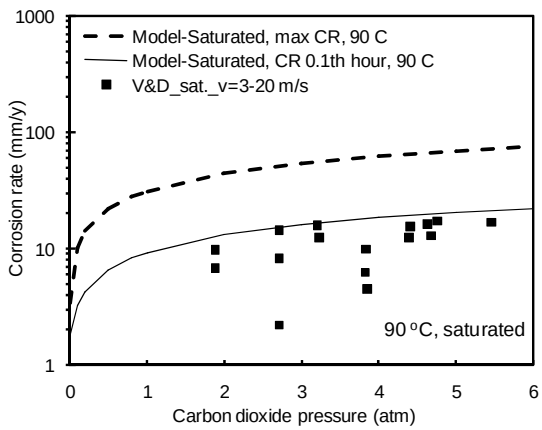

Figure 5. Model-predicted maximum (or initial) and at 0.1th hour instant corrosion rates vs. experimental data measured in a saturated solution at 90 °C.[6]

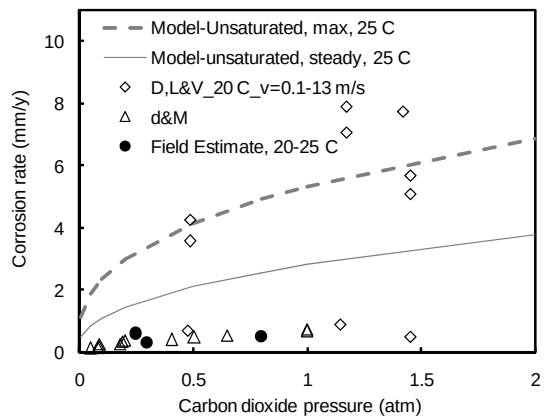

Figure 6. Model-predicted maximum (or initial) and steady state corrosion rates vs. experimental data measured in lab[1,7] and estimated from field[3] in an unsaturated solution at 25 °C with flow.

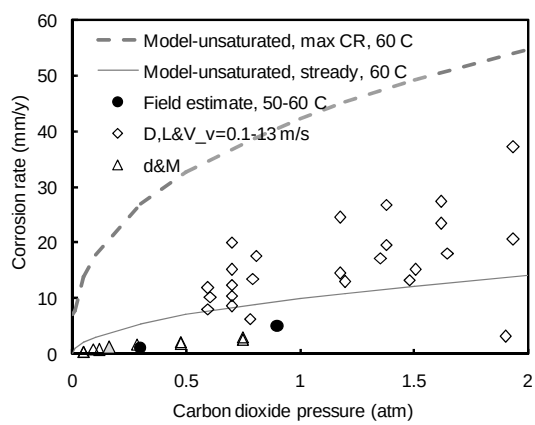

Figure 7. Model-predicted maximum (or initial) and steady state corrosion rates vs. experimental data measured in lab[7] and estimated from field[3] in an unsaturated solution at 60 °C with flow.

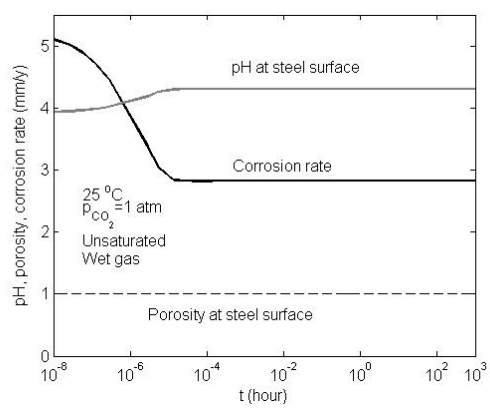

Figure 8. Model predicted corrosion rates for both wet and dry gas systems at 25 °C and p_{CO2}=1 atm. The boundary layer thickness is 10 μm and initially contains negligible ferrous ion.

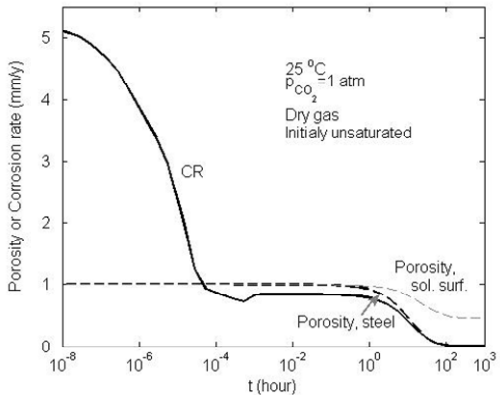

Figure 9. Predicted corrosion rates and porosity for only the dry gas system at the same condition of Figure 8.

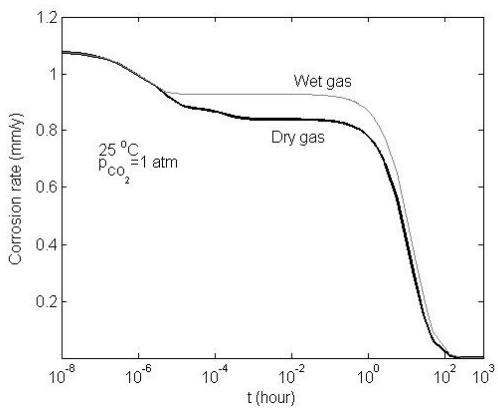

Figure 10. Model predicted corrosion rates for both wet and dry gas systems at 25 °C and p_{CO2}=1 atm. The boundary layer thickness is 10 μm and it is initially saturated with ferrous carbonate. For wet gas, the bulk solution is also saturated with ferrous carbonate.

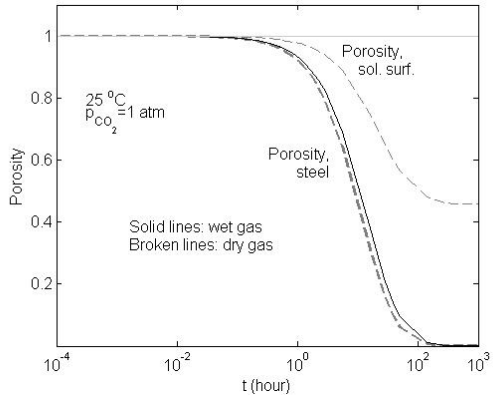

Figure 11. For the same conditions of Figure 10, the porosity variations with time for both wet and dry gas systems.

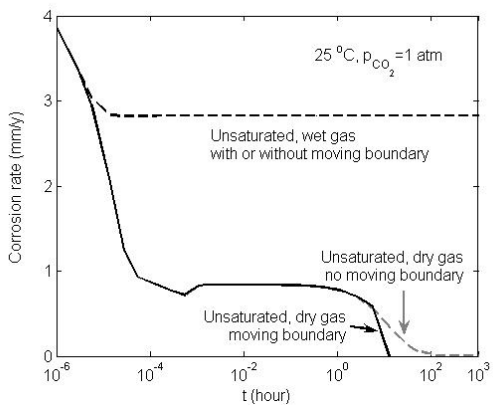

Figure 12. For wet and dry gas systems, predicted corrosion rates when the solution is unsaturated, and when the boundaries are considered moving and not moving.

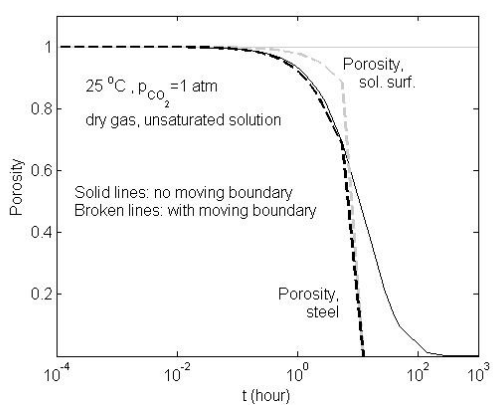

Figure 13. For wet and dry gas systems, predicted corrosion rates when the solution is unsaturated, and when the boundaries are considered moving and not moving.

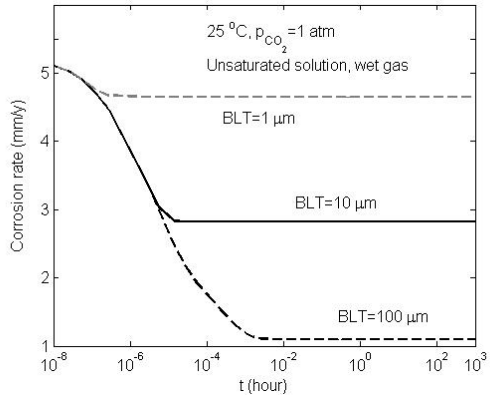

Figure 14. For a wet gas system, predicted corrosion rates when the boundary layer is unsaturated and its thickness varies by flow.

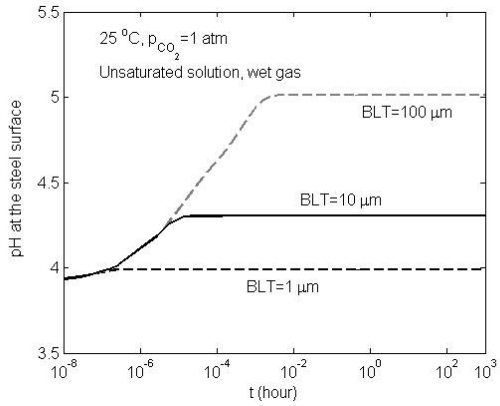

Figure 15. For a wet gas system, predicted pHs for the same condition of Figure 14.

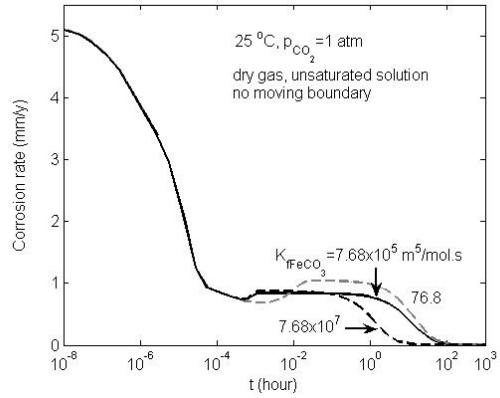

Figure 16. For a dry gas system, predicted corrosion rates for an initially unsaturated boundary layer and the effect by the use of different precipitation rate constants of ferrous carbonate.

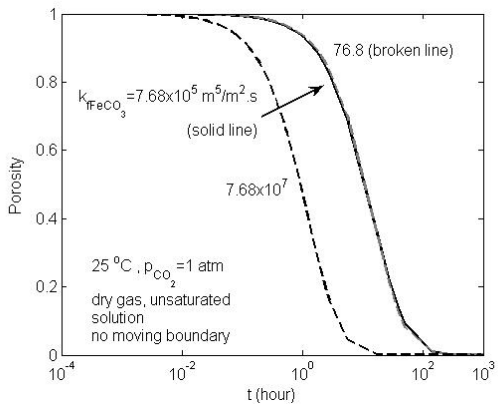

Figure 17. For a dry gas system, predicted porosity at the steel surface for the same condition of Figure 16.